

24P
M14
P

NATIONAL AERONAUTICS AND SPACE ADMINISTRATION

The Deep Space Network Progress Report 42-20

January and February 1974

(NASA-CR-138077) THE DEEP SPACE NETWORK
Progress Report, Jan. - Feb. 1974 (Jet
Propulsion Lab.) 201 p HC \$13.25

N74-21494

CSCL 20D

G3/30

Unclas
36286



**JET PROPULSION LABORATORY
CALIFORNIA INSTITUTE OF TECHNOLOGY
PASADENA, CALIFORNIA**

April 15, 1974

NATIONAL AERONAUTICS AND SPACE ADMINISTRATION

*The Deep Space Network
Progress Report 42-20*

January and February 1974

JET PROPULSION LABORATORY
CALIFORNIA INSTITUTE OF TECHNOLOGY
PASADENA, CALIFORNIA

April 15, 1974

**Prepared Under Contract No. NAS 7-100
National Aeronautics and Space Administration**

Preface

Beginning with Volume XX, the Deep Space Network Progress Report will change from the Technical Report 32- series to the Progress Report 42- series. The volume number will continue the sequence of the preceding issues. Thus, Progress Report 42-20 is the twentieth volume of the Deep Space Network series, and is an uninterrupted follow-on to Technical Report 32-1526, Volume XIX.

This report presents DSN progress in flight project support, TDA research and technology, network engineering, hardware and software implementation, and operations. Each issue presents material in some, but not all, of the following categories in the order indicated:

Description of the DSN

Mission Support

- Interplanetary Flight Projects
- Planetary Flight Projects
- Manned Space Flight Projects
- Advanced Flight Projects

Radio Science

Supporting Research and Technology

- Tracking and Ground-Based Navigation
- Communications, Spacecraft/Ground
- Station Control and Operations Technology
- Network Control and Data Processing

Network Engineering and Implementation

- Network Control System
- Ground Communications
- Deep Space Stations

Operations and Facilities

- Network Operations
- Network Control System Operations
- Ground Communications
- Deep Space Stations
- Facility Engineering

In each issue, the part entitled "Description of the DSN" describes the functions and facilities of the DSN and may report the current configuration of one of the five DSN systems (Tracking, Telemetry, Command, Monitor and Control, and Test and Training).

The work described in this report series is either performed or managed by the Tracking and Data Acquisition organization of JPL for NASA.

Contents

DESCRIPTION OF THE DSN

DSN Functions and Facilities	1
N. A. Renzetti	
DSN Test and Training System	5
H. C. Thorman	
NASA Code 311-03-42-94	

MISSION SUPPORT

Planetary Flight Projects

Mariner Venus/Mercury 1973 Mission Support	13
E. K. Davis	
NASA Code 311-03-21-60	
Pioneer Venus 1978 Mission Support	17
R. B. Miller	
NASA Code 311-03-21-20	

SUPPORTING RESEARCH AND TECHNOLOGY

Tracking and Ground-Based Navigation

Short Baseline QVLBI Doppler Demonstrations—Part II	20
C. C. Chao, R. A. Preston, and H. E. Nance	
NASA Code 310-10-60-50	
Report of the Two-Station Doppler (VLBI) Demonstration Conducted With Mariner 9	27
B. D. Mulhall, C. C. Chao, D. E. Johnson, and J. W. Zielenbach	
NASA Code 310-10-60-50	
Redesign of High-Power Transmitter Control and Indicator Cards	41
J. R. Paluka and S. F. Moore	
NASA Code 310-10-64-01	
X-Band Radar Development	44
M. A. Gregg and R. B. Kolbly	
NASA Code 310-10-64-01	

Communications, Spacecraft/Ground

Microwave Maser Development: Automatic Monitoring of Closed Cycle Refrigerators for Masers	49
E. Wiebe	
NASA Code 310-20-66-01	

Contents (contd)

On DSN Antenna Scheduling	53
L. H. Harper, R. J. McEliece, and A. M. Odlyzko	
NASA Code 310-20-67-08	
S/X Experiment: A New Configuration for Ground System Range Calibrations With the Zero Delay Device	57
T. Y. Otoshi and C. T. Stelzried	
NASA Code 310-20-66-06	
S/X Band Experiment: Zero Delay Device Antenna Location	64
C. T. Stelzried, T. Y. Otoshi, and P. D. Batelaan	
NASA Code 310-20-66-06	
DSS Tests of Sequential Decoding Performance	69
J. W. Layland	
NASA Code 310-20-67-08	
S/X-Band Experiment: Zero Delay Device Z Correction	78
P. T. Batelaan	
NASA Code 310-20-66-06	
Preliminary S-Band Noise Temperature Statistics at DSS 14 for 1971 and 1972	84
R. W. D. Booth, M. S. Reid, and T. J. Cullen	
NASA Code 310-20-66-06	
Shaped Antenna Designs and Performance for 64-m Class DSN Antennas	92
P. D. Potter	
NASA Code 310-20-65-03	
Antenna Bias Rigging for Mission-Dependent Performance Objective	112
R. Levy	
NASA Code 310-20-65-01	

Station Control and Operations Technology

Fourth Harmonic Analyzer	121
R. H. Smith	
NASA Code 310-30-68-11	
DSN Research and Technology Support	124
E. B. Jackson	
NASA Code 310-30-69-02	
Cost Effective Spares Provisioning for the Deep Space Network	128
I. Eisenberger, F. Maiocco, and G. Lorden	
NASA Code 310-30-69-01	
Automated Pulsar Receiver	135
C. F. Foster	
NASA Code 310-30-68-10	

Contents (contd)

Open-Loop Receiver/Predetection Recording System for the DSN	139
S. S. Kent and A. G. Slekys	
NASA Code 310-30-68-06	

Network Control and Data Processing

High-Speed Data Block Bursts	149
J. P. McClure	
NASA Code 310-40-70-03	

NETWORK ENGINEERING AND IMPLEMENTATION

Deep Space Stations

Helios Spin Modulation Simulation Tests	154
N. C. Ham	
NASA Code 311-03-42-47	
DSN Programmed Oscillator	167
M. R. Wick	
NASA Code 311-03-42-52	

OPERATIONS AND FACILITIES

Network Operations

DSN Data Record Generation	178
E. C. Gatz	
NASA Code 311-03-42-94	

Deep Space Stations

Short-Term Frequency Measurement Capability in DSN Equipment Maintenance Facilities	182
R. M. Smith, D. Crawford, and C. H. Fournier	
NASA Code 311-03-14-64	
Verification of Commands From the Transmitting Medium	186
J. R. Lesh	
NASA Code 311-03-14-52	
Tracking Operations During the Pioneer 10 Encounter	190
A. L. Berman	
NASA Code 311-03-12-40	

DSN Functions and Facilities

N. A. Renzetti
Mission Support Office

The objectives, functions, and organization of the Deep Space Network are summarized. The Deep Space Instrumentation Facility, the Ground Communications Facility, and the Network Control System are described.

The Deep Space Network (DSN), established by the National Aeronautics and Space Administration (NASA) Office of Tracking and Data Acquisition under the system management and technical direction of the Jet Propulsion Laboratory (JPL), is designed for two-way communications with unmanned spacecraft traveling approximately 16,000 km (10,000 mi) from Earth to planetary distances. It supports or has supported, the following NASA deep space exploration projects: Ranger, Surveyor, Mariner Venus 1962, Mariner Mars 1964, Mariner Venus 67, Mariner Mars 1969, Mariner Mars 1971, Mariner Venus-Mercury 1973 (JPL); Lunar Orbiter and Viking (Langley Research Center); Pioneer (Ames Research Center); Helios (West Germany); and Apollo (Manned Spacecraft Center), to supplement the Spaceflight Tracking and Data Network (STDN).

The Deep Space Network is one of two NASA networks. The other, STDN, is under the system management and technical direction of the Goddard Space Flight Center. Its function is to support manned and unmanned Earth-orbiting and lunar scientific and communications satellites. Although the DSN was concerned with unmanned lunar spacecraft in its early years, its primary objective now and into the future is to continue its support of planetary and interplanetary flight projects.

A development objective has been to keep the network capability at the state of the art of telecommunications and data handling and to support as many flight projects as possible with a minimum of mission-dependent hardware and software. The DSN provides direct support of each flight project through that project's tracking and

data system. This management element is responsible for the design and operation of the hardware and software in the DSN which are required for the conduct of flight operations.

Beginning in FY 1973 a modified DSN interface has been established with the flight projects. In lieu of the SFOF, a multimission Mission Control and Computing Center (MCCC) has been activated as a separate functional and management element within JPL. This function, as negotiated with each flight project, will provide all computing and mission operations support for missions controlled from JPL. DSN computing support will be provided separately by the DSN. Radio metric, telemetry, and command data interfaces with the DSN are a joint DSN, MCCC, and flight project responsibility. The organization and procedures necessary to carry out these new activities will be reported in this document in the near future.

The DSN function, in supporting a flight project by tracking the spacecraft, is characterized by five network systems:

- (1) DSN Tracking System. Generates radio metric data; i.e., angles, one- and two-way doppler and range, and transmits raw data to mission control.
- (2) DSN Telemetry System. Receives, decodes, records, and retransmits engineering and scientific data generated in the spacecraft to Mission Control.
- (3) DSN Command System. Accepts coded signals from mission control via the GCF and transmits them to the spacecraft in order to initiate spacecraft functions in flight.
- (4) DSN Monitor and Control System. Instruments, transmits, records, and displays those parameters of the DSN necessary to verify configuration and validate the network. Provides operational direction and configuration control of the network and primary interface with flight project Mission Control personnel.
- (5) DSN Test and Training System. Generates and controls simulated data to support development, test, training and fault isolation within the DSN. Participates in mission simulation with flight projects.

The facilities needed to carry out these functions have evolved in three technical areas: (1) the Deep Space Stations (DSSs) and the telecommunications interface

through the RF link with the spacecraft is known as the Deep Space Instrumentation Facility (DSIF); (2) the Earth-based point-to-point voice and data communications from the stations to Mission Control is known as the Ground Communications Facility (GCF); (3) the network monitor and control function is known as the Network Control System (NCS).

I. Deep Space Instrumentation Facility

A. Tracking and Data Acquisition Facilities

A world-wide set of Deep Space Stations with large antennas, low-noise phase-lock receiving systems, and high-power transmitters provide radio communications with spacecraft. The DSSs and the deep space communications complexes (DSCCs) they comprise are given in Table 1.

Radio contact with a spacecraft usually begins when the spacecraft is on the launch vehicle at Cape Kennedy, and it is maintained throughout the mission. The early part of the trajectory is covered by selected network stations of the Air Force Eastern Test Range (AFETR) and the STDN of the Goddard Space Flight Center.¹ Normally, two-way communications are established between the spacecraft and the DSN within 30 min after the spacecraft has been injected into lunar, planetary, or interplanetary flight. A compatibility test station at Cape Kennedy (discussed later) tests and monitors the spacecraft continuously during the launch checkout phase. The deep space phase begins with acquisition by 26-m DSSs. These and the remaining DSSs listed in Table 1 provide radio communications until the end of the mission.

To enable continuous radio contact with spacecraft, the DSSs are located approximately 120 deg apart in longitude; thus a spacecraft in deep space flight is always within the field-of-view of at least one DSS, and for several hours each day may be seen by two DSSs. Furthermore, since most spacecraft on deep space missions travel within 30 deg of the equatorial plane, the DSSs are located within latitudes of 45 deg north and south of the equator. All DSSs operate at S-band frequencies: 2110-2120 MHz for Earth-to-spacecraft transmission and 2290-2300 MHz for spacecraft-to-Earth transmission. An X-band capability is being readied for future missions beginning in 1973.

¹The 9-m (30-ft) diam antenna station established by the DSN on Ascension Island during 1965 to act in conjunction with the STDN orbital support 9-m (30-ft) diam antenna station was transferred to the STDN in July 1968.

To provide sufficient tracking capability to enable returns of useful data from around the planets and from the edge of the solar system, a 64-m (210-ft) diam antenna subnet will be required. Two additional 64-m (210-ft) diam antenna DSSs are under construction at Madrid and Canberra and will operate in conjunction with DSS 14 to provide this capability. These stations are scheduled to be operational by the middle of 1973.

B. Compatibility Test Facilities

In 1959, a mobile L-band compatibility test station was established at Cape Kennedy to verify flight-spacecraft/DSN compatibility prior to the launch of the Ranger and Mariner Venus 1962 spacecraft. Experience revealed the need for a permanent facility at Cape Kennedy for this function. An S-band compatibility test station with a 1.2-m (4-ft) diameter antenna became operational in 1965. In addition to supporting the preflight compatibility tests, this station monitors the spacecraft continuously during the launch phase until it passes over the local horizon.

Spacecraft telecommunications compatibility in the design and prototype development phases was formerly verified by tests at the Goldstone DSCC. To provide a more economical means for conducting such work and because of the increasing use of multiple-mission telemetry and command equipment by the DSN, a Compatibility Test Area (CTA) was established at JPL in 1968. In all essential characteristics, the configuration of this facility is identical to that of the 26-m (85-ft) and 64-m (210-ft) diameter antenna stations.

The JPL CTA is used during spacecraft system tests to establish the compatibility with the DSN of the proof test model and development models of spacecraft, and the Cape Kennedy compatibility test station is used for final flight spacecraft compatibility validation testing prior to launch.

II. Ground Communications Facility

The GCF provides voice, high-speed data, wideband data, and teletype communications between the Mission Operations Center and the DSSs. In providing these capabilities, the GCF uses the facilities of the worldwide NASA Communications Network (NASCOM)² for all long

²Managed and directed by the Goddard Space Flight Center.

distance circuits, except those between the Mission Operations Center and the Goldstone DSCC. Communications between the Goldstone DSCC and the Mission Operations Center are provided by a microwave link directly leased by the DSN from a common carrier.

Early missions were supported by voice and teletype circuits only, but increased data rates necessitated the use of high-speed and wideband circuits for DSSs. Data are transmitted to flight projects via the GCF using standard GCF/NASCOM formats. The DSN also supports remote mission operations centers using the GCF/NASCOM interface.

III. Network Control System

The DSN Network Control System is comprised of hardware, software, and operations personnel to provide centralized, real-time control of the DSN and to monitor and validate the network performance. These functions are provided during all phases of DSN support to flight projects. The Network Operations Control Area is located in JPL Building 230, adjacent to the local Mission Operations Center. The NCS, in accomplishing the monitor and control function does not alter, delay, or serially process any inbound or outbound data between the flight project and tracking stations. Hence NCS outages do not have a direct impact on flight project support. Voice communications are maintained for operations control and coordination between the DSN and flight projects, and for minimization of the response time in locating and correcting system failures.

The NCS function will ultimately be performed in data processing equipment separate from flight project data processing and specifically dedicated to the NCS function. During FY 1973, however, DSN operations control and monitor data will be processed in the JPL 360/75 and in the 1108. In FY 1974 the NCS data processing function will be partly phased over to an interim NCS processor, and finally, in FY 1975, the dedicated NCS data processing capability will be operational. The final Network Data Processing Area will be located remote from the Network Operations Control Area so as to provide a contingency operating location to minimize single point of failure effects on the network control function. A preliminary description of the NCS appears elsewhere in this document.

Table 1. Tracking and data acquisition stations of the DSN

DSCC	Location	DSS	DSS serial designation	Antenna		Year of initial operation
				Diameter, m (ft)	Type of mounting	
Goldstone	California	Pioneer	11	26(85)	Polar	1958
		Echo	12	26(85)	Polar	1962
		(Venus) ^a	13	26(85)	Az-El	1962
		Mars	14	64(210)	Az-El	1966
Tidbinbilla	Australia	Weemala (formerly Tidbinbilla)	42	26(85)	Polar	1965
		Ballima (formerly Booroomba)	43	64(210)	Az-El	1973
—	Australia	Honeysuckle Creek	44	26(85)	X-Y	1973
—	South Africa	Hartebeesthoek	51	26(85)	Polar	1961
Madrid	Spain	Robledo	61	26(85)	Polar	1965
		Cebreros	62	26(85)	Polar	1967
		Robledo	63	64(210)	Az-El	1973

^aA maintenance facility. Besides the 26-m (85-ft) diam Az-El mounted antenna, DSS 13 has a 9-m (30-ft) diam Az-El mounted antenna that is used for interstation time correlation using lunar reflection techniques, for testing the design of new equipment, and for support of ground-based radio science.

Deep Space Network Test and Training System

H. C. Thorman
DSN Systems Engineering

A description of the Deep Space Station Test and Training Subsystem is presented including the evolution and usages of the Simulation Conversion Assembly, capabilities of the present subsystem (Mark III-73) and planned expansion (Mark III-75) to meet Viking requirements. A brief discussion of present and planned capabilities of the Network Control Test and Training Subsystem is included. These are both subsystems of the Deep Space Network Test and Training System.

I. Deep Space Station Test and Training Subsystem

The block diagram in Fig. 1 shows the elements and flow paths of the Deep Space Station (DSS) Test and Training Subsystem, Mark III-73, and also the new elements to be implemented at DSS 14, 42/43, and 61/63 to upgrade the subsystem to the Mark III-75 configuration in the 64-m subnet. The Mark III-73 configuration is currently in operation at all DSSs and CTA 21 and MIL 71. The Mark III-75 configuration will be implemented in the latter part of 1974 and will become operational in the early part of 1975.

A. Telemetry System Test Support

Telemetry System testing and participation in mission telemetry simulation are supported by the Simulation

Conversion Assembly (SCA) at each DSS¹ and CTA 21 and MIL 71. The SCA is interfaced to an XDS-910 computer, which serves as the Simulation Processing Assembly (SPA) when operating with Test and Training subsystem software². Provisions are made for both manual and computer control of a multiplicity of SCA functions.

The original SCA configuration was implemented in 1970 as part of the former DSN Simulation System (Ref. 1). The SCA replaced the earlier Multimission Telemetry (MMT) Test Assembly and also the DSIF/GCF Interface (DGI) Assembly that had supported Mariner Mars 1969

¹A single SCA at each conjoint station (DSS 42/43 and DSS 61/63) supports both the 26-m and the 64-m DSS telemetry strings.

²The XDS-910 computer in the 26-m DSSs is also used for operation of the Antenna Pointing Subsystem.

mission preparations. The SCA was used for Mariner Mars 1971 and Pioneer 10 and 11 pre-mission testing and training.

Upgrading to the present SCA-I configuration (Fig. 2) was completed at all stations by early 1973. The modification consisted primarily of the addition of the Data Selection Panel which incorporated new functions required for simulation of Mariner Venus/Mercury 1973 telemetry characteristics and also increased the operational versatility of the SCA. The SCA-I configuration was extensively utilized for Mariner Venus/Mercury 1973 mission preparations, and it is currently supporting Helios mission testing and training.

SCA-I capabilities provide composite output signals to represent up to two dual-channel spacecraft. Additional SCA equipment and new software are being fabricated for use in the 64-m subnet, to provide an SCA-II configuration for the DSS Test and Training Subsystem Mark III-75 configuration. SCA-II will supply signals representing up to three dual-channel spacecraft, to support DSN preparations for the planetary operations of the Viking-Mars 1975 mission (Ref. 2).

B. Digital Telemetry Simulation

The digital section of the SCA (Fig. 1) has the capability to output multiple data streams at controlled rates and also the capability to provide various types of coding on one or more of the streams, as described in Table 1. SCA-I has a 4-channel output capacity and SCA-II has a 6-channel output capacity.

Each channel can be independently operated in any of three modes as described in the following paragraphs.

1. Manual mode. In the manual mode the channel can be operated independently of the 910 computer. Simple data patterns such as square-wave, pseudonoise sequence, etc. can be generated in this mode. The manual mode is used primarily for checkout and calibration of station equipments.

2. Computer-local mode. In the computer-local mode, the channel can be supplied with simulated telemetry data generated in the XDS 910 computer. The computer-generated data can be patterned to include frame synchronization codes and other repetitive features so that it can be processed and decommutated when received at the Mission Control Center. The computer-local mode is used primarily for prepass data transfer checks and for DSN operational verification tests.

3. Computer-remote mode. In the computer-remote mode, data from an external simulation source (such as the MCCC Simulation Center) is inputted to the XDS 910 computer via the GCF high-speed data (HSD) subsystem or the GCF wideband data (WBD) subsystem. The computer extracts and buffers a specified number of data words from each HSD or WBD block for conversion into an SCA data stream. Control of SCA functions in this mode is typically exercised from the remote simulation source by transmitting HSD blocks containing appropriate mnemonic entries to establish initial conditions or to change conditions during a test sequence.

High-speed and wideband data block format requirements for this operating mode are described in Ref. 3.

The computer-remote mode is utilized for "long-loop" Ground Data System testing, joint Flight Project and DSN training, and for operational readiness tests. This mode of operation permits Flight Project-furnished, dynamic, command-responsive simulated telemetry data to be transmitted and processed through the entire ground data system.

C. Analog Telemetry Simulation and Radio Frequency Controls

The analog section of the SCA (Fig. 1) provides "video conditioners" (video-bandwidth signal conditioners), driven by subcarrier-frequency generators, to modulate subcarriers onto the telemetry data streams. Other capabilities include subcarrier mixing, modulation-index control, and downlink carrier modulation and signal level control, as described in Table 2.

The interface between the digital and analog sections of the SCA is through the switching matrix of the Data Selection Panel (Fig. 3). Each of the functions on this panel can be exercised by either manual or computer control. The switch matrix allows each digital data stream to be assigned to any signal conditioner. The panel provides local display of switching assignments and modulation index attenuator settings, by pushbutton selection.

D. Command System Testing

On-site testing of the DSS command subsystem is accomplished by operating a test program in the Digital Instrumentation Subsystem (DIS) computer (XDS 920) to output HSD blocks to the station communications terminal for loop-back to the Telemetry and Command Processor (TCP) XDS 920.

For end-to-end DSN Command System testing the DSS command subsystem is operated in its normal configuration, except that the uplink signal is radiated to a dummy load. The command data blocks are transmitted to the DSS via the GCF HSD subsystem from either the Network Control System or the Mission Control and Computing Center.

E. Tracking System Test Support

DSS test and training functions related to the tracking subsystem presently include the following:

- (1) Test signals from the Tracking Data Handling (TDH) assembly provide inputs to the DIS XDS 920 which formats and outputs radio metric data in HSD blocks for transmission to the MCCC and NCS to test loading and to exercise accountability processing.
- (2) The Block IV Receiver/Exciter Subsystem that is being installed at the 64-m DSSs offers an opportunity to simulate doppler-frequency shifts by manual input of ramp-control parameters into the frequency synthesizer control unit, as indicated in Figure 1.

F. Time Simulation

A time code generator mounted on the SCA provides a simulated time signal which can be substituted for the standard GMT input to the DSS time distribution assembly (Fig. 1). The simulation time code generator is driven by signals from the DSS frequency distribution assembly.

II. Network Control Test and Training Subsystem

Table 3 describes the test and training capabilities for each of the three implementation blocks of the Network Control System (NCS).

A. NCS Block I

The Block I NCS, currently in operation, includes a capability for DSN Command System testing and a capability for transmission of pregenerated HSD blocks for "short-loop" testing of the NCS.

B. NCS Block II

A Block I software modification, tentatively planned for Block II implementation in the latter part of 1974 would add a capability for transmitting control messages to the SCA in the same manner that commands are transmitted to the TCP.

C. NCS Block III

Design of the Block III NCS, planned for implementation in the latter part of 1975, includes a Test and Training Subsystem with capability for real-time generation of data patterns required for testing of the Block III NCS telemetry, tracking, command, monitor, support, and display subsystems and for DSN systems testing and operations training. Reference 4 provides the Block III functional requirements for the NC Test and Training Subsystem.

References

1. Thorman, H. C., "DSN Simulation System," in *The Deep Space Network Progress Report*, Technical Report 32-1526, Vol. VI, pp. 5-7, Jet Propulsion Laboratory, Pasadena, Calif., Dec. 15, 1971.
2. Mudgway, D. J., and Johnston, D. W., "Viking Mission Support," in *The Deep Space Network Progress Report*, Technical Report 32-1526, Vol. XIX, pp. 10-22, Jet Propulsion Laboratory, Pasadena, Calif., Feb. 15, 1974.
3. *DSN System Requirements, Detailed Interface Design*, JPL Document 820-13, Rev. A, Sect. VII (JPL internal document in modular form, continuously updated).
4. *Deep Space Network Control System Requirements, NC Test and Training Subsystem*, JPL Document 822-8, Feb. 1, 1973 (JPL internal document).

Table 1. Digital channel capacities of DSS simulation conversion assembly

Capability	SCA I	SCA II
Total output of independent data streams	4 channels	6 channels
Variable rate control, 1 bit/s to 250 ksymbols/s	Available on 3 channels	Available on 4 channels
Selection of discrete rates, 8-1/3, 16 2/3, 33-1/3, 133-1/3 bits/s	Available on 2 channels	Available on 3 channels
Selection of block coding (32, 6) and (16, 5)	Available on 2 channels	Available on 4 channels
Selection of convolutional coding, systematic (1/2) and (1/3) or non-systematic (1/2) and (1/3)	Available on 1 channel	Available on 1 channel

Table 2. Analog channel capacities of DSS simulation conversion assembly

Capability	SCA I	SCA II
Data and subcarrier signal conditioning	Biphase modulation, 4 subcarrier channels	Biphase modulation, 6 subcarrier channels
Subcarrier frequency generation	3 Different frequencies, 1 Hz to 10 MHz range	4 Different frequencies, 1 Hz to 10 MHz range
Selection of interplex modulation	Available on all signal conditioners	Available on all signal conditioners
Modulation-index angle control	Controllable attenuator on output of each signal conditioner	Controllable attenuator on output of each signal conditioner
Subcarrier mixing and downlink carrier modulation	In pairs onto each of 2 S-band carriers	In pairs onto each of 3 S-band carriers
Downlink carrier signal level control	Controllable attenuator on output of each test transmitter	Controllable attenuator on output of each test transmitter

Table 3. Network control test and training subsystem capabilities

Functions	Block I capability	Block II capability	Block III capability
Radio metric data patterns	Canned block stream only	Same as block I	Realistic enough to exercise pseudo-residuals
Telemetry data patterns	Canned block stream for NCS self test only	Same as block I	Yes, real-time frame synched
Remote control of DSS simulation conversion assembly	None	Possibly, using block I command capability	Yes
Simulation of project commands	Yes, in NC CMD subsystem	Same as block I	Yes, in T & T Subsystem
Simulation of DSS CMD responses	None	None	Yes
Simulated DSS monitor data	Canned block stream only	Same as block I	Yes, real-time controllable

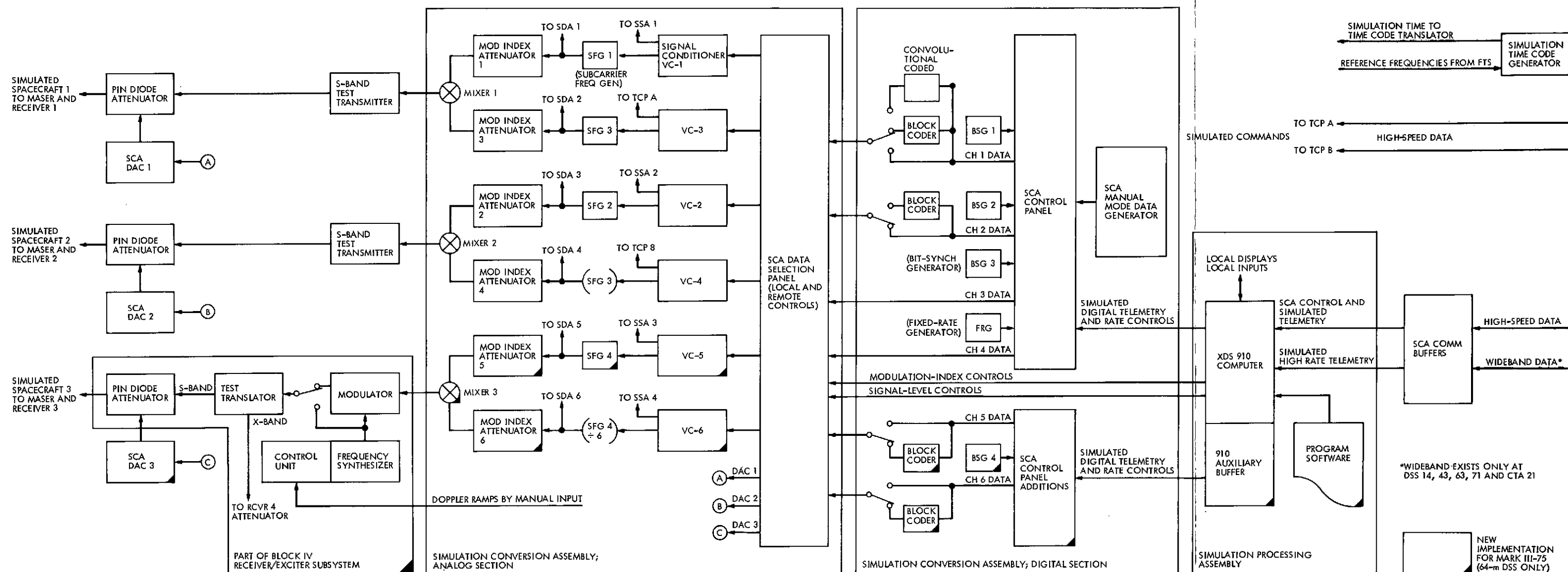


Fig. 1. DSS Test and Training Subsystem block diagram, Mark III-73 and Mark III-75

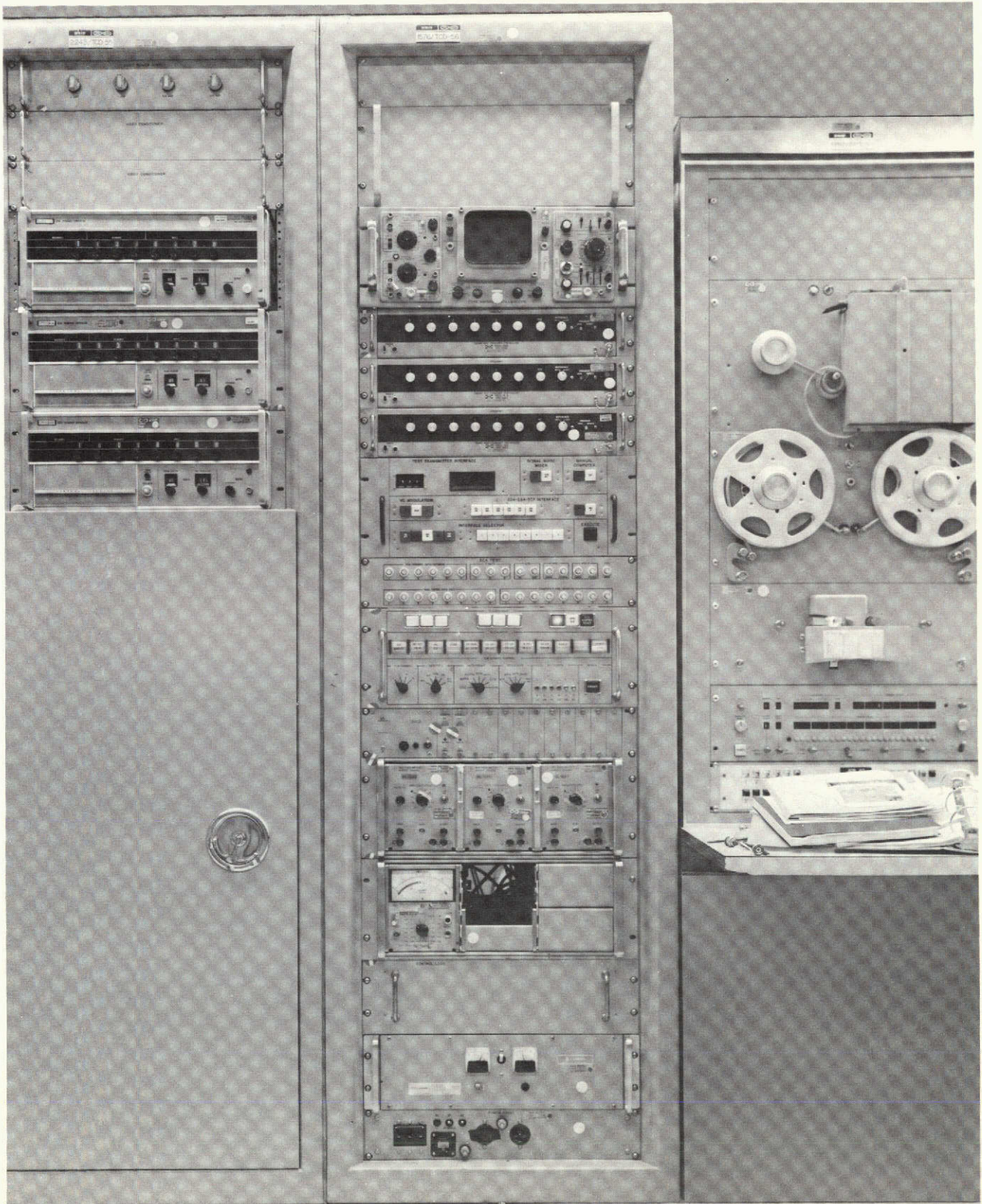


Fig. 2. DSS simulation conversion assembly and XDS 910 computer

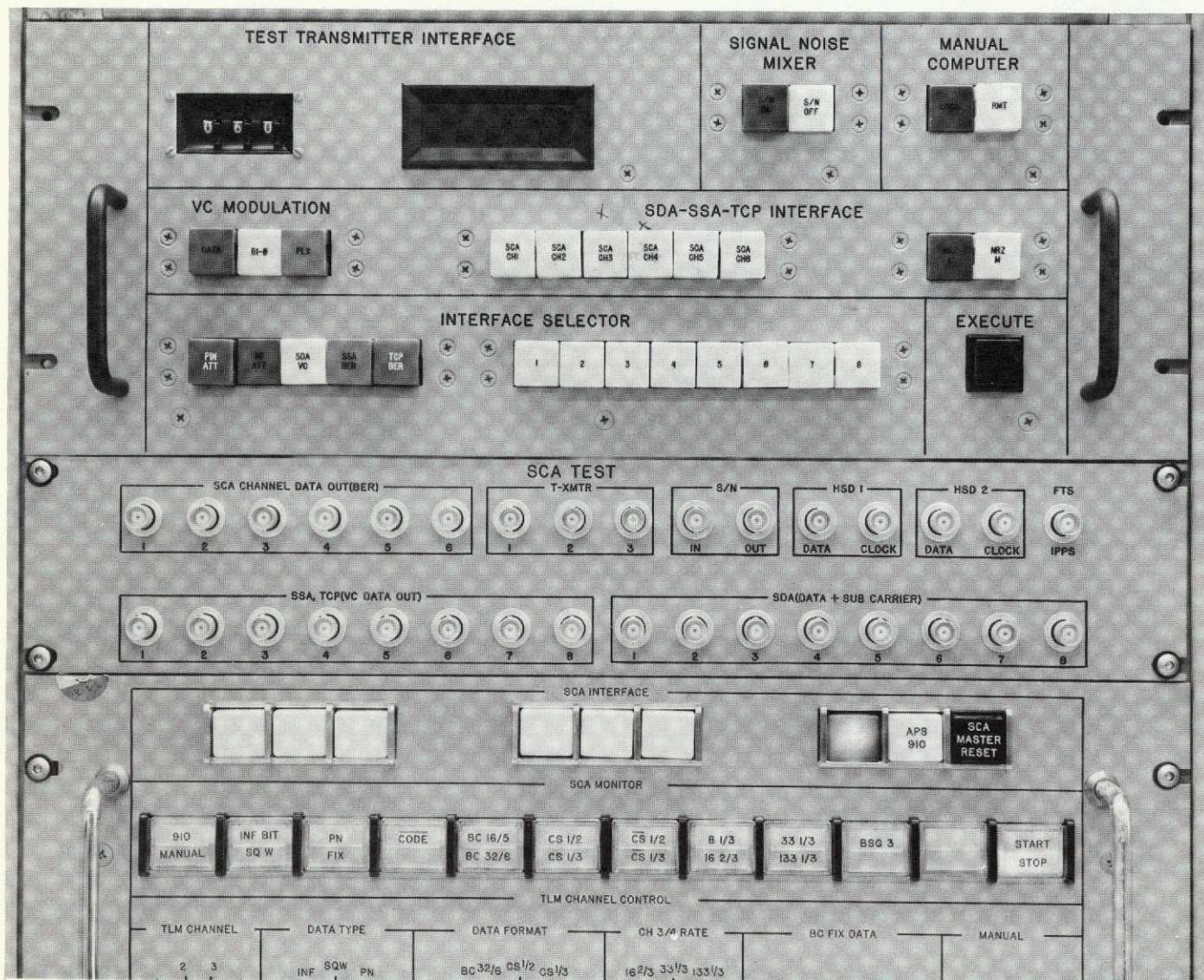


Fig. 3. SCA data selection panel, test panel, and control panel

Mariner Venus/Mercury 1973 Mission Support

E. K. Davis
DSN Systems Engineering Office

Following the successful launch on November 3, 1973, DSN emphasis for Mariner Venus/Mercury (MVM'73) switched from premission preparations to flight support. However, a high level of implementation activity continued in parallel to achieve operational readiness of additional capabilities committed to be available by January 1, 1974.

I. Planning Activities

A. NASA Support Plan (NSP)

NASA Headquarters acted quickly on the NSP, which was revised and resubmitted for approval on October 25, 1973. Approval was completed on October 31, 1973, and the DSN published and distributed Revision 1 immediately thereafter. This will be the final issue for the MVM'73 primary mission, which extends to April 15, 1974. Support commitments for extended mission operations, if approved, will be documented in a new NSP scheduled for publication in April 1974.

B. DSN Operations Planning

During November and December 1973, emphasis was on proper execution of the previously published DSN Operations Plan for MVM'73. However, to accomplish this in the heavy support load environment, daily planning sessions with the Project were required to produce workable, detailed schedules and sequences of events. The

Pioneer/Mariner 10 64-m subnet sharing plan described in the previous article was made more complex by the occurrence of Mariner 10 spacecraft problems resulting in numerous real-time changes to DSN schedules, sequences, and procedures.

II. Program Control

A. Status Reviews and Reports

Weekly status meetings with the Project continued throughout this reporting period. Subsequent to the successful completion of launch and near-Earth television operations, additional items pertinent to Mariner 10 cruise and encounter operations were added to the "Critical Lien List:" DSSs 43 and 63 planetary ranging, DSS 14 S/X-band, DSSs 43 and 63 high-rate video telemetry data handling, open-loop receiver/occultation recorder verification, 10 sample/s doppler capability, and recall capability for DSS radio metric original data records (ODRs). The DSN has issued daily and weekly status reports to a

wide distribution during the critical and cruise phases respectively. Submission of monthly inputs to the Project Management Report continues.

III. Implementation Activities

Following the very successful support given to Mariner 10 in the early part of November 1973, the DSN gave full attention to the resolution of problem areas and to open implementation required to be completed by January 1, 1974. A summary of these items is given in Table I.

1. Telemetry and command data subsystem (TCD). Previously reported problems regarding telemetry original data recording quality were resolved prior to launch except for time tag errors. A hardware solution for random occurrences of large timing errors in the timing distribution system/Telemetry and Command Processor (TCP) clock was not possible for MVM73; therefore, operational procedures were designed to reduce or eliminate effects on data records. The Network Operations/Analysis Team checks timing accuracy of real-time telemetry blocks during each DSS prepass countdown. If timing errors are observed, front panel restarts are accomplished on TCD subsystem assemblies to reset the clock to the correct time. Checks are continued hourly during DSS tracks and the procedure is repeated as necessary.

The third Data Decoder Assembly required to complete the DSSs 61 and 63 conjoint DSS three-string configuration was installed and checked out. Three strings are required at the conjoint 26- and 64-m DSS to accommodate (1) real-time recording of 117 kilobits/s video, (2) real-time handling of 2450 bits/s nonimaging science, and (3) near-real-time, reduced-rate playback of video data via 28.5 kilobits/s wideband communications circuits.

Digital recording of radio metric data in the DSS digital instrumentation subsystem (DIS) was initiated during the MVM73 preparation period. However, the capability for posttrack recall/replay of these data was not developed in parallel. To achieve this capability in a timely manner, an overlay modification for an existing telemetry replay software program is being prepared for delivery in January 1974. This will involve replay of DIS recorder-produced digital tapes via the TCP/recorder requiring DIS/TCP tape deck compatibility. In the interim, radio metric data may be recalled via low-speed punch recorder replay.

2. Tracking data handling subsystem (TDH). Implementation of planetary ranging capabilities continued at DSSs 43 and 63 during this period; however, there was little productive time due to Pioneer 10 encounter configuration freezes. In addition, installation kits were not complete in that a few required cables were not available. Consequently, the January 1, 1974 readiness date was not met. The impact of this late implementation on Project navigation was, at first, not significant since the DSN Mark IA Lunar Ranging Assembly was still providing good ranging data from 26-m DSSs. Mark IA support could have continued through late January 1974; however, on December 25, 1973, the spacecraft high-gain antenna experienced a problem that resulted in a significant loss in downlink signal performance. Since ranging from 26-m DSSs was no longer possible, priority action was taken to assure completion of planetary ranging checkout by January 15, 1974.

3. Digital instrumentation subsystem (DIS). Although the TDH subsystem was modified earlier to generate doppler data at a rate of 10 samples/s, the existing DIS software program could not handle this rate. This capability is required for radio science experiment support at planetary encounters, particularly at Mercury. Final checkout of the necessary software program update is in process and is scheduled for release in January 1974.

4. Antenna microwave subsystem. Analysis of DSS 14 low-noise ultracone performance indicated that this capability would most likely permit sufficient RF link performance to support a video data rate of 117 kilobits/s at Mercury encounter. This would significantly increase the science return from Mercury since rather high-resolution coverage of the entire lighted disk would be possible. Consequently, the decision was made to install an ultracone at DSS 43 to provide 117 kilobits/s coverage of the Mercury out-going TV sequence. The cone has been shipped to Australia, and installation is planned in mid-January 1974.

5. S/X-band equipment. As reported in Ref. 1, installation of the R&D S/X-band equipment, except the Command Modulator Assembly switch, was completed at DSS 14 in late October 1973. However, completion of checkout and an operable status was not achieved by January 1, 1974, as planned due to a number of problems. First, S/X-band checkout during November–December 1973 at DSS 14 was very difficult and at times impossible due to conflicts with the load, configuration control, and freeze imposed at the station for Pioneer 10 encounter. Secondly, subsystem interface cable noise problems and faulty assembly modules further delayed achievement of

valid data. Most problems exhibited themselves in the X-band rather than S-band data in the form of frequent doppler cycle slips and offsets. Increased use of DSS 14 by Mariner 10 in January 1974 should improve this situation in preparation for Venus encounter.

IV. Operations Summary

Final DSN operational readiness tests were satisfactorily completed during the last week of October 1973, in preparation for Mariner 10 launch and near-Earth TV operations. Mariner 10 was launched on November 3, 1973 as planned, and the DSN has provided continuous coverage to date via a combination of 26-m and 64-m subnet deep space stations: DSSs 12, 42, 62, 14, 43, and 63.

During November and December 1973, most coverage was provided by the 26-m subnet, with DSS 14 averaging about three passes per week. DSSs 43 and 63 tracks of Mariner 10 were nil due to higher priority support for Pioneer 10. DSS 44 was brought into use for Mariner 10 on a rush basis to avoid a 4-h gap in coverage on December 3, 1973 due to Pioneer 10's use of both DSSs 42 and 43 during encounter closest approach.

DSN support for Mariner 10, including the high-activity Earth-Moon TV sequence and trajectory correction maneuver, has to date been excellent. As expected in a continuous coverage operation, the DSN has experienced problems and equipment failures; however, none has had a significant impact on mission operations and data recovery.

Reference

1. Davis, E. K., "Mariner Venus-Mercury 1973 Mission Support," in *The Deep Space Network Progress Report*, Vol. XVIII, pp. 5-15. Jet Propulsion Laboratory, Pasadena, Calif., Dec. 15, 1973.

Table 1. Postlaunch implementation and problems

Open implementation (I) and problems (P)		Location
Block IV S/X-band ranging/ doppler	(I)	DSS 14
Planetary ranging	(I)	DSSs 43 and 63
10 Sample/s doppler	(I)	All DSSs
Radio metric original data record replay	(I)	All DSSs
Open-loop analog recording	(I/P)	DSSs 14 and 43
Standard analog recording validation and improvement	(P)	All DSSs
Low-noise ultracore	(I)	DSS 43
Third Data Decoder Assembly	(I)	DSS 61/63
Digital telemetry ODR time tag error	(P)	All DSSs
Command Modulator Assembly (CMA) switch	(I)	DSS 14

Pioneer Venus 1978 Mission Support

R. B. Miller
DSN Systems Engineering

The current concept for DSN support of the Pioneer Venus 1978 probe mission is described.

I. Introduction

Pioneer Venus 1978 current mission concept is for a two-spacecraft mission with both launches in the 1978 Venus opportunity. One spacecraft will consist of a bus and four probes which will all enter the Venusian atmosphere. The second spacecraft will use the same basic bus but with the probes replaced by a propulsion package sufficient for achieving an orbit around Venus with a life in orbit of seven months or one Venusian year. This article is an introduction of the current DSN concept of supporting the telemetry for the probe mission.

II. Probe Mission Characteristics

The probe mission will involve delivering an array of aerodynamic probes over the surface of Venus from a spin-stabilized bus. The probes will consist of three identical small probes and one larger probe, each carrying an

assortment of instruments to measure the characteristics of the atmosphere down to the lowest atmospheric scale height above the surface. It will not be a mission objective for the probes to function after impacting the surface of the planet. The bus will carry independent scientific instruments to measure the characteristics of the atmosphere above 130 km altitude. The bus will not be designed to survive atmospheric entry. After separation of the probes from the spinning bus, some 5 to 15 days prior to entry, the bus will be retarded so as to enter the atmosphere after the probe entries have been completed. This will enable the bus to serve as a frequency reference for an interferometric tracking experiment to determine the wind drifts of the probes during their descent through the atmosphere.

The probes will have direct communication with Earth. The large probe and bus will carry coherent transponders, and the small probes will have stable oscillator-controlled

transmitters (on the order of 10^{-9} stability after turn on). Since the probes will be battery powered, their radio subsystems will be turned on only a short time (on the order of an hour) prior to entry. In the current mission concept this means that the probe frequencies would not be seen on the ground from launch in August 1978 until shortly before entry in December of 1978. The descent phase will last on the order of one hour, and current mission concept has all four probes entering simultaneously during the DSS 14 and DSS 43 overlap in view period. In the interface region between 120 km and 80 km altitude, there will be a blackout of communications. Since the bus must be tracked simultaneously by the same stations as the probes for the sake of the wind drift measurements, both DSS 14 and DSS 43 must be equipped to receive all five signals simultaneously, although it may not prove necessary for bus telemetry to be received at the 64-meter stations.

III. DSN Support Plans

For the sake of redundancy there will be duplicate telemetry capability at DSS 14 and DSS 43 for each probe. The prime source of telemetry data will be through the closed-loop receivers. The current plan calls for five open-loop receivers at each station, which is one more than the Viking configuration. The fifth closed-loop receiver will give flexibility in the initial acquisition search prior to entry, or alternately allow for tracking of the bus for telemetry at a 64-meter station, if required.

Because of the higher risks associated with this multi-probe mission and to increase the data return surrounding the blackout region during entry, a predetection telemetry recovery system utilizing open-loop receivers will be provided. Four open-loop receivers, two more than the Viking configuration, will be provided at both DSS 14 and DSS 43. Telemetry data would be analog recorded for later playback. Playback of the predetection analog recordings will utilize a digital wow and flutter compensator being developed by the Jet Propulsion Laboratory. The technique involves an A to D conversion, then the digital compensation utilizing a pilot tone recorded with the data, then an A to D conversion, up conversion to S-band, and finally play-in through a standard closed-loop

receiver and telemetry system. Losses associated with the predetection recording and playback compared to the real-time closed-loop system will be less than $1\frac{1}{2}$ dB. The bandwidth at S-band of the predetection telemetry systems to be used for Pioneer Venus will be about 300 kHz so that tuning of the open-loop receiver should not be necessary during the descent.

The wind drift measurement will require that all five signals received from the probes and bus (if the probe entries are simultaneous) be received through a single open-loop receiver. The frequency allocations will be such that a bandwidth on the order of 1 MHz will be required. To avoid the necessity of an additional open-loop receiver, two ports on one of the open-loop receivers is being provided for telemetry. One port would be 300 kHz for telemetry, and the other port would be 1 MHz for the wind drift measurement. The details of how the differential interferometry data will be taken for the wind drift experiment have not been established; however, it appears the project will request that experimenter-provided equipment be placed at DSS 14 and DSS 43. It is against usual Office of Tracking and Data Acquisition (OTDA) policy to have project-provided equipment at the stations, so further negotiation will be required on this point.

The operation of nine receivers simultaneously at each DSS to acquire 5 separate carriers for a 90-minute primary mission will be interesting, to say the least. To make this complex operation more manageable, each receiver will be provided with manually programmed, digitally controlled oscillators so that any tuning required can be set and checked prior to the turn on of the probe transmitters. The bus will be in two-way (its transmitted signal coherent to a signal received from the ground) during the probe entries, and it is hoped that the mission design will enable the uplink to the bus to be from a 26-meter DSS to avoid this additional complexity at the 64-meter DSSs. It may also be required to maintain an uplink to the large probe prior to blackout. This uplink could be from one of the 64-meter DSSs or an additional 26-meter DSS. In any case, dual uplink from a single station will not be provided.

A block diagram of the receiver configuration discussed is shown in Fig. 1.

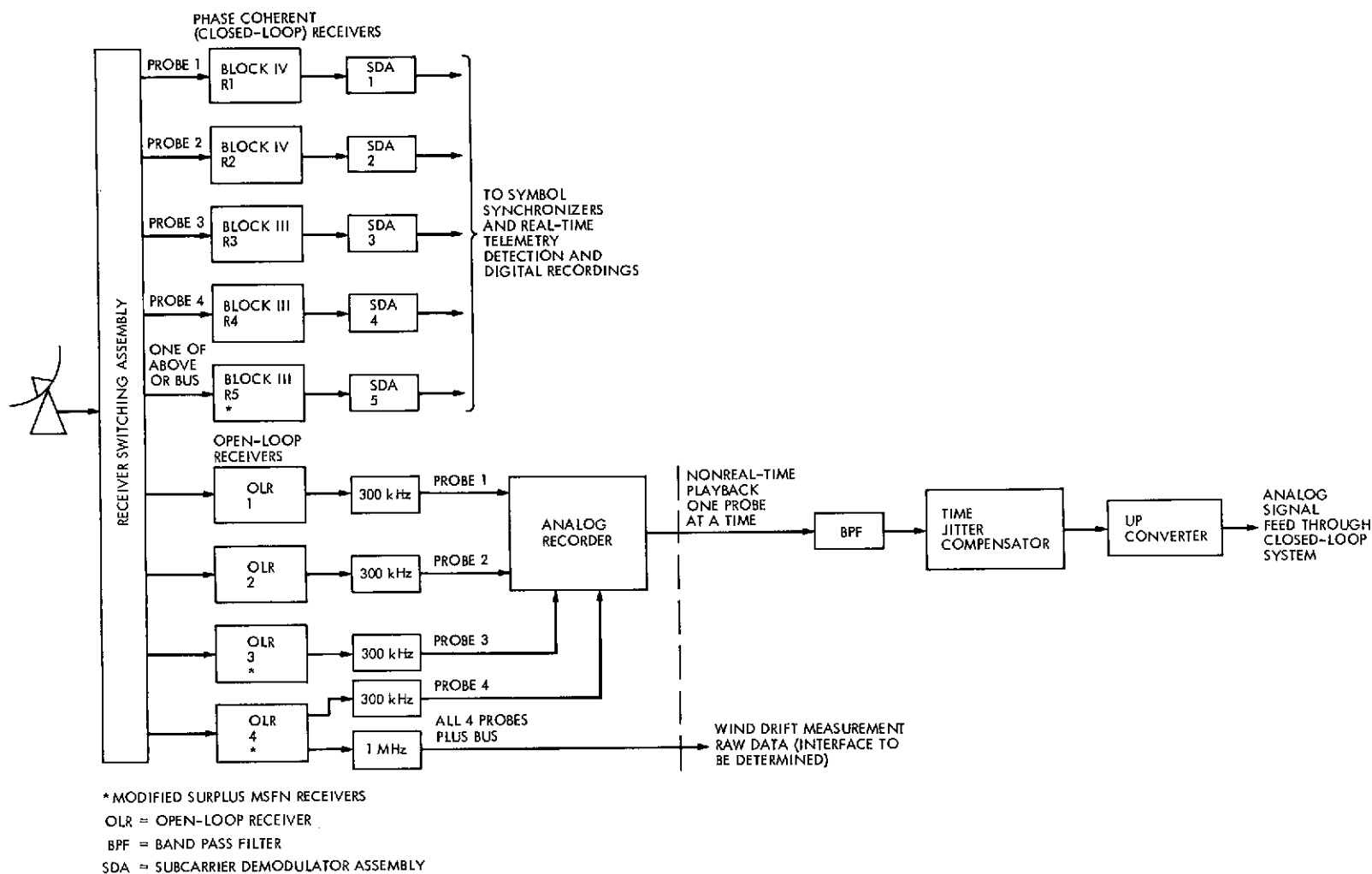


Fig. 1. Receiver configuration for telemetry data recovery and interferometry experiment

Short Baseline QVLBI Doppler Demonstrations-Part II

C. C. Chao and R. A. Preston
Tracking and Orbit Determination Section

H. E. Nance
DSN Systems Engineering

This report describes the continuation of the short baseline QVLBI demonstrations, which are designed to examine the stability of the current Doppler frequency system. A total of six passes of simultaneous two-way and three-way doppler data from Pioneer 10 were obtained at Deep Space Station (DSS) 11 and DSS 14. Results indicate that the short-term (min), medium-term (hr) and long-term (month) stabilities of the new rubidium frequency standard (HP 5065A) are 8 parts in 10^{13} , 1.3 parts in 10^{13} , and 1.9 parts in 10^{12} , respectively. The relative drift rate between the two systems (DSS 11 and DSS 14) is around 6 mHz/month. This indicates that the long-term stability of the current frequency system exceeds our limit level and makes the coming quasi very-long baseline interferometer (QVLBI) (MVM73) demonstration very difficult.

I. Introduction

Accuracy analysis (Ref. 1) has shown that QVLBI data (differenced simultaneous two-way and three-way doppler) reduce navigation error produced by unmodeled spacecraft accelerations by 2 or 3 orders of magnitude. The inherent limitation of these data appears to be the frequency systems at the participating stations. In Ref. 2, it is shown that to account for spacecraft accelerations as small as 10^{-12} km/sec² (equivalent to about 5 m error in station location) requires frequency stabilities over one month of 2×10^{-14} .

This report describes the continuation of the short-baseline QVLBI demonstrations (Ref. 2), which are designed to examine the stability of the current doppler frequency system. The aim of this project is to determine

whether the current frequency system using the new rubidium frequency standard (HP 5065A) is capable of supporting two-station tracking demonstrations (QVLBI). Results from Part I (Ref. 2) indicate that the long-term ($\approx 10^6$ sec) stability of the current system is on the order of 5 parts in 10^{12} ($\Delta f/f$). However, the measured value from Part I was based on only two passes of QVLBI data, and the second pass, which occurred 16 days after the previous one, had relatively poor data quality. Thus continued demonstrations as proposed in Part I were conducted.

A total of six passes of simultaneous two-way and three-way doppler data from Pioneer 10 were obtained at DSS 11 and DSS 14 from August 21, 1973, to September 23, 1973. By differencing these data types (QVLBI), we can study the stability of the entire local oscillator fre-

quency chain at the DSSs, of which the station frequency standard is only a single component. A direct microwave link between the two stations was used as a less accurate means of monitoring the relative drift between the station frequency standards alone. During the same time period, two similar passes of doppler data from Pioneer 10 were obtained at DSSs 42 and 43. Because these two stations, which are about 200 m apart, use a common frequency standard, the QVLBI data will be free from the effects of frequency standard instabilities, and should provide us with an accurate method of examining the stability of the remainder of the frequency system for that station pair. This will help us to estimate the expected performance of the frequency system when a better frequency standard (cesium or hydrogen maser) is installed.

II. Data Acquisition and Processing

A summary of the data taken during the continuation of short baseline QVLBI demonstrations is shown in Table 1. The six passes of two-way and three-way doppler data obtained at DSSs 11 and 14 during a one month period have data arcs that vary from 2 to 6 hours. Since these six passes are rather evenly spaced over the month, we should be able to estimate the long-term stability of the frequency system. The two passes of data obtained from DSSs 42 and 43 are separated by a one-week interval and are 1.5 and 7 hours in length. All the doppler data were taken at S-band with a 60-second sampling rate.

To have a quick look at the results, pseudo residuals¹ were differenced by hand immediately after the completion of each pass. Such a procedure can be helpful in promptly locating problems in the performance of a demonstration, and affording an opportunity to correct the problems before the next scheduled pass of data.

For example:

- (1) A 2-second difference between the time lags of the two-way and three-way data was found in the first pass of Doppler data at DSS 42 and 43. Unfortunately, efforts to correct this discrepancy were unsuccessful.
- (2) A jump of approximately 80 mHz was noticed in the frequency bias for the fourth pass of data between DSSs 11 and 14. This was quickly attributed to an epoch error of 0.180 sec in the setting of the DSS 14 clock.

¹Differences between real and predicted doppler data that are provided in real-time by DSN.

After all the data were obtained, the current orbit determination program (Ref. 3) was used to calculate the best theoretical estimates of the two-way and three-way doppler observables. The program Differ (Ref. 4) then produced the difference between the two-way and three-way residuals. During this demonstration the Sun-Earth-spacecraft angle was nearly 180 deg. Thus, the space plasma and ionospheric effects are at a minimum. This gives us confidence that the noise from charged-particle effects should be negligibly small when the two-way and the three-way data are differenced. The insensitivity of short baseline QVLBI data to uncertainties in tropospheric effects, baseline parameters and spacecraft position has been shown in Part I (Ref. 2). Hence, the differenced residuals should provide a good measure of the entire local oscillator frequency chain bias between the two stations. Observing the changes in this measured bias over a number of different passes of data allows the stability of the frequency system to be analyzed. A single pass of two-way and three-way doppler residuals and their differences is plotted in Fig. 1. It is interesting to note that the systematic rise in both sets of original residuals due to transmission media modeling errors at low elevation angles vanishes when the residuals are differenced.

III. Results and Discussion

As in Part I, we will discuss the short-term (minutes), medium-term (hours) and long-term (days and months) stabilities separately:

A. Short-Term Stability

Since the doppler data were sampled at one-minute intervals, the standard deviations of the QVLBI data residuals should give us a reasonable estimate for the short-term stability of the frequency system. Figure 2 shows the QVLBI doppler residuals for a number of the passes of data taken at DSSs 11 and 14. The values of the standard deviations of the residuals for each pass can be found in Table 1. The average value of the standard deviations, including the two passes from Part I, is 2.5 mHz. This corresponds to a stability of $\Delta f/f = 1.1 \times 10^{-12}$ for the entire two-station tracking system. Assuming the same performance at both stations, the contribution from each station is

$$\Delta f/f = \frac{1.1 \times 10^{-2}}{\sqrt{2}} = 7.8 \times 10^{-13}$$

Based on the two passes of QVLBI residuals (Fig. 3) from the Australian baseline (DSSs 42/43), we can estimate the stability of the system excluding the effects of the fre-

quency standard. The average standard deviation of the QVLBI residuals using the DSSs 42-43 data is 1.11 mHz² or $\Delta f/f = 4.8 \times 10^{-13}$. The corresponding value for one station is

$$\Delta f/f = \frac{4.8 \times 10^{-13}}{\sqrt{2}} = 3.4 \times 10^{-13}$$

If the noise from rubidium standards is uncorrelated with that from other parts of the system, the estimated short-term stability for the new rubidium standard (HP 5065A) will be

$$\Delta f/f = \sqrt{7.8^2 - 3.4^2} \times 10^{-13} = 7 \times 10^{-13}$$

This value is in good agreement with the HP 5065A manufacturer's specifications (Fig. 4).

B. Medium-Term Stability

The medium-term stability (hours) may be estimated from the values of the slopes of straight lines that were fit through each pass (2 to 6 hours) of QVLBI residuals. The rms value of those computed slopes including the two passes from Part I is about 0.33 mHz/hr (Table 1). The rms slope of the residuals from the Australia baseline is 0.041 mHz/hr. The equivalent $\Delta f/f$ values are displayed in Table 2.

The observed medium-term stability for the rubidium standard is almost one order of magnitude smaller than the short-term stability. It is interesting to note that this medium-term value essentially agrees with the value obtained from a previous short baseline (DSSs 12 and 14) VLBI demonstration (Ref. 5), but is smaller than the HP 5056A manufacturer's specification.³

C. Long-Term Stability

The long-term (month) stability attracts most of our interest because, as shown from computer simulation studies (Ref. 2), it can seriously affect the accuracy of trajectories determined by QVLBI data. Figure 5 shows the pass-to-pass variation of the frequency biases obtained from QVLBI residuals on the Goldstone baseline. It is seen that a 6.0 ± 0.2 mHz change was found during the one month period. This is indicative of the long-term stability of the entire frequency system. Using the data from

the Australian baseline, the long-term (8 days) contribution due to frequency system components other than the frequency standard was found to be 1.0 ± 0.4 mHz. The corresponding long-term $\Delta f/f$ stabilities are shown in Table 2. It should be remembered that these stabilities have been determined from only a limited amount of data, and hence, should be considered only order-of-magnitude estimates.

A comparison of the microwave measurements of the rubidium standard frequency bias on the Goldstone baseline and the QVLBI measurements of the corresponding local oscillator frequency chain bias is also shown in Fig. 5. The good agreement of these measurements indicates that the majority of the observed local oscillator frequency bias is indeed caused by a bias between the rubidium standards. The estimated uncertainty of microwave measurements is slightly less than 1 part in 10^{12} for a 4-hr integration time, which amounts to 1 ~ 2 mHz uncertainty at S-band. Thus, we see from Fig. 5 that more than 90% of the bias is due to the new rubidium standards. This agrees with the medium- and long-term results from the DSS 42-43 baseline (Table 2).

D. Capability of Supporting QVLBI Demonstrations

As discussed in Part I, the desired level of long-term frequency stability was set at $\Delta f/f = 2 \times 10^{-14}$. This will allow the elimination of the error produced by 10^{-12} km/s² accelerations (Mariner-type spacecraft are typically subject to these levels). The observed stability of the current tracking system is about two orders of magnitude worse than the desired level. If the variation in the frequency bias may be simply modeled (e.g., linear ramp) over a few weeks time period, the stability requirements might be eased somewhat by allowing the bias model to be incorporated into the orbit determination program. The QVLBI determinations of frequency bias on the Goldstone baseline did seem to exhibit a linear drift (neglecting data prior to power failure on August 26), but the data length is not long enough (only one month) to draw definite conclusions.

IV. Concluding Remarks

The short-baseline QVLBI demonstrations provide us with a better understanding of the stability of the current tracking system. The results are summarized below:

- (1) Short-term (min) stability is 8 parts in 10^{13}
- (2) Medium-term stability (hr) is 1.3 parts in 10^{13}
- (3) Long-term stability (month) is 1.9 parts in 10^{12}

²The 1.11-mHz noise may be partly due to the 2-sec difference between the time tags of the two-way and three-way data.

³The values of $\Delta f/f$ in this report have not been computed exactly according to the definition of an Allan variance, the most common means of judging the stability of a frequency standard.

The medium- and long-term values are approximate estimates due to limited samples. Additionally, it was found that more than 90% of the relative frequency bias between two DSSs was due to the frequency standards (HP 5065A).

The long-term stability of the current tracking system exceeds the desired as well as acceptable level of stability of high-precision QVLBI demonstrations. With the current system, the success of the present QVLBI demon-

strations (MVM'73) becomes uncertain for spacecraft acceleration levels lower than 10^{-10} or 10^{-11} km/s². It appears that better frequency standards, like hydrogen masers, are highly desirable for QVLBI demonstrations. The nature of the long-term drifts of current rubidium standards should continue to be examined. This would increase the accuracy of the bias model in the orbit determination program, and also allow a better evaluation of how frequency uncertainties affect orbit determination.

Acknowledgment

The authors wish to thank Don Chaney, who scheduled the two-way tracking discussed herein, and other DSN and Pioneer mission personnel who helped in these demonstrations.

References

1. Ondrasik, V. J., and Rourke, K. H., "Applications of QUASI-VLBI Tracking DATA Types to the Zero Declination and Process Noise Problems," AAS 71-399.
2. Chao, C. C., et al., "Short Baseline QVLBI Demonstrations--Part I," JPL TR 32-1526, Vol. XVIII.
3. Moyer, T. D., "Mathematical Formulation of the Double Precision Orbit Determination Program," Technical Report 32-1527, Jet Propulsion Laboratory, Pasadena, Calif., May 15, 1971.
4. Johnson, D. E., "User's Guide to Differenced Partial Program," TM 391-333, June 9, 1972 (JPL internal document).
5. Thomas, J. B., private communication.

Table 1. Experimental summary: measured frequency biases and bias rates for individual passes of QVLBI data

	Date	Bias a,* mHz	Bias rate b,* mHz/hr	Standard deviation of QVLBI (σ) data, mHz	No. of data points
Goldstone Baseline DSS 11 & DSS 14 (F3 ₁₁ -F2 ₁₄)	8/21	-34.86 \pm 0.14	-0.258 \pm 0.081	2.65	328
	8/22	-34.98 \pm 0.17	-0.196 \pm 0.246	2.08	137
	8/30	-29.93 \pm 0.20	0.021 \pm 0.024	2.51	147
	9/7	-31.73 \pm 0.34	-2.920 \pm 0.60	3.34	96
	9/13	-33.94 \pm 0.30	0.841 \pm 0.70	2.28	59
	9/23	-36.04 \pm 0.13	-0.316 \pm 0.10	2.03	225
	RMS		0.330	2.49	990
					(Total)
Australia Baseline DSS 42 & DSS 43 (F3 ₄₂ -F2 ₄₃)	8/30	-0.158 \pm 0.21	-0.108 \pm 0.43	1.66	65
	9/7	+1.342 \pm 0.07	+0.010 \pm 0.023	1.00	406
	RMS		0.041	1.11	471
					(Total)

*Fit to a straight line $a + b(t - t_m)$, t_m time of mid-point of each pass

$$\frac{\Delta f}{f} = \frac{2.49 \times 10^{-3}}{2.3 \times 10^9} = 1.1 \times 10^{-12} \quad \text{short term}$$

$$\frac{\Delta f}{f} = \frac{0.33 \times 10^{-3}}{2.3 \times 10^9} = 1.5 \times 10^{-13} \quad \text{median term}$$

$$\frac{\Delta f}{f} = \frac{6 \times 10^{-3}}{2.3 \times 10^9} = 2.6 \times 10^{-12} \quad \text{long term}$$

Table 2. Measured frequency stabilities

	No. of Stations	Short term (min)	Medium term (hr)	Long term (days ~ month)
Entire tracking system	Two ^a	1.1×10^{-12}	1.54×10^{-13}	2.6×10^{-12}
	One ^a	7.8×10^{-13}	1.10×10^{-13}	1.85×10^{-12}
System excluding standards HP5065A	Two	4.8×10^{-13}	1.8×10^{-14}	4.4×10^{-14}
	One	3.4×10^{-13}	1.3×10^{-14}	3.1×10^{-14}
Frequency standards HP5065A	Two	7.8×10^{-13}	1.50×10^{-13}	2.6×10^{-12}
	One	7.0×10^{-13}	1.10×10^{-13}	1.85×10^{-12}
^a One-station system = $\frac{\text{two-station system}}{\sqrt{2}}$				

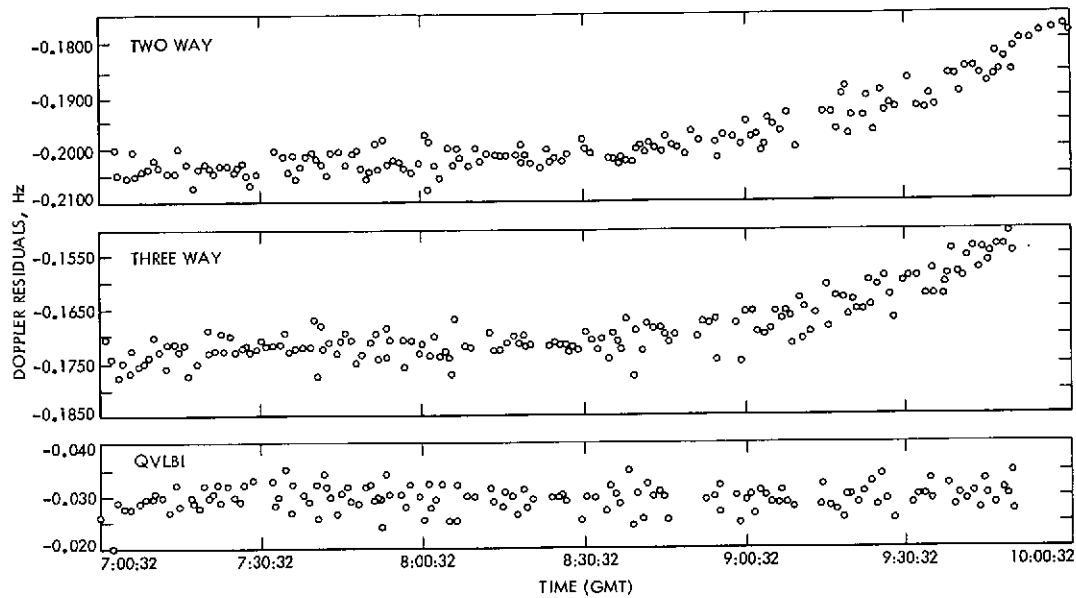


Fig. 1. Two-way, three-way, and QVLBI doppler residuals on Aug. 30, 1973, at DSS 11/41

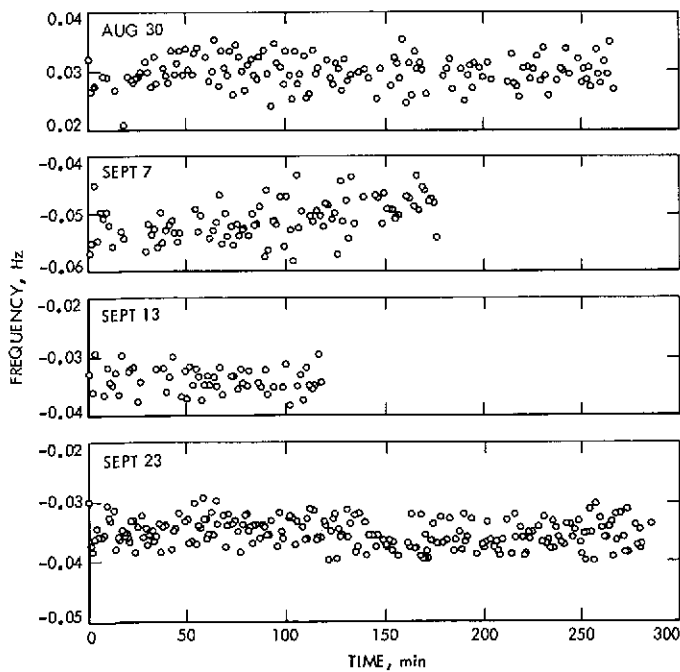


Fig. 2. QVLBI doppler residuals for a number of passes on the DSS 11/14 baseline

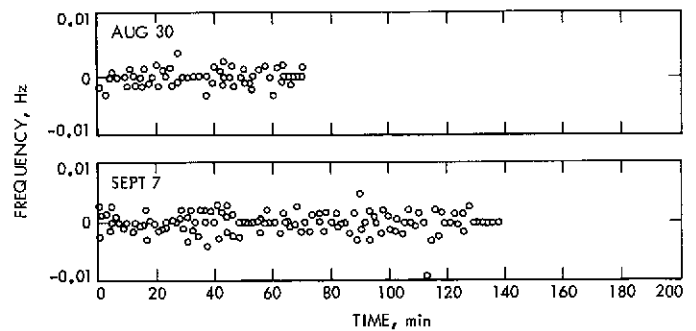


Fig. 3. QVLBI doppler residuals on the DSS 42/43 baseline

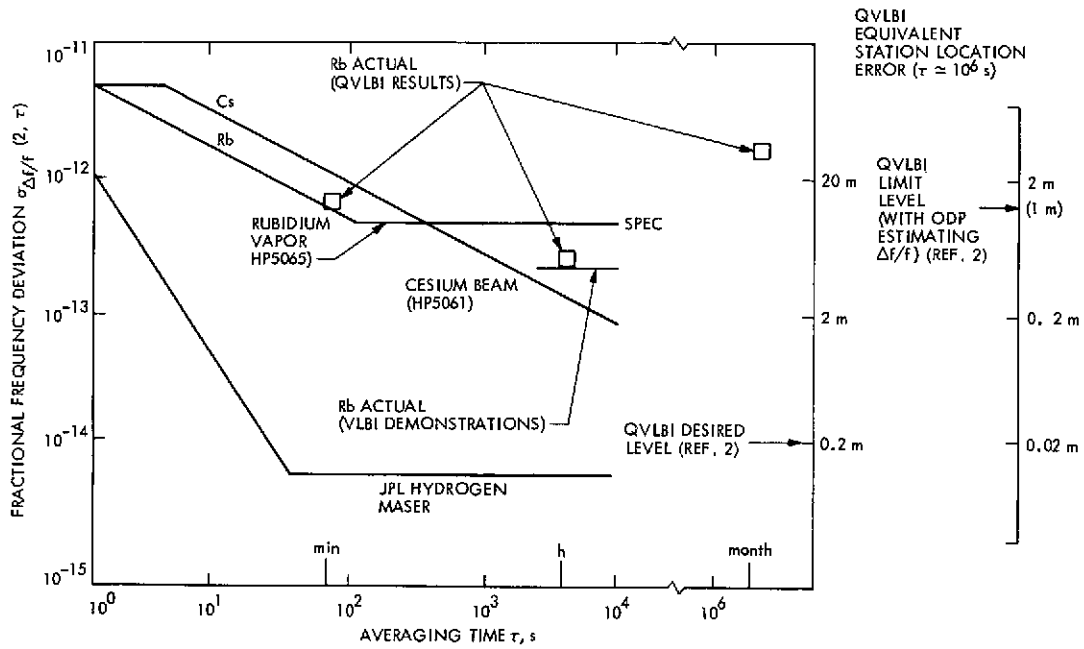


Fig. 4. Comparison of short-baseline QVLBI demonstration results with specifications of various frequency standards and requirements of the QVLBI data type

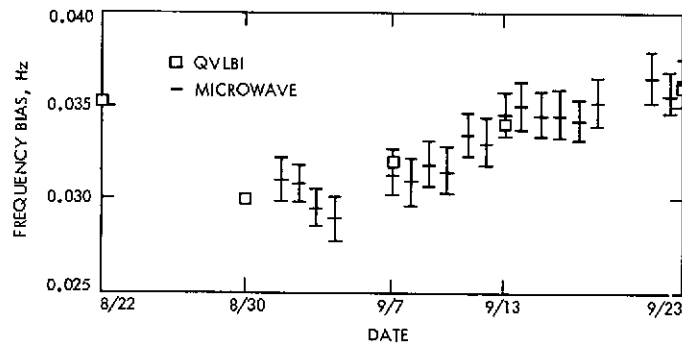


Fig. 5. Comparison of QVLBI determinations of system frequency bias (DSS 11/14) and microwave determinations of frequency standard bias

Report of the Two-Station Doppler (VLBI) Demonstration Conducted With Mariner 9

B. D. Mulhall
DSN Systems Engineering

C. C. Chao, D. E. Johnson, and J. W. Zielenbach
Tracking and Orbit Determination Section

The Mariner 9 spacecraft was simultaneously tracked by the Echo Deep Space Station in the Goldstone Deep Space Communications Complex and Woomera Deep Space Station (no longer operational) during the month and a half prior to Mars encounter. The doppler data obtained were generated using hydrogen masers in the Frequency and Timing System. The benefits gained by tracking with two stations simultaneously and the difficulties encountered in processing the data are described. The results indicate that it is necessary to difference the two-way and three-way doppler explicitly if batch filtering is to be employed when there is significant process noise related to the spacecraft. The results, though promising, are not as conclusive as might be hoped for due to the limited amount of data.

I. Introduction

Analysis and simulations have shown that orbit determination for a spacecraft with process noise, e.g., unmodeled nongravitational forces, can be greatly enhanced by simultaneously obtaining doppler from two remote stations. These simulations are described in Ref. 1 and also described in the second section of this article.

To demonstrate the validity of these assertions, an experiment was undertaken with the Mariner 9 spacecraft. Hydrogen masers had been installed and were operational at two deep space stations—Echo (DSS 12) at Goldstone DSCC and DSS 41 at Woomera, Australia.¹ These hydrogen masers, provided by the Goddard Space Flight Center (GSFC), offered an excellent opportunity to demonstrate two-station doppler. The California-Australia baseline was quite well suited for this demonstration, since an overlap (mutual view period) of 4 hours was available for Mariner 9 during the latter part of the cruise phase.

In addition to the special equipment at the two stations, the experiment could also take advantage of an unusually high level of nitrogen gas leakage from the spacecraft attitude-control subsystem. The leakage (shown in Fig. 1) could not be perfectly modeled, and represented the type of process noise that two-station tracking is intended to overcome.

Consequently, permission was obtained to extend the coverage by DSSs 12 and 41 to track throughout their mutual view period on 18 days during the period October 4 to November 14, 1971. The demonstration had to be performed before the spacecraft went into orbit around the planet Mars since after Mars orbit insertion, the acceleration of the spacecraft by Mars would mask any process noise effect.

The DSN was requested to perform the handover (reassignment of transmitters) at the center of the overlap. By this tracking pattern, equal amounts of three-way data could be obtained from both stations. During the demon-

¹No longer operational.

stration, this request could not always be met since the Mariner Mars 1971 (MM71) Project required that DSS 12 transmit all the way to the end of the view period, so that commands could be entered into the spacecraft from Goldstone. Consequently, only four handovers were executed in the center of the overlap, which proved very unfortunate, as will be discussed later.

II. Description of the Experiment

The two-station doppler demonstration had as its original objectives:

- (1) To demonstrate that three-way data can be processed by the tracking system and orbit determination programs.
- (2) To demonstrate that two-way and three-way doppler can be used to overcome the process noise problem in spacecraft navigation.
- (3) To evaluate the merits of explicitly differencing two-way and three-way doppler as opposed to merely using the two data types together.

The Mariner 9 spacecraft experienced fairly high gas leakage¹ for a Mariner class spacecraft, as shown in Fig. 1. The MM71 Navigation Team had overcome this problem, and was successful in this effort, by using telemetry data to correct the trajectory to compensate for the gas leakage. Although there was some uncertainty in the magnitude of the leaks, their time of occurrence was quite well known from the spacecraft telemetry.

In the initial stages of data analysis, the Orbit Determination Program (ODP) was used with a trajectory which had been corrected for gas leakage. The F2-only solutions (using only two-way doppler) were so close to the Project's current best estimate that there was little hope of improvement when three-way data were added. Consequently, a trajectory which ignored the gas leakage was used, so that improvements by employing two-station doppler could show their potential advantage if the gas leakage was not detected, or if the magnitude of the leakage was very uncertain.

The long arc solution designated by the Project as its best estimate was employed as a standard of comparison for all target plane results determined by this experiment. Station location solutions were compared to the DSN station location work performed after the Mariner 9 Mission since these are the current best estimates of these parameters.

¹Accelerations due to gas leaks are usually $<10^{12}$ km/sec².

The accuracy or reasonableness of other parameters was based on discussions with experts in each particular field.

In the case of the clock frequency offset, the discussions with S. Ward and F. Borncamp of Division 33 indicated that the biases which result from the difference in frequency between the two clocks should be less than 10 mHz. In addition to this, it was known that the bias should be equal in magnitude but opposite in sign on each side of a handover—i.e., when the transmitter assignment is changed from one station to the other.

A third measure of acceptability of experimental results for the frequency bias was to compare the value obtained when the bias was estimated by the ODP with the average of the three-way minus two-way residuals when three-way data were not in the solution. As discussed in later sections, all three criteria have some inherent problems.

Table 1 and Fig. 2 show the data used. These data include two-way doppler (F2), three-way doppler (F3), their difference (F3-2), and discrete spectrum range (Mu). Although the two-way data were available through most of the view period, they were restricted to a short interval near meridian transit for each station, and the mutual view period.

The one-minute F2 and F3 data obtained were compressed up to 10 minutes and synchronized to maximize the number of usable points.

As shown by Table 1 and Fig. 2, there were not as many three-way data obtained as had been hoped for. There are actually only about six days in which the overlap is well covered, and only four of these have the handover near the middle of the overlap. In addition to the doppler data, there are Mu-ranging points fairly evenly distributed throughout the arc. These proved very valuable.

III. Discussion of Solutions

The analysis was all performed postflight. Test philosophy was to process the data as though ignorant of any gas leaks and to compare results using various combinations of four data types (two-way doppler (F2), 3-way doppler (F3), their difference (F3-2) and discrete spectrum range (Mu)). It was assumed that some F2 and Mu data would be needed to establish the geocentric orbit, but a method had to be found to weight the data to give only as much geocentric information as necessary without falling prey to the process noise present in these data.

The more important difficulties occurred in trying to eliminate the three-way frequency biases and transmission media effects.

Even though the expected three-way biases using the hydrogen masers were only about 5 mHz, they had a significant effect on target plane results and had to be removed. Analysis of the instrument calibration data showed that the uncertainty in the determination of the clock drifts (which cause the biases) was much larger than the magnitude of the drifts themselves (Fig. 3), which seemed to indicate those independent measurements could not be used to model the biases. The only recourse was to estimate the biases in the ODP. There were some constraints that could be applied. However, the exceptional stability of the masers would suggest slowly varying biases, if any, although short period changes might be induced from other portions of the tracking system, like the synthesizer. The biases were assumed constant over any pass from a given station and in some solutions, constant over the entire 45-day arc.

It was also found necessary to develop some criteria for judging the quality of the results, because they showed the typical intermediate arc dispersions of 100-200 km in $B \cdot R$ (the component in the target plane parallel to the ecliptic).

We established the following criteria for judging the credibility of the bias values obtained from the ODP solution:

- (1) The biases should be invariant with data weight and parameter set.
- (2) The biases should be less than 0.01 Hz and fairly constant over the 45-day span.

IV. Solutions for Frequency Bias

Early attempts at fitting two-way and three-way doppler with partials for the frequency bias resulted in values which did not meet any of the two criteria listed in the above paragraph. These first attempts used partials which modeled the frequency offset as a constant for each station for each day. Realizing that this most obvious approach was not working, a simulation was attempted to investigate the problem.

This simulation consisted of replacing all the two-way residuals with zero and all the three-way residuals with the value 3 mHz. When a solution was attempted with this simulated data, erroneous values resulted, even

though the data were "perfect" and the model was a perfect description of the data. On certain days, the value obtained from the solution for the bias was as far off as 0.5 mHz.

The covariance matrices from these solutions showed that the position of the spacecraft was highly correlated (correlation of X and $Z \sim 0.9$ correlation of Y and $Z \sim 0.98$). To overcome this singularity in position, ranging data were entered and with the addition of this data type, the simulated bias could be solved for with very good accuracy.

When ranging data were used to solve for the three-way frequency bias with real data, the values for the biases which resulted still did not fill the two criteria mentioned earlier. Consequently, other approaches were tried. These consisted of adding off diagonal terms to the *a priori* covariance matrix to model the correlation of the bias from day to day. In addition to these aids, the negative correlation between the three-way frequency bias at the two stations at the time of handover was also modeled by making the partial for the three-way bias one parameter for the two stations with a value of $+1$ for DSS 12 and -1 for DSS 41. Finally solutions were attempted with a single bias over the entire 45-day period.

Even with all these crutches, the values of the biases were still not consistent from two-way and three-way doppler as compared to differenced doppler. These results are shown in Fig. 4a.

The two requirements for reasonable answers are nearly met by those solutions with F3-2 which solve for differenced station locations rather than one station and the baseline position. These values agree quite well with the difference between the two-way and three-way residuals when the three-way data are not in the solution.

Since the data have been calibrated for the troposphere and ionosphere, it is not believed to be due to this atmospheric effect. The errors in this calibration could cause some of the scatter shown in Fig. 4 on the values obtained for the biases.

Finally, solutions were attempted solving for a single bias over the entire 45-day arc. The bias was arbitrarily assigned a partial of $+1$ for DSS 12 and -1 for DSS 41. Figures 4a and 4b show the resultant values of the bias and the target plane results. Solutions employing F2 and F3 agree fairly well with differenced doppler solutions solving for differenced station locations in terms of the values of the bias. These results for the bias also tend to

agree with solutions for individual (by pass) biases. However, the effect on station locations and target plane results do not agree.

Even more disturbing is the result obtained when we solve for one bias, one station location (DSS 12) and the baseline. The result for the bias in this case has a sign different from most other solutions.

This is due to the limited data set. In this solution the F2 data from DSS 41 are ignored since they could not be employed to solve for DSS 41's location. Solving for the locations of DSS 12 and DSS 41 as well as the baseline would have been solving for six parameters only four of which are independent.

V. Two-Way Data Only

Two different nominal trajectories, with and without gas leakage corrections were used to process the F2 data described earlier, giving the results shown in Fig. 5. The solutions based on the trajectory with gas leakage corrections (Case A to G) agreed better with the Project's current best estimate (CBE), than the other set (Case A' to G') ignoring gas leakage, and were not particularly sensitive to the inclusion of various parameters except solar pressure. Two-way solutions without gas leakage calibrations spread out perpendicular to the **B** vector bear out the predicted sensitivity of station location and solar pressure solutions to gas leakage when only F2 data are present.

When all the DSS 12 and DSS 41 F2 data between Oct. 4 and Nov. 13 (2600 points) were included the results based on the trajectory without leaks improved somewhat, but the solutions involving station locations, solar pressure and mass (GM) of the moon were still quite volatile. The station longitude corrections from Case G of this set were 2 to 3 m more than the usual 6 m seen in all the other conventional processing and when GM of the moon was not included in the solution the longitude corrections became as large as 18 m.

The sigma used for weighting all the F2 data was 0.045 Hz per 60-s count time. The results of the truncated arc of F2 data processed without gas leakage correction were chosen as a reference for later comparisons because

- (1) It involved the same number of passes as were available for the F2 and F3 data.
- (2) It gave reasonable solutions for the various estimated parameters.

- (3) The absence of gas leak corrections gave the differenced data an opportunity to show the potential improvement for unmodeled accelerations.

VI. Two-way Doppler and Range

When 14-Mu ranging points ($\sigma = 150$ m) were included with the truncated F2 data, the **B**·**T** components of the errors were all decreased by 50 km, bringing them into closer agreement with the CBE (Fig. 6). Although the longitude at each station changed 2m from the F2-only solutions (Fig. 7) no other parameters changed significantly. The spread of these results in the target plane (**B**-plane) indicates that solutions involving station locations and GM of the moon are still seeing the gas leakage but that the solar pressure parameters no longer are as important, since certain components of the position of the spacecraft are tied tightly down by range data.

VII. Two-way Doppler, Three-way Doppler, and Range

Once F3 points were included, the frequency offset between the two station clocks had to be estimated.

A total of 28 bias parameters representing the frequency offset at each station on each day were added to the "solve for" sets A-G. The results for the biases were discouraging because they varied with changes in data weight and solve for parameters, and were not slowly varying as anticipated. The bias parameters were absorbing not only the frequency offset, but also all the effects due to process noise (gas leakage) and uncalibrated transmission media effects. Unfortunately there was no way to separate these phenomena. The values of **B**-plane and station location solutions are not significantly different from those of two-way doppler and range (Figs. 6, 7, and 8).

VIII. Differenced Doppler Alone

Differencing F2 from F3 data gave significantly better residuals than either data type taken separately. Figure 9 shows the residuals of F2, F3 and F3-2 during two relatively noisy passes on October 23, 24, 28 and 29 and clearly indicates that the noise of unknown source which is common to both F2 and F3 data has been removed during the differencing. The squares represent the residuals of F3 before the fit and the circles and triangles show the residuals after the fit.

Solutions were studied which contained only F3-2 data but the six state parameters were highly correlated due to the poor geometry covered by this particular arc. As mentioned earlier the differencing destroys geocentric range-rate information leaving only the right ascension and declination of the spacecraft. As with classical astronomical observations, the restriction to angular measurement demands longer arcs or a better geometry to determine the orbit. Thus loosely weighted two-way doppler and ranging data were introduced to resolve this problem without excessively reintroducing process noise.

IX. Differenced Doppler, Two-way Doppler and Range

Once the geocentric information (F2 and Mu) is included, the indeterminacy of the orbit decreases. Although about half the correlations in spacecraft state are still above 0.9 when F2 and Mu data are included, the improved B-plane behavior gives us confidence that the problem is disappearing. There were other encouraging results as well. The estimated values of station location which are provided by the F2 and Mu data are about -4 m in longitude change and less than 2 m in spin axis change (Fig. 7). The estimated value of baseline longitude is also close to -4 m which is consistent with the change occurring at each station. However, the estimated value of the change of baseline projection Δr_b , which is about 12 m is larger than we expected. This could be due to the large *a priori* value used for r_b ($\sigma_{r_b} = 1$ km) and the relatively high correlations with those bias parameters ($\rho \approx 0.7$).

There was also good repeatability of the estimated values of frequency bias for solutions with different data weights and estimated parameters. The average magnitude of the estimated biases was about 4 mHz and they were slowly varying most of the time. This implies that the earlier variations were in fact due to absorption of process noise on a pass by pass basis.

B-plane solutions show significant improvement when the differenced data were tightly weighted (Fig. 10). Among the solutions, cases A, B, and C coincide with one another and cases E, F, and G do also. This indicates that the differenced data with F2 and Mu are not sensitive to solar pressure, attitude control, GM Moon, GM Mars and ephemerides, which is to be expected since they all affect the geocentric motion. It is only sensitive to station locations and baseline parameters.

X. Differenced Doppler and Two-way Doppler

Solutions with data weights: $\sigma_{F3-2} = 0.002$ Hz, $\sigma_{F2} = 0.011$ Hz, without Mu data were attempted but they moved the B-plane results further away from the CBE. The residuals induced in Mu were far too large, and the station location changes were unreasonable.

XI. Differenced Doppler and Range

A solution with data weights: $\sigma_{F3-2} = 0.002$ Hz, $\sigma_{Mu} = 50$ m was tried. Similarly to the previous case the results moved the B-plane solutions further away from the CBE but in the opposite direction. The residuals induced in F2 were quite large. Station location changes were also unreasonable.

The last two solutions (F3-2 with F2 and F3-2 with Mu) indicate that the poor geometry seriously degrades the stability of the orbit determination, and it becomes necessary to include both geocentric range and range-rate information to obtain a correct solution.

XII. Conclusions and Recommendations

This demonstration shows that differencing two-way and three-way doppler data can reduce the effect of process noise in the spacecraft. However, referring to Fig. 11, it is not as clearly demonstrated as was hoped for. The F2-only solution using trajectory corrected for gas leakage performs almost as well as the solution using differenced data and a trajectory that ignores gas leakage. It is not clear from this demonstration whether F3 data without differencing can help the gas leakage problem, since no really good solution was obtained from this data type. However, this may be due to the pathological data arc which undermines attempts to remove the three-way frequency bias. It remains to be seen how effectively sequential filtering can employ three-way data, possibly without differencing, in a high process noise environment.

Future demonstrations of two-station tracking should be made over sufficiently long arcs, so that singularity between parameters can be more readily overcome. With a sufficiently long arc of data, the problem of solving for the three-way bias which beset this demonstration very likely could be handled. Even with hydrogen masers, the elimination of the three-way bias can be a significant problem. As previously noted, the two-way and three-way

solutions as well as differenced data solutions did not produce consistent values for these biases (Fig. 4). To obtain a consistent set of values for the three-way biases, it was necessary to weight the F2 data, corrupted by process noise, more heavily than was desirable. Future demonstrations should ensure that handovers of transmitter assignments be performed at the middle of the overlap when-

ever possible, since this greatly reduces the difficulty in solving for the three-way frequency bias.

In addition, the ODE should be modified, so that synchronization between two-way and three-way data can be obtained when compressions of these data types are performed.

Acknowledgments

The authors wish to acknowledge the assistance of Neil Mottinger for many helpful suggestions and for several changes to his program which enabled us to manipulate ODP files; F. B. Winn, who suggested using ranging data to overcome the singularity in position; D. Curkendall, who suggested representing the negative correlation of frequency bias from one station to another by changing the sign on the partial; F. Borncamp and S. Ward, for providing much useful information about the nature of the frequency biases, and V. J. Ondrasik, B. Thomas, and D. Trask for their helpful suggestions.

Reference

1. Ondrasik, V. J., and Rourke, K. H., "Applications of Quasi-VLBI Tracking Data Types to the Zero Declination and Process Noise Problems," paper presented at AAS/AIAA, Astrodynamics Specialties Conference, AAS No. 71-399, Aug. 17, 1971.

Table 1. Number of data points

Data type		DSS 12	DSS 41	Subtotal
F2	Truncated ^a F2	295	130	425
	Near meridian passage	130	63	193
F3		36	180	216
F3-2		35	170	205
Mu		14	0	14
Total		370	480	850

^aF2 data outside the common view periods were deleted.

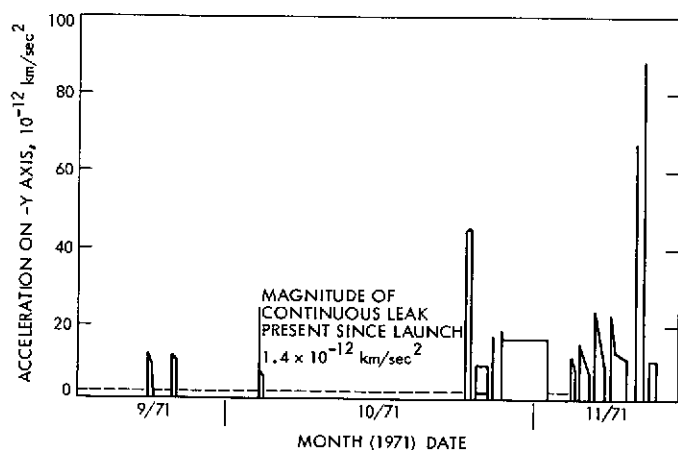


Fig. 1. Mariner Mars '71 spacecraft accelerations due to attitude-control gas leakage

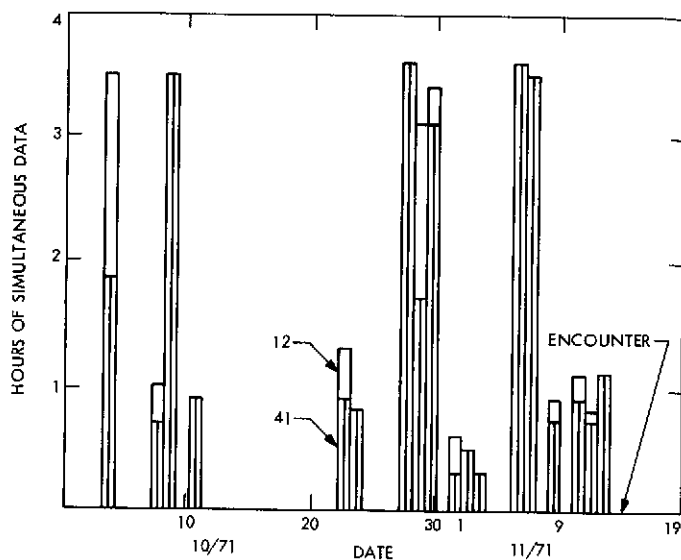


Fig. 2. Mariner 9 simultaneous doppler data (hydrogen masers)

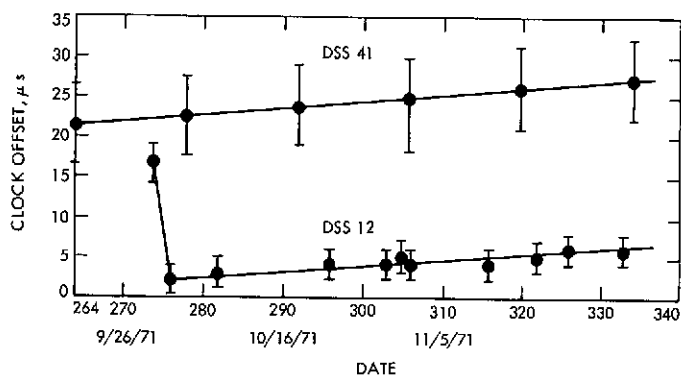


Fig. 3. DSSs 12 and 41 clock offsets

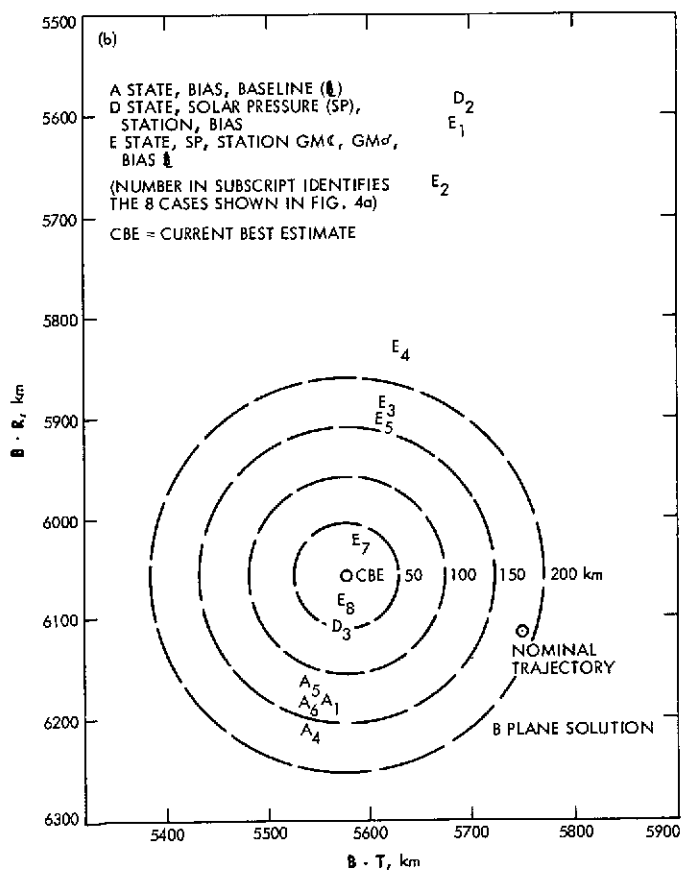
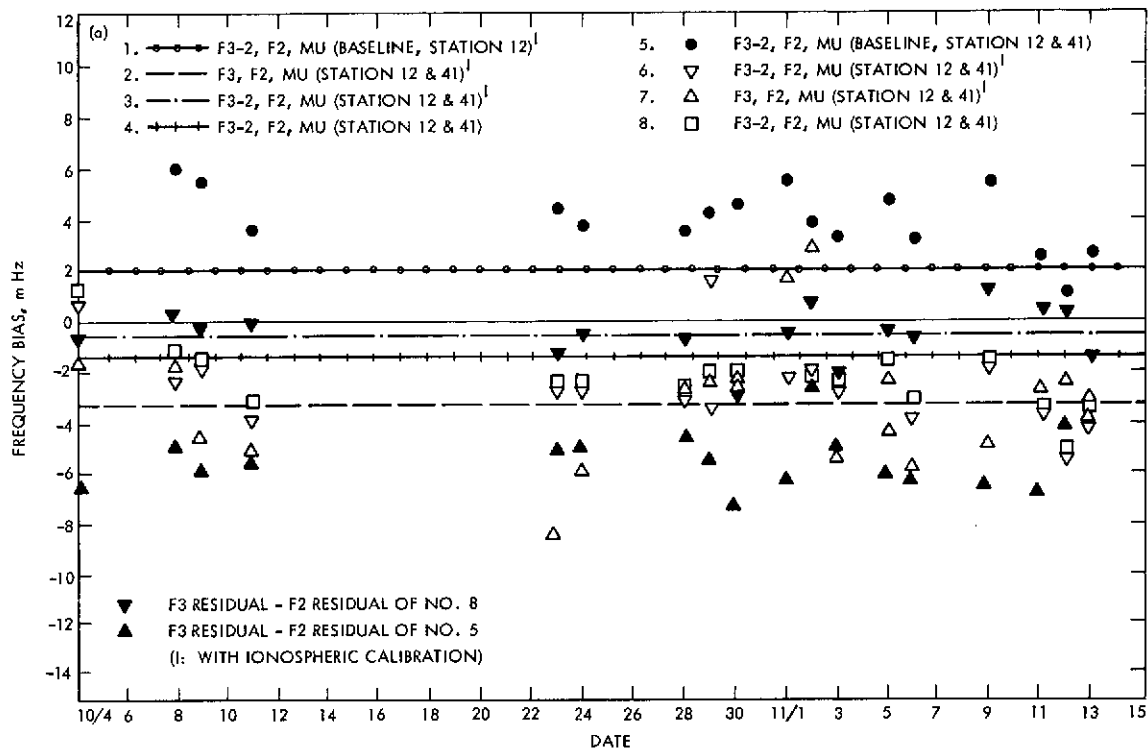


Fig. 4. Two-station doppler solutions: (a) Estimated frequency offset between two frequency standards, (b) target plane solutions

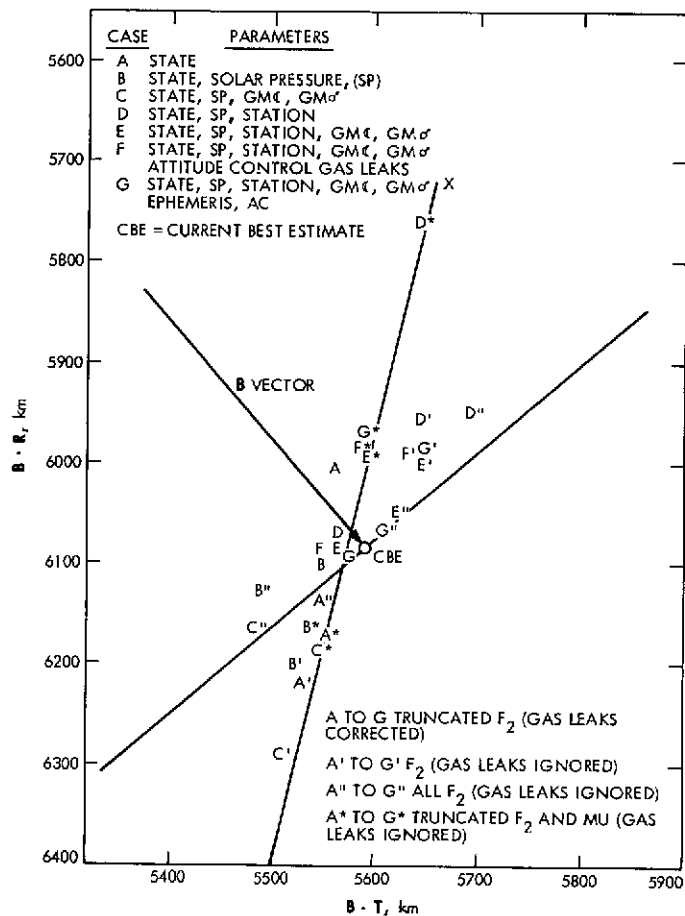
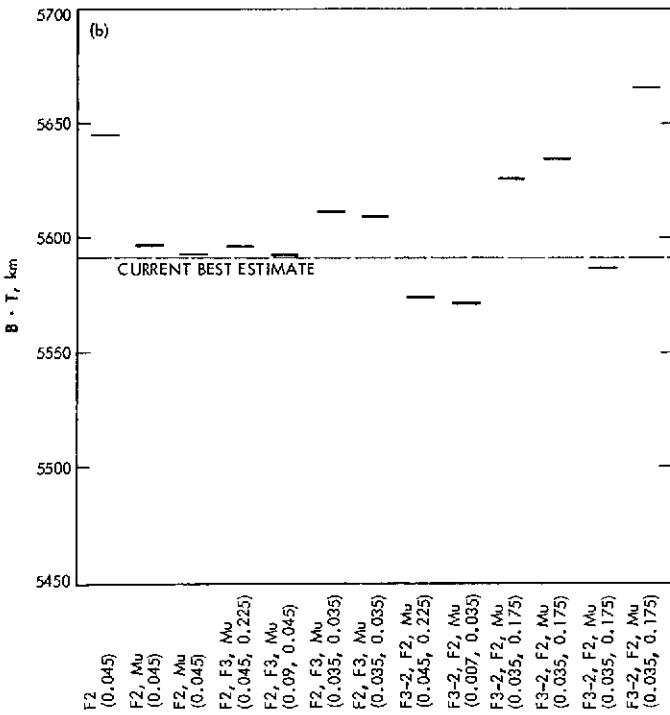
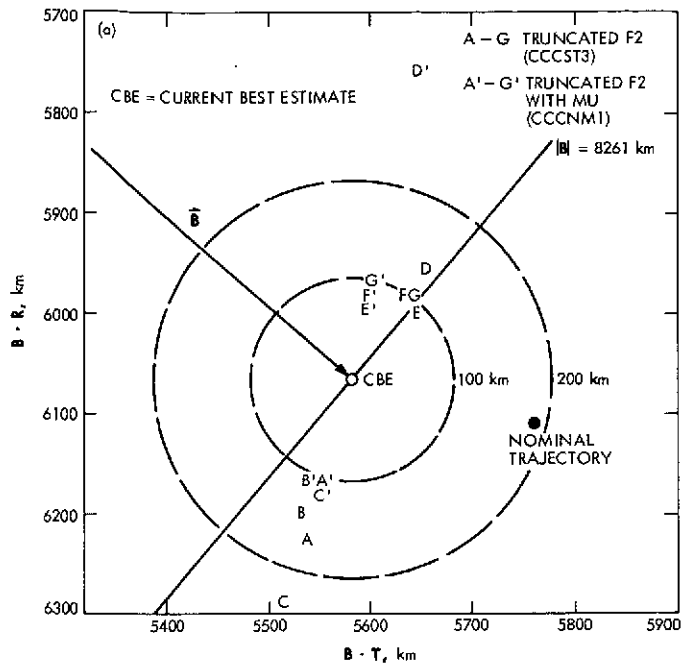


Fig. 5. Two-way doppler B-plane solutions



NOTE: DATA WEIGHTS IN PARENTHESES ARE IN Hz OR ns

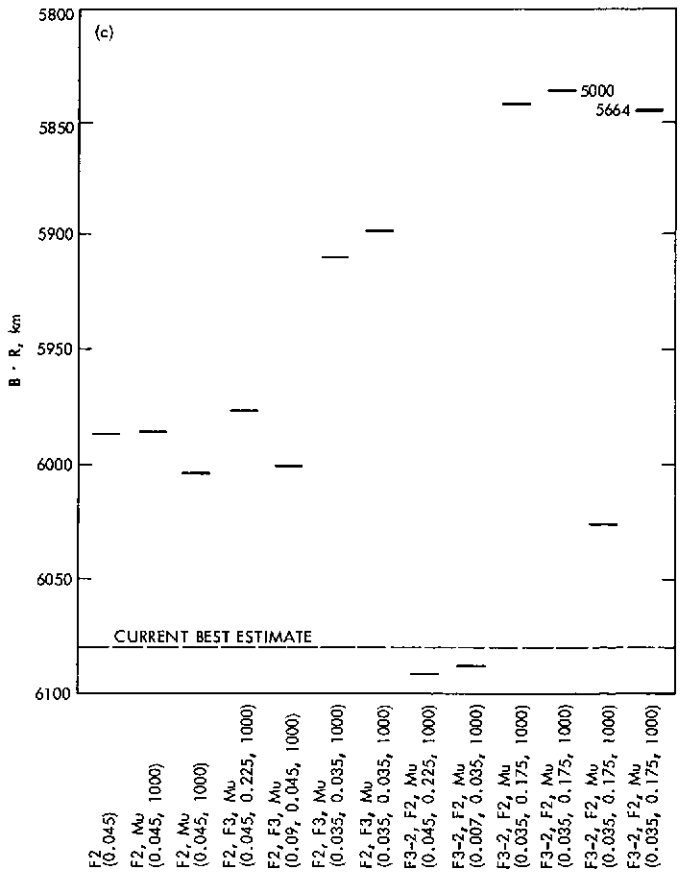
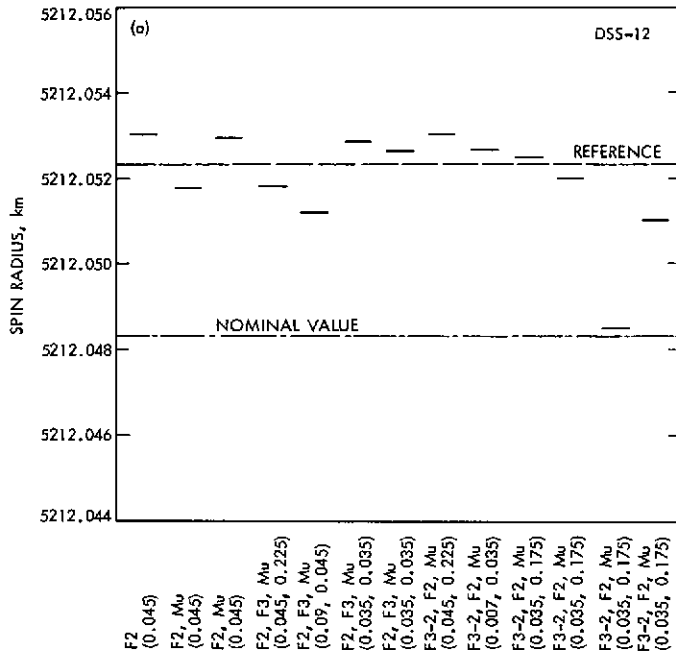


Fig. 6. Two-way doppler B-plane solutions: (a) target plane solutions, (b) $B \cdot T$ results, (c) $B \cdot R$ results



NOTE: DATA WEIGHTS IN PARENTHESES IN Hz OR ns

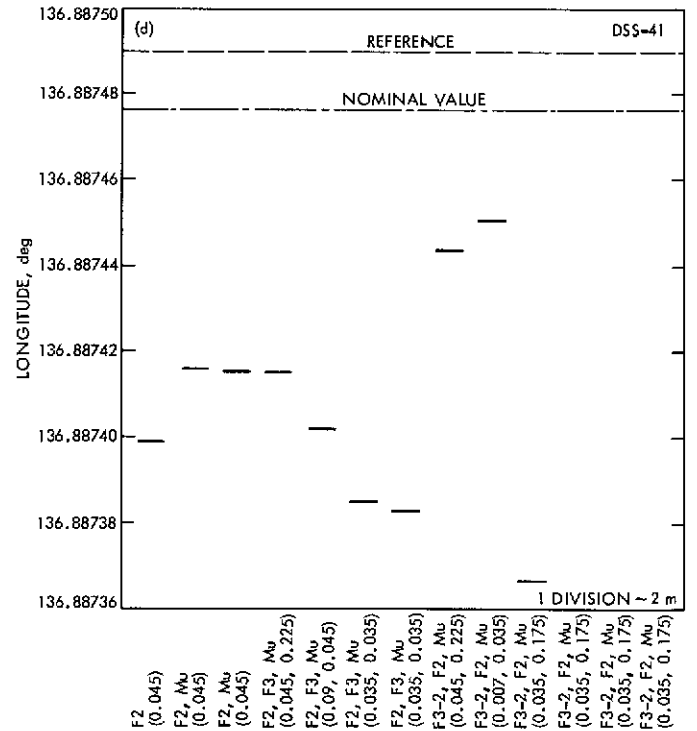
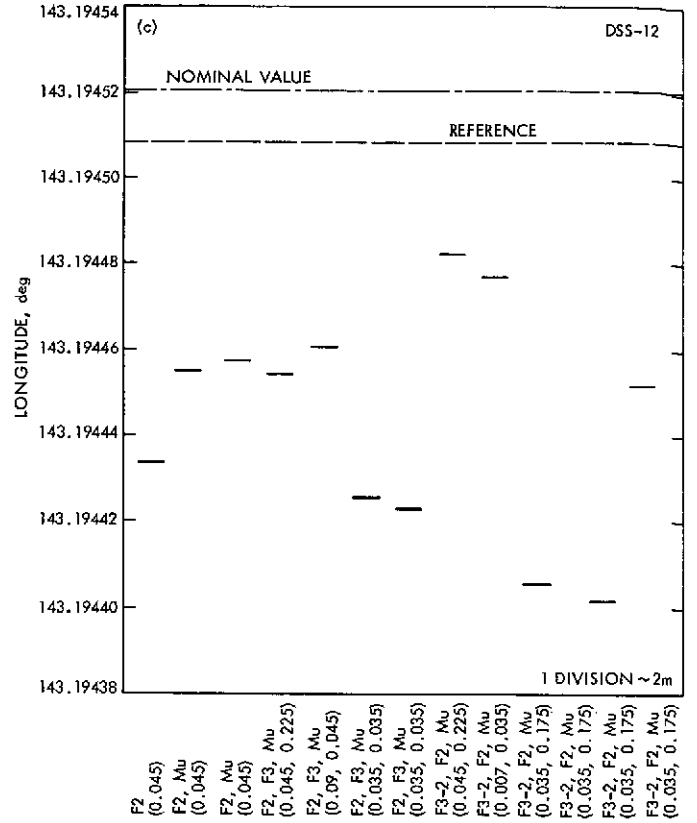
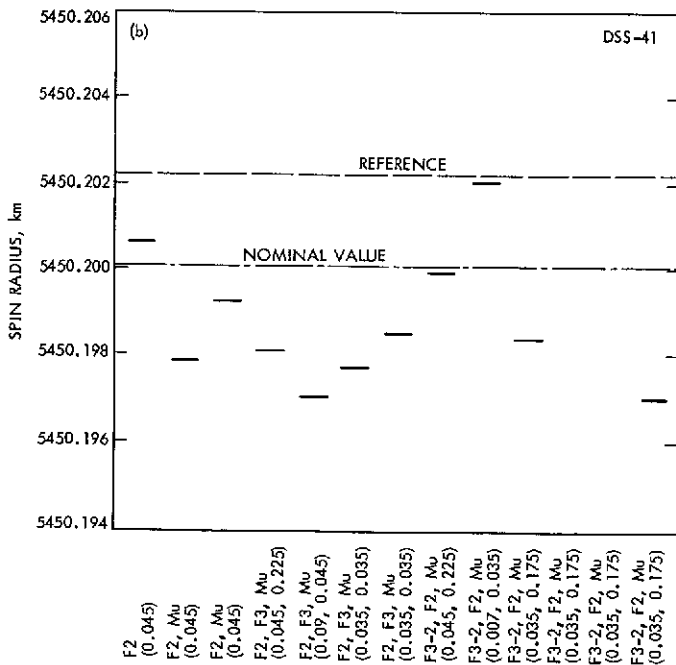


Fig. 7. Station location results: (a) distance off spin axis, DSS 12, (b) distance off spin axis, DSS 41, (c) geocentric longitude, DSS 12, (d) geocentric longitude, DSS 41

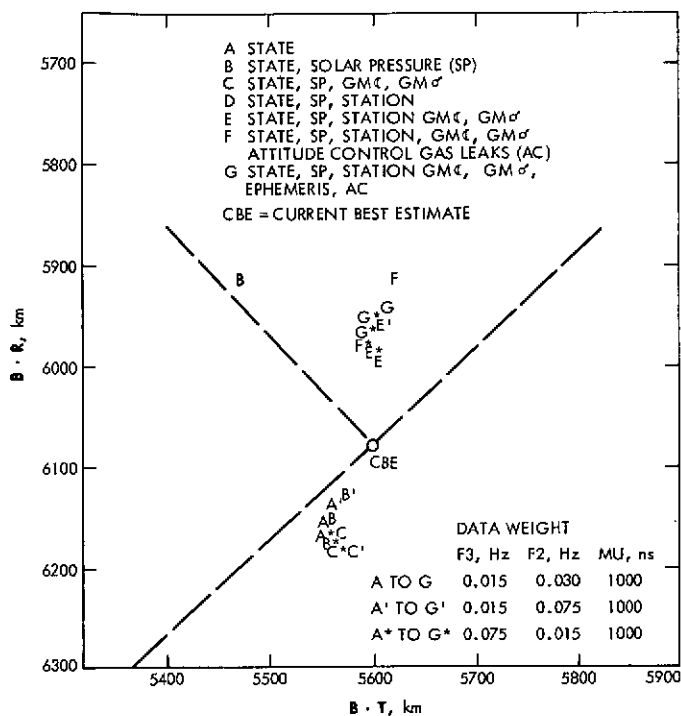


Fig. 8. Two-way and three-way doppler B-plane solutions

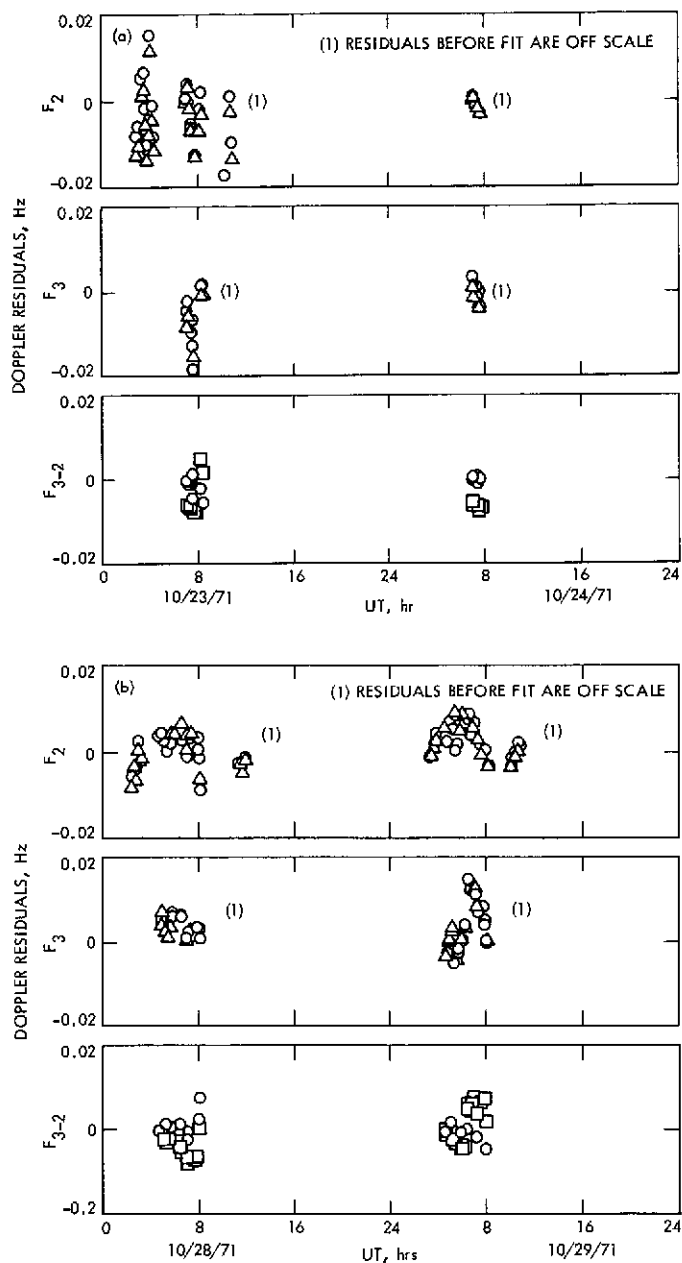


Fig. 9. Mariner 9 doppler residuals: (a) on October 23 and 24, 1971, (b) on October 28 and 29, 1971

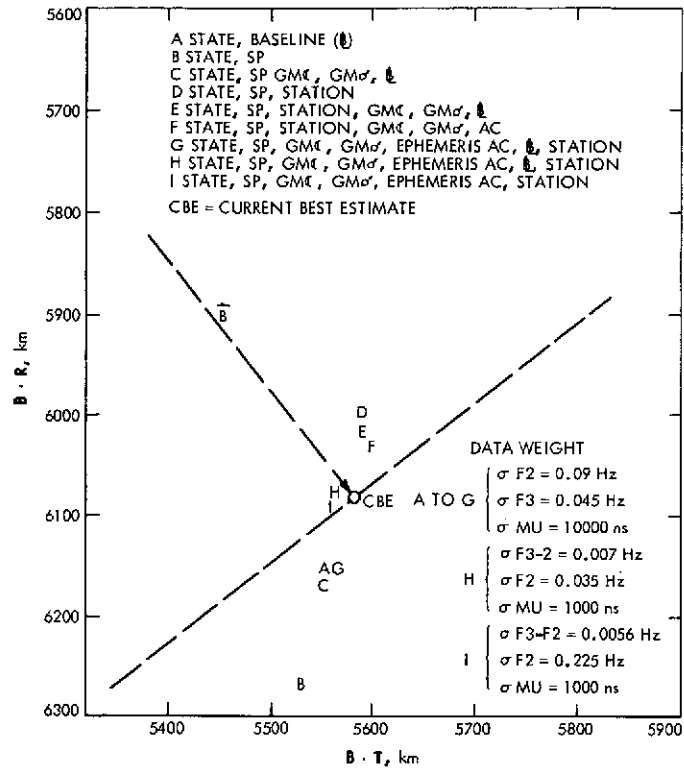


Fig. 10. Two-way and differenced doppler with range
B-plane solutions

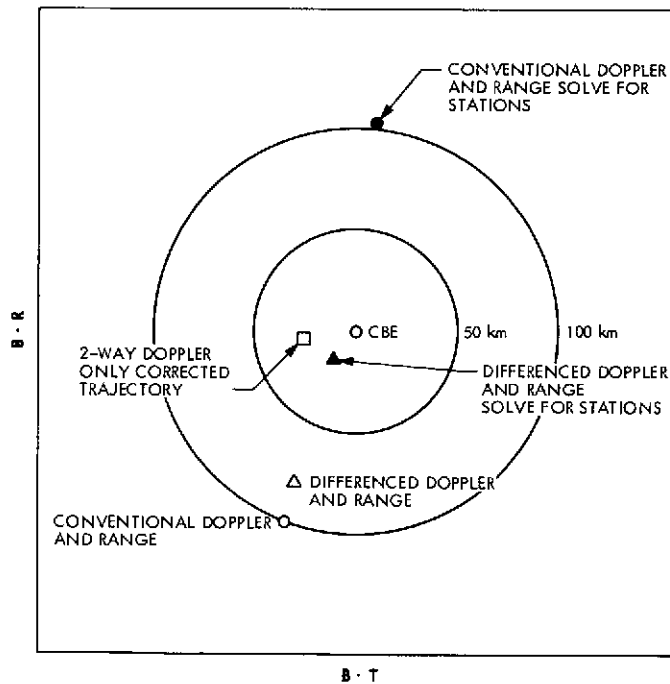


Fig. 11. Summary of results from Mariner 9 two-station
doppler demonstration

Redesign of High-Power Transmitter Control and Indicator Cards

J. R. Paluka
R.F. Systems Development Section

S. F. Moore
Resdel Engineering
Arcadia, California

The control and indicator printed circuit cards used in the DSN high-power transmitter and the high-power X-band radar transmitter have been redesigned to incorporate short-circuit protection into their outputs. This redesign will increase the overall reliability of these transmitters by eliminating transistor burnouts resulting from shorted interconnection lines, inadvertent shorts while troubleshooting, and other overloads.

I. Introduction

The high-power transmitter was installed at DSS 14 in 1969. A review of its faults since that time has indicated a large percentage to be circuit card failures resulting from overloaded output transistors. Some of these overloads resulted from shorts in interconnection cables that are up to 600 m in length; others have resulted from inadvertent shorts across control or indicator circuits while performing subsystem maintenance. In most cases the result was the same: burned-out transistors and card failure.

With the installation of new high-power transmitters at DSS 43 and DSS 63 during 1974 and 1975, it was resolved to correct this overload problem by redesigning the control logic, metering, and other indicator circuit cards. It was also resolved to preserve the individual circuit card dimensions and connector interface so that the new cards could be retrofitted into the DSS 14 transmitter with no wiring changes.

II. Development

Of the seven types of printed circuit cards in the transmitter controls requiring protection, the most representative of the problem was the lamp/relay driver card. Accordingly, this card was selected for use in the initial development work with a goal of applying similar short-circuit protection to the other types of cards in the controls.

The old lamp/relay driver card provided five independent signal channels, each having a set of complementary outputs. An additional goal of putting seven such channels on each card, to allow for future expansion of the transmitter to an X-band radar, was also made. As with the old cards, each channel was required to provide a minimum of 300 mA of steady-state current.

Additional problems existed in the case of the lamp/relay driver card. One such problem is that each channel

may have to drive up to four parallel incandescent indicator lamps. Such lamps have a cold resistance in the order of six to eight times less than their normal hot resistance. Thus, while providing semiconductor protection when the circuit was shorted to ground, the circuit should not be prevented from working when presented with a cold resistance load typically requiring 1.3 A for only 50 ms before dropping to a nominal value of 160 mA. A similar requirement was put on the lamp/relay driver output circuit when required to drive the solenoids of the interlock event recorders. The choice of a current limiter circuit for this card was restricted further by space and the requirement that the entire channel develop a minimum of 25-V output at 300 mA from a supply voltage of 28 V.

As indicated in Fig. 1, a schematic of one of the seven channels of the new lamp/relay driver card, the solution to the current limiter problem was a three-terminal regulator. This is a device that limits the current to approximately 2-A peak current while providing a steady-state current of 500 mA. Since this device is protected by an internal thermal shut-down circuit, it is mounted without a heat sink, thus using the internal heat it produces to protect the circuit. A drawback of this device is that the maximum available output is 24 V; however by biasing the ground terminal to three volts, the regulator will be full on and provide 26.5 V.

When the regulator is overloaded because of a short or other reason, it reduces its output voltage to a safe value. This is accomplished by internal current limiting and by thermal shutdown. This reduction in output voltage increases the voltage across the regulator, turning on the light emitting diode (LED) across the regulator and indicating which channel has an overload fault. The seven LEDs for the entire board are located in a row near the printed circuit card handle where they are clearly visible to the operator when the board is in service. Upon removal of the fault, the circuit returns itself to normal operation and the LED is extinguished.

To gain space and decrease parts count an integrated circuit was chosen for an input device. The LM2900 was selected because it will operate at +28 V on a single supply. This operational amplifier (known as a Norton amplifier) is a type that differentiates between input currents rather than input voltages. Although no advantage was gained by this feature, it provided the necessary open loop gain and, more importantly, the output current sink is sufficient to keep the output transistors (2N5783)

always saturated, thus reducing the power dissipated in them to a safe value.

Because the IC selected contains four differential amplifiers, two amplifiers per IC were used to produce the set of complementary outputs required for each signal channel. The point at which the amplifiers switch is selected by the value of resistor dividers R3 and R4. This selection point is a low-impedance point relative to the input resistors R5 and R8. This makes selection of the switching point an easy matter when the circuit is used in other applications.

The normal process for an operational amplifier is to use a feedback resistor to set the gain of the amplifier. This was dispensed with because the amplifier was to have as high a gain as possible. An additional resistor per channel was saved by not having a "pull-up" resistor to keep the output transistors off. These are not needed because the emitter-base is back-biased by the input driver amplifier. The transistor back-bias results from the voltage difference produced by the current limiter.

The 1N649 diode in each output is to prevent high currents that result from the inductive kick of relay coils in the loads destroying the output transistors, and to protect the circuit when connected to a voltage higher than +28 V.

III. Conclusion

A prototype of the new lamp/relay driver card was built and successfully tested in the DSS 14 high-power transmitter. The protective circuit developed for this card was subsequently applied to the summing logic, final logic, warning circuit, bistable on-off, and deenergize delay printed circuit cards. The seventh type of card requiring short-circuit protection was the meter driver. Since other extensive development work had to be performed on this board to provide two meter channels and to provide variable gain for different applications, it was decided to provide the required short-circuit protection by selection of an integrated circuit having inherent protection. Such a device is adequate for this circuit since large output power is not required. As indicated in Fig. 2, a single 747 was selected to provide two meter channels.

Acknowledgment is made for the assistance of Resdel Engineering Corporation of Arcadia, California, particularly Mr. S. F. Moore, for much of the circuit development portion of this undertaking.

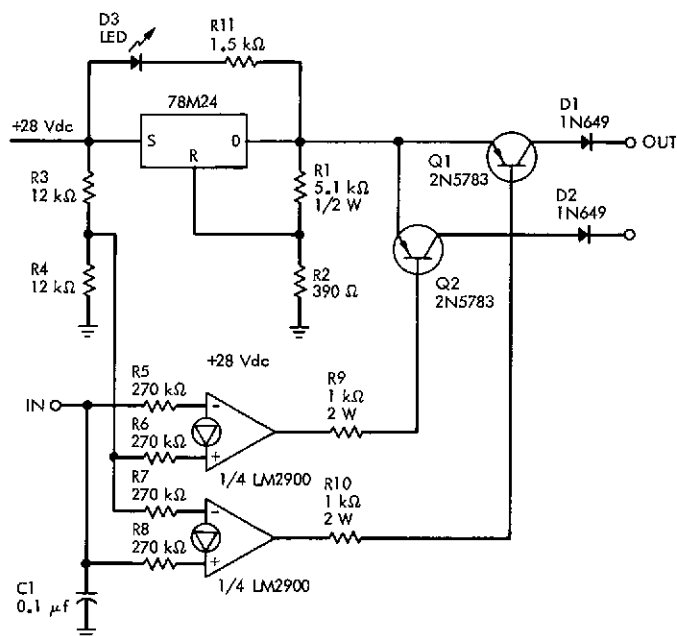


Fig. 1. Schematic, single channel of lamp/relay driver card

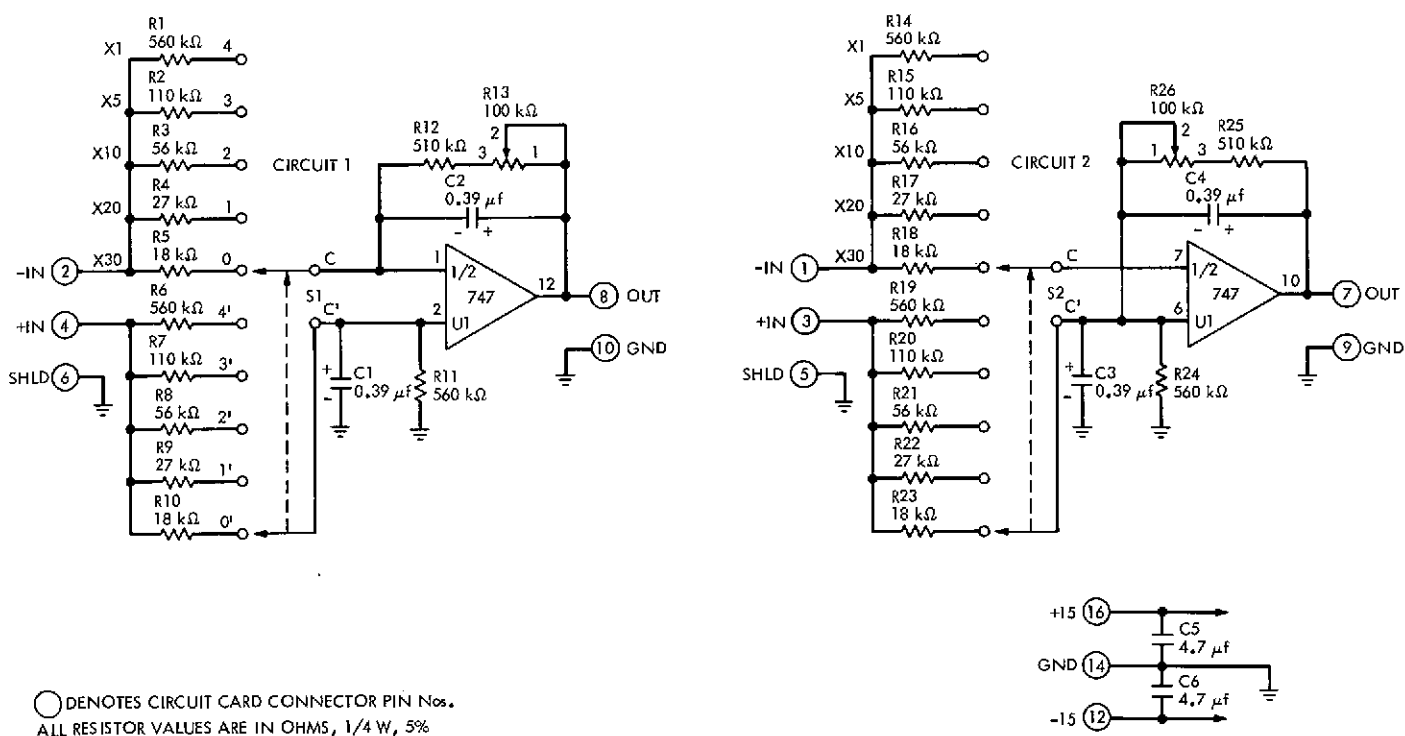


Fig. 2. Schematic, meter driver circuit

X-Band Radar Development

M. A. Gregg and R. B. Kolbly
R. F. Systems Development Section

Development progress of the DSS 14 X-band radar transmitter is described. Specific subassemblies discussed are the exciter, combiner controller for the two 250-kW klystrons, and various high-power components associated with klystron output combining and monitoring.

I. Introduction

This portion of the X-band radar development effort involves the installation and integration of two 250-kW klystrons into the lower part of a Cassegrain cone which will be mounted onto the tricone assembly of the DSS 14 64-m antenna. The object of the effort is to obtain 400 kW (+86 dBm) output using a hybrid combiner, power splitters, directional couplers, waveguide switches, and an associated exciter-combiner control.

Because of the limited space in the Cassegrain cone, a special handling fixture and carriage were designed to install and remove the klystrons with the cone mounted on the antenna.

II. Exciter-Buffer Amplifier

Figure 1 is a block diagram of the buffer amplifier and combiner control subsystem. The high-power klystron amplifiers used in the X-band radar system require approximately 5 watts (+37 dBm) of drive, when operating at full power output in a saturated mode. To assure adequate drive at the klystron, two Varian model VTH-6079H1 traveling wave tube amplifiers are used as buffer amplifiers. The helix of this traveling wave tube (TWT) will change the relative phase shift through the TWT by approximately 1.6 deg for each volt change in the helix voltage. Therefore, the helices of the TWT amplifiers will be used as phase control elements to keep the output of the high-power klystron amplifiers in proper phase. The

phase-error signal from the combiner control unit is converted to a push-pull signal and applied to the helices of both TWT amplifiers to minimize amplitude variations of the drive signal. A diode phase switch is incorporated in one of the drive lines to reverse the relative phase between the two outputs of the buffer amplifier. Such a phase reversal will cause the power output of the high-power combiner to be delivered to the "waster" load instead of the antenna. The diode phase switch, operating at a few milliwatts of power, is performing the function of a high-speed 500-kW RF switch.

III. RF Drive Control Circuitry

In order to provide remote control of the drive power supplied to each klystron, P-intrinsic-N (PIN) diode modulators are used to control the drive power to each TWT amplifier. A voltage-controlled constant current source supplies the required bias current to the PIN-diode modulators. Voltage for the current source is derived from a digital-to-analog (D/A) converter. A remotely controlled up/down counter is used to furnish the data for the (D/A) converter. This method allows the klystron drive to be controlled from many locations and effectively prevents any noise on the control lines from amplitude-modulating the klystron drive. In addition, it is necessary that the drive control circuitry allow rapid removal of drive from the klystron in the event of a waveguide arc. If an arc is detected in the waveguide, a signal is applied to one or more of the arc detector inputs, and the drive control logic drives the PIN-diode attenuators to maximum attenuation. For redundancy, a PIN-diode switch on the output of the $\times 16$ multiplier is also opened. An arc detector signal at any one of the inputs will cause the drive to both klystrons to be removed.

IV. Combiner Control Circuitry

Samples of the outputs from the two high-power klystron amplifiers are compared in the phase detector section of the combiner control unit. This phase error signal then drives a high-gain amplifier with appropriate filtering to drive the helices of the TWT amplifiers in the buffer amplifier assembly. Since the sense of the phase detector

is reversed when the phase switch in the buffer amplifier is in a position to deliver the output power to the "waster" load, it is necessary to incorporate an inversion in the combiner control amplifier when it is desired to deliver the power to the "waster" load. Provision is also made to open the control loop and operate with a variable voltage source for manual phase control.

V. Power Amplifier

To date, three 250-kW klystrons have been received and tested. All three have failed in test before reaching full output power. Two failed with shorted cathodes which resulted from arcing; the third would not hold the required high voltage. Additionally, one of the first two klystrons had a cracked output window. All have been returned to the manufacturer.

Three waterloads, one of the three repaired dual directional couplers, one of the 400-kW single directional couplers, one of the waveguide switches, two waveguide elbows, and the prototype arc detector head and package have been tested at 200 kW for a short time only because of failure of the klystrons.

The cooling manifolds, associated mounting hardware, klystron assemblies, filament transformer mounting, body current probe brackets, high-voltage resistor and corona balls, flow and temperature panels, and associated housing have been designed, fabricated, and installed in the test fixture for fitting and harnessing in the cone. Refer to Figs. 2 and 3 for views of the test fixture.

Most of these units are now being passivated and assembled in the cone structure for expediency in testing a 400-kW system with delivery of the klystrons.

VI. Conclusion

Because of the failure of the klystrons, the testing of the components at 250 kW will have to be extended, and the 400-kW testing will be delayed considerably. All klystrons, associated hardware, and monitor (with the exception of the electronic package, exciter, and waveguide) should be installed in the cone by early March 1974.

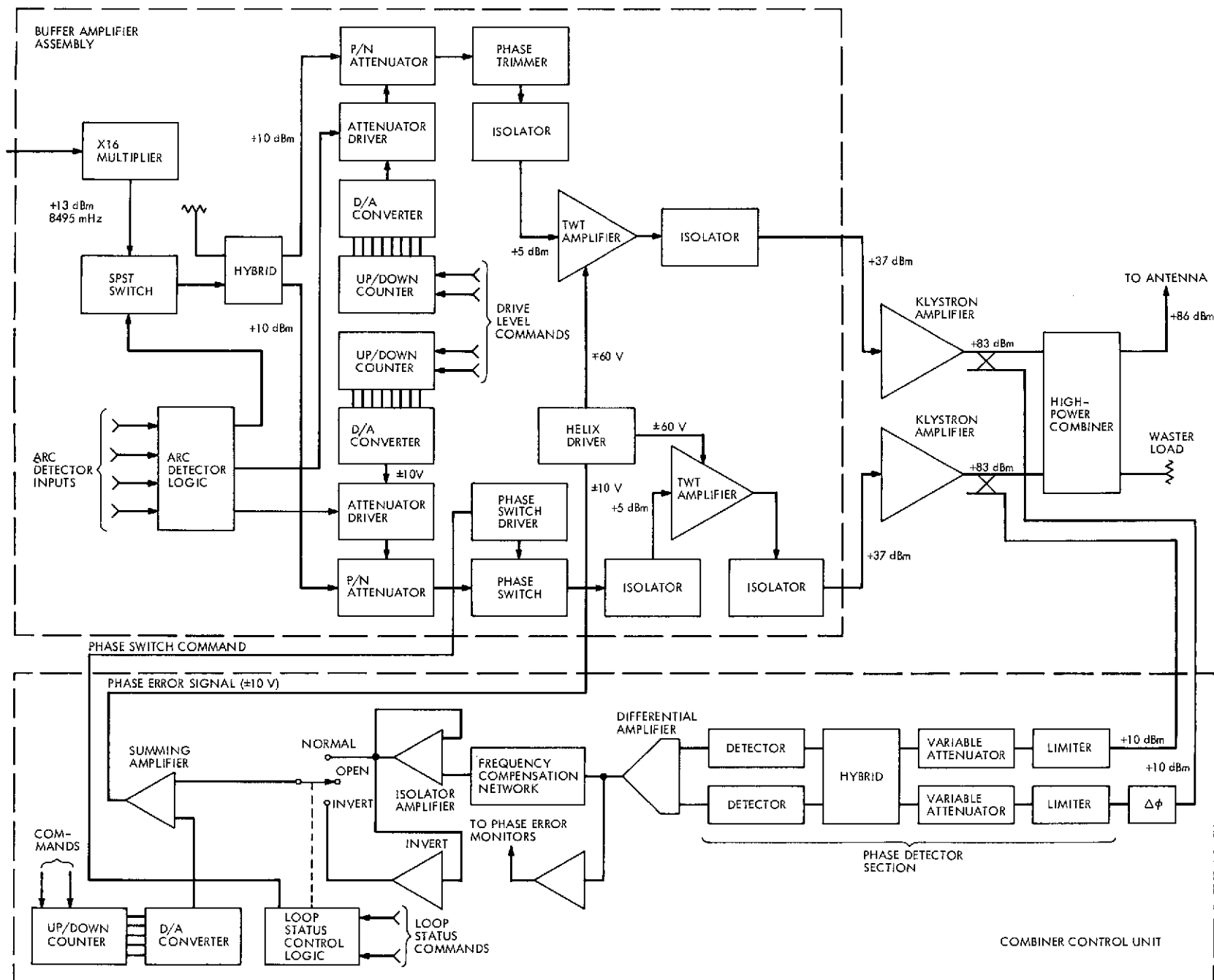


Fig. 1. Buffer amplifier and combiner control block diagram

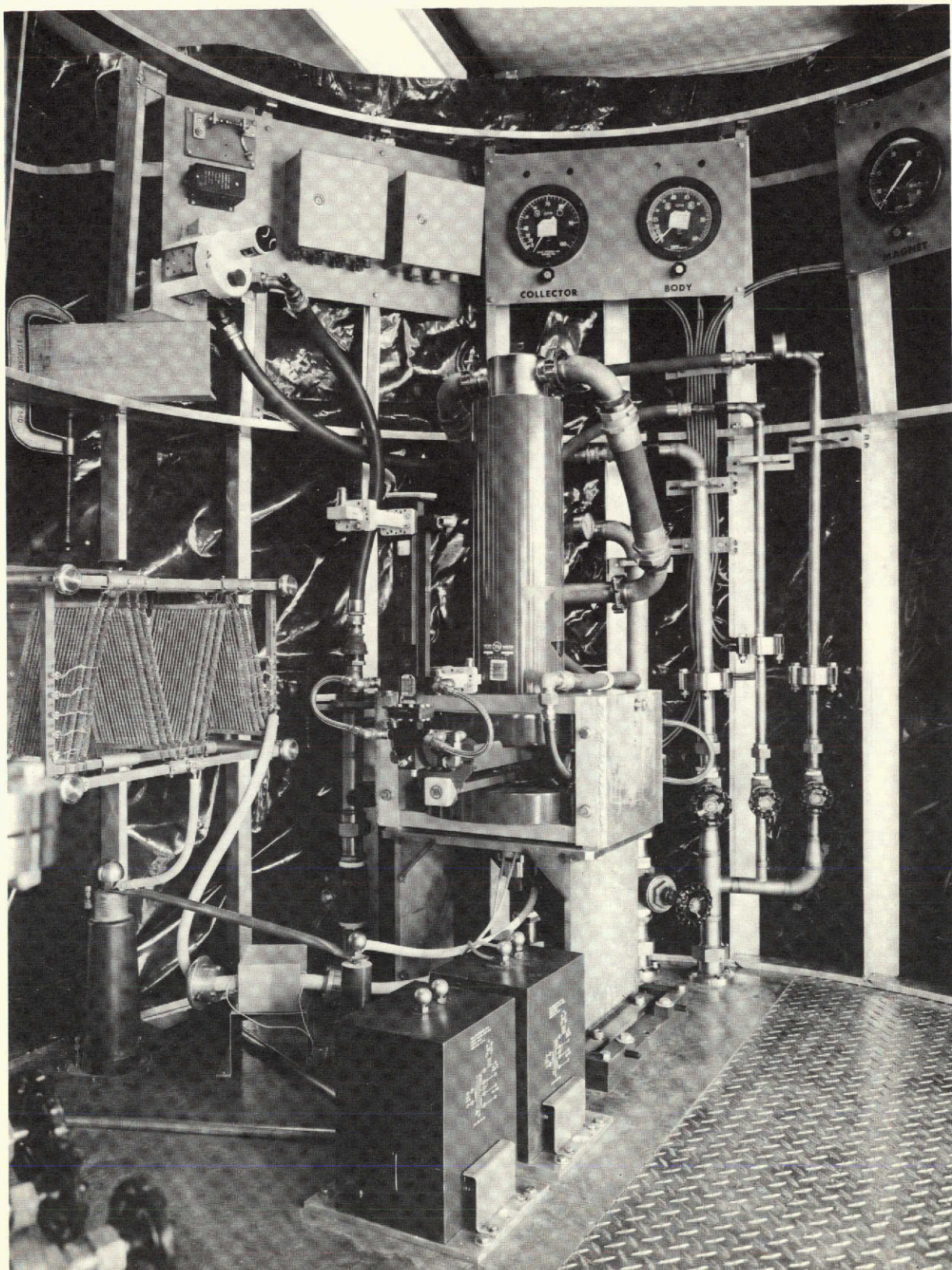


Fig. 2. Test fixture, front view

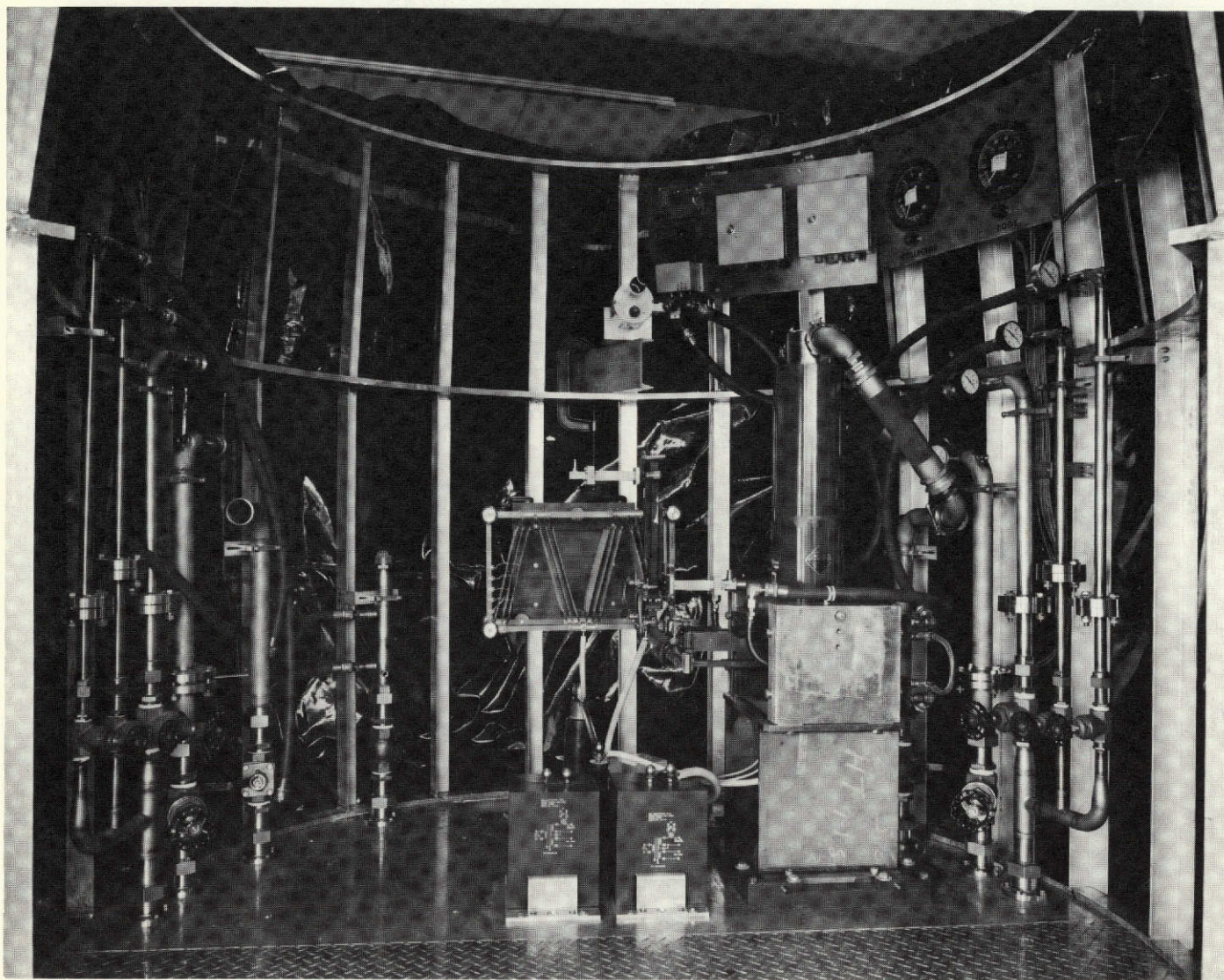


Fig. 3. Test fixture, side view

Microwave Maser Development: Automatic Monitoring of Closed Cycle Refrigerators for Masers

E. Wiebe

Communications Elements Research Section

A method for automatically monitoring the reserve capacity of a closed cycle refrigerator (CCR) has been developed and tested. The principal feature of the present design is that the measuring device adds negligible thermal load to the CCR. The instrumentation is particularly applicable to automated tracking station operation.

I. Introduction

In the past, the performance capability of a CCR was measured by actually applying a thermal load (by electric heaters) to the 4.2K station of the CCR. When the applied load was equal to the CCR capacity, the refrigerator warmed, and the measurement was complete. During a mission, when it is important to monitor the CCR, the above method cannot be used.

A new technique is described here which overcomes the above disadvantage. The new method consists of measuring the temperature gradient in the heat exchanger between the 15K and 4.2K stations.

II. Description of New Approach

Figure 1 shows a schematic diagram of a liquid-helium maser cooling refrigerator with an inset diagram of the novel condition monitoring circuit in dotted outline 10. The two temperature sensors 11 and 12 are in thermal contact with the Liquid-Helium Stage Heat Exchanger (Joule-Thomson (J-T) circuit) so as to measure the temperature gradient along its length. These resistors are preferably of the carbon type designed for operation at cryogenic temperatures and having a logarithmic coefficient of resistance. External resistors 13 and 14 together with battery 15 and galvanometer 16 (5-place digital voltmeter) complete the temperature indicating bridge.

Figure 2 shows a typical calibration chart for a CCR. In this case the CCR was one equipped with an X-band TWM and superconducting magnet assembly; the heat load at 4.5K is estimated to be some 200 to 300 mW.

The strip chart recording of Fig. 2 shows the change in voltage across the bridge circuit as thermal load was applied in 100-mW steps. It is to be noted that once a traveling-wave maser (TWM)-CCR system has been calibrated as shown in Fig. 2, the output voltage may thence-

forth be used as a measure of the CCR reserve capacity. Moreover, degradation in the engine portion or J-T circuit will be reflected immediately in temperature difference in the bridge circuit. In other words, the imminence of CCR problems will be apparent in the new method, but exact location of fault will not be pinpointed.

The CCR has been operated in all positions to verify that the technique is applicable in all cases.

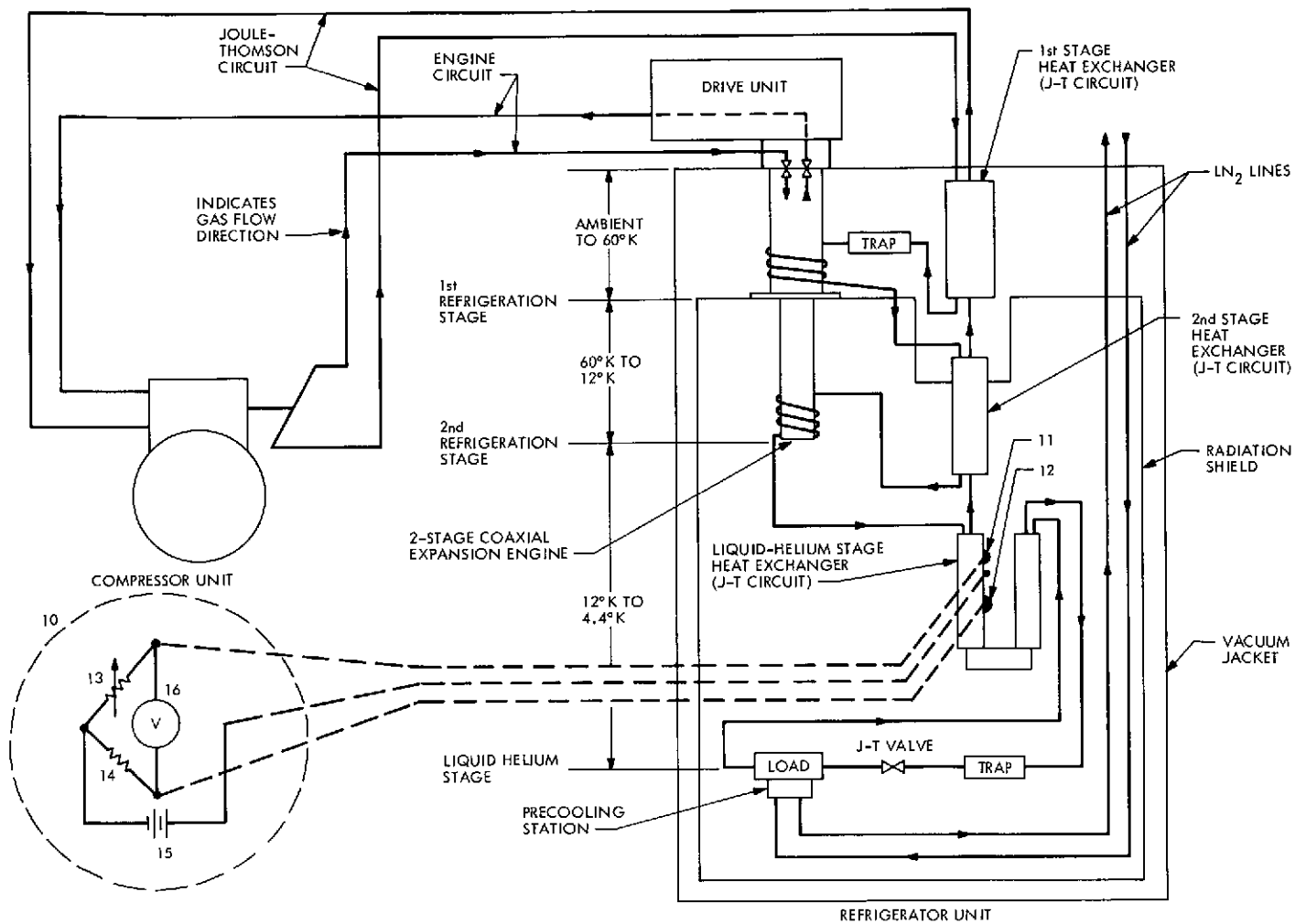


Fig. 1. System schematic for monitoring CCR capacity

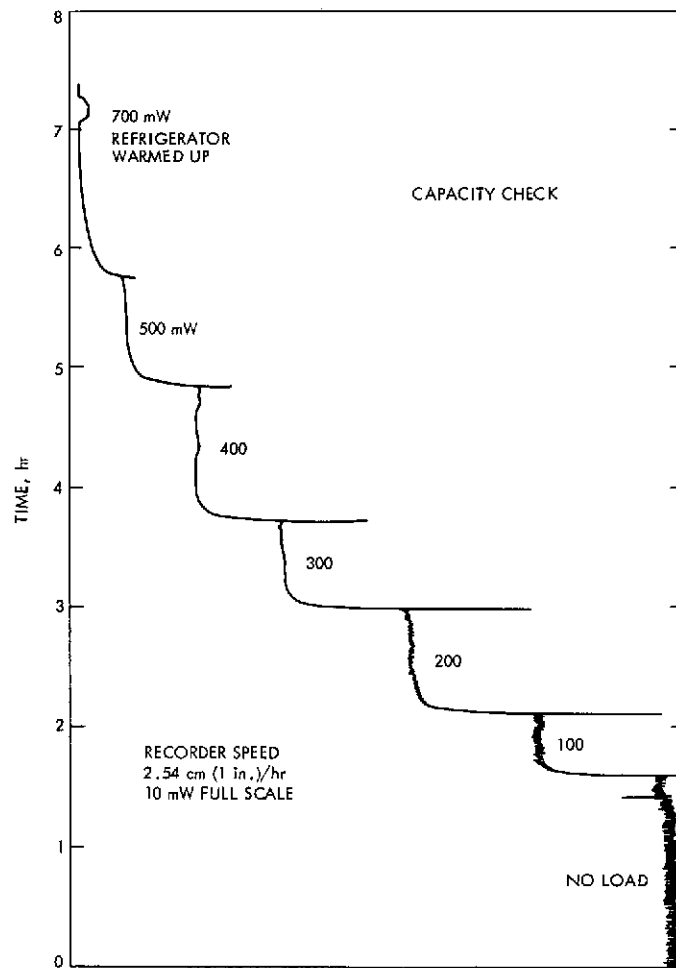


Fig. 2. Calibration chart for a CCR

On DSN Antenna Scheduling

L. H. Harper, R. J. McEliece, and A. M. Odlyzko
Communications Systems Research Section

We formulate and solve a problem related to the efficient assignment of DSN antennas to astronomical objects. The solution involves the well-developed theory of network flow.

I. Introduction

At any given time, the DSN may be required to observe simultaneously a large number of astronomical objects (spacecraft, planets, stars, comets, etc.). In general each object is not "visible" to each DSN site, and in addition it may be necessary to observe certain objects from more than one site, for example for interferometry experiments or for accurate tracking of accelerating spacecraft. It is the object of this article to give an efficient algorithm for assigning DSN antennas to astronomical objects under these circumstances. The method we shall give is derived from the theory of network flows (Ref. 1). Although we shall be concerned in this paper only with the static problem of DSN scheduling, in a future paper we will show how network flow theory can be used to solve dynamic scheduling problems, i.e., to take into account the fact that the demands on the network are time-varying.

Here is our general formulation of the static problem. We denote the antenna sites by x_1, x_2, \dots, x_n , and suppose that the i -th site contains h_i antennas. We suppose there

are m astronomical objects to be observed, and we denote by A_j the subset of the antenna sites from which the j -th object is visible. We further suppose that the j -th object must be observed from k_j different sites. A *solution to the assignment problem* is a collection of subsets of the antenna sites, say B_1, B_2, \dots, B_m (B_j represents the sites from which the j -th object is to be observed) with the following property: B_j contains k_j elements, and no x_i appears in more than h_i of the B_j s. In the next section we shall give a necessary and sufficient condition for the assignment problem to have a solution, and give an efficient algorithm for finding a solution, if it exists.

II. Solution to the Problem

Let $X = \{x_1, x_2, \dots, x_n\}$ be a finite set, and let A_1, A_2, \dots, A_m be subsets of X ; let nonnegative integers $h_1, h_2, \dots, h_n; k_1, k_2, \dots, k_m$ be given.

PROBLEM A: Under what circumstances is it possible to find subsets $B_j \subseteq A_j$ $j = 1, 2, \dots, m$, with $|B_j| = k_j$, and such that no x_i appears in more than h_i of the subsets B_j ?

Let us observe first of all that there are many conditions which clearly must be satisfied in order for the problem to possess a solution. Thus suppose a solution (B_j) exists, let J be any subset of $\{1, 2, \dots, m\}$ and denote by B_J the multiset union $\bigcup_{j \in J} B_j$. Furthermore define $h_i(J)$ by:

$$h_i(J) = \min(h_i, \sum_{j \in J} c_{ij})$$

Clearly x_i could occur no more than $h_i(J)$ times in the multiset B_J . Hence it follows that

$$\sum_{i=1}^n h_i(J) \geq \sum_{j \in J} k_j \quad (1)$$

for all subsets J . Condition (1), then, is a *necessary* condition for the existence of a solution to our problem. It is a remarkable fact, however, that taken together these 2^m conditions are also *sufficient*:

THEOREM 1. *If Condition (1) is satisfied for all subsets $J \subseteq \{1, 2, \dots, m\}$, Problem A can be solved.*

PROOF. This theorem is actually a special case of a known theorem on supply-demand networks. Rather than state the general theorem, however, we shall only describe the supply-demand network which applies to our particular problem.

The appropriate directed network has $n + m$ nodes; they are labeled $x_1, x_2, \dots, x_n, A_1, A_2, \dots, A_m$. There is a directed edge from x_i to A_j if and only if $c_{ij} = 1$, i.e., if $x_i \in A_j$. Each of these edges is assigned a capacity of 1. The nodes x_i are designated supply nodes; the supply at x_i is h_i . The nodes A_j are designated demand nodes; the demand at A_j is k_j . A flow in this network is an integral-valued function f_{ij} which satisfies $f_{ij} \leq c_{ij}$.

One thinks of f_{ij} as the amount of some quantity supplied to the demand node A_j from the supply node x_i . The flow is said to be *feasible* if the demands are met and the supplies are not exceeded, i.e., if

$$\begin{aligned} \sum_{i=1}^n f_{ij} &\geq k_j & j = 1, 2, \dots, m \\ \sum_{j=1}^m f_{ij} &\leq h_i & i = 1, 2, \dots, n \end{aligned}$$

Notice that such a feasible flow yields a solution to Problem A; merely take

$$B_j = \bigcup \{x_i : f_{ij} = 1\}$$

Conversely a solution to Problem A yields a feasible flow; define

$$\begin{aligned} f_{ij} &= 1 & \text{if } x_i \in B_j \\ &= 0 & \text{if } x_i \notin B_j \end{aligned}$$

Now according to a theorem of Gale (see Ref. 1, Chapter 2: Theorem 1.1 and Corollary 1.2) a feasible flow exists if, corresponding to every subset of demand nodes, there is a flow that satisfies the aggregate demand of the subset without exceeding the supply limitations at each source. This result is clearly equivalent to Theorem 1.

Q.E.D.

While Theorem 1 is perhaps esthetically satisfying, it is clearly inefficient to check all 2^m conditions (1) in order to discover if Problem A has a solution. Even if one could check the conditions it is not clear how one could then actually construct a solution to the problem. A better way is to apply the "labeling algorithm" of Ford and Fulkerson (Ref. 1, Chapter 1) to the extended network corresponding to Problem A. This algorithm will quickly either produce a solution to Problem A, or a subset J such that Condition (1) is violated.

The extended network is obtained from the network described in the proof of Theorem 1 by adjoining two additional nodes: " s " (the source) and " t " (the sink). There are edges from s to each x_i ; the capacity of the edge (s, x_i) is h_i . There are also edges from each A_j to t ; the capacity of (A_j, t) is k_j . In this extended network a flow is a function $f(a, b)$ on directed edges (a, b) such that $f(a, b) \leq c(a, b)$, the capacity of the edge (a, b) , and such that the net flow at each node other than s and t is 0; i.e.,

$$\sum_b f(a, b) = \sum_b f(b, a) \quad \text{for all } a \neq s, t$$

The *value* of the flow is

$$v = \sum_b f(s, b) = \sum_b f(b, t)$$

The object of the labeling algorithm is to find a flow of maximum possible value. It turns out (see Ref. 1, Chapter 2) that a maximal flow in this extended network, when restricted to the original network, will be a feasible flow if a feasible flow exists, and in any case will be a flow which meets as many as possible of the demands without exceeding the supplies. If no feasible flow exists, the nodes A_j which are *unlabeled* at the termination of the algorithm will be a subset violating Condition (1). Here is the algorithm: initially the flow is identically zero.

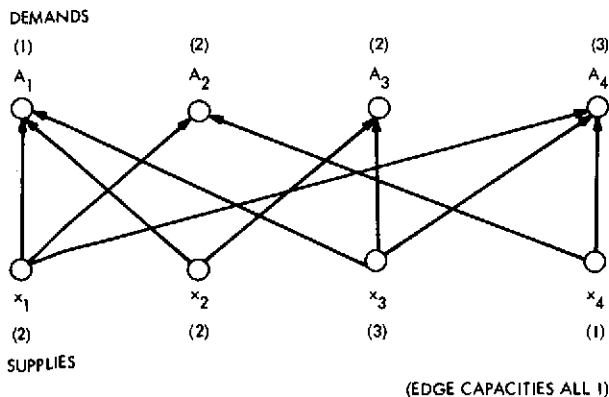
Labeling Algorithm

- (1) Give the sink s the label $[\phi]$.
- (2) (Scan a). Select any labeled, unscanned node a , with label $[c\pm]$. Give every unlabeled b , such that $f(a,b) < c(a,b)$, the label $[a+]$; give every unlabeled b , such that $f(b,a) > 0$, the label $[a-]$; a is now "scanned."
- (3) Repeat step 2 until either the sink t is labeled [go to 4], or until no further labels can be assigned and t is unlabeled [go to 6].
- (4) Set $b = t$.
- (5) If b is labeled $[a+]$, increase $f(a,b)$ by 1; if b is labeled $[a-]$, decrease $f(b,a)$ by 1. If $a = s$, erase all labels and go to 1; otherwise set $b = a$ and repeat step 5.
- (6) Either all demands h_i are satisfied and Problem A is solved, or the set of unlabeled A_i s have an aggregate demand in excess of the total supply, and the problem is unfeasible.

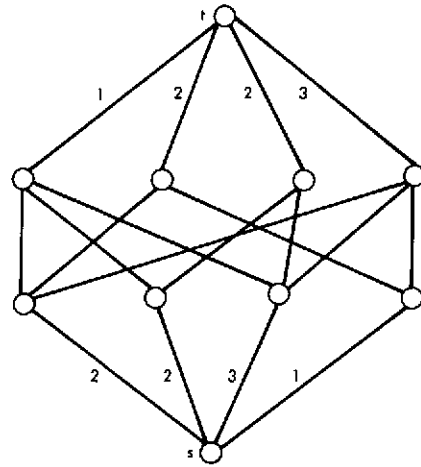
The labeling algorithm is quite efficient: notice that since this value of the flow is increased by 1 each time step 5 is executed, and that during the labeling process each edge needs to be examined at most twice, the total work involved is at most

$$2 \cdot \sum_{j=1}^m k_j \cdot \sum_{i,j} c_{ij} \leq 2m^2 n k_{\max} \quad \text{if } k_{\max} = \max(k_j)$$

We conclude with an example which illustrates these techniques. Let $n = m = 4$, $A_1 = \{x_1, x_2, x_3\}$, $A_2 = \{x_1, x_4\}$, $A_3 = \{x_2, x_3\}$, $A_4 = \{x_1, x_3, x_4\}$; $h_1 = 2$, $h_2 = 2$, $h_3 = 3$, $h_4 = 1$; $k_1 = 1$, $k_2 = 2$, $k_3 = 2$, $k_4 = 3$. The corresponding supply-demand network is



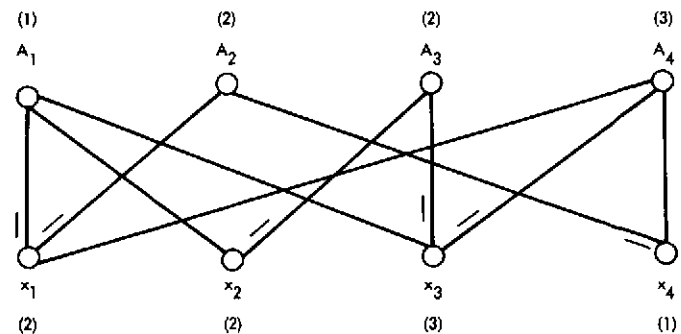
and the extended network is



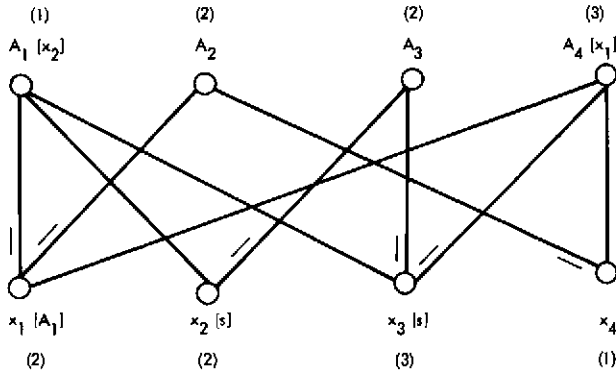
We now apply the labeling algorithm to the extended network. For the purposes of this example, we will always scan a labeled A_j if the sink t can be labeled from A_j , i.e., if $f(A_j, t) < k_j$. Otherwise our scanning priority will be $(x_1, x_2, x_3, x_4, A_1, A_2, A_3, A_4)$. The problem is solved in 9 passes through the algorithm, which we list below:

Pass number	Order in which nodes are scanned
1	s, x_1, A_1, t
2	s, x_1, A_2, t
3	s, x_2, A_3, t
4	s, x_2, x_3, A_3, t
5	s, x_2, x_3, A_4, t
6	s, x_2, x_3, x_4, A_2, t
7	$s, x_2, x_3, A_1, x_1, A_4, t$
8	s, x_2, A_1, t
9	s, x_3, A_1, x_2

Notice that pass 7 involves backtracking, viz., $f(x_1, A_1)$ is decreased. Immediately prior to the execution of pass 7, the network looks like this (omitting the nodes s and t):

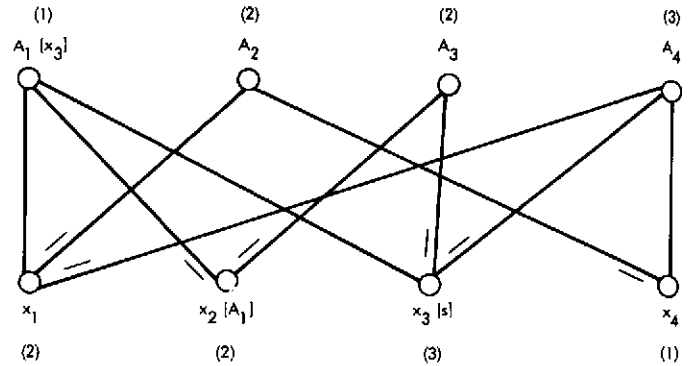


(An edge (x_i, A_j) with $f(x_i, A_j) = 1$ is indicated by a short dash parallel to that edge.) After the labels have been added, and the sink t has been reached via A_4 , the network looks like this:



(We have omitted the \pm signs on the labels, since labels on the x_i are always either $[s-]$ or $[A_j+]$ and those on the A_j are always $[x_i-]$.) The execution of step 5 now increases $f(A_4, y)$ by 1, increases $f(x_1, A_4)$ by 1, decreases $f(x_1, A_1)$ by 1, increases $f(x_2, A_1)$ by 1, and increases

$f(s, x_2)$ by 1. After this the algorithm runs smoothly, and ends in the following configuration:



No further labels can be assigned, since all labeled nodes are also scanned. Thus the illustrated flow is maximal, but the demand at A_4 is unsatisfied. The unlabeled A_j s $\{A_2, A_3, A_4\}$ have an aggregate demand of 7, whereas the total supply into $\{A_2, A_3, A_4\}$ is $2 + 1 + 2 + 1 = 6$, and so the problem is palpably unfeasible. Notice that if $k_j = 2$ instead of 3 the algorithm would have terminated with all demands being met.

Reference

1. Ford, L. R., and Fulkerson, D. R., *Flows in Networks*, Princeton University Press, Princeton, New Jersey, 1962.

S/X Experiment: A New Configuration for Ground System Range Calibrations With the Zero Delay Device

T. Y. Otoshi and C. T. Stelzried
Communications Elements Research Section

A new configuration for ground system range calibrations with the zero delay device (ZDD) was recently implemented at DSS 14 for the S/X experiment. In this new configuration, the original ZDD horns and associated air paths are eliminated. The uplink test signal is now coupled out of the transmitter waveguide path and brought directly to the ZDD by calibrated cables of known delays. The downlink signals generated by the ZDD are injected directly into the masers via calibrated cables and waveguide couplers. Preliminary tests on the new system indicate that, in the absence of the air path, the ground system range change as a function of antenna elevation angle is typically less than 3 ns at S-band and X-band.

I. Introduction

With the exception of DSS 14, all stations of the Deep Space Network use the conventional zero delay ranging configuration, in which the zero delay device (ZDD) is mounted on the dish surface. A zenith range measurement to a dish-mounted ZDD and a simple Z-height correction (Ref. 1) should provide all of the needed ground station information for determining the true range to the spacecraft. However, as was pointed out in a separate article (Ref. 2) in this volume, results of tests showed that large changes in range occurred as a function of antenna elevation angle when a ZDD was placed on the 64-m antenna dish surface. Since the changes could be due to a multipath phenomenon, one cannot assume that a zenith measured value is the correct value. It was further reported in Ref. 2 that a satisfactory location in the Mod-3 area was found for the ZDD at S-band, but the performance at X-band was unsatisfactory.

Because of the described problems with the conventional ZDD configuration, it was proposed by G. S. Levy that, for the S/X experiment, the ZDD horns and associated air paths be eliminated and replaced by semirigid cables. This article describes the new configuration and presents results of some preliminary tests.

II. New Configuration

A block diagram of the current ZDD calibration system at DSS 14 may be seen in Fig. 1. This new configuration was installed on the 64-m antenna system at DSS 14 on January 12, 1974.¹ In this new configuration, the uplink 2113-MHz signal is now sampled from a directional coupler in the waveguide transmit line and carried directly to the ZDD by coaxial cables of known delay. The downlink signals of 2295 and 8415 MHz generated by the ZDD are carried by calibrated cables and injected directly into the respective S- and X-band masers via directional couplers. Figure 2 shows the block diagram of the ZDD assembly as presently modified for this new configuration. The original block diagram for the ZDD was previously shown in Refs. 3 and 4.

The main disadvantage of the new method is that, by elimination of the air path, one is not able to use the ZDD to detect problems which might occur in the microwave optics subsystem. With the new ZDD configuration, one is restricted to testing only the portion of the ground

¹A previous similar configuration was installed on December 20, 1973, but is not described in this article. This previous system could only be used with the 20-kW transmitter.

system that includes the transmitter, masers, Block 4 receivers, and associated waveguide and cable paths. A second disadvantage of the new method is that there is no longer just a simple Z-height correction that must be added to the measured ZDD range value. As described in an article elsewhere in this volume (Ref. 5), the new Z-correction now requires knowledge of range delays in all portions of the uplink and downlink signal paths that are not mutually common to the "Range-on-ZDD" path and "Range-on-Spacecraft" path as defined up to the antenna bench mark. Knowledge of these delays requires (1) group delay calibrations of cables to and from the ZDD, (2) group delay calibrations of portions of the transmit/receive waveguide paths, and (3) calculations of air path delays via the microwave optics path. A tabulation of the delays as calibrated with a phase-locked network analyzer system is presented in Table 1 for the DSS 14 ground system depicted in Fig. 1. It should be pointed out that any new equipment installation in the paths described in Table 1 will invalidate the calibrations.

The advantage of the new method is that the range and phase calibrations will be more stable and repeatable. As will be shown later, the range delay variation with antenna tipping is very small. A second advantage is that a theoretically calculated air path delay should be more accurate than a ZDD measured value which is apparently corrupted by multipath effects. A theoretical analysis can account for the total integrated effects of a far-field illuminator and therefore more closely represent the actual spacecraft range configuration. The elevation angle dependence of range to quadripod blockage, reflector surface distortions and sagging, reflections from antenna-mounted structures, and subreflector defocussing can be studied analytically.

III. Test Results

Figures 3 and 4 show preliminary results of range tests on the new ZDD configuration using the 100- and 20-kW transmitters, respectively. It can be seen that the maxi-

mum range change with elevation angle was about 3 ns for S-band and X-band. Additional tests showed that insignificant changes of range occurred as functions of azimuth angles for either the S- or X-band system. These preliminary test results indicate that the group delays of the transmitters, masers, Block 4 receivers, and associated cabling are nearly insensitive to antenna motion.

The ZDD was also used to test the doppler phase stability of the S- and X-band systems as functions of antenna tipping. The peak phase changes due to doppler phase jitter and antenna tipping were typically found to be less than ± 30 deg for S-band and X-band. Some of the phase changes that were observed could be attributed to the quantization error of the S/X doppler resolvers. The peak error due to the resolvers is about ± 18 deg for a 5-MHz biased doppler. It should be pointed out again that the measured values do not include possible changes in the air path.

IV. Conclusions

The new ZDD configuration using cable paths rather than the air paths has been found to be virtually insensitive to antenna motion. This new configuration therefore appears to be superior to the original system in terms of repeatability. Since the new configuration does not include the air path, the effects of antenna sag on range and phase stability must now be determined theoretically.

At present the ZDD range values are being taken with the antenna at zenith during the precalibration and post-calibration periods of the Mariner 10 spacecraft tracking passes. Over a period of about 30 days, the differential S/X ZDD range appears to be stable to within 10 ns. The long-term absolute group delay instabilities are about two times greater. An attempt is being made to analyze the changes and correlate them with ambient temperature, maser gain, and Block 4 equipment modifications.

References

1. *TRK-2-8 Module of DSN System Requirements Detailed Interface Design Document 820-13, Rev. A*, Jet Propulsion Laboratory, July 1, 1973 (JPL internal document).
2. Stelzried, C. T., Otoshi, T. Y., and Batelaan, P. D., "S/X Band Experiment: Zero Delay Device Location," in *The Deep Space Network Progress Report*, Technical Report 42-20, Jet Propulsion Laboratory, Pasadena, Calif., Apr. 15, 1974 (this issue).
3. Otoshi, T. Y., and Batelaan, P. D., "S/X Band Experiment: Zero Delay Device," in *The Deep Space Network Progress Report*, Technical Report 32-1526, Vol. XIV, pp. 73-80, Jet Propulsion Laboratory, Pasadena, Calif., Apr. 15, 1973.
4. Otoshi, T. Y., and Batelaan, P. D., "S/X Band Experiment: Preliminary Tests of the Zero Delay Device," in *The Deep Space Network Progress Report*, Technical Report 32-1526, Vol. XVII, pp. 68-77, Jet Propulsion Laboratory, Pasadena, Calif., Oct. 15, 1973.
5. Batelaan, P. D., "S/X Band Experiment: Zero Delay Device Z Corrections," in *The Deep Space Network Progress Report*, Technical Report 42-20, Jet Propulsion Laboratory, Pasadena, Calif., Apr. 15, 1974 (this issue).

Table 1. Summary of group delay measurements pertinent to DSS 14 Z-corrections for the new ZDD configuration implemented on January 12, 1974

Input port (Figs. 1 and 2)	Output port (Figs. 1 and 2)	Measured group delay, ns
2'	A	$42.35 \pm 0.09 (1\sigma)$
A	B	$14.11 \pm 0.76 (1\sigma)$
B	4	$87.38 \pm 0.12 (1\sigma)$
A	C	$9.49 \pm 0.80 (1\sigma)$
C	7	$70.63 \pm 0.10 (1\sigma)$
2'	3	$32.77 \pm 0.08 (1\sigma)$
3	4	$37.57 \pm 0.12 (1\sigma)$
6	7	$0.91 \pm 0.03 (1\sigma)$

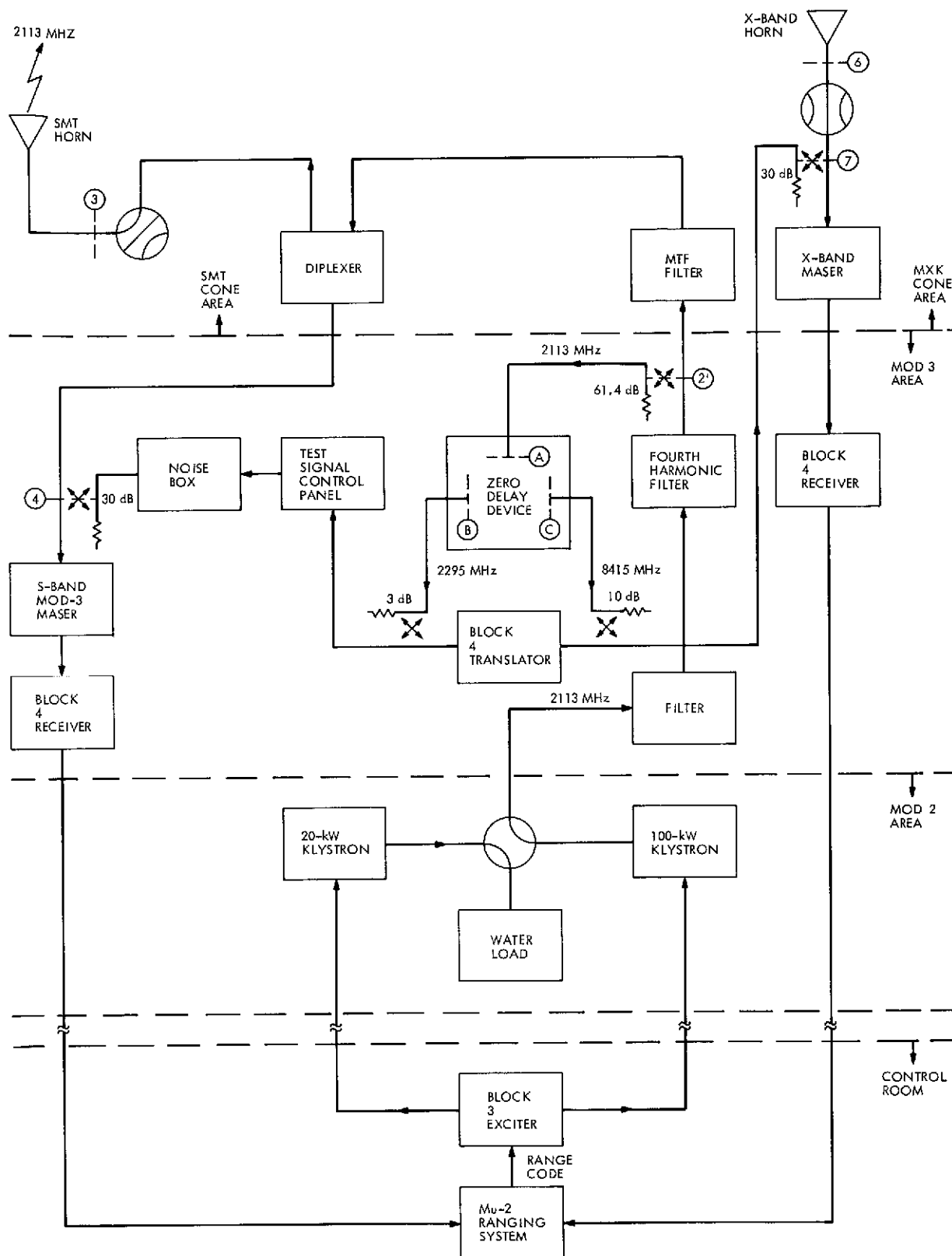


Fig. 1. Block diagram of the new configuration at DSS 14 for ground system range calibrations

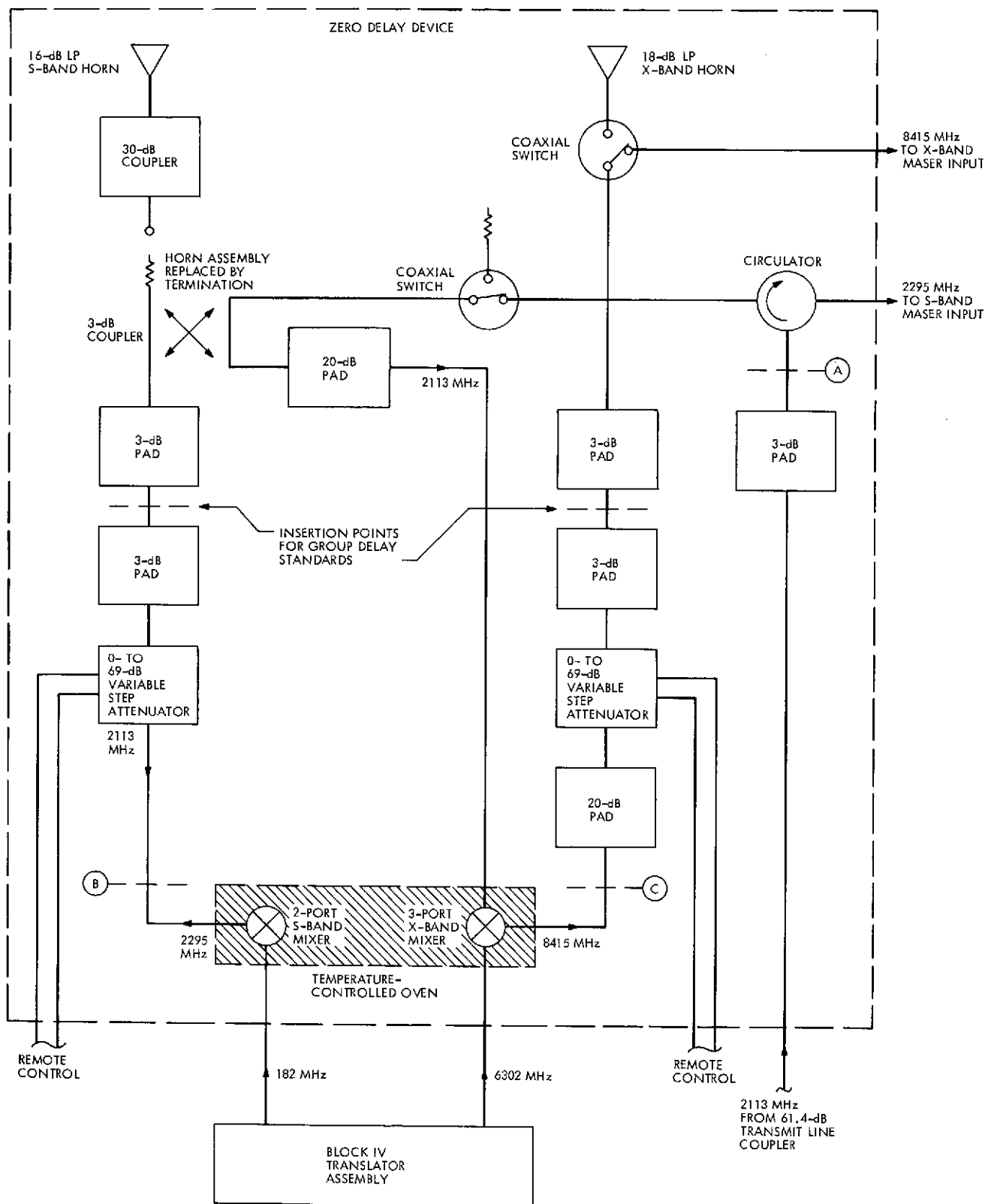


Fig. 2. Block diagram of the current zero delay device assembly at DSS 14

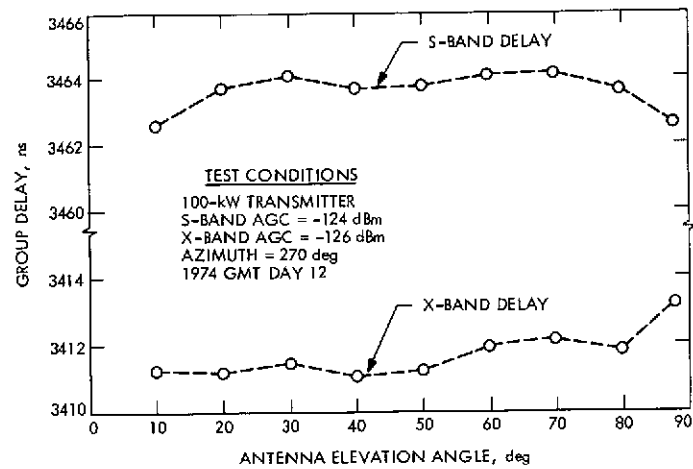


Fig. 3. Range delay as a function of elevation angle using the new ZDD configuration and the 100-kW transmitter

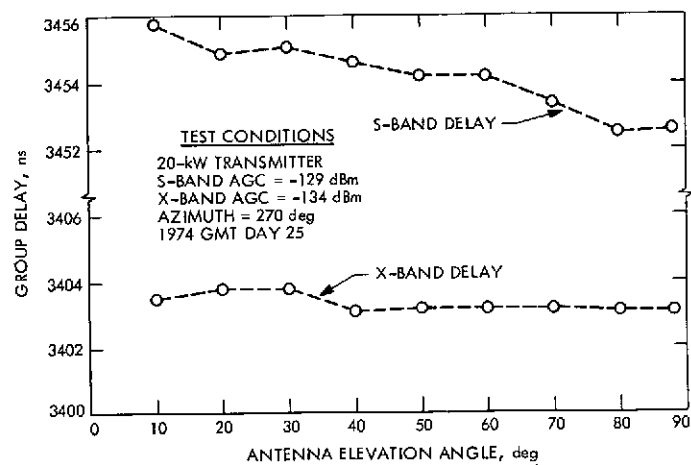


Fig. 4. Range delay as a function of elevation angle using the new ZDD configuration and the 20-kW transmitter

S/X Band Experiment: Zero Delay Device Antenna Location

C. T. Stelzried, T. Y. Otoshi, and P. D. Batelaan
Communications Elements Research Section

Representative data are presented for the original Block 3 and Block 4 zero delay devices as a function of antenna elevation angle. Instabilities on the order of 33 nanoseconds as obtained with the original S-band Block 3 system are reduced by relocation of the zero delay device (ZDD) horn. However, unsatisfactory performance at X-band for the Mariner Venus/Mercury 1973 (MVM'73) S/X experiment ZDD requires a reconfiguration eliminating the horns and associated air path.

I. Introduction

The S/X-band experiment (Ref. 1) requires a zero delay device (ZDD) for routine calibrations and receiving system performance verification tests. The Block 4 ZDD (Ref. 2) developed for the S/X-band experiment is an antenna-mounted transponder that receives an uplink signal of 2113 MHz and reradiates downlink signals of 2295 and 8415 MHz. It utilizes the Mu-2 ranging and Block 4 receiving systems.

This article presents results of some preliminary tests at S-band made to determine the Block 3 ZDD range change sensitivity to antenna tipping and horn location. In addition, the Block 4 ZDD performance at both S- and X-band with antenna tipping is presented. Figure 1 shows the DSS 14 64-m antenna and indicates the various test locations for the ZDD on the dish surface (positions 1-3) and the ZDD installation exterior to the Mod 3 area (position 4).

II. Test Setup

A series of S-band tests was performed on the 64-m antenna at DSS 14 from August 1972 to January 1973 to evaluate the performance of the ZDD. Three test setups were as follows:

- (1) The S-band Block 3 ZDD was used and consisted of an open-ended WR 430 waveguide/type N coaxial transition and a mixer diode. The local oscillator (LO) frequency of 181 MHz was supplied by the Block 3 receiver/exciter assembly, and ranging was done with the Mu-1 ranging system. The ZDD was first mounted on the 64-m antenna surface near the base of a quadripod leg (Fig. 1, position 1). This location has been used in conjunction with Mu-1 ranging for previous flight missions. The ZDD was then moved to other locations (Fig. 1, positions 2, 3) and tested. The polarization diversity S-band (PDS) cone duplex system and PDS maser were used for this test setup.

- (2) The second test setup involved radiating from the PDS cone and receiving with several types of small antennas at a location exterior to the roof of the Mod 3 level (Fig. 1, position 4). Relative phase was measured with a network analyzer, and range was determined by a frequency variation method.
- (3) The third test configuration may be seen in Fig. 2. In this test configuration the Block 4 ZDD is installed at a location exterior to the Mod 3 level, below and near the roof ladder access hatch (Fig. 1, position 4). The ZDD is enclosed in a special RF-shielded welded box with remotely controllable lid for RF noise burst suppression. The location for this configuration was selected on the basis of results obtained in the above test setups. This location has the added advantage that the source of the LO frequencies is physically close to the ZDD from the Mod 3 area, thus resulting in greater phase stability.

III. Test Results

Ranging stability using the Block 3 ZDD was found to be very sensitive to antenna elevation angle. Data were typically taken at 10-deg increments of elevation angle. A summary of the data is shown in Table 1. In addition, a test was performed using the Block 3 translator, which bypasses the transmitter and air path completely. Approximately 1 nanosecond of range change was measured with antenna tipping indicating good stability of the overall maser/receiver system. These data indicate that the location of the ZDD "antennas" is a key factor in determining the magnitude of the instabilities, which are presently assumed to be due to elevation-dependent multipath phenomena.

The comparable results for Tests 1 and 6 are to be noted in that they were made at different times with independent equipment and measurement setups but at the same location (Fig. 1, position 4).

Figure 3 shows the system ranging performance for the dual channel S- and X-band systems using Block 4 receivers and the Mu-2 ranging system with the ZDD mounted in the shielded box (Fig. 1, position 4) and with the S/X reflex feed system installed. Considering the large instability with elevation angle at X-band and the requirement to provide a stable calibration system for the MVM73 S/X experiment, it was decided to modify the original ZDD block diagram. This was accomplished by bypassing the horns and providing the 2113 MHz from a directional coupler on the transmitter output and injecting the S (2295-MHz) and X (8415-MHz) signals directly into the respective masers via waveguide couplers and semirigid cables. This configuration eliminated the assumed multipath-originated range instabilities (Ref. 4).

IV. Conclusions

Tests for proper location of a ZDD were conducted only at S-band frequency and before installation of the S/X reflex feed mechanisms. These tests indicated that, under those conditions, the location exterior to the Mod 3 level would be satisfactory.

Based on these data, the Block 4 ZDD was installed at the Mod 3 location in the shielded RF box. After installation of the Block 4 receiver/exciter, Mu-2 ranging and the S/X reflex feed, tests showed that the location, while acceptable for S-band, was not acceptable for X-band. This required a reconfiguration eliminating the horns and associated air path.

References

1. Levy, G. S., et al., "RF Techniques Research: S/X Band Experiment," in *The Deep Space Network*, Space Programs Summary 37-61, Vol. III, p. 93, Jet Propulsion Laboratory, Pasadena, Calif., Feb. 1970.
2. Otoshi, T. Y., and Batelaan, P. D., "S/X Band Experiment: Zero Delay Device," in *The Deep Space Network Progress Report*, Technical Report 32-1526, Vol. XIV, pp. 73-80, Jet Propulsion Laboratory, Pasadena, Calif., Apr. 15, 1973.
3. Otoshi, T. Y., and Batelaan, P. D., "S/X Band Experiment: Preliminary Tests of the Zero Delay Device," in *The Deep Space Network Progress Report*, Technical Report 32-1526, Vol. XVII, pp. 68-77, Jet Propulsion Laboratory, Pasadena, Calif., Oct. 15, 1973.
4. Otoshi, T. Y., and Stelzried, C. T., "S/X Band Experiment: A New Configuration for Ground System Range Calibrations with the Zero Delay Device," in *The Deep Space Network Progress Report*, Technical Report 42-20, Jet Propulsion Laboratory, Pasadena, Calif., Apr. 15, 1974 (this issue).

Table 1. Summary of DSS 14 zero delay device performance in S-band antenna tipping tests

Test	Description	pk/pk range variation with antenna elevation angles between zenith and 11 deg, ns
1	Test setup 2 (Fig. 1, position 4)	<1
2	Test setup 1, Block 3 ZDD, original position (Fig. 1, position 1)	33
3	Test setup 1, Block 3 ZDD (Fig. 1, position 2)	6
4	Test setup 1 Block 3 ZDD (Fig. 1, position 3), 1.5 panels from antenna edge	15
5	Test setup 1, Block 3 ZDD, Mod 3 location (Fig. 1, position 4)	13
6	Test setup 1, same as Test 5 except pyramidal horn added to Block 3 ZDD	3

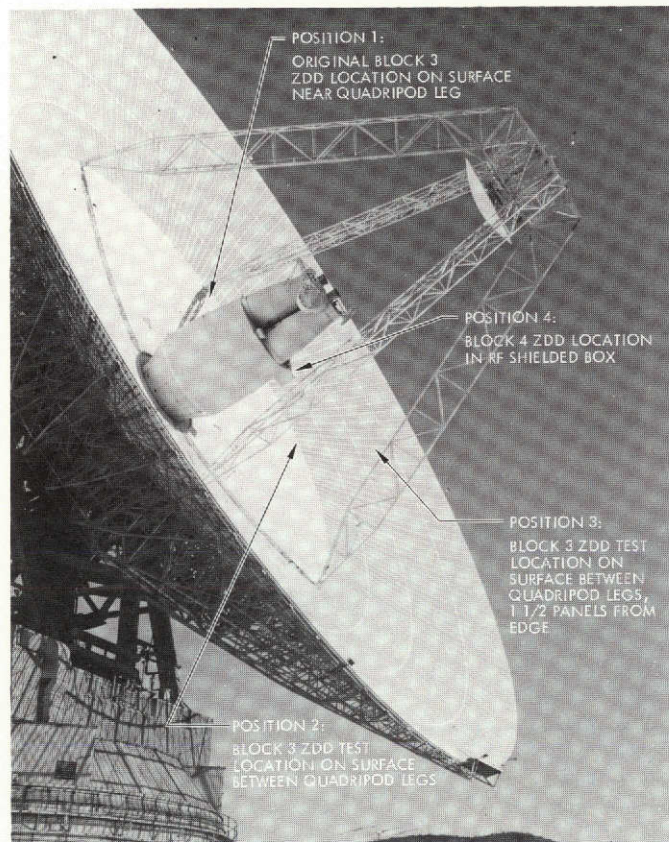


Fig. 1. DSS 14 64-m antenna showing various locations of ZDD test positions (1 through 3) and RF shielded box (position 4) used for the Block 4 ZDD installation

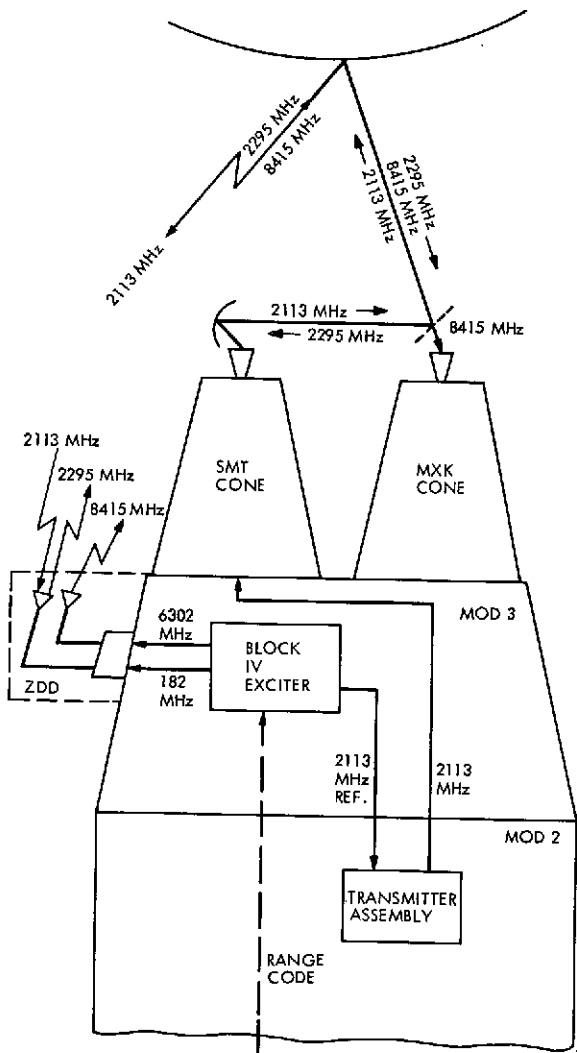


Fig. 2. Simplified block diagram of the original ZDD calibration system for S/X-band experiment

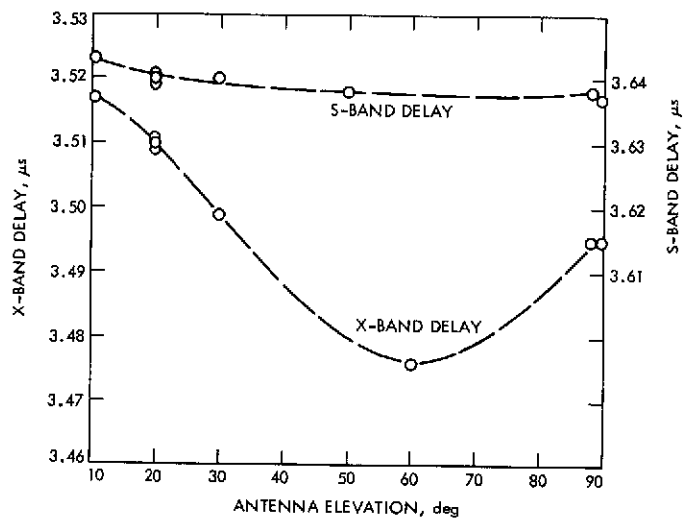


Fig. 3. DSS 14 dual-channel S/X-band ranging on the ZDD as a function of antenna elevation angle using the Block 4 ZDD (Fig. 1, position 4)

DSS Tests of Sequential Decoding Performance

J. W. Layland

Communications Systems Research Section

This article describes the results to date of a series of one-way tests of the DSN sequential decoding capability, which have been performed at DSS 71. The tests utilize the Data Decoder Assembly as configured for the Helios formats and data rates, and are aimed principally at establishing the telemetry threshold for the Helios requirement of 10^{-4} deletions probability.

I. Introduction

Convolutional encoding with sequential decoding is a very powerful technique for communicating at low-error probability with deep space probes. It has been used successfully with several Pioneer spacecraft, and is planned for use on Helios, the German solar probe. Performance predictions for decoding on the spacecraft to DSN links have been developed by modeling (Ref. 1), and by nonreal-time tests (Ref. 2). Since midsummer of 1973, one-way real-time tests of sequential decoding, as configured for Helios data format, have been under way at DSS 71. These tests represent the cooperative efforts of numerous members of JPL's Office of Technical Divisions and Tracking and Data Acquisition Office, the crew of DSS 71, and the use of many hundreds of hours of test

time in DSS 71. The results obtained to date with this test program are described in this article.

The tests have had two principal goals: to improve confidence and reduce tolerances in performance threshold predictions provided to Helios Project for their formats, data rates, and chosen modulation indices of 42 deg and 55 deg; and to obtain experimentally the dependence of performance upon modulation index. Tests at lower data rates were accelerated by time scaling of loop bandwidth and data rates of 8 bits/s to 2048 bits/s, but the planned pattern of tests at multiple modulation indices has been completed only at the four highest data rates. The tests have shown a 0.5- to 1.3-dB poorer performance than expected.

II. Test Configuration, Procedure, and Problems

The test configuration for sequential decoding testing is shown in Fig. 1. The output from the test is a magnetic tape Original Data Record (ODR) containing, for each data frame processed by the Data Decoder Assembly (DDA), the number of decoding computations that were used in processing it. These ODR tapes are later analyzed off-line to determine the cumulative distribution of computations, which is then used to evaluate system performance. In the DSN station, the tests require the use of the Simulation Conversion Assembly (SCA), the test transmitter, the Antenna Microwave Assembly, the Y-Factor Assembly, a receiver, the Subcarrier Demodulator Assembly (SDA), two telemetry/command processors (TCPs) with Symbol Synchronizer Assemblies (SSAs), and one DDA. The TCP-DDA-SSA string operates under control of nonstandard DSS software, the DDA Stand-Alone TCP Verification Program, and provides the ODR end-product of the tests. The second TCP-SSA string operates with the MM71 Test Program No. DOI-5087-TP, and acts as a monitor for the telemetry channel to verify station set-up accuracy, and to identify drifts in parameters.

The SCA provides a pseudorandom data sequence for the test transmitter. The subcarrier frequency used is 32993 Hz, and data rates of interest range from 16 to 4096 symbols/s. The biphasic modulated subcarrier, in turn, phase modulates the carrier at the test transmitter with a modulation index that may vary from 35 deg to 75 deg depending upon data rate, and other factors. This simulated telemetry signal is then processed by the station receiving equipment much like the signal from a spacecraft. The "received" signal strength is set as required using the Y-factor measurement technique (Ref. 4) prior to the start of a test. The modulation indices are set by precision attenuators. Extreme care is required in this setup because of the sensitivity of decoding performance; the decoding erasure rate can vary by an order of magnitude with a 0.5-dB change in signal strength. After setup, the Test Program 5087 output monitors channel statistics, and when stable operation of the receiver and SDA is observed, the TCP/DDA Program is activated to develop the ODR of decoder performance.

The signal strength was set to a value slightly above that which had previously been predicted would provide a 10^{-4} deletion probability. This signal strength was specified as a desired signal power times symbol duration-to-noise spectral density ratio (ST_{sym}/N_0) at a 45-deg modulation angle, and all Y-factor setup and calibration was

derived from that point. The modulation index for the actual run was subsequently established through precision attenuators. For some of the tests, this was specifically the Helios modulation angles of 42 deg or 55 deg. For the four highest data rates this also included a four-point pattern of three modulation indices and two signal strengths intended to bracket the performance at the optimum modulation index. The primary data point was selected to achieve a 10^{-4} deletion probability at the approximately optimum modulation index. The secondary data points were set at that signal strength but at approximately 7-deg above and below optimum modulation index, and at the approximately optimum modulation index with 0.5 dB lower signal strength to achieve an estimated 10^{-3} deletion probability. The test parameter selections were based upon the previous modeling effort (Ref. 1).

The ODR tapes from tests in November and December have been transferred to a single master tape for final processing. Table 1 is an overall catalog of these tests, organized by data rate. Each file of the master tape is derived from one of the ODR tapes. A number of problems were encountered in reviewing these data. In a few cases, station parameter drifts of up to several tenths of a dB occurred during a test run. Such drifts were most evident in reviewing the decoder statistics, but could also be seen in the signal-to-noise ratio (SNR) estimates from the monitoring TCP. As a result of this drift, later parts of some of the longer data runs have been rejected. The second major problem is that "glitches", in the form of bursts of adjacent frames with large numbers of computations per frame, appeared in many of the data records. These bursts ranged in length up to several hundred frames and are definitely *not* an artifact of sequential decoding. Some of these bursts were traced to an intermittent problem in the SCA encoder. The bursts, and sections of the apparently normal data before and after them, were rejected, and in all cases, the remaining data from these tests displayed statistics that agreed reasonably well with expectations. It is almost certain, however, that some of the isolated single erasures that remain in the data were also caused by the problem that caused the bursts, and hence that the measured performance is somewhat poorer than would occur in flight operation. There was no trace of this problem in the SNR estimates from the monitoring TCP. The third problem encountered was that test results are consistently poorer than had been predicted, by 0.5 to 1.3 dB. No explanation for this seems to exist, except possibly for the undocumented information that DSS 71 is consistently at the low-performance end of known station-to-station variation.

III. Test Results

A summary of the principal test result appears in Table 2. Threshold tolerances in this table correspond to the 2-sigma confidence interval based upon sample size, and do not include the tolerance for test parameter setup. The accepted setup tolerances for the tests are a maximum of 0.4 dB for Y-factor setup, and a maximum of 0.3 dB for setting of the modulation index. Most of the test setups should be in fact much better than this maximum budgeted tolerance of 0.7 dB. Figure 2 shows the estimate threshold signal strength needed to achieve a 10^{-4} deletion probability as a function of data Rate R . The signal strength is given in terms of $P_t/N_0 \times 1/R$: the total power-to-noise spectral density ratio, normalized by data rate. The secondary comparison curves on Fig. 2 show two types of prior predictions of Helios telemetry threshold. One set of curves is for the predictions based upon the medium-rate model (Ref. 1). The second set is a heuristic composite prediction of the Helios telemetry threshold based upon nonreal-time tests (Ref. 2) and the medium-rate model. As can be seen, the current test data from DSS 71 exhibit noticeably poorer performance than the prior predictions. While this may be entirely due to station-to-station variations in performance, conducting part of these tests at other DSSs is necessary to ascertain that fact. The minimum of additional tests at DSS 71 needed to complete Fig. 2 consists of the points at 42-deg modulation index (MI), 128 bits/s and 64 bits/s, and a refinement of the point at 55 deg, 128 bits/s. These points are important because they define the crossover in performance between the two Helios modulation indices.

Figures 3(a) through 3(d) show computation distribution curves for the multimodulation-index subset of the tests for data rates of 2048 bits/s to 256 bits/s. The separation between computation distribution curves for runs with similar or identical parameters, while it is significant, is still within the experimental tolerances ascribed to the test setup. Figure 4(a) through 4(d) show the deletion probability as a function of modulation index as estimated via the medium-rate model (Ref. 1). Principal data points from the multimodulation-index test subset are shown on this figure for comparison. The differences between model and experiment are in all cases within the experimental tolerances of the test.

Figures 5(a) through 5(e) show the computation distribution curves for data rates of 128 bits/s to 8 bits/s, and include comparison of scaled-time and normal configura-

tion tests where available. There is excellent agreement between scaled and nonscaled tests at 32 bits/s — the sharp separation at low probability is believed to be a remnant of the burst-erasure problem mentioned earlier. At 8 bits/s, the agreement is far less perfect in the high-probability segment of the distribution, where there appears to be more than 0.5 dB separation in the additive *white* noise component. The parallel SNR monitoring TCP also indicated approximately 0.7 dB more degradation in the 8 bits/s run than in the time-scaled 128 bits/s run, which in turn showed more degradation than expected. Despite this, the tail of the computation distributions shows acceptable agreement. Since it is this tail that determines erasure probability, and since the distribution tail is dominated by the correlated carrier reference noise instead of the additive white noise, it has been tentatively determined to accept the scaled 8 bits/s test results, subject to change by further testing. The scaled test at 16 bits/s is also considered conditionally acceptable since it is bracketed by one clearly good test and one conditionally acceptable test. The scaled test at 128 bits/s was adjudged bad data, but prior tests at CTA 21 had shown agreement (Ref. 3). Hence the scaled test at 64 bits/s is believed valid, being bracketed by two successful comparisons. One additional weak point in these tests is evident from Fig. 5: because of the poorer than predicted performance at DSS 71, several tests had deletion probabilities above 10^{-3} , and while the extrapolation to 10^{-4} deletion probability is reasonably straightforward, it could introduce biases on the order of several tenths of a dB.

IV. Commentary and Future Work

The principal results of tests conducted to date appear in Fig. 2, and Figs. 3(a) through 3(d). The tests are complete as planned at the four highest data rates. With respect to determining Helios telemetry threshold, the main requirements are to fill in three weak points at midrange data rates, to perform some tests at 8 and 16 bit/s that achieve a 10^{-4} deletion probability, and to determine if the performance difference between current tests and prior predictions is due to station-to-station variations, or some other causes. The tolerance due to sample size in the current tests is generally below the tolerance ascribed to setup parameters. This tolerance is also below the performance difference between the current test and predictions. Hence the most fruitful area for future testing appears to be in evaluating and (hopefully) reducing setup tolerances, and in evaluating station-to-station variation.

References

1. Layland, J. W., "A Sequential Decoding Medium Rate Performance Model" in *The Deep Space Network Progress Report*, Technical Report 32-1526, Vol. XVIII, Jet Propulsion Laboratory, Pasadena, Calif., Dec. 15, 1973.
2. Lumb, D., NASA Ames Research Center, Moffett Field, Calif. Private communication at Helios Working Group Splinter Session, Sept. 27, 1973.
3. Butman, S., et al., "A Scaled Time Telemetry Test Capability for Sequential Decoding" in *The Deep Space Network Progress Report*, Technical Report 32-1526, Vol. XIX, Jet Propulsion Laboratory, Pasadena, Calif., Feb. 15, 1974.
4. DSIF Program Library, *Documentation for Y-Factor Computer Program*, DOI-5343-SP-B, Jet Propulsion Laboratory, Pasadena, Calif., Sept. 29, 1972.

Table 1. Catalog of Phase 2 tests

Symbol rate, symbols/s	Day of year	File number	Receiver PLL	ST_{sym}/N_0 , dB	MI, deg
4096	324	11	DSN (12)	0.0	67.5
	320	12		0.5	75
	319	15		0.5 ^a	60
	319	15		0.5 ^a	67.5
	360	21		0.5	55
	360	22		0.5	60
2048	325	1	DSN	0.7	67
	325	7		0.7	60
	330	13		0.2	60
	324	14		0.7	53
	361	20		0.7	55
1024	330	2	DSN	1.0	48
	332	3		1.0	53
	332	3		1.0	62
	331	4		1.0	48
	331	4		1.0	53
	333	5		1.0	62
	333	5		0.5	55
512	333	16	DSN	0.8 ^b	52
	345	23		1.6	55
	340	24		1.3	62
	337-338	26		1.3	42
	338-339	26		1.3	52
256	352	25	DSN	2.3	55
128	312	6	DSN	3.1 ^c	45
	313	8		3.1 ^{a,c}	40
	317	9		3.1 ^c	50
	318	10		3.1 ^{a,c}	55
64	344	18	DSN	3.4	67
	351	19		3.7	42
32	No Data				
16	353	30	DSN	5.3	42
4096	351	27	192 Hz	2.3 ^c	55
2048	351	28	192 Hz	3.0	55
1024	344	18	192 Hz	3.4	45
	344	18		3.4 ^c	67
	348	28		3.7	42
	348	28		3.7 ^b	55
	362	29		4.2	42
512	345	23	192 Hz	4.5	42
256	346	17	192 Hz	5.3	42

^aMaster-tape label says 99.0 dB.

^bParameter drifts.

^cBad data.

Table 2. Test Result Summary

Bit rate R , bits/s	Sample size, frames	Optimum MI, deg	Telemetry threshold at $P_d = 10^{-4}$ $P_t/N_0 \times 1/R$, dB	
			55 deg	42 deg
2048	7×10^4	65	7.0 ± 0.2	—
1024	6×10^4	62	7.2 ± 0.2	—
512	5×10^4	60	7.4 ± 0.2	—
256	4×10^4	57	7.7 ± 0.2	8.3 ± 0.5
128	10^3	—	8.8 ± 0.8	—
64	10^4 (scaled)	—	9.7 ± 0.4	—
32	9×10^2 and 2×10^4 (scaled)	—	—	10.0 ± 0.3
16	8×10^3 (scaled)	—	—	11.0 ± 0.4
8	9×10^2 and 10^4 (scaled)	—	—	12.0 ± 0.4

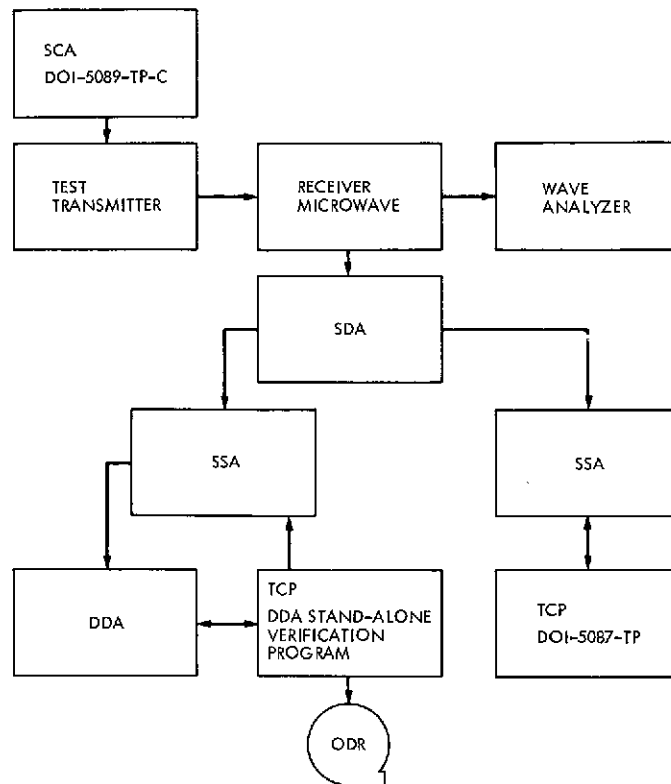


Fig. 1. Telemetry test configuration

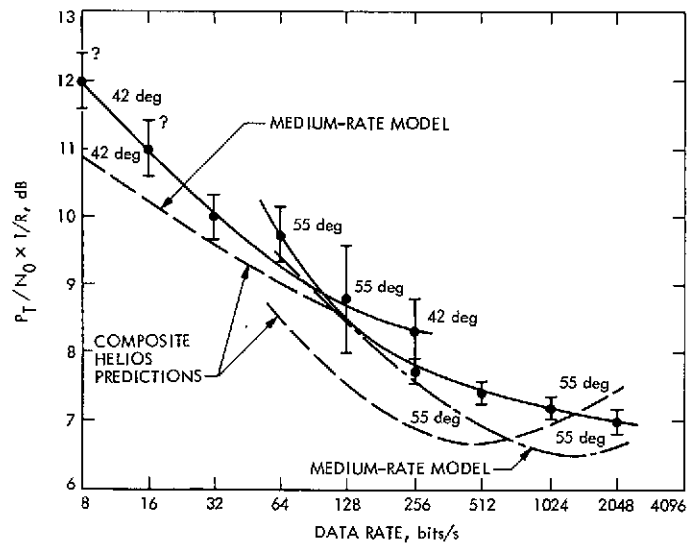


Fig. 2. Telemetry thresholds of 10^{-4} Pd comparison of DSS-71 tests and prior predictions

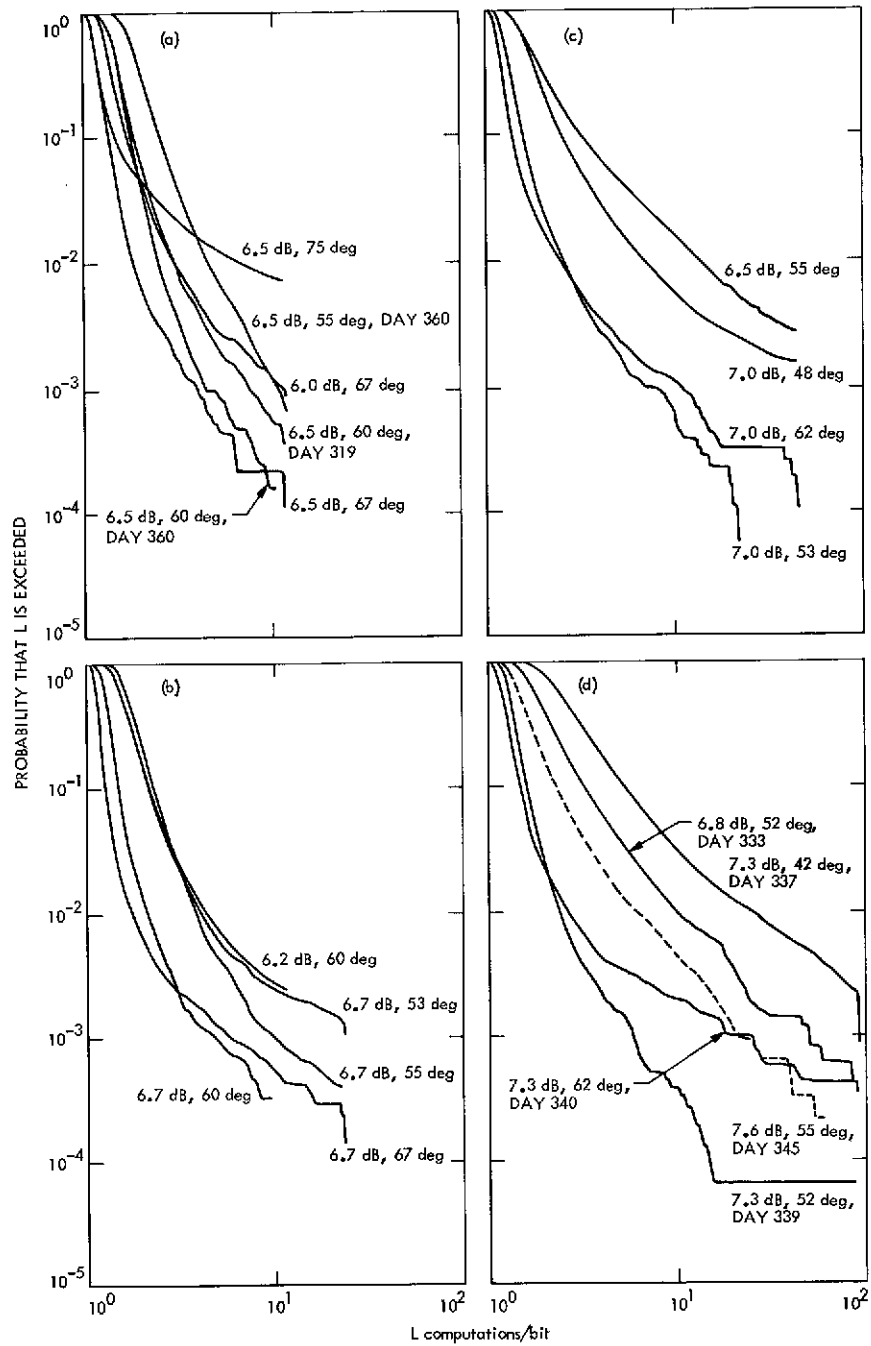


Fig. 3. Experimental computation distributions for: (a) 4096 SPS, (b) 2048 SPS, (c) 1024 SPS, (d) 512 SPS

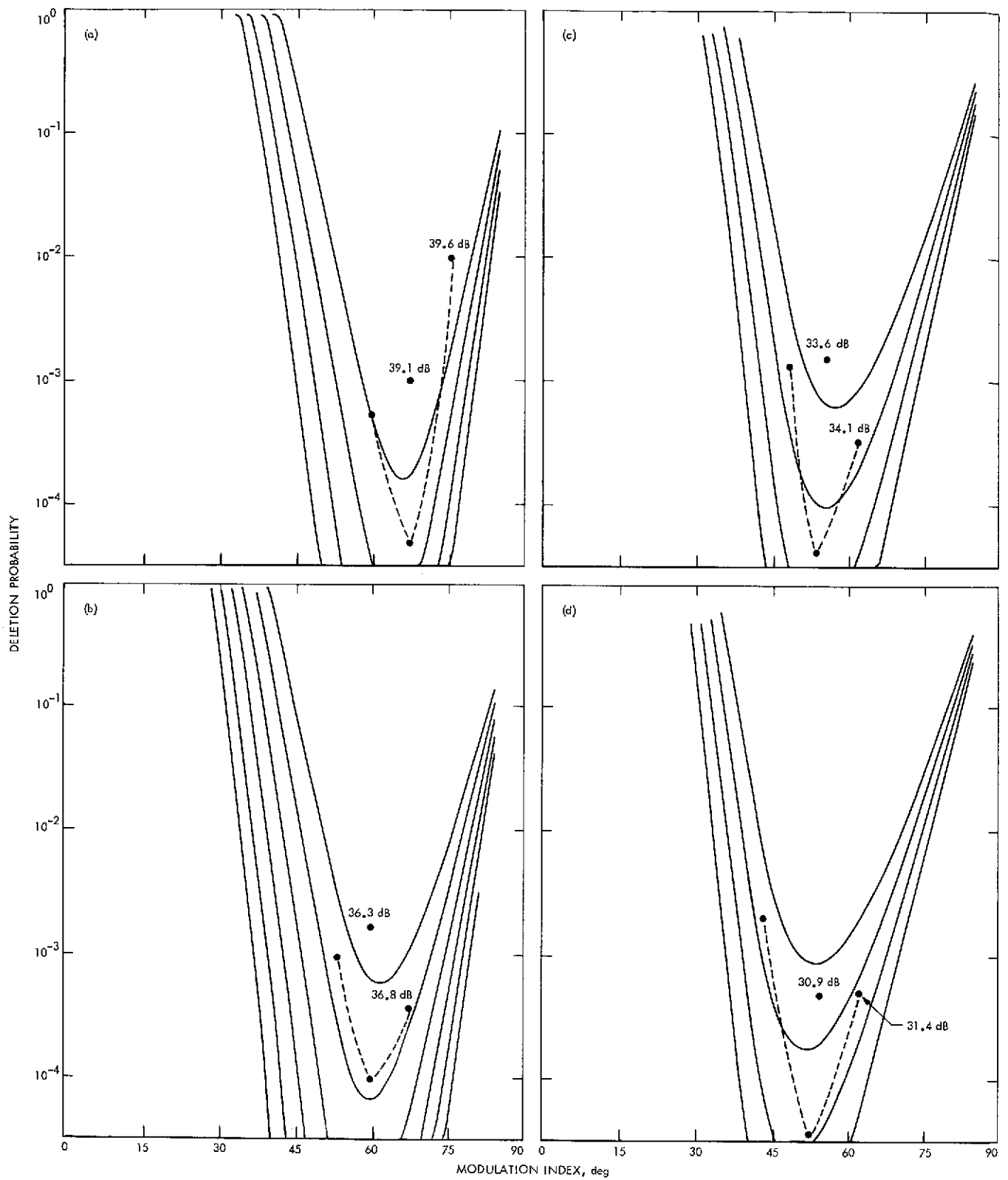


Fig. 4. Deletion probability as a function of modulation index: comparison of test and model for: (a) 4096 SPS, $P_i/N_0 = 39, 39.5, 40, 40.5$; (b) 2048 SPS, $P_i/N_0 = 36, 36.5, 38, 38.5$; (c) 1024 SPS, $P_i/N_0 = 33.5, 34, 34.5, 35$; (d) 512 SPS, $P_i/N_0 = 31, 31.5, 32, 32.5$

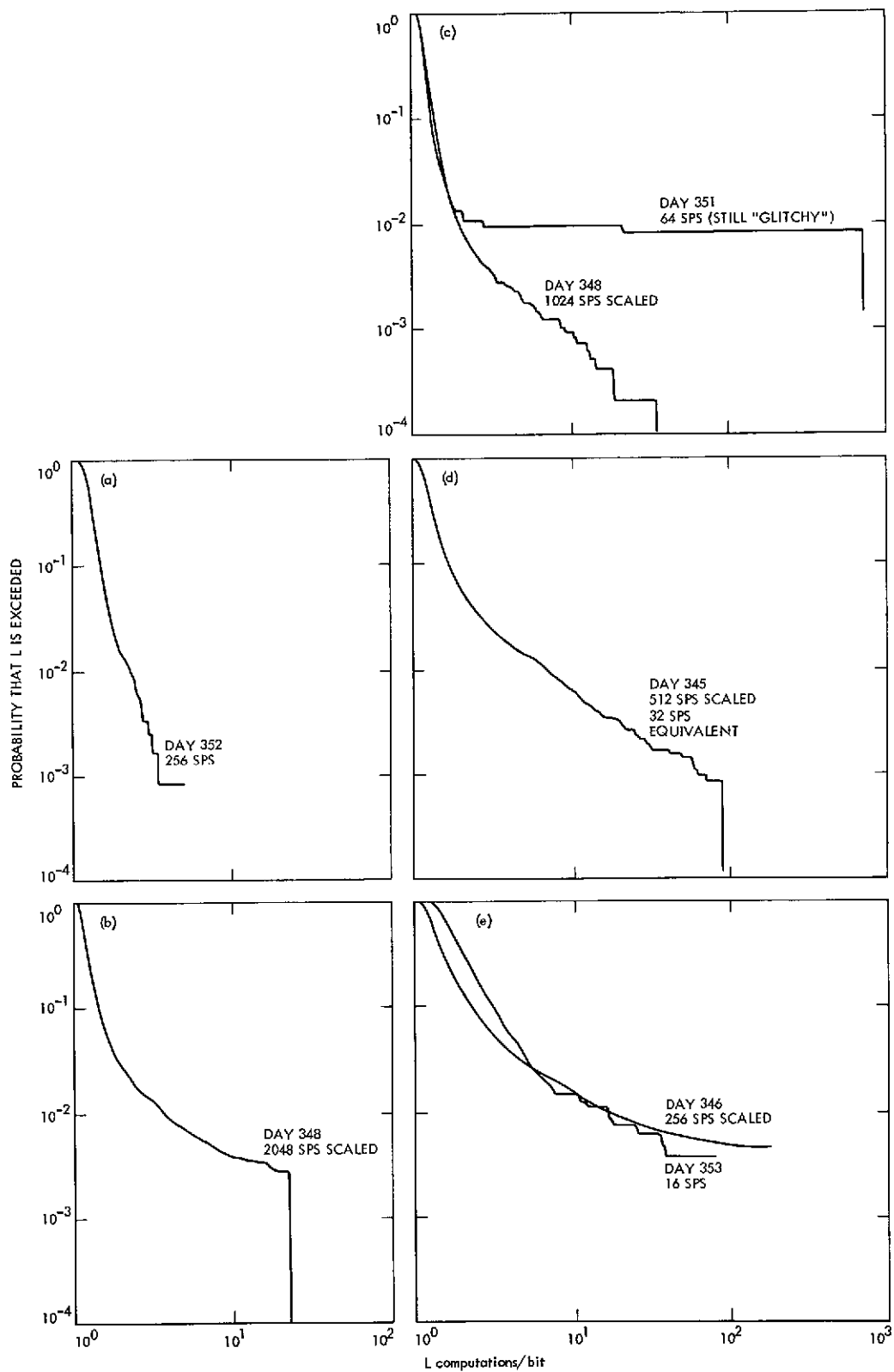


Fig. 5. Experimental computation distributions for: (a) 256 SPS, $P_t/N_0 \times 1/R = 8.3$ dB, MI = 55 deg; (b) 128 SPS, $P_t/N_0 \times 1/R = 9.0$ dB, MI = 55 deg; (c) 64 SPS, $P_t/N_0 \times 1/R = 9.7$ dB, MI = 42 deg; (d) 32 SPS, $P_t/N_0 \times 1/R = 10.5$ dB, MI = 42 deg; (e) 16 SPS, $P_t/N_0 \times 1/R = 11.3$ dB, MI = 42 deg

S/X-Band Experiment: Zero Delay Device Z Correction

P. D. Batelaan
Communications Elements Research Section

A new dual-frequency (S-band and X-band) zero delay device (ZDD) was required for the MVM73 S/X experiment at DSS 14. To properly utilize the "zero" calibration provided by the ZDD, an evaluation of the "Z" term in the ranging equations must be made. An equation for this term is derived, and values are determined for several configurations.

I. Introduction

A new dual frequency (S-band and X-band) zero delay device (ZDD) was required for the MVM73 S/X experiment at DSS 14 (Refs. 1, 2).¹ To properly utilize the "zero" calibration provided by the ZDD, an evaluation of the Z term in the ranging equations must be made (Ref. 3). An equation for this term is derived and values are determined for several configurations.

¹Discussions of the preliminary location tests and calibration of this ZDD are presented by C. T. Stelzried, et al. and by T. Y. Otoshi and C. T. Stelzried elsewhere in this issue.

II. Discussion

By referring to Figs. 1 and 2, it is possible to write an equation for the ranging machine "gross indicated" value of round-trip light time (RTLTL) while tracking the spacecraft:

$$A_{S/C(s)} = [B_U + B'_U + C_U - D + E_S] + F_S \\ + [E_S - D + C_{DS} + B'_{DS} + B_{DS}] \quad (\text{S-band}) \quad (1)$$

where

$A_{S/C}$ = ranging machine "gross indicated" round-trip light time while locked on the spacecraft (S/C), i.e., time for a signal to go from the ranging machine, through the complete system and back to the ranging machine²

B_U = time for a signal to travel from the ranging machine to the uplink sampling point for the ZDD

B'_U = time for a signal to travel from the uplink sampling point for the ZDD to the radio frequency (RF) ϕ center of the ground antenna feed horn

C_U = time for a signal to travel from the feed-horn phase center, through the dichroic feed system, subreflector and parabolic surface to the aperture plane of the paraboloid

D = distance (in equivalent time units) between the aperture plane and the antenna "bench mark"³

E = time for a signal to travel between the ground antenna bench mark and the spacecraft antenna aperture plane

F = two-way or round trip time for a signal to travel from the S/C antenna aperture plane, through the S/C radio subsystem and return to the S/C aperture plane

B'_D = time for a signal to travel from the RF ϕ center of the ground antenna feed horn to the ZDD simulated downlink injection point

B_D = time for a signal to travel from the ZDD simulated downlink injection point to the ranging machine

Subscripts U and D indicate uplink and downlink, respectively, and S indicates S-band. X will indicate X-band. Where no S or X designation appears, the terms are identical for S- and X-band signals.

A similar equation may be written for X-band:

$$A_{S/C(X)} = [B_U + B'_U + C_U - D + E_S] + F_X + [E_X - D + C_{DX} + B'_{DX} + B_{DX}] \quad (\text{X-band}) \quad (2)$$

²"Times" discussed here mean equivalent free-space light times.

³For DSS 14, the "bench mark" designated here is the intersection of the azimuth and elevation axes.

Similarly, equations can be written for the ranging machine "gross indicated" value of round-trip light time while "tracking" the ZDD:

$$A_{ZDD(S)} = [B_U + G_U] + H_S + [G_{DS} + B_{DS}] \quad (3)$$

$$A_{ZDD(X)} = [B_U + G_U] + H_X + [G_{DX} + B_{DX}] \quad (4)$$

where

A_{ZDD} = ranging machine "gross indicated" round-trip light time while locked on ZDD, i.e., time for a signal to go from the ranging machine, through the complete system and back to the ranging machine

G_U = time for a signal to travel from the uplink sampling point to the input port of the ZDD

H = two-way or round-trip time for a signal to travel from the ZDD input port through the ZDD and back to the appropriate output port

G_D = time for a signal to travel from the ZDD output port to the appropriate downlink injection point

Now, subtract Eq. (3) from Eq. (1) and combine terms

$$A_{S/C(S)} - A_{ZDD(S)} = B'_U + B'_{DS} + C_U + C_{DS} - 2D + E_S + E_S + F_S - [G_U + G_{DS} + H_S] \quad (5)$$

Rearrange

$$(E_S + E_S) = A_{S/C(S)} - A_{ZDD(S)} - F_S + [-(B'_U + B'_{DS} + C_U + C_{DS}) + 2D + G_U + G_{DS} + H_S] \quad (6)$$

The corresponding X-band equation is

$$(E_S + E_X) = A_{S/C(X)} - A_{ZDD(X)} - F_X + [-(B'_U + B'_{DX} + C_U + C_{DX}) + 2D + G_U + G_{DX} + H_X] \quad (7)$$

Now, compare Eqs. (6) and (7) with the R/D S/X ranging equation (repeated here for convenience) of Ref. 3:

$$RTL T = RU \frac{1}{(128)(48)F_T} + M \frac{64 \times 2^N}{3F_T} - BIAS_{DSN} \frac{1}{(128)(48)F_T} - BIAS_{S/O} + Z \quad (8)$$

The results of this comparison, term by term, are

$$(E + E) = \text{RTL T} \quad (9)$$

$$A_{S/C} = RU \frac{1}{(128)(48) F_T} + M \frac{64 \times 2^N}{3F_T} \quad (10)$$

$$A_{ZDD} = \text{BIAS}_{DSN} \frac{1}{(128)(48) F_T} \quad (11)$$

$$F = \text{BIAS}_{S/C} \quad (12)$$

and finally,

$$[-(B'_U + B'_D + C_U + C_D) + 2D + G_U + G_D + H] = Z \quad (13)$$

(The frequency subscripts S and X have been omitted for convenience as the comparison applies to both frequencies.)

Some comments on the terms comprising the expression for Z are in order:

- (1) The term C has the effect of moving the RF reference point from the ground antenna appropriate feed horn phase center to the aperture plane.

- (2) Then, the term D further moves the resulting RF reference from the aperture plane to the "bench mark."
- (3) The terms $(-B'_U + G_U)$ and $(-B'_D + G_D)$ compensate for the fact that the ZDD is not at the ground antenna feed horn phase center when taking a "zero delay" reading.
- (4) Finally, term H is exactly analogous to the S/C term F where each corrects for the signal turnaround time of its appropriate device.

The differential (S) - (X) Z term can be determined simply by subtracting the S and X forms of equation (13), the Z equation:

$$Z_S - Z_X = -(B'_{DS} - B'_{DX} + C_{DS} - C_{DX} - G_{DS} + G_{DX} - H_S + H_X) \quad (14)$$

Notice that since uplink terms are common to both S- and X-band signals, virtually all of them have dropped out of the differential (S) - (X) Z term.

References

1. Otoshi, T. Y., and Batelaan, P. D., *S/X-Band Experiment: Zero Delay Device*, Technical Report 32-1526, Vol. XIV, pp. 78-80, Jet Propulsion Laboratory, Pasadena, Calif., Apr. 15, 1973.
2. Otoshi, T. Y., and Batelaan, P. D., *S/X Experiment: Preliminary Tests of the Zero Delay Device*, Technical Report 32-1526, Vol. XVII, pp. 68-77, Jet Propulsion Laboratory, Pasadena, Calif., Oct. 15, 1973.
3. DSN System Requirements Document 820-13, Rev. A, Detailed Interface Design, TRK-2-8, pg. 20, paragraph 3.
4. Otoshi, T. Y., and Stelzried, C. T., "S/X Experiment: A New Configuration for Ground System Range Calibrations with the Zero Delay Device," (this issue).
5. Private communication, D. Bathker to P. Batelaan, 1/11/74.
6. Private communication, Smoot Katow to P. Batelaan, 11/14/73.

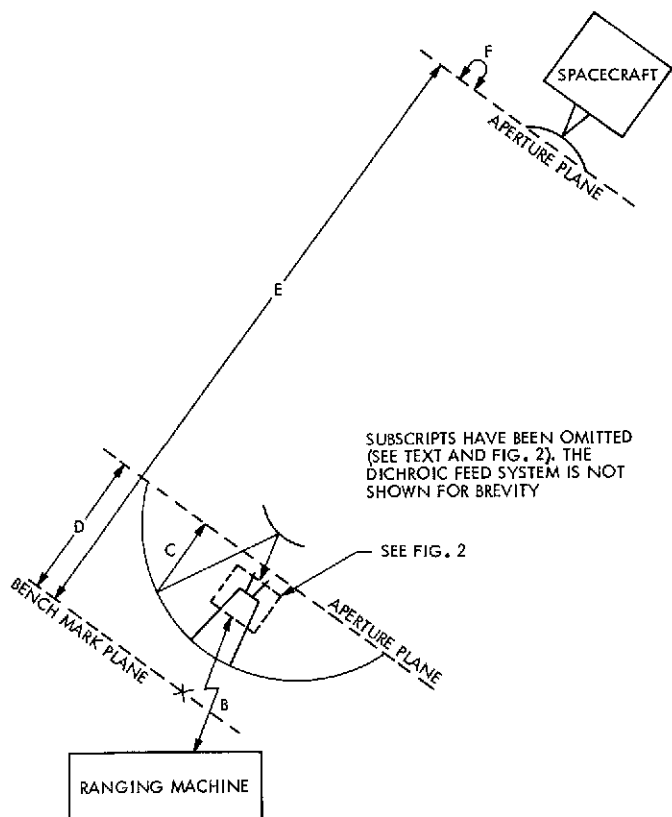


Fig. 1. Overall ranging path

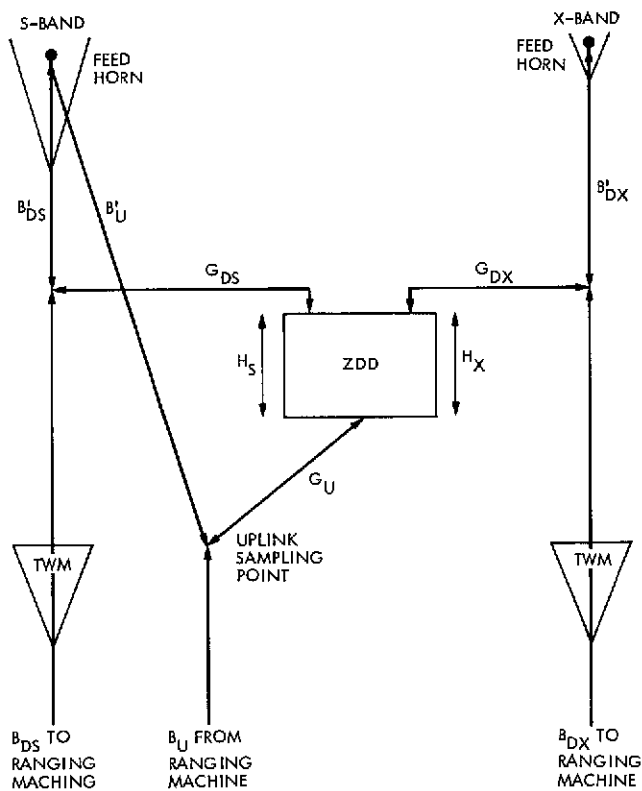


Fig. 2. Detail ranging path

Appendix A

Values of Z_s and Z_x for DSS 14 for the Period 12/21/73 Through 1/12/74

Values of Z_s and Z_x for DSS 14 for the period 12/21/73 through 1/12/74 are:

$$Z_s = -169.00 \pm 0.86 \text{ ns, } 1\sigma$$

$$Z_x = -137.58 \pm 0.86 \text{ ns, } 1\sigma$$

These numbers were arrived at by evaluating the appropriate forms of Eq. (13) with the values in Table A-1 substituted for the various indicated parameters (they do not, however, include the effects of the instabilities described in the articles of footnote 1)

Table A-1. Values of parameters

Parameter		Value, ns	Source
B'_U	=	91.29 ± 0.26	τ_{23} (Ref. 4) + τ (2113 feed and components) (Ref. 5)
B'_{DS}	=	47.37 ± 0.28	τ_{34} (Ref. 4) + τ (2295 feed and components) (Ref. 5)
B'_{DX}	=	3.52 ± 0.08	τ_{67} (Ref. 4) + τ (8415 feed and components) (Ref. 5)
C_U	=	168.95 ± 0.02	Ray optics tracing of path from S-band feed horn to aperture plane via dichroic system, subreflector and paraboloid
C_{DS}	=	168.95 ± 0.02	Ray optics tracing of path from S-band feed horn to aperture plane via dichroic system, subreflector and paraboloid
C_{DX}	=	160.01 ± 0.06	Ray optics tracing of path from X-band feed horn to aperture plane via dichroic system, subreflector and paraboloid
D	=	58.62 ± 0.01	Ref. 6 and print 9437255
G_U	=	88.83 ± 0.09	τ_{2A} (Ref. 4)
G_{DS}	=	87.38 ± 0.12	τ_{B4} (Ref. 4)
G_{DX}	=	70.63 ± 0.10	τ_{C7} (Ref. 4)
H_S	=	14.11 ± 0.76	τ_{AB} (Ref. 4)
H_X	=	9.49 ± 0.80	τ_{AC} (Ref. 4)

Appendix B

Values of Z_s and Z_x for DSS 14 for 1/14/74 and Later

On 1/13/74 the uplink sampling point was moved from the 10/20 kW transmitter in the MOD II area to the junction of the megawatt transmitter filter (MTF) and the 4th harmonic filter in the MOD III area. This was done so that the sampling point would be independent of which transmitter was in use: 10, 20, 100 or 400 kW. Because of this relocation, the values of Z_s and Z_x have changed to:

$$Z_s = -166.50 \pm 0.86 \text{ ns, } 1\sigma$$

$$Z_x = -135.08 \pm 0.86 \text{ ns, } 1\sigma$$

These numbers were arrived at by evaluating the appropriate forms of Eq. (13) with the values in Table B-1 substituted for the various indicated parameters.

Table B-1. Values of parameters

Parameter		Value, ns	Source
B'_U	=	42.31 ± 0.26	$\tau_{2'3}$ (Ref. 4) + τ (2113 feed and components) (Ref. 5)
B'_{DS}	=	47.37 ± 0.28	τ_{34} (Ref. 4) + τ (2295 feed and components) (Ref. 5)
B'_{DX}	=	3.52 ± 0.08	τ_{67} (Ref. 4) + τ (8415 feed and components) (Ref. 5)
C_U	=	168.95 ± 0.02	Ray optics tracing of path from S-band feed horn to aperture plane via dichroic system, subreflector and paraboloid
C_{DS}	=	168.95 ± 0.02	Ray optics tracing of path from S-band feed horn to aperture plane via dichroic system, subreflector and paraboloid
C_{DX}	=	160.01 ± 0.06	Ray optics tracing of path from X-band feed horn to aperture plane via dichroic system, subreflector and paraboloid
D	=	58.62 ± 0.01	Ref. 6 and print 9437255
G_U	=	42.35 ± 0.09	$\tau_{2'A}$ (Ref. 4)
G_{DS}	=	87.38 ± 0.12	τ_{B4} (Ref. 4)
G_{DX}	=	70.63 ± 0.10	τ_{C7} (Ref. 4)
H_s	=	14.11 ± 0.76	τ_{AB} (Ref. 4)
H_x	=	9.49 ± 0.80	τ_{AC} (Ref. 4)

Preliminary S-Band Noise Temperature Statistics at DSS 14 for 1971 and 1972

R. W. D. Booth, M. S. Reid, and T. J. Cullen
Communications Elements Research Section

This article reports on the continuing effort to statistically characterize microwave weather-induced parameters as part of an overall effort to optimize the spacecraft-to-ground communications link. This report considers S-band 1971 and 1972 weather project data only. The statistics of interest are distribution tables for each year, distribution tables for each quarter, and tables of average excess noise temperature duration.

I. Introduction

This article reports on the continuing effort to characterize microwave weather statistics as part of the overall objective to optimize the spacecraft-to-ground communications link. The system operating noise temperature of the S-band systems was monitored and recorded for 1971 and 1972. Excess system noise temperatures were computed from these data. The excess noise temperature is defined as that portion of the total measured system noise temperature which is in excess of that value to be expected on a clear, dry day for the given antenna elevation angle. X- and K-band data will be reported in a subsequent article.

The excess noise temperature distributions for each year and each quarter are tabulated. Estimates of the average duration in time of the periods of excess system

temperature have been calculated and are reported. These statistics may be important in planning for critical periods such as planetary encounters, etc.

II. Analysis

The distribution tables were formulated by dividing the total elevation range into four sections; 6–15, 15–25, 25–45, and 45–90 degrees. The excess noise temperature range was divided into sections of 10 K per section. The first section is 0–10 K and, for the accuracy of the measurements, represents the normal, or zero excess, section. The percentage of time the excess system noise temperature fell in each noise temperature section was calculated for each elevation angle section. In addition, these percentages were calculated for the entire elevation angle range of 6–90 degrees.

In addition to the distribution tables, means, standard deviations, and confidence intervals for the means were calculated for each range of elevation angle. The 50 and 95% confidence intervals for the mean were calculated. For these intervals, it was assumed that the distribution of the mean had converged to a gaussian distribution.

Finally, some preliminary estimates of excess noise temperature variations were made. At a fixed elevation angle, the total noise power at the output of the receiver varies with time. The primary contribution to this variation is from atmospheric effects, provided all other effects such as system configuration changes and data handling are removed. One may expect several short-term contributions to the noise received such as clouds and water vapor variations, especially near sunrise and sunset. The noise has a tendency to increase for a while and then decrease. Noise bursts from the transmitter and other ground equipment are excluded. The parameter of interest is the average duration of time that the noise temperature is above some threshold.

An average clear, dry background system temperature as a function of elevation angle was determined for S-band. This is an average baseline background profile. Six additional profiles were generated from this baseline profile. These new profiles were at 1, 2, 3, 4, 5 and 6 dB above the baseline profile. When the measured system temperature crossed one of the thresholds, the time was monitored until the system temperature dropped below the threshold, and these times were used to calculate mean-time durations and standard deviations that the thresholds were exceeded. The total number of events (i.e., number of times that a threshold was crossed) and the average number of events per 24-hour day were also calculated.

III. Tables

The odd-numbered tables from 1 through 19 are distribution tables and the even-numbered tables from 2 through 20 are tables of statistics. The distribution tables list the percentages of time that the excess system noise temperature was between the various 10 K increments, and the antenna elevation angle was between the given limits. For example, in Table 1 the entry 8.6 under 6-15 deg and opposite 0-10 K indicates that for 8.6 percent of the time the excess system noise temperature was between 0 and 10 K, and the antenna elevation angle was between 6 and 15 deg. The last column on the right is the total percentage of time the excess system noise temperature

was between the indicated values of excess temperature, independent of elevation angle. The row at the bottom indicates the total percentage of time the antenna elevation angle was between the indicated values of elevation angle independent of excess noise temperature.

The statistical tables list the mean and standard deviation of the excess noise temperatures and are given for each elevation angle range. The 50% and 95% confidence intervals are given for the mean value. For example, for Table 2, the value 0.1 under 6-15 and opposite 50% confidence interval, indicates that with probability = 0.5, the actual mean is within plus or minus 0.1 K of the calculated mean value of 8.5 K.

Tables 21 and 22 are tables of the time duration of the periods when the system temperature exceeded the clear, dry weather baseline. Tables 21 and 22 are for all data for 1971 and 1972, respectively. These tables indicate the mean duration of time the system noise temperature was in excess of the indicated threshold. The total number of recorded events is also shown as well as the average number of events per day (equal to the total days of recorded data divided by the total number of recorded events), the mean time-duration of excess system temperature periods and its standard deviation.

In every table a blank indicates either zero or a value less than 0.05. The distribution and the statistical calculations were repeated, both for 1971 and for 1972, on a monthly basis, and these data are available for reference and comparisons.

In order to summarize all the distribution tables in a single figure, the percent of time the excess system noise temperature was greater than 10 K was chosen as a representative number for each table. These values were plotted for each quarter and for the whole calendar year for both 1971 and 1972 and are shown in Fig. 1.

The Goldstone area experienced unusually severe weather conditions, which included a heavy snowstorm in December 1971 (Ref. 1). This is reflected in the high value in Fig. 1 for the winter quarter. The difference, in general, between 1971 and 1972 as seen in Fig. 1 cannot be attributed only to weather conditions, however. The amount of data recorded in each quarter and in each year must be taken into account. Significantly more data were recorded in 1972 than in 1971. For example, for the winter quarter, usable data were recorded for only 9.8% of the possible time in 1971, whereas the figure for 1972 was

22.5%. For the March, April, and May quarter the figures were 4.2% and 29.7% for 1971 and 1972, respectively. For the June, July, August and September, October, November quarters the 1971 and 1972 figures were 2.7%, 25.8% and 4.2%, 28.6%, respectively. Data were recorded for 5.2% of the time in 1971 and 26.6% of the time in 1972. These figures clearly demonstrate the need for more consistent data recording.

In order to estimate the effect of a single period of severe weather, such as the snowstorm in December 1971, the 1971 data were recomputed using only the January through November recordings. These data were compared with the 1972 data and the conclusions are that the

effect of the unusual data was to lengthen the average duration of time the excess system noise temperature remained above each of the thresholds and to increase significantly the standard deviations of these periods of excess system temperature, for some thresholds as much as 100 percent.

Other conclusions are that, even omitting December 1971, and if all other effects have been removed, then there were fewer periods of excess system temperature due to inclement weather conditions in 1972 than there were in 1971; the magnitudes of the 1972 excesses were less severe than they were in 1971, and that year-to-year differences must be expected.

Reference

1. Reid, M. S., *An Analysis of System Performance Under the Severe Weather Conditions at Goldstone, December 1971*, Technical Report 32-1526, Vol. XII, pp. 32-37, Jet Propulsion Laboratory, Pasadena, Calif., December 15, 1972.

Table 1. S-band distribution for all data for 1971

Excess noise tempera- ture, K	Antenna elevation angle, deg				
	6-15	15-25	25-45	45-90	6-90
Percentage of time of excess noise temperature					
0-10	8.6	20.5	44.6	9.4	83.1
10-20	3.4	3.2	4.5	0.9	12.0
20-30	0.2	0.4	0.6	0.2	1.5
30-40	0.1	0.7	"	0.2	1.0
40-50	"	0.2	0.3	0.4	0.9
50-60	"	"	"	"	"
60-70	"	"	"	0.3	0.3
70-80	"	"	"	0.2	0.2
80-90	"	"	0.4	0.1	0.5
90-100	"	"	0.3	"	0.3
100-110	"	"	"	0.3	0.3
Totals	12.3	24.9	50.8	12.0	100.0

"Zero or less than 0.05.

Table 2. S-band statistical table for all data for 1971

	Antenna elevation angle, deg				
	6-15	15-25	25-45	45-90	6-90
Mean, K	8.5	6.9	6.3	11.4	7.3
Standard deviation, K	5.2	6.6	11.4	22.3	12.0
50% confidence interval, K	0.1	0.1	0.1	0.3	0.1
95% confidence interval, K	0.2	0.2	0.2	0.8	0.2

Table 3. S-band distribution table for December, January, February, 1971

Excess noise tempera- ture, K	Antenna elevation angle, deg				
	6-15	15-25	25-45	45-90	6-90
Percentage of time of excess noise temperature					
0-10	7.2	19.6	43.7	3.4	73.9
10-20	2.6	4.3	7.8	1.1	15.8
20-30	0.2	0.9	1.4	0.5	3.0
30-40	0.2	1.4	0.1	0.5	2.2
40-50	"	0.4	0.7	0.8	1.8
50-60	"	"	"	"	"
60-70	"	"	"	0.6	0.6
70-80	"	"	"	0.4	0.4
80-90	"	"	0.9	0.2	1.2
90-100	"	"	0.6	"	0.6
100-110	"	"	"	0.6	0.6
Totals	10.1	26.6	55.3	8.0	100.0

"Zero or less than 0.05.

Table 4. S-band statistical table for December, January, February, 1971

	Antenna elevation angle, deg				
	6-15	15-25	25-45	45-90	6-90
Mean, K	9.6	8.1	8.5	29.7	10.2
Standard deviation, K	5.7	8.7	15.6	33.0	16.7
50% confidence interval, K	0.1	0.1	0.1	0.7	0.1
95% confidence interval, K	0.3	0.3	0.4	2.0	0.3

Table 5. S-band distribution table for March, April, May, 1971

Excess noise temperature, K	Antenna elevation angle, deg				
	6-15	15-25	25-45	45-90	6-90
	Percentage of time of excess noise temperature				
0-10	4.0	8.3	40.4	35.4	88.1
10-20	1.1	3.6	4.3	2.2	11.2
20-30	0.7	a	a	a	0.7
Totals	5.8	11.9	44.8	37.5	100.0

^aZero or less than 0.05.

Table 6. S-band statistical table for March, April, May, 1971

	Antenna elevation angle, deg				
	6-15	15-25	25-45	45-90	6-90
Mean, K	9.4	6.4	3.8	3.2	4.2
Standard deviation, K	8.6	5.0	3.4	4.3	4.7
50% confidence interval, K	0.3	0.1	a	0.1	a
95% confidence interval, K	0.9	0.4	0.1	0.2	0.1

^aZero or less than 0.05.

Table 7. S-band distribution table for June, July and August, 1971

Excess noise temperature, K	Antenna elevation angle, deg				
	6-15	15-25	25-45	45-90	6-90
	Percentage of time of excess noise temperature				
0-10	21.7	44.9	24.4	a	91.0
10-20	8.9	a	a	a	9.0
Totals	30.6	44.9	24.4	a	100.0

^aZero or less than 0.05.

Table 8. S-band statistical table for June, July, August, 1971

	Antenna elevation angle, deg				
	6-15	15-25	25-45	45-90	6-90
Mean, K	7.5	5.2	4.1	a	5.7
Standard deviation, K	3.4	2.0	1.8	a	2.8
50% confidence interval, K ^a	0.1	a	a	0.1	a
95% confidence interval, K ^a	0.2	0.1	0.1	0.2	0.1

^aZero or less than 0.05.

Table 9. S-band distribution table for September, October, November, 1971

Excess noise temperature, K	Antenna elevation angle, deg				
	6-15	15-25	25-45	45-90	6-90
	Percentage of time of excess noise temperature				
0-10	8.0	18.6	64.2	3.3	94.1
10-20	3.7	2.2	a	a	5.9
Totals	11.7	20.8	64.2	3.3	100.0

^aZero or less than 0.05.

Table 10. S-band statistical table for September, October, November, 1971

	Antenna elevation angle, deg				
	6-15	15-25	25-45	45-90	6-90
Mean, K	7.7	5.8	4.5	3.4	5.1
Standard deviation, K	3.6	2.6	1.9	0.8	2.6
50% confidence interval, K ^a	0.1	0.1	a	a	a
95% confidence interval, K ^a	0.3	0.2	0.1	0.1	0.1

^aZero or less than 0.05.

Table 11. S-band distribution table for all data for 1972

Excess noise temperature, K	Antenna elevation angle, deg				
	6-15	15-25	25-45	45-90	6-90
	Percentage of time of excess noise temperature				
0-10	11.0	14.1	30.3	43.6	99.1
10-20	0.1	0.1	0.2	0.3	0.7
20-30	a	a	a	0.1	0.1
30-40	a	a	a	0.1	0.1
40-50	a	a	a	a	a
50-60	a	a	a	a	a
60-70	a	a	a	a	a
Totals	11.2	14.2	30.6	44.0	100.0

^aZero or less than 0.05.

Table 12. S-band statistical table for all data for 1972

	Antenna elevation angle, deg				
	6-15	15-25	25-45	45-90	6-90
Mean, K	1.1	0.8	0.7	0.5	0.7
Standard deviation, K	2.4	2.1	2.0	2.7	2.4
50% confidence interval, K	a	a	a	a	a
95% confidence interval, K	a	a	a	a	a

^aZero or less than 0.05.

Table 13. S-band distribution table for December, January, February, 1972

Excess noise temperature, K	Antenna elevation angle, deg				
	6-15	15-25	25-45	45-90	6-90
	Percentage of time of excess noise temperature				
0-10	10.9	13.2	29.3	46.6	100.0
Totals	10.9	13.2	29.3	46.6	100.0

Table 14. S-band statistical table for December, January, February, 1972

	Antenna elevation angle, deg				
	6-15	15-25	25-45	45-90	6-90
Mean, K	0.1	0.1	a	a	a
Standard deviation, K	0.5	0.5	0.1	a	0.3
50% confidence interval, K	a	a	a	a	a
95% confidence interval, K	a	a	a	a	a

^aZero or less than 0.05.

Table 15. S-band distribution table for March, April, May, 1972

Excess noise temperature, K	Antenna elevation angle, deg				
	6-15	15-25	25-45	45-90	6-90
	Percentage of time of excess noise temperature				
0-10	10.0	12.5	26.5	50.9	100.0
10-20	a	a	a	a	a
Totals	10.1	12.5	26.5	50.9	100.0

^aZero or less than 0.05.

Table 16. S-band statistical table for March, April, May, 1972

	Antenna elevation angle, deg				
	6-15	15-25	25-45	45-90	6-90
Mean, K	0.3	0.2	0.1	0.1	0.1
Standard deviation, K	1.1	0.8	0.5	0.4	0.6
50% confidence interval, K	a	a	a	a	a
95% confidence interval, K	a	a	a	a	a

^aZero or less than 0.05.

Table 17. S-band distribution table for June, July, August, 1972

Excess noise temperature, K	Antenna elevation angle, deg				
	6-15	15-25	25-45	45-90	6-90
	Percentage of time of excess noise temperature				
0-10	9.4	13.4	26.4	49.6	98.8
10-20	0.1	a	a	0.5	0.6
20-30	a	a	a	0.3	0.3
30-40	a	a	a	0.2	0.2
40-50	a	a	a	a	a
50-60	a	a	a	a	a
60-70	a	a	a	a	a
Totals	9.5	13.4	26.4	50.7	100.0

^aZero or less than 0.05.

Table 18. S-band statistical table for June, July, August, 1972

	Antenna elevation angle, deg				
	6-15	15-25	25-45	45-90	6-90
Mean, K	1.2	0.9	0.5	0.7	0.7
Standard deviation, K	2.3	1.8	1.3	3.7	2.9
50% confidence interval, K	a	a	a	a	a
95% confidence interval, K	0.1	0.1	a	0.1	a

^aZero or less than 0.05.

Table 19. S-band distribution table for September, October, November, 1972

Excess noise temperature, K	Antenna elevation angle, deg				
	6-15	15-25	25-45	45-90	6-90
	Percentage of time of excess noise temperature				
0-10	13.7	17.3	38.7	28.0	97.7
10-20	0.3	0.2	0.9	0.5	1.9
20-30	0.1	0.1	a	0.1	0.3
30-40	a	a	a	a	a
40-50	a	a	a	0.1	0.1
50-60	a	a	a	a	a
Totals	14.0	17.6	39.6	28.8	100.0

^aZero or less than 0.05.

Table 20. S-band statistical table for September, October, November, 1972

	Antenna elevation angle, deg				
	6-15	15-25	25-45	45-90	6-90
Mean, K	2.2	1.7	1.5	1.6	1.7
Standard deviation, K	3.3	2.9	3.0	4.2	3.4
50% confidence interval, K	a	a	a	a	a
95% confidence interval, K	0.1	0.1	a	0.1	a

^aZero or less than 0.05.

Table 21. Average excess noise temperature duration and frequency for S-band data, 1971, all elevation angles

Threshold	Number of events	Average events/ 24-hr day	Mean time duration, min	Standard deviation, min
1 dB	73	1.61	62.1	113.0
2 dB	15	0.33	80.5	143.7
3 dB	3	0.066	243.0	187.2
4 dB	2	0.044	301.5	134.5
5 dB	1	0.022	407.0	
6 dB	1	0.022	301.0	
7 dB	1	0.022	31.0	

Table 22. Average excess noise temperature duration and frequency for S-band data, 1972, all elevation angles

Threshold	Number of events	Average events/ 24-hr day	Mean time duration, min	Standard deviation, min
1 dB	41	0.42	38.8	95.0
2 dB	13	0.13	42.3	73.2
3 dB	5	0.051	22.0	18.9
4 dB	5	0.051	7.0	5.0
5 dB	2	0.021	2.5	1.5

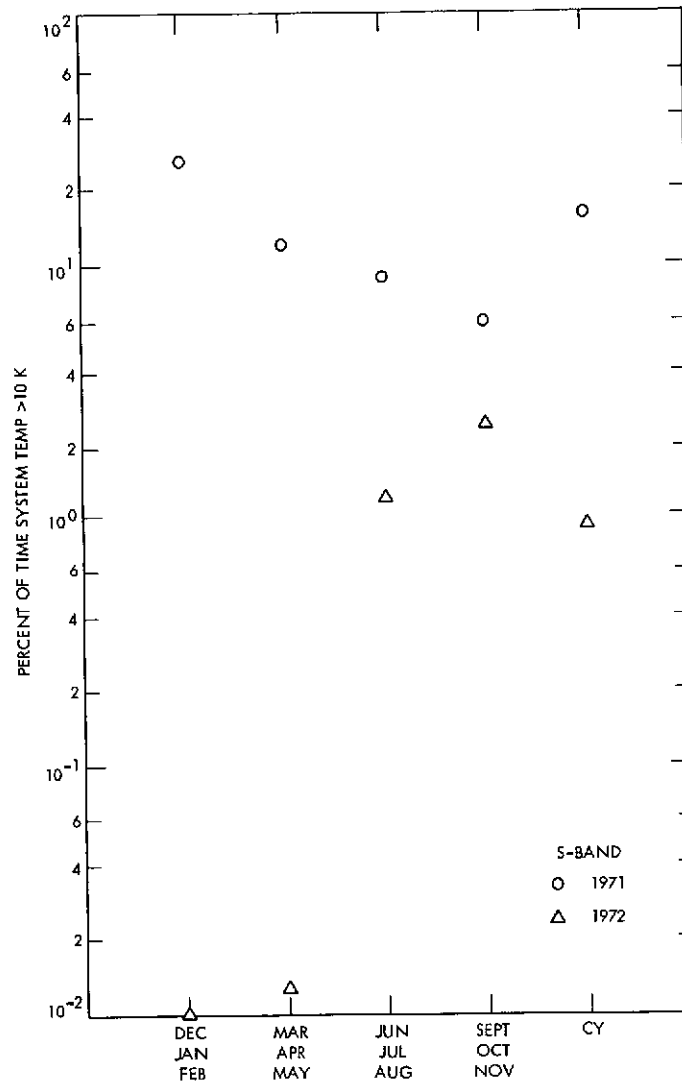


Fig. 1. Percent of time excess system temperature greater than 10 K as a function of time, S-band, 1971 and CY 1972

Shaped Antenna Designs and Performance for 64-m Class DSN Antennas

P. D. Potter

Communications Elements Research Section

Significant DSN antenna performance enhancement is possible through the use of shaped dual reflector antenna techniques. A detailed study has been performed to optimize configurations for maximum performance. Four designs in the antenna diameter size range of 64 to 72 m were carried out and are reported here. Complete performance predictions and mechanical configurations are given.

I. Introduction

Several possibilities exist for enhancement of the gain and noise temperature performance of the Deep Space Network (DSN) 64-m class antennas. The DSS 14 antenna noise temperature degradation due to quadripod scatter has been recently calibrated (Ref. 1), a possible technique for performance improvement has been proposed (Ref. 2) and related field tests are presently being performed at DSS 13. This article deals with possible improvement of antenna aperture efficiency (and hence gain) and reduction of spillover noise contribution by use of reflector surface shaping.

For two-reflector quasi-Cassegrain antennas, a technique was developed by Galindo (Refs. 3, 4) for achievement of almost 100% aperture efficiency by use of specially-shaped reflector surfaces to transform the

(arbitrary) feed radiation pattern into a uniformly (in amplitude and phase) illuminated antenna aperture. The Galindo technique uses geometric optics to solve the reflector surface simultaneous differential equations such that the feed radiation pattern is transformed into uniform aperture illumination. Being optical, the resulting solution is essentially frequency independent. The Galindo method was reduced to practice some time ago by Williams (Ref. 5) and its possible application to the DSS 14 64-m antenna was studied by Ludwig (Ref. 6). The Galindo technique has also been successfully used by numerous other organizations to realize ultrahigh aperture efficiency in ground antennas.

All of the above shaped antenna designs involve antenna surfaces that are figures of revolution. With the DSN 64-m antenna asymmetric tricone feed system, such

designs are not applicable. The general case of arbitrary shaped dual reflector systems has been studied by Yeh (Ref. 7) and results in a set of extremely complex nonlinear partial differential equations to be solved. A further difficulty is that the DSN antenna tricone concept is such that the main reflector must be a figure of revolution.

An approximate asymmetric shaping technique that circumvents the above difficulties has been recently developed by Potter (Ref. 2). This method is optical and involves a perturbation of the symmetric surfaces generated by the standard Galindo method. The main reflector is left unperturbed and a minimum perturbation of the subreflector is made to maintain constant path length for all system rays. The result of this process is uniform, frequency-independent aperture phase and an aperture amplitude that is slightly asymmetric. The resulting asymmetry gain loss is, however, small (about 0.1 dB for the DSN antenna geometry).

In this article, the results of a detailed shaping design study are presented. Shaped designs were synthesized for DSN antenna diameters of 64 m, 68 m, 70 m, and 72, and are presented here. Performance level was analyzed in detail and is also presented. The following section discusses the design method.

II. Design Method

Figure 1 shows the shaped antenna geometry. Because of the finite wavelength of operation and the requirement for ultralow noise performance (low rear spillover) the outer part of the main reflector is in reality a "noise shield." The optical edge of the symmetrically shaped main reflector thus exists at a radius $XMAX$, where $XMAX < DMAIN/2$. Visualizing the antenna as receiving an axial signal, an incoming ray that strikes the main reflector at a radius of $XMAX$ is reflected at an angle β_D and is directed towards the point O . All such rays lie in a right circular cone of semiangle β_E , as shown in Fig. 1. These cone rays are intercepted by the asymmetric subreflector, whose edge also lies in this conical surface, and are directed to the feed at the point P . The subreflector surface is mathematically constructed such that all other axial rays that strike the main reflector within a radius of $XMAX$ also focus to the point P .

The noise shield angle ($\Psi_2 - \Psi_1$) is determined by the diffraction characteristic of the subreflector at the design frequency. Visualizing the antenna as being in the transmitting mode, the phase characteristic of the scattered field changes rapidly near the cutoff at $XMAX$.

To constructively use the energy between $XMAX$ and $DMAIN/2$, the surface is shaped to fit the scattered field phase characteristic at the design frequency. It actually turns out to be necessary to do nonoptical surface modification somewhat inside the radius $XMAX$.

Figures 2(a) and (b) show, respectively, the design procedure that was used and the associated JPL computer software for performing the calculations. Considering Fig. 2(a) first, step 1 consists of making certain fundamental decisions; in this case antenna diameters of 64, 68, 70 and 72 m, a subreflector size of 6.096 m (20 ft.), the existing feedhorn phase center location, and a forward spillover of 1%.

The JPL hybrid horn computer program (Ref. 8) has demonstrated the ability to exactly predict antenna feedhorn radiation patterns as a function of physical geometry and was used in step 2 of Fig. 2(a). The required feedhorn is approximately twice as large as the presently-used DSN hybrid-mode feedhorn. This size would not pose a serious problem at X-band, but would probably require some other approach (such as reflex optics) at S-band. Attempts to reduce horn length by flare-angle increase were unsuccessful, resulting in an unacceptable horn sidelobe level and phase distortion of the pattern. The Cramer efficiency program was used to integrate the horn radiation pattern and determine forward spillover level. Figure 3 shows the final horn design dimensions and radiation pattern at 8.450 GHz.

The symmetrical ($R_D = 0$ in Fig. 1), shaped subreflector was designed with the Galindo-method Ludwig shaping program, and the feedhorn-subreflector scattered fields were evaluated with the Rusch physical-optics scattering program. Figures 4, 5, and 6 show, respectively, the existing DSS 14 X-band scattered pattern, a quasi-uniformly-illuminated subreflector test case, and the final symmetrical shaped subreflector scattered pattern at X-band. In deriving the system whose pattern is shown in Fig. 6, the Cramer efficiency program was utilized to evaluate antenna efficiency and rear spillover vs the cut-off angle β_E (see Fig. 1), and the design was iterated (two tries, actually) until satisfactory performance was achieved. A tricky parallax problem arises here, however. The subreflector is so large that the main reflector is in its near field. The actual fields in the vicinity of the main reflector edge may be calculated, in principle, using spherical wave techniques (Ref. 9). The associated parallax problem can be seen with reference to Fig. 1. The fields at the main reflector edge are absolute, independent

of radiation pattern origin. On the other hand, the radiation pattern cutoff angle clearly depends on the origin choice.

To calculate the true near-field spillover level, the X-band scattered pattern was expanded in modal waves with the Cramer expansion program. It was discovered that a maximum order of 170 waves could be used before serious numerical difficulties developed. This restriction resulted in a poor fit to the input pattern with only 99.2% of the input pattern power being accounted for. Figure 7 shows the total mode energy vs maximum order for this and also an S-band scattered pattern (Fig. 8). For the latter, an excellent fit was obtained. Figure 8 shows clearly the parallax effect at S-band. In the vicinity of the edge cutoff, the near-field pattern is shifted by approximately 1.3 deg. A spillover analysis of the near- and far-field S-band pattern shows the same spillover results for an angular displacement (relative to a focal point, F , origin) of 2.9 deg. This is in fair agreement with the value of 2.794 deg for $(\Psi_1 - \beta_E)$. An anticipated future effort is to upgrade the spherical wave software so that X-band near-field effects can be accurately analyzed.

The Potter asymmetric shaping/scattering program generates the required asymmetric subreflector surface and then calculates the scattered pattern using two-dimensional numerical integration. By using a symmetric configuration (a special case for the program) and comparing results against the Rusch symmetric scattering program, the required number of integration points was determined. It was determined that the program, which uses the Ludwig integration algorithm (Ref. 10) required 40 polar and 80 azimuthal integration points to reduce errors to a -40 -dB level. This integration grid corresponds to a polar point spacing of 0.6 wavelength and checks with previous studies of the Ludwig algorithm (Ref. 11). The resulting S-band asymmetric scattering run machine time for the Univac 1108 was 27 min (31 polar \times 7 azimuthal observation points). This time amounts to approximately 2 ms per point, which is typical for this type of program on the Univac 1108. The overall result of these tests is that X-band asymmetric scattering runs are not economically feasible.

Figure 9 shows the S-band asymmetric scattered patterns; as expected a certain amount of amplitude asymmetry is present. The degree of the asymmetric effect is determined with the azimuthal Fourier program (see Ref. 12 for a discussion of the theory and application of this method). As with the reflex feed (Ref. 12) the primary contributors to the asymmetry are the $m = 0$ and $m = 2$

components (both approximately -20 dB relative to the desired $m = 1$ component). Figure 10 shows the $m = 1$ component (this component alone contributes to the axial antenna gain) radiation pattern. This pattern turns out to be virtually identical to the pattern of a symmetric shaped system (Fig. 8).

The asymmetric effects introduced by the subreflector (0.1-dB gain/loss) are expected to be essentially frequency independent, since the design is optical. Thus asymmetric X-band performance may be established from a combination of symmetric X-band and asymmetric S-band computations, thereby avoiding the necessity for expensive asymmetric X-band scattering calculations.

Having designed and optimized the system optics for X-band, it remained to optimize the S-band illumination. Figures 11 and 12 show the symmetric S-band far-field scattered patterns for feed apertures scaled up by ratios of 1.25 and 1.50, respectively, from the X-band design. From a rear spillover standpoint, it appears that the 1.25 case is desirable (see Table 2 below).

In the following section the computed performance data are presented.

III. Computed Performance

Table 1 shows the computed performance for the X-band shaped system and for the existing DSS 14 X-band system. In the case of the shaped system amplitude illumination factor, a rather large tolerance is assigned because of the near-field parallax problem discussed above. It is expected that future JPL spherical wave software improvement will enable a more exact calculation of this parameter. The overall result is an X-band gain improvement from shaping of approximately 0.7 dB.

Table 2 shows the computed shaped system performance at S-band for three feed sizes and for the existing DSS 14 standard feed. A shaping improvement of approximately 0.5 dB (aperture ratio 1.25) is predicted.

All of the design optimization and performance evaluation was done for a main reflector diameter of 68 m, which is centered in the study range of 64- to 72-m diameter. Aperture efficiency and spillover performance is expected to be completely insensitive to the diameter. Actual mechanical configurations for each antenna diameter are given in the following section.

IV. Mechanical Configuration

The geometrical configuration parameters are defined in Figs. 1 and 13. Table 3 gives the values for the parameters for the selected four antenna diameters.

V. Conclusions

Using a set of very sophisticated JPL software, detailed shaped antenna designs have been performed for diameters of 64 m, 68 m, 70 m, and 72 m; the associated performance has been computed. Relative to the existing DSS 14 64-m antenna system, X-band forward spillover has been reduced from 5.5% to 1%, rear spillover has been reduced from 0.2% to 0.04%, and aperture efficiency has been increased by 0.7 dB.

At S-band, forward spillover has been reduced from 5.5% to 0.4%, rear spillover has been reduced from 0.3%

to 0.04%, and aperture efficiency has been increased by 0.5 dB.

Complete main reflector/subreflector/feed configuration geometry is presented. The configurations are compatible with the existing tricone system but would require quadripod modification to fit the shaped subreflector.

The performance enhancement data presented here do not include possible reduction of aperture blockage that might be achieved with the required new quadripod design. It is to be noted (Tables 1 and 2) that the existing quadripod aperture efficiency degradation (0.6 dB) is approximately the same as the possible enhancement due to shaping. The quadripod degradation of system noise temperature, expressed in decibels, is several times this large. Thus it appears that an implementation of shaping would logically be combined with a new low-blockage quadripod design.

References

1. Potter, P. D., "Efficient Antenna Systems: Calibration of the Mars Deep Space Station 64-m Antenna System Noise Temperature Degradation Due to Quadripod Scatter", in *The Deep Space Network Progress Report*, Technical Report 32-1526, Vol. XVI, pp. 22-29. Jet Propulsion Laboratory, Pasadena, Calif., Aug. 15, 1973.
2. Potter, P. D., "Antenna Study: Performance Enhancement", in *The Deep Space Network Progress Report*, Technical Report 32-1526, Vol. X, pp. 129-134. Jet Propulsion Laboratory, Pasadena, Calif., Aug. 15, 1972.
3. Galindo, V., *Synthesis of Dual Reflector Antennas*, Report No. 64-22. Electronics Research Laboratory, University of California, Berkeley, Calif., July 1964.
4. Galindo, V., "Design of Dual-Reflector Antennas With Arbitrary Phase and Amplitude Distributions", *IEEE Trans. on Ant. and Prop.*, Vol. AP-12, pp. 403-408, 1964.
5. Williams, W. F., "High Efficiency Antenna Reflector", *Microwave Journal*, pp. 79-82, July 1965.
6. Ludwig, A. C., "Antennas for Space Communication: Shaped Reflector Cassegrainian Antennas", in *Supporting Research and Advanced Development*, Space Programs Summary 37-35, Vol. IV, pp. 266-268. Jet Propulsion Laboratory, Pasadena, Calif., October 31, 1965.
7. Yeh, C., *Arbitrarily Shaped Dual-Reflector Antennas*, Technical Report 32-1503. Jet Propulsion Laboratory, Pasadena, Calif., May 1, 1971.
8. Potter, P. D., "Efficient Antenna Systems: A New Computer Program for the Design and Analysis of High-Performance Conical Feedhorns", in *The Deep Space Network Progress Report*, Technical Report 32-1526, Vol. XIII, pp. 92-107. Jet Propulsion Laboratory, Pasadena, Calif., Feb. 15, 1973.
9. Ludwig, A. C., "Near-Field Far-Field Transformations Using Spherical-Wave Expansions", *IEEE Trans. on Ant. and Prop.*, Vol. AP-19, No. 2, pp. 214-220, Mar. 1971.
10. Ludwig, A. C., "Computation of Radiation Patterns Involving Numerical Double Integration", *IEEE Trans. on Ant. and Prop.*, Vol. AP-16, No. 6, pp. 767-769, Nov. 1968.
11. Brunstein, S. A., Cormack, R. E., and Ludwig, A. C., "Accuracy of Numerically Computed Electromagnetic Scattered Patterns", in *Supporting Research and Advanced Development*, Space Programs Summary 37-52, Vol. III, pp. 233-238. Jet Propulsion Laboratory, Pasadena, Calif., August 1968.
12. Potter, P. D., "S- and X-Band RF Feed System", in *The Deep Space Network Progress Report*, Technical Report 32-1526, Vol. VIII, pp. 53-60. Jet Propulsion Laboratory, Pasadena, Calif., April 15, 1972.
13. Potter, P. D., "S- and X-Band RF Feed System", in *The Deep Space Network Progress Report*, Technical Report 32-1526, Vol. IX, pp. 141-146. Jet Propulsion Laboratory, Pasadena, Calif., June 15, 1972.

Table 1. Computed performance, 8.450 GHz

Factor	Standard feed, 64 m		Shaped system, 68 m	
	Ratio	dB	Ratio	dB
Forward spillover	0.94470	-0.2471	0.98980	-0.0445
Rear spillover	0.99826	-0.0076	0.99965	-0.0015
Nonuniform amplitude illumination	0.84737	-0.7193	0.92965	-0.3168 (± 0.2 dB)
Nonuniform phase illumination	0.97175	-0.1244	0.99337	-0.0289
Cross-polarization	0.99994	-0.0003	1.00000	-0.0000
Energy ($m \neq 1$)	0.99805	-0.0085	0.97808	-0.0963
Central blockage	0.94407	-0.2500	0.96866	-0.1383
Quadripod blockage ^a	0.87498	-0.5800	0.87498	-0.5800
Main reflector/subreflector surface tolerance loss (0.1524 cm rms) ^b	0.74748	-1.2640	0.74748	-1.2640
Total	0.47851	-3.2012	$0.56620 \pm .025$	-2.4703 ± 0.2
Gain for 100% efficiency	3.211676×10^7	+75.0673	3.625681×10^7	+75.5939
Gain	1.536819×10^7	+71.8661	2.052860×10^7 $\pm .097 \times 10^7$	$+73.1236 \pm 0.2$

^aPossible small change with illumination and quadripod modification unknown.

^bPossible small change with illumination, and subreflector change and diameter increase unknown.

Table 2. Computed performance, 2.295 GHz

Factor	Standard feed, 64 m ^a		Shaped feed, 68 m					
	Ratio	dB	Relative aperture size, 1.00 ^b		Relative aperture size, 1.25 ^b		Relative aperture size, 1.50 ^b	
			Ratio	dB	Ratio	dB	Ratio	dB
Forward spillover	0.94470	-0.2471	0.98980	-0.0445	0.99602	-0.0173	0.99846	-0.0067
Rear spillover	0.99738	-0.0114	0.99718	-0.0123	0.99957	-0.0019	0.99929	-0.0031
Nonuniform amplitude illumination	0.84207	-0.7465	0.96157	-0.1702	0.89165	-0.4980	0.83234	-0.7970
Nonuniform phase illumination	0.97999	-0.0878	0.98305	-0.0742	0.96358	-0.1611	0.97154	-0.1254
Cross-polarization	0.99982	-0.0008	1.00000	-0.0000	1.00000	-0.0000	1.00000	-0.0000
Energy ($m \neq 1$)	0.99805 ^c	-0.0085 ^c	0.97808 ^c	-0.0963 ^c	0.98741 ^d	-0.0550 ^d	0.99369 ^d	-0.0275 ^d
Central blockage	0.94148	-0.2619	0.97009	-0.1319	0.96140	-0.1710	0.95271	-0.2104
Quadripod blockage ^e	0.87498	-0.5800	0.87498	-0.5800	0.87498	-0.5800	0.87498	-0.5800
Main reflector/subreflector surface tolerance loss (0.1524 cm rms) ^f	0.97876	-0.0932	0.97876	-0.0932	0.97876	-0.0932	0.97876	-0.0932
Total	0.62557	-2.0372	0.75812	-1.2026	0.69541	-1.5775	0.65414	-1.8433
Gain for 100% efficiency	2.366795×10^6	+63.7416	2.671890×10^6	+64.2682	2.671890×10^6	+64.2682	2.671890×10^6	+64.2682
Gain	1.480608×10^6	+61.7044	2.025613×10^6	+63.0656	1.858059×10^6	+62.6907	1.747790×10^6	+62.4249

^aFrom Ref. 13.^bFeed wavelength aperture size relative to 8.450 GHz shaped system.^cComputed.^dEstimated.^ePossible small change with illumination and quadripod illumination unknown.^fPossible small change with illumination, subreflector change and diameter increase unknown.

Table 3. Geometrical parameters

Parameter value	<i>D</i> MAIN = 64 m	<i>D</i> MAIN = 68 m	<i>D</i> MAIN = 70 m	<i>D</i> MAIN = 72 m
<i>X</i> MAX, cm	3029.003 (1192.521 in.)	3283.151 (1292.579 in.)	3320.186 (1307.160 in.)	3417.245 (1345.372 in.)
<i>Y</i> MAX, cm	846.099 (333.110 in.)	994.039 (391.354 in.)	1016.591 (400.233 in.)	1076.898 (423.975 in.)
<i>A</i> , cm	-497.383 (-195.820 in.)	-349.674 (-137.667 in.)	-327.119 (-128.787 in.)	-266.611 (-104.965 in.)
β_g , deg	55.4327	59.5972	60.1938	61.7299
<i>Z</i> ₀₂ , cm	1265.959 (498.409 in.)	1273.589 (501.413 in.)	1274.361 (501.717 in.)	1277.252 (502.855 in.)
RADIUS 1, cm	293.779 (115.661 in.)	292.930 (115.327 in.)	292.875 (115.305 in.)	292.410 (115.122 in.)
RADIUS 2, cm	321.940 (126.748 in.)	323.553 (127.383 in.)	323.875 (127.510 in.)	324.330 (127.689 in.)
ΔZ_1 , cm	121.158 (47.700 in.)	131.282 (51.686 in.)	132.837 (52.298 in.)	136.512 (53.745 in.)
ΔZ_2 , cm	101.755 (40.061 in.)	113.314 (44.612 in.)	115.080 (45.307 in.)	119.344 (46.986 in.)

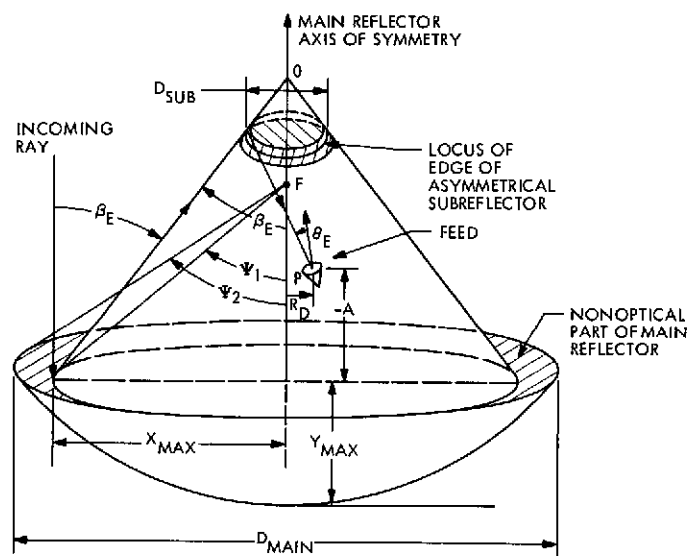
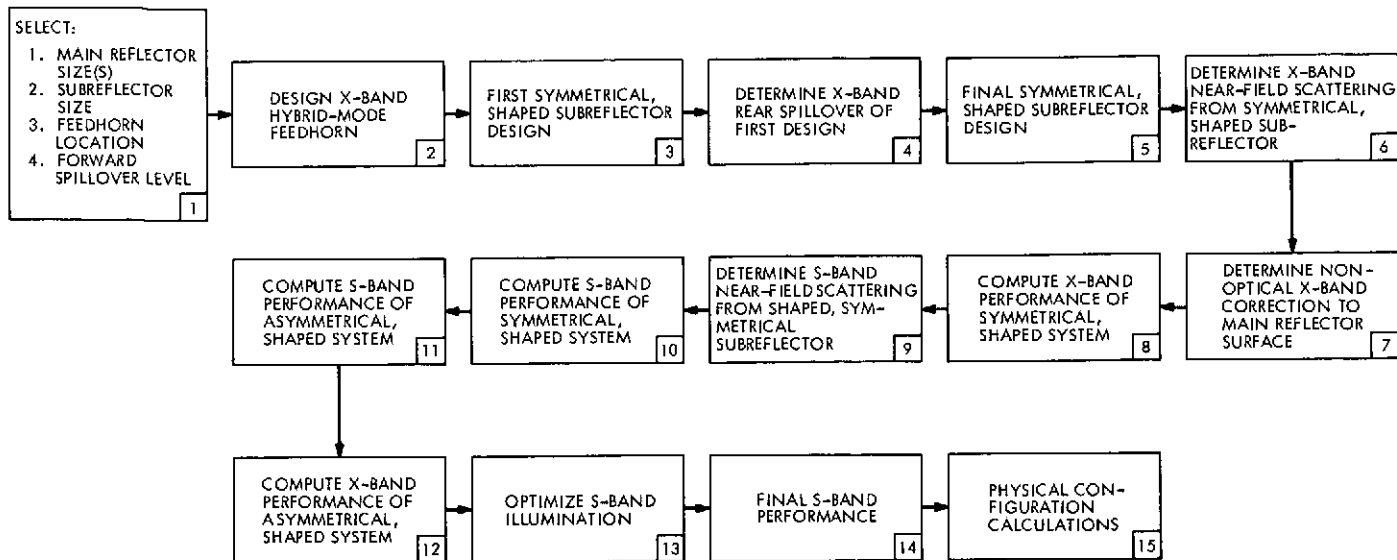


Fig. 1. Asymmetric, shaped antenna system geometry

(a)



(b)

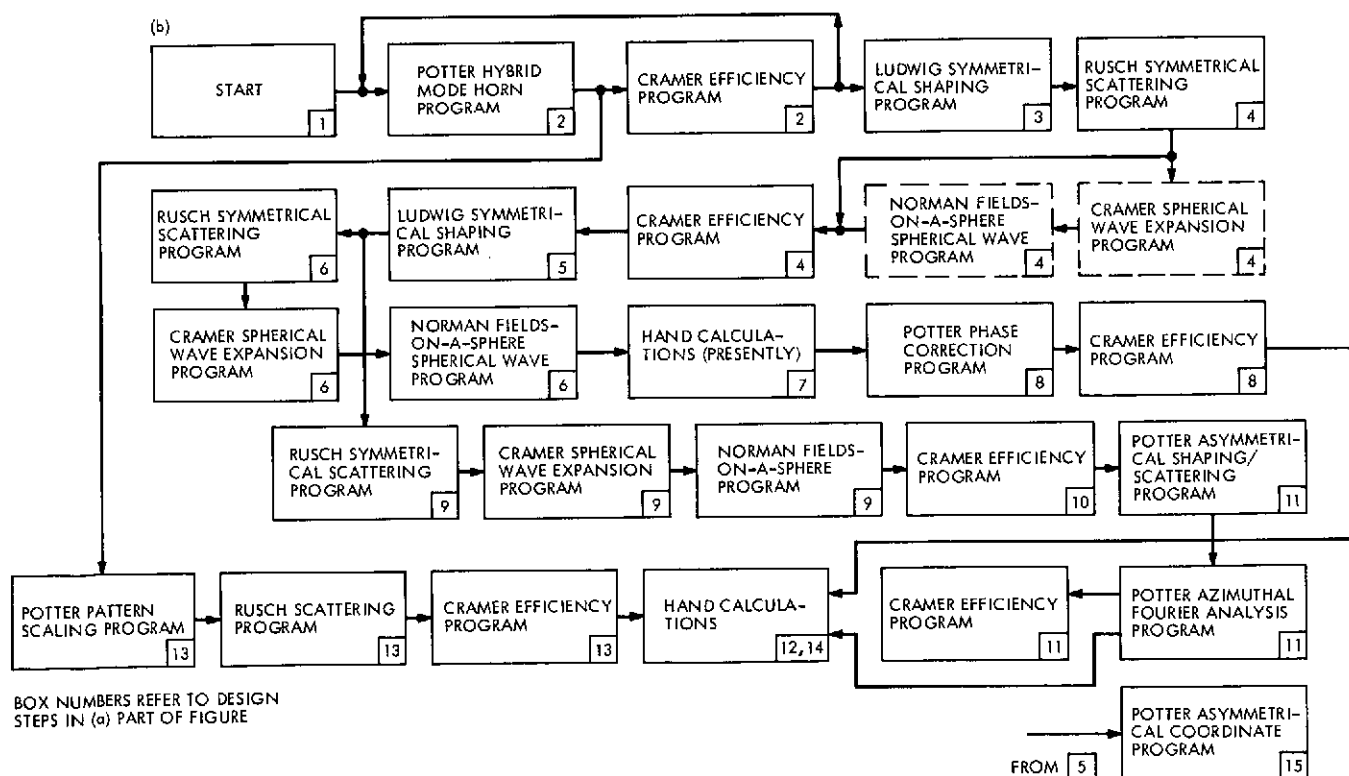


Fig. 2. Multifrequency asymmetrical antenna system design; (a) procedure, (b) computational method

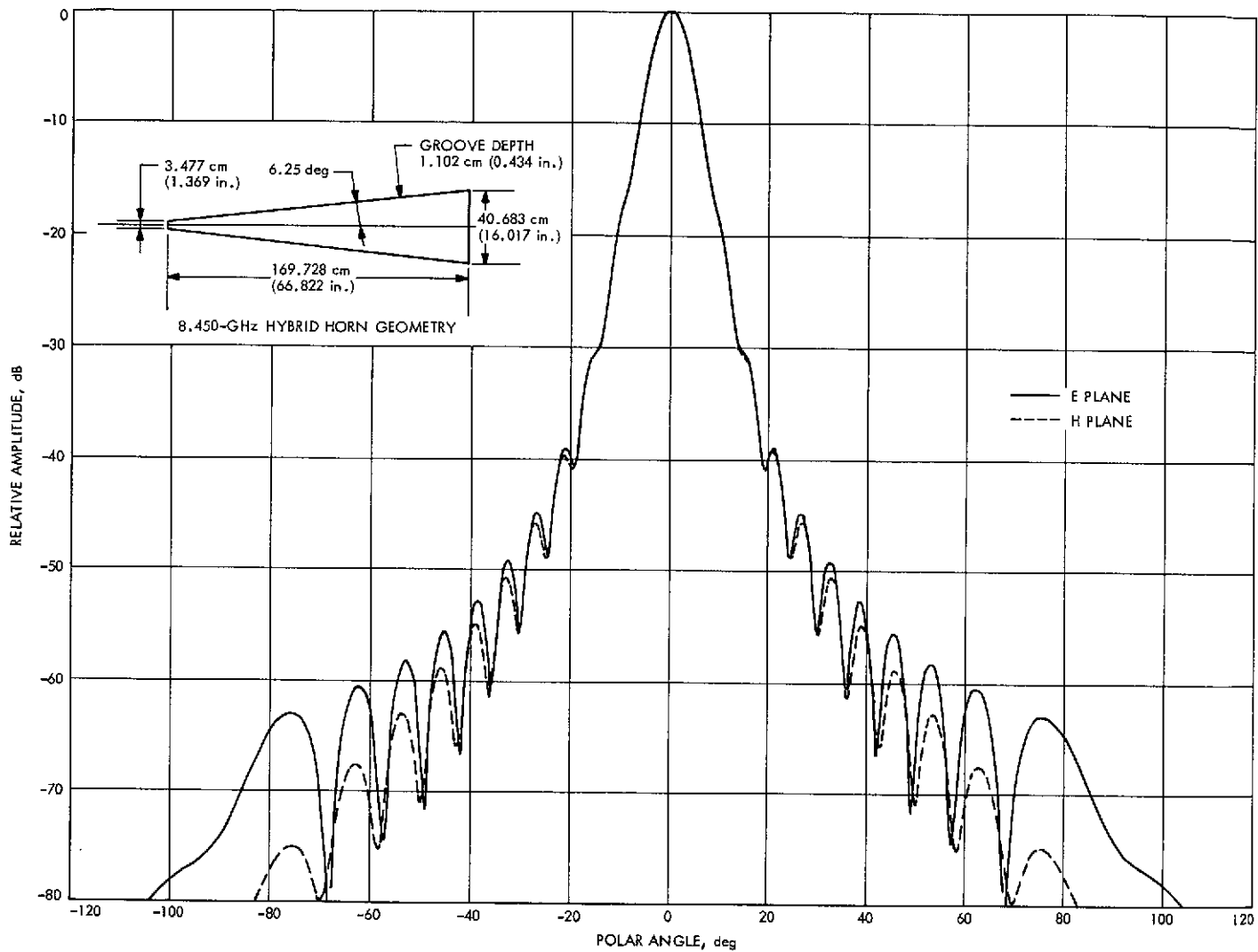


Fig. 3. Hybrid mode feedhorn radiation pattern

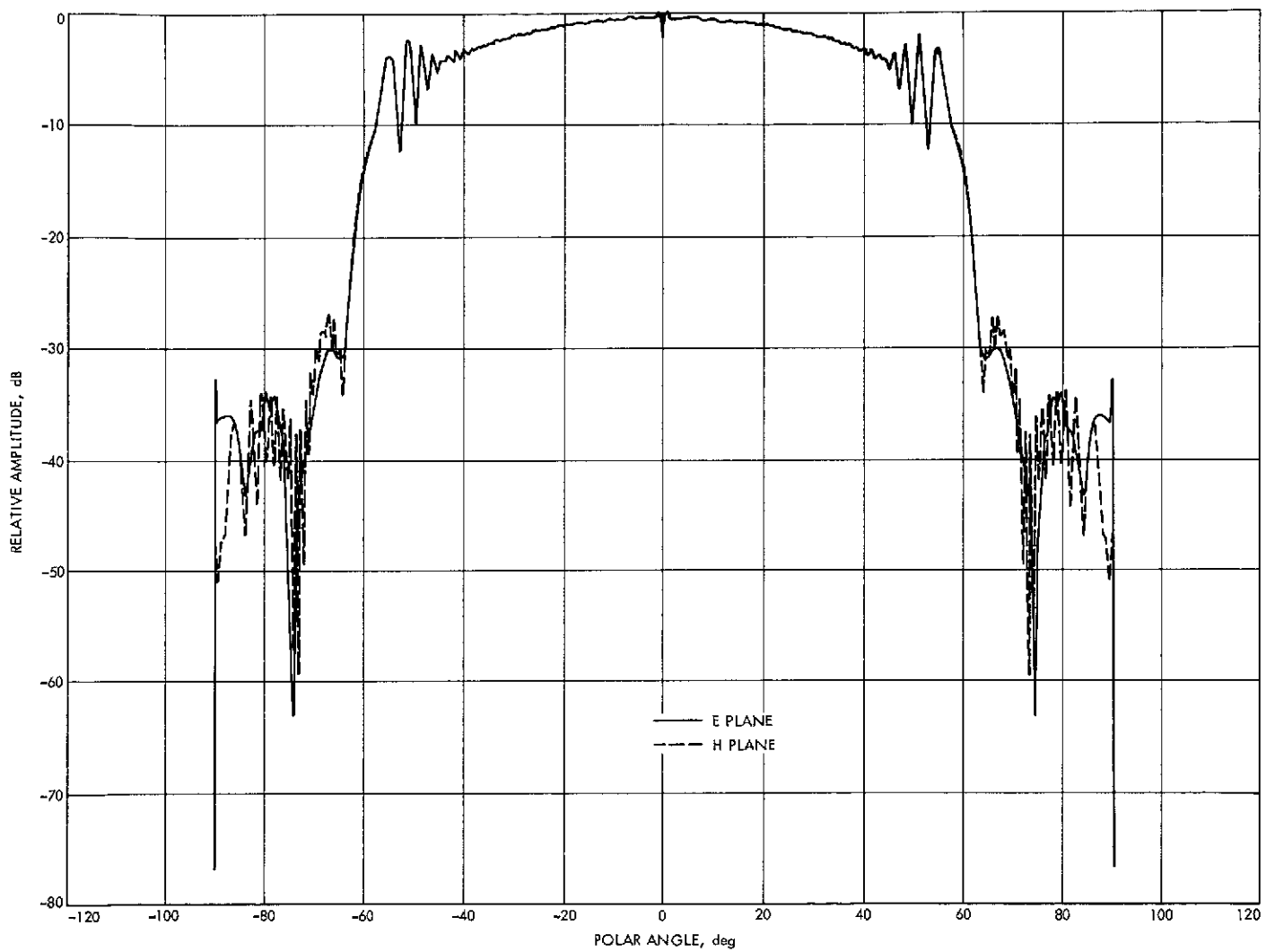


Fig. 4. 8.450-GHz scattered pattern for symmetrical equivalent to existing 64-m antenna feed

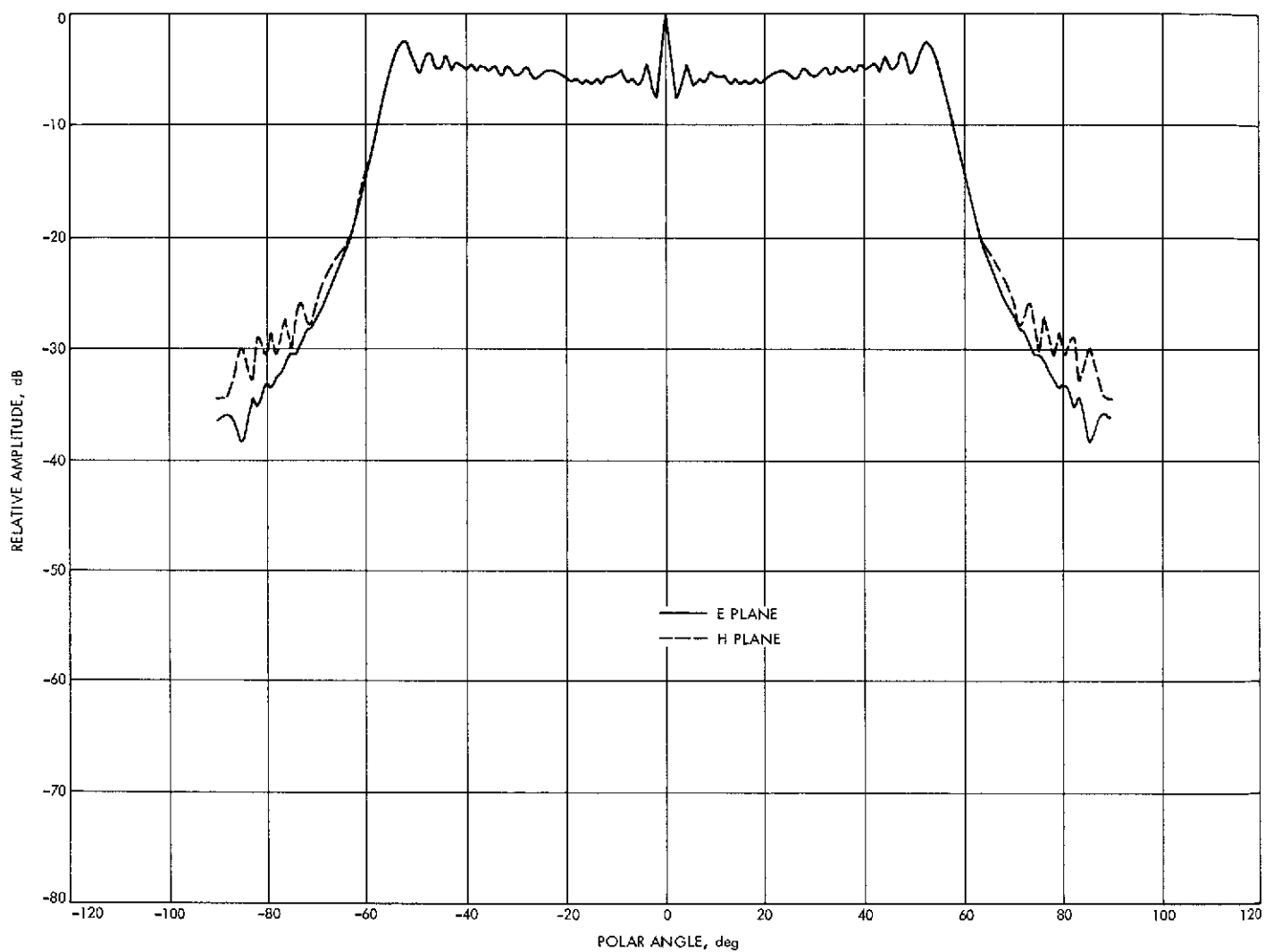


Fig. 5. 8.450-GHz uniform illumination test case

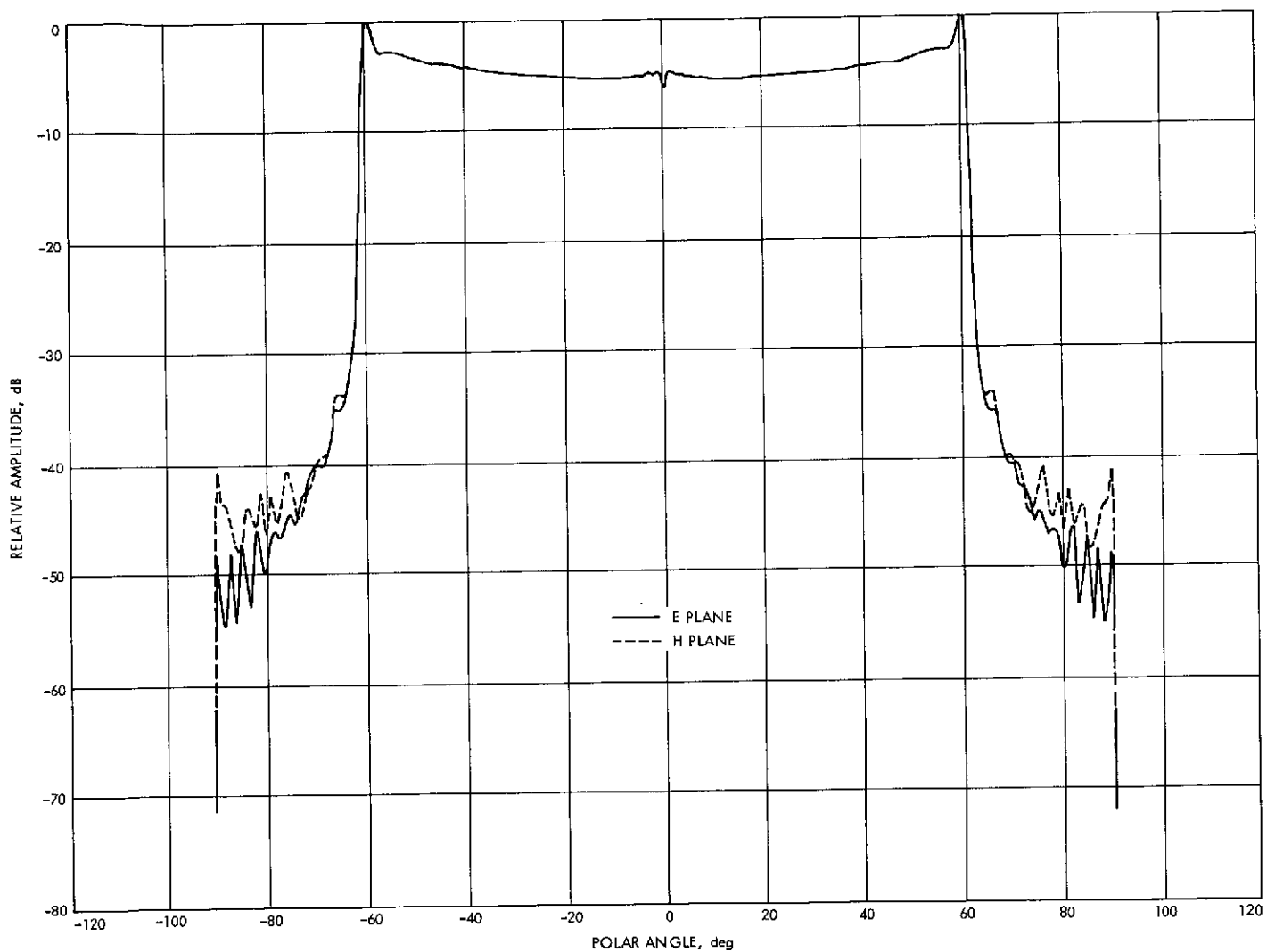


Fig. 6. Shaped system 8.450-GHz far-field radiation pattern

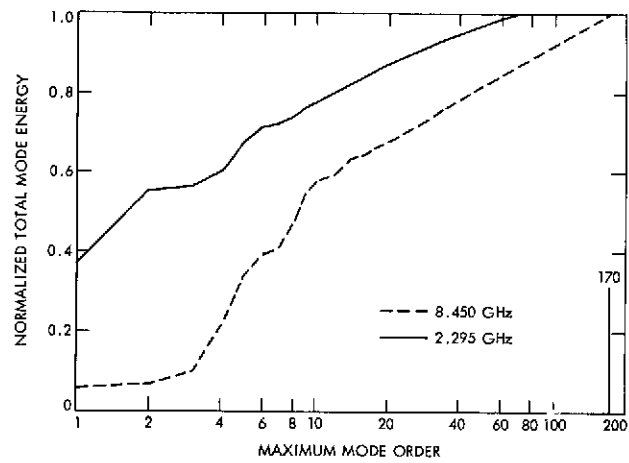


Fig. 7. Spherical wave expansion total mode energy vs maximum mode order

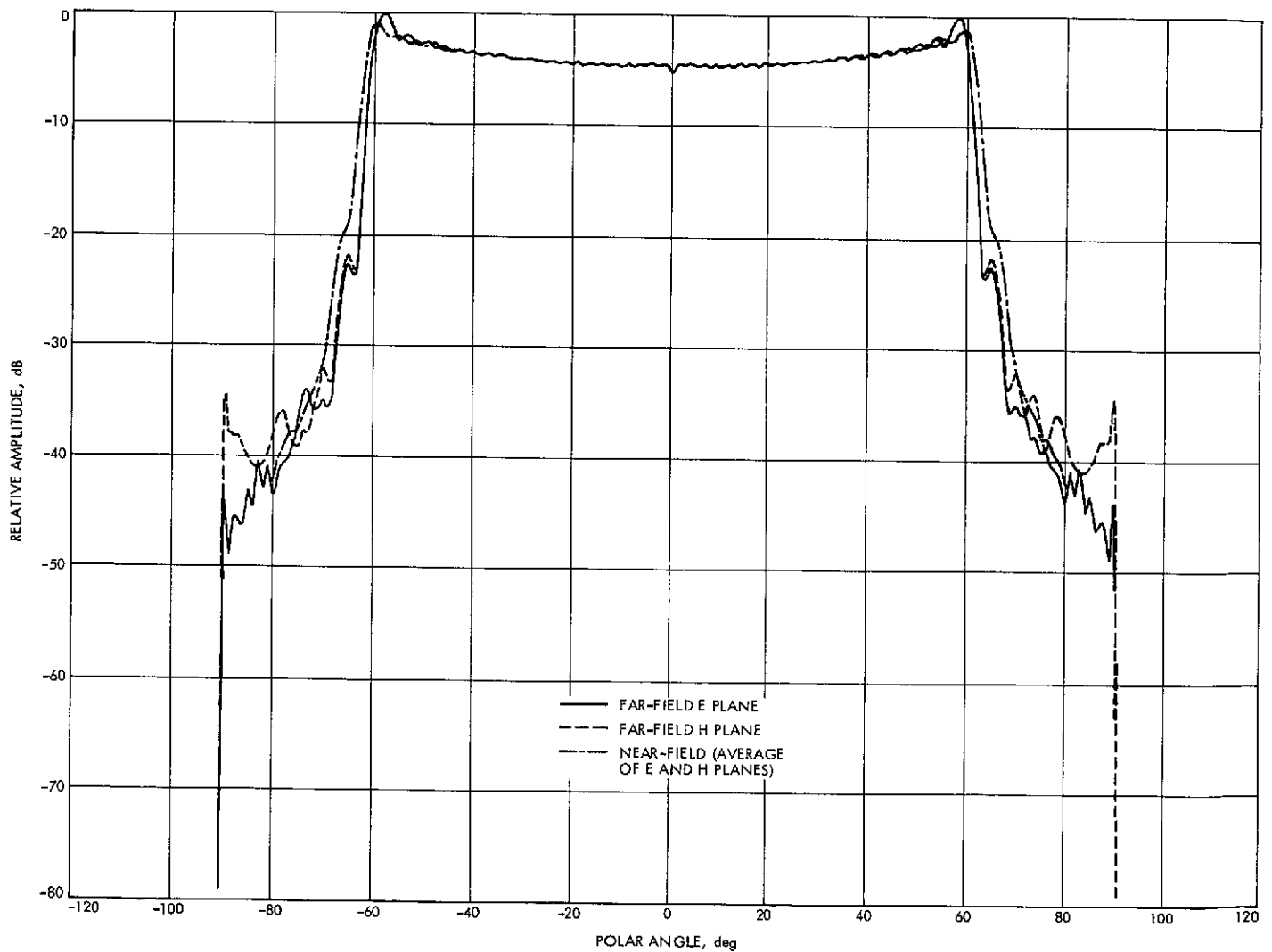


Fig. 8. Near and far-field 2.295-GHz shaped system radiation patterns

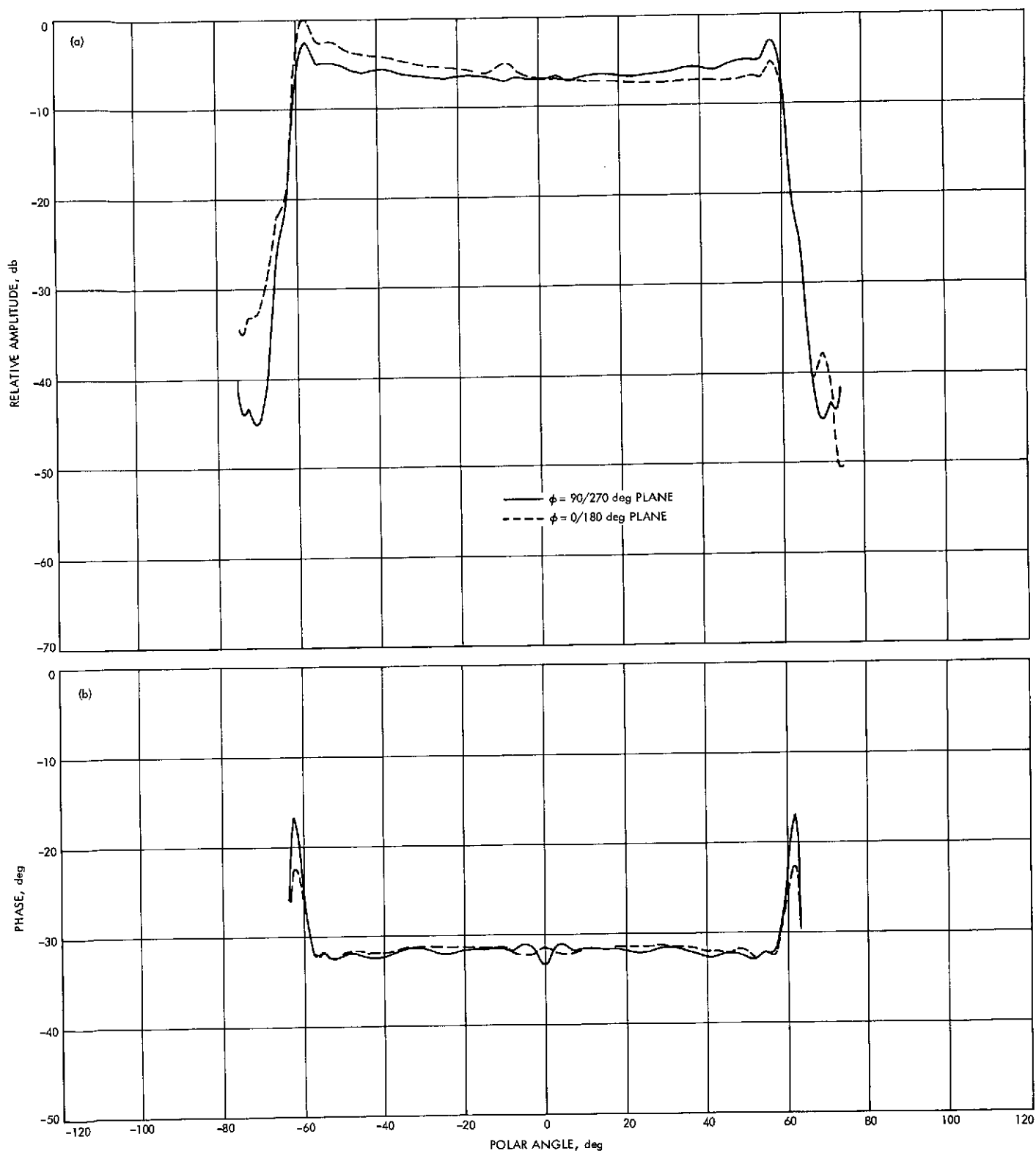


Fig. 9. 2.295-GHz asymmetric, shaped system radiation patterns; (a) amplitude, (b) phase

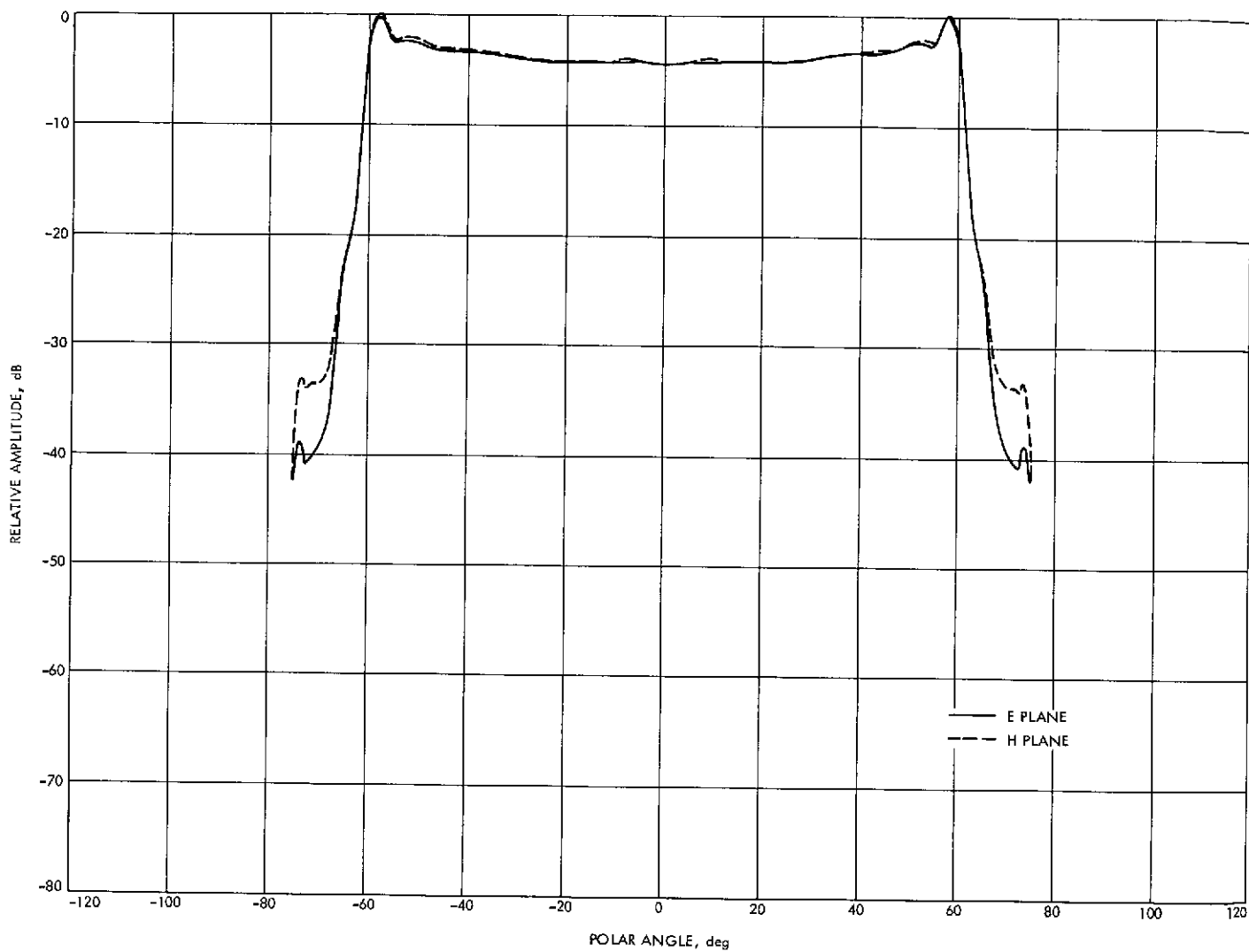


Fig. 10. 2.295-GHz ($m = 1$) component of asymmetric, shaped system radiation patterns

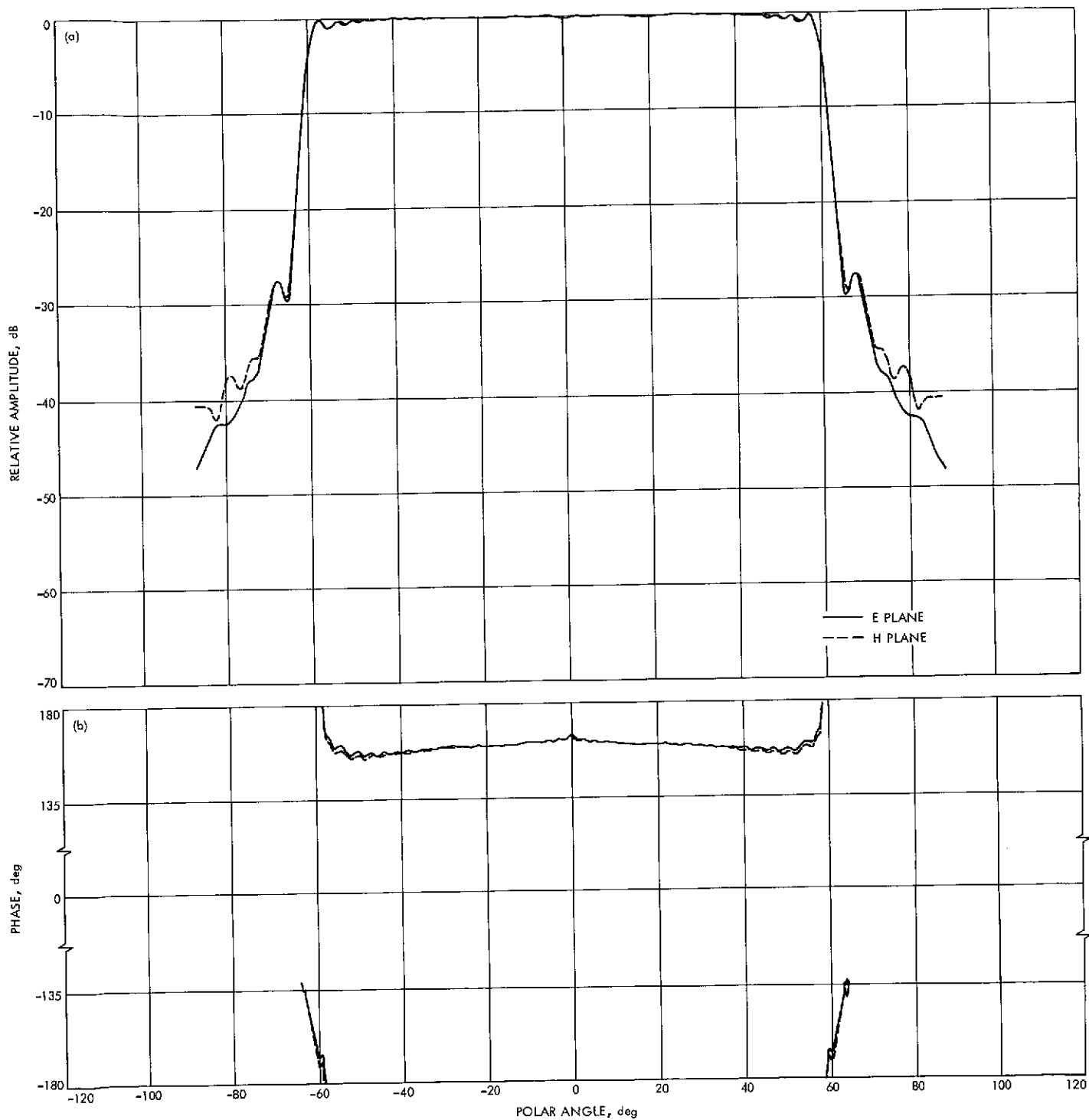


Fig. 11. 2.295-GHz symmetric, shaped system with illuminating aperture scaled by 1.25; (a) amplitude, (b) phase

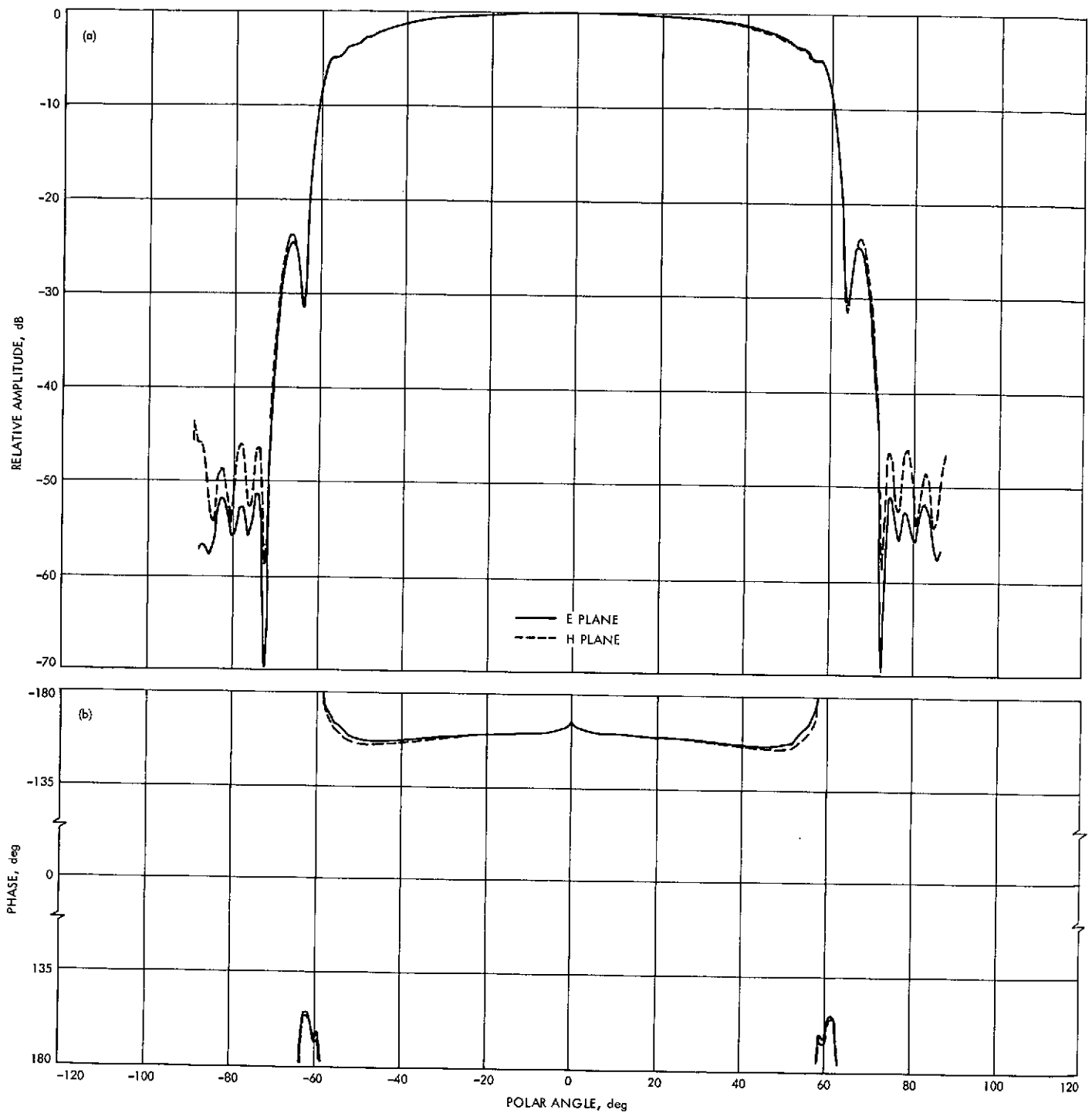


Fig. 12. 2.295-GHz symmetric, shaped system with illuminating aperture scaled by 1.50; (a) amplitude, (b) phase

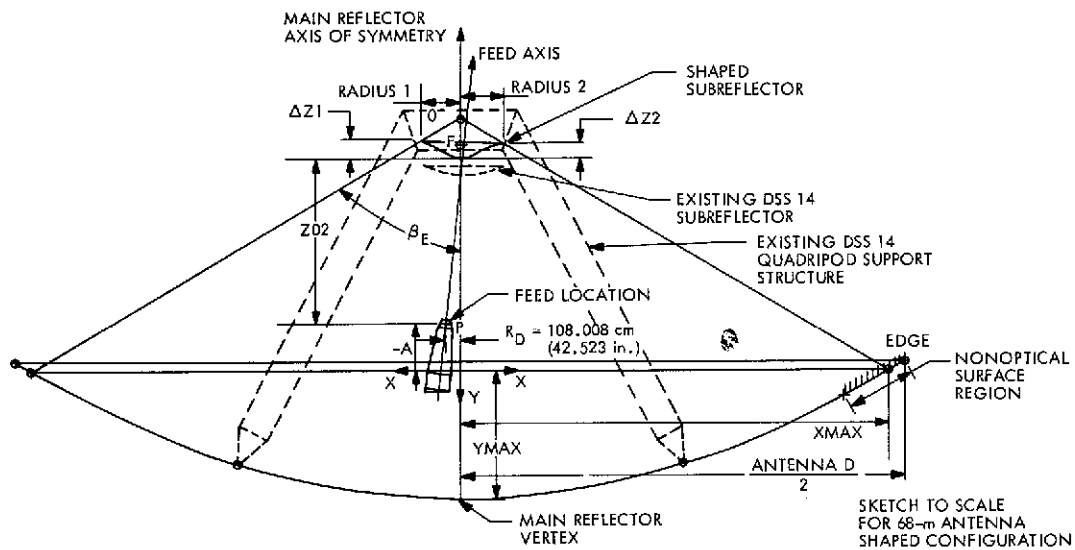


Fig. 13. Shaped antenna mechanical configuration

Antenna Bias Rigging for Mission-Dependent Performance Objective

R. Levy
DSN Engineering Section

A procedure is described for computation of the optimum paraboloidal antenna rigging angle to minimize the expected average mean square half pathlength surface deviations for gravity loading. Statistics of deep space planetary missions are employed to develop weighting factors for antenna elevation angles during these missions. Comparisons for the existing Mars Deep Space Station antenna show that average gain losses from gravity loading can be reduced by 15 to 30 percent for this antenna by using the optimal rigging angle of approximately 35 degrees rather than the current rigging angle of 45 degrees.

I. Introduction

Bias rigging is a method of optimizing the performance characteristics of the surface-supporting structure of a paraboloidal radio-frequency (RF) transmitting and receiving antenna reflector. The approach is to set the reflecting surface panels to an ideal paraboloid at some particular elevation rigging angle, intermediate between horizon and zenith pointing attitudes. This can provide a built-in bias to improve accuracy of the reflecting surface with respect to the adverse effects of structural deformations. In particular, loss of accuracy from deformations caused by variable gravity loading over the elevation attitude range can be reduced.

An antenna-reflector system, such as shown in Fig. 1, is used extensively in communications, space exploration, and radio astronomy. The function of the reflecting surface during a receiving cycle is to collect RF energy emanating from a distant source and redirect this to a focal collection point or subreflector. A converse function is performed during a transmitting cycle.

During operation, deviations of the reflecting surface from an ideal paraboloid cause losses in performance efficiency from pathlength changes and undesirable phase shifts within the energy beam. These deviations are the result of tolerance accumulation from manufacture and installation, or are the result of response of the

structure to environmental loading. Tolerance accumulation deviations can often be effectively controlled by current manufacturing, inspection, and quality assurance techniques. Consequently, the loading deformations from the effects of gravity, wind, temperature, and shock are more significant. Of these loadings, the gravity loading, which is both omnipresent and deterministic, tends to have the most adverse effect upon performance. Consequently, control of the gravity loading deformations is a logical and feasible approach to improve performance reliability. In addition to the intensity of loading, the deformations also depend upon properties of the supporting structure. Compared to comprehensive procedures that can develop the design of the supporting structure (Refs. 1, 2), bias-rigging is a simple procedure that can be readily implemented to help achieve this control.

II. Antenna Surface Performance Efficiency

A convenient measure of antenna surface accuracy is given by Ruze's conventional (Ref. 3) efficiency equation that relates surface accuracy to RF wavelength as

$$e = \exp[-(4\pi \text{rms}/\lambda)^2] \quad (1)$$

in which e is the efficiency of the surface, λ is the wavelength, and rms is the square root of the mean square half pathlength deviation of the reflecting surface from a best-fitting ideal paraboloid. The gain-loss can be computed in decibels from Eq. 1 as

$$G_r = 10 \log_{10} e \quad (2)$$

When the antenna is subjected to gravity loading, the rms term to be used in Eq. 1 is a function of the particular elevation angle attitude at which the antenna is pointing. In Ref. 4, it was shown that the mean square half pathlength deviation, SS_a at elevation angle α can be determined from

$$SS_a = \eta^2 SSY + \zeta^2 SSZ + 2\eta\zeta SYZ \quad (3)$$

and the rms half pathlength deviation is

$$(\text{rms}_a) = (SS_a)^{1/2} \quad (4)$$

In Eq. 3, SSY and SSZ are the mean square half pathlength deviations for gravity loading applied parallel to the respective Y and Z axes shown in Fig. 1, and SYZ is

the mean inner product of the corresponding half pathlength deviation vectors. The loading coefficients η , ζ , depend upon the elevation angle α and the rigging angle γ and are given by

$$\begin{aligned} \eta &= \cos \gamma - \cos \alpha \\ \zeta &= \sin \gamma - \sin \alpha \end{aligned} \quad (5)$$

The polar plot in Fig. 2 illustrates an example pattern of the change in the rms half pathlength deviation over the elevation attitude range. The deviation can be seen to be zero at the rigging attitude (rms_γ) and to have extreme values at the horizon (rms_0) and zenith (rms_{90}) attitudes. It can be observed from this figure that choice of rigging angle can have a significant effect on the performance of the antenna.

Relationships were discussed in Refs. 4 and 5 that considered either the minimization of the extreme rms pathlength deviations over the elevation range, or minimization of the expected average pathlength deviations for antennas that track targets uniformly distributed within the hemisphere above the horizon. Here we will consider bias rigging to minimize the expected average pathlength deviations for an antenna that is required to track missions of a collection of planets with known orbits.

III. Selection of Rigging Angle for Mission-Weighted Elevation Angle Usage Factors

Assume that the projected tracking mission of the antenna is known so that it is possible to determine the elevation angle time history for the antenna for a particular mission or the average time history for a collection of missions. The elevation angle weighting factor W_a can be developed to supply the probability of antenna targets occurring at elevation angle α . A set of weighting factors is developed by dividing the elevation angle range into a set of elevation class marks equally spaced at some constant class interval. Consequently the weighting factors represent the probability of antenna targets occurring at elevations within the class interval centered on particular class marks. When the class marks are closely spaced, and with appropriate normalization of the weighting factors, the elevation angle probability density function is approximately equal to the weighting factor divided by the class interval. In this case it follows that

$$\sum W_a = 1.00 \quad (6)$$

Optimum performance for a particular antenna with respect to the mission elevation angle weighting is obtained by choosing the rigging angle to minimize the elevation-weighted mean square half pathlength deviations. In particular, from Eq. (3), we choose γ to minimize the objective expression

$$OBJ = \sum_a W_a (\eta^2 SSY + \zeta^2 SSZ + 2\eta\zeta SYZ) \quad (7)$$

This objective represents the expected average mean square half pathlength deviation. Substituting Eqs. (5) in (7), expanding, using Eq. (6), and simplifying leads to the objective in the following form:

$$OBJ = A^2 SSY + B^2 SSZ + 2C SYZ \quad (8)$$

where

$$A^2 = \cos^2 \gamma + \sum W_a \cos^2 \alpha - 2 \cos \gamma \sum W_a \cos \alpha$$

$$B^2 = \sin^2 \gamma + \sum W_a \sin^2 \alpha - 2 \sin \gamma \sum W_a \sin \alpha$$

$$C = \sin \gamma \cos \gamma + \sum W_a \sin \alpha \cos \alpha - \cos \gamma \sum W_a \sin \alpha - \sin \gamma \sum W_a \cos \alpha$$

Although there are methods of numerical analysis for choosing to minimize the objective in Eq. 8, a simple and stable method is to consider this as a problem of operations research and use a search method (Ref. 6). Standard subroutines¹ can execute the search rapidly and furnish the optimum rigging angle with any desired precision.

IV. Computation of Elevation Angle Mission Weights

The weighting factor is computed as proportional to the amount of time in a given period that the antenna elevation angle is within the particular class interval. For convenience, we consider an annual period of 365 days. The time in hours is 1/15 of the difference of hour angle (in degrees) of the target in passing through the lower and upper elevation class mark boundaries. The hour angle H is a function of latitude of the site ϕ , the declination angle of the target δ , and the elevation angle α . From spherical trigonometry

$$H = \cos^{-1} \frac{(\sin \alpha - \sin \phi \sin \delta)}{\cos \phi \cos \delta} \quad (9)$$

¹See, for example, Subroutine FIBMIN, coded by C. L. Lawson, JPL, Sect. 914

Eq. (9) can be solved for the maximum elevation α_{\max} at a particular declination, which occurs at 0 degree hour angle, thus

$$\alpha_{\max} = \sin^{-1} (\cos(\phi - \delta)) \quad (10)$$

On a given day, assume that the target's declination δ_j is approximately constant. The tracking time t_j on this day is twice the time interval in following the target from the minimum operational elevation angle α_{\min} to the maximum elevation angle given by Eq. (10). Therefore

$$t_j = 2/15 H(\alpha_{\min}, \phi, \delta_j) \quad (11)$$

If analysis has been made of the missions to be considered and declination angle weighting factors D_j have been established to give the probability of target declinations being within declination class marks δ_j , the annual hours T_j at this declination class mark are

$$T_j = 365 D_j t_j \quad (12)$$

At declination class mark δ_j targets will be encountered at elevation class marks between α_{\min} and α_{\max} . The daily time t_{ij} spent in tracking at elevation class mark α_i with upper and lower class mark boundaries a_i and b_i , respectively, is

$$t_{ij} = 2/15 (H(\alpha_i, \phi, \delta_j) - H(b_i, \phi, \delta_j)) \quad (13)$$

On a 365-day basis, declination class mark δ_j contributes the following tracking time hours to elevation class mark α_i

$$T_{ij} = 365 t_{ij} D_j \quad (14)$$

and the total tracking time T_i at this elevation class mark is the sum of the contributions from all declination class marks. That is

$$T_i = \sum_j T_{ij} \quad (15)$$

Finally, the normalized elevation angle mission-weighting factor is

$$W_i = T_i / \sum T_i \quad (16)$$

As a check, compare Eq. (14) with Eq. (12)

$$\sum_i T_{ij} = T_j \quad (17)$$

V. Mission-Weighted Declination Angles

In Ref. 7 an analysis has been made of the most significant NASA-JPL deep space planetary mission tracking orbits to determine composite declination angle weighting factors for missions in the time period from 1973 to 1981. Three mission categories of declination angle weighting factors have been developed for declinations spaced at one degree class intervals from -50 to $+50$ deg. The mission categories are

- (1) Approved Missions
 - Pioneer 6-9
 - Pioneer 10
 - Pioneer 11
 - Mariner Venus/Mercury
 - Helios A and B
 - Mars Viking 1 and 2
 - Mariner Jupiter/Saturn
- (2) Projected Missions
 - Pioneer Venus Probe
 - Pioneer Venus Orbiter
 - Pioneer Saturn Probe
 - Mariner Jupiter/Uranus 1 and 2
 - Pioneer Saturn/Uranus FB
 - Pioneer Saturn/Uranus Probe
 - Mars Viking
 - Mariner Jupiter Orbiter
 - Pioneer H
- (3) Combined Approved and Projected Missions

For comparison, a fourth category has been established, which is equivalent to a solar mission. That is, the mission target is the Sun. In this case, the declination is given by

$$\delta = 23.5 \sin(2\pi d/365) \quad (18)$$

in which d is the number of days from the vernal equinox. In this case the declination probability density function, which is approximately equivalent to the declination angle weighting factor for a one degree class interval declination angle is given by

$$f(\delta) = \frac{1}{23.5\pi [1 - (\delta/23.5)^2]^{1/2}} \quad (19)$$

for $|\delta| < 23.5$.

VI. Results and Discussion

Figure 3a shows the declination angle probability density functions for the approved and the projected missions. Figure 3b shows these functions for the combined and the solar missions. The two curves in Fig. 3b exhibit considerable differences, but the combined mission curve in Figure 3b tends to follow the solar mission curve within a reasonable amount of oscillation.

The corresponding elevation angle probability density curves are shown in Figs. 4a and 4b. Again there are differences in the curves of Fig. 4a, while the combined and solar mission curves of Fig. 4b are reasonably similar. These elevation angle probability density curves were computed for the following parameters:

$$\phi = 35.4 \text{ deg (latitude of Goldstone, Calif.)}$$

$$\text{Elevation class interval} = 2.5 \text{ deg}$$

$$\text{Minimum tracking elevation} = 6.0 \text{ deg}$$

$$\text{Maximum tracking elevation cut-off (overrides } \alpha_{\max}) = 88.0 \text{ deg}$$

Table 1 shows the statistics of the elevation weighting factors that are used for computation of antenna rigging angles. Figure 5 is a plot of gain/loss versus antenna elevation angle for the DSN 64-m Mars antenna. The elevation weighting factors used were for combined missions. One curve is for the optimum rigging angle of 35.4 deg computed according to the procedure given here and the other curve is for the same antenna with the current 45 -deg rigging angle. Table 2 is a summary of results obtained for this antenna for all mission categories comparing optimum rigging with the existing 45 -deg rigging angle.

It can be noted from the last line in Table 2 that, although the expected average gain loss for this antenna is relatively small for all mission categories, the optimal rigging angle results in gain losses of from 15 to 30 percent less than the gain loss with 45 deg rigging. It can also be observed from Fig. 5 that the relatively higher gain losses with optimal rigging, which occur at the elevation angles close to the zenith attitude, occur with low probability (weighting factor).

References

1. Levy, R., "Iterative Design of Antenna Structures," in *The Deep Space Network Progress Report*, Technical Report 32-1526, Vol. XII, pp. 100-111, Jet Propulsion Laboratory, Pasadena, Calif., Dec. 15, 1972.
2. Levy, R., and Melosh, R., "Computer Design of Antenna Reflectors," *J. Struct Div.*, ASCE, Vol. 99, No. ST11, Nov. 1973, pp. 2269-2285.
3. Ruze, J., "Antenna Tolerance Theory—A Review," *Proc. IEEE*, Vol. 54, No. 4, April 1966, pp. 633-640.
4. Levy, R., "A Method for Selecting Antenna Rigging Angles to Improve Performance," in *The Deep Space Network*, Space Programs Summary 37-65, Vol. II, pp. 72-76, Jet Propulsion Laboratory, Pasadena, Calif., Sept. 1970.
5. Levy, R., "Antenna Rigging Angle Optimization Within Structural Member Size Design Optimization," in *The Deep Space Network Progress Report*, Technical Report 32-1526, Vol. I, pp. 81-87, Jet Propulsion Laboratory, Pasadena, Calif., Feb. 15, 1971.
6. Wilde, D. J., *Optimum Seeking Methods*, Prentice-Hall, Inc., Englewood Cliffs, N.J., 1964.
7. Khatib, A. R., JPL Interoffice Memorandum 392.1-3-ARK, Dec. 11, 1973 (JPL internal document).

Table 1. Mission-weighted elevation angle statistics

	Weighting factor			
	Approved missions	Projected missions	Combined missions	Solar missions
ΣW_a	1.0000	1.0000	1.0000	1.0000
$\Sigma W_a \sin^2 \alpha$	0.3886	0.3334	0.3755	0.3641
$\Sigma W_a \cos^2 \alpha$	0.6114	0.6666	0.6245	0.6358
$\Sigma W_a \sin \alpha$	0.5712	0.5282	0.5610	0.5526
$\Sigma W_a \cos \alpha$	0.7523	0.7937	0.7621	0.7717
$\Sigma W_a \sin \alpha \cos \alpha$	0.3796	0.3778	0.3791	0.3805
Average annual tracking hours				
	4112	3857	4056	3996

Table 2. Comparison for existing Mars antenna

	Approved missions		Projected missions		Combined missions		Solar missions	
	Optimum	Existing	Optimum	Existing	Optimum	Existing	Optimum	Existing
Rigging angle, deg	36.2	45.0	32.8	45.0	35.4	45.0	34.7	45.0
Expected average gain loss for mission, dB at X-Band (= 8.45 GHz)	0.0347	0.0418	0.0296	0.0434	0.0337	0.0421	0.0322	0.0420
Relative gain loss, percent	83	100	68	100	80	100	77	100
SSZ mm ² (in. ²) = 0.760(0.001176)								
SSY mm ² (in. ²) = 0.393(0.000610)								
SYZ mm ² (in. ²) = 0.030(0.000046)								

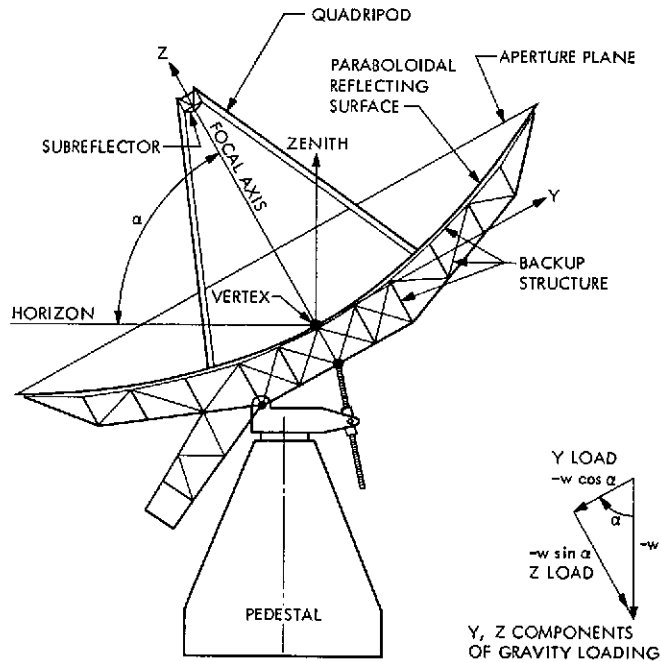


Fig. 1. Antenna-reflector system

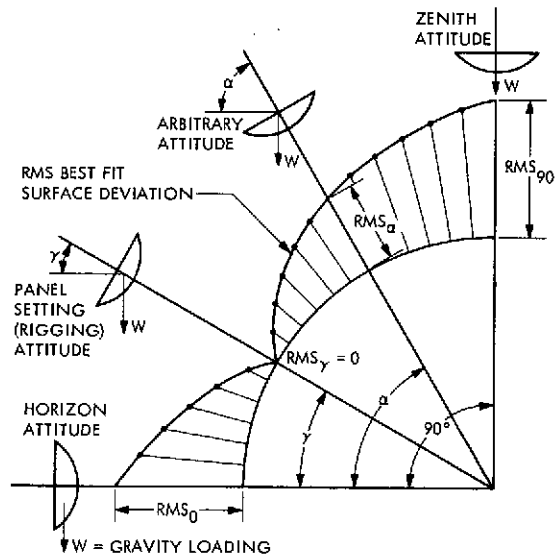


Fig. 2. RMS deviation change with elevation angle

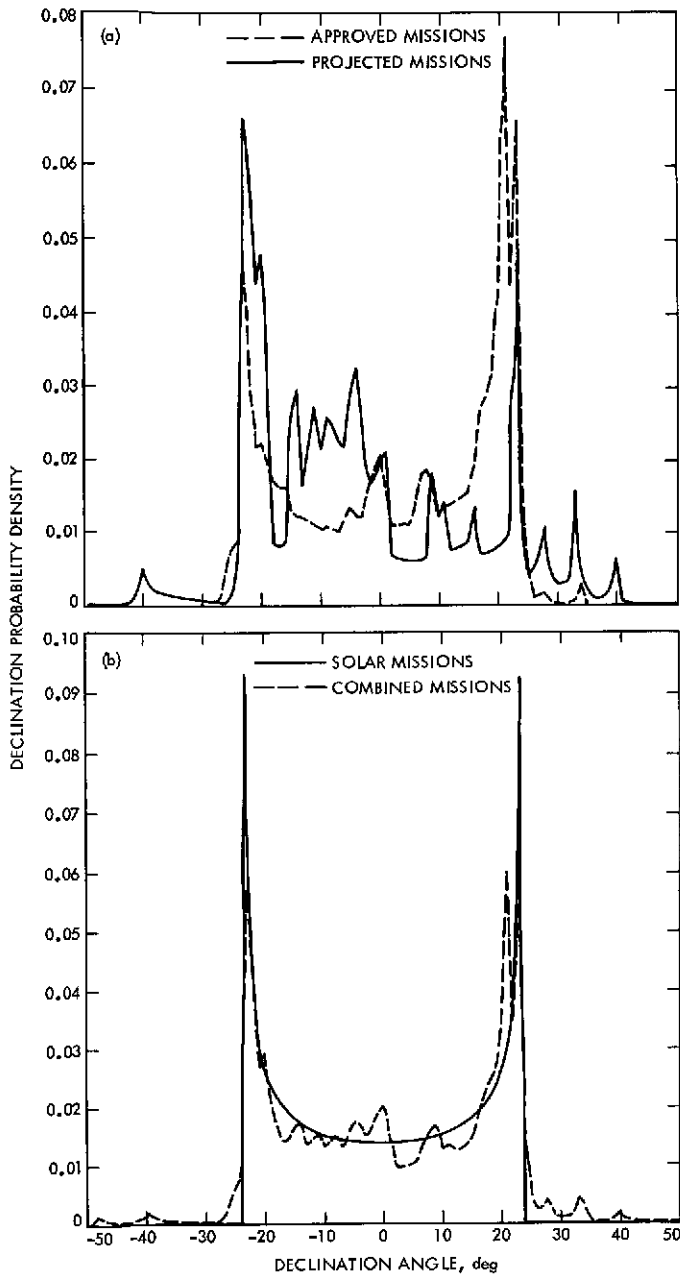


Fig. 3. Declination angle probability density: (a) approved and projected missions, (b) solar and combined missions

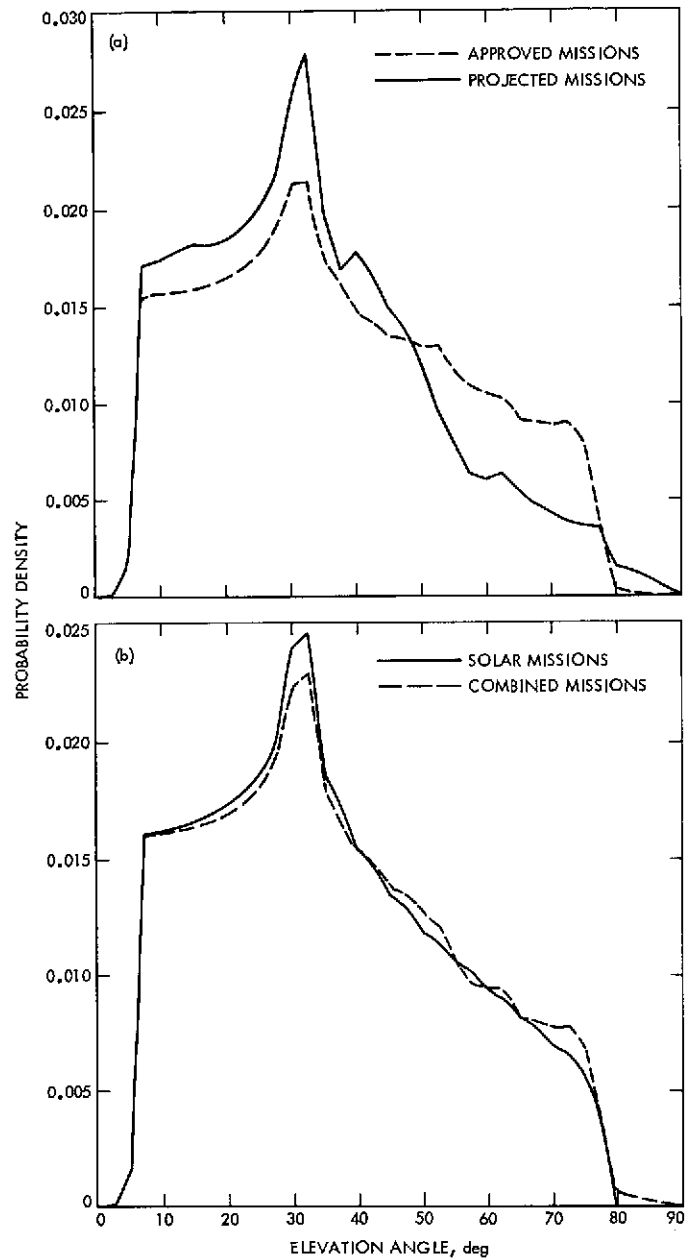


Fig. 4. Elevation angle probability density: (a) approved and projected missions, (b) solar and combined missions

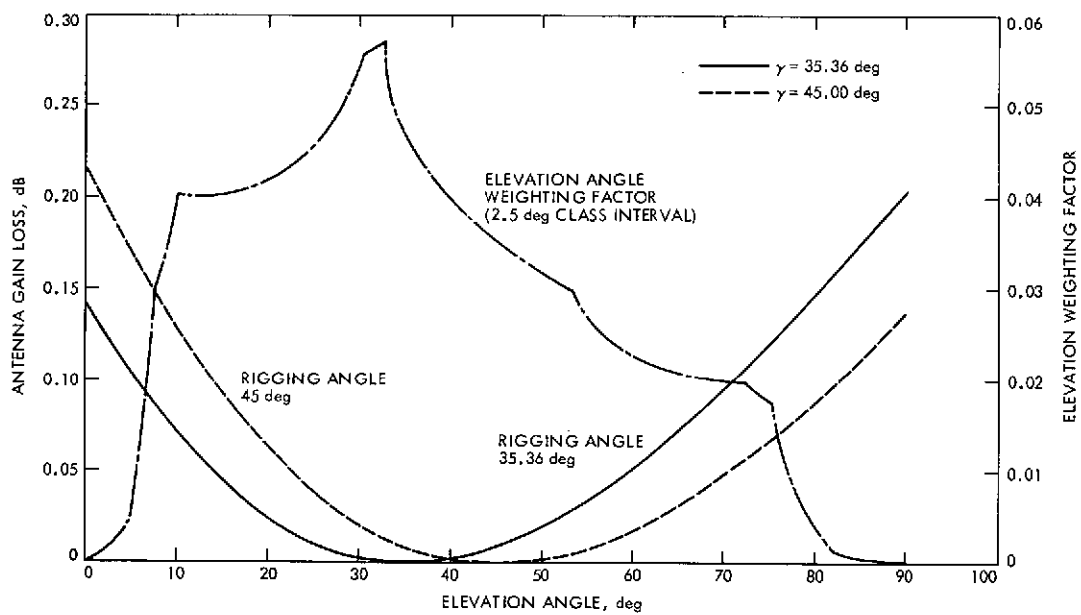


Fig. 5. Mars antenna gravity deformation gain loss at 8.45 GHz for combined missions

Fourth Harmonic Analyzer

R. H. Smith

R.F. Systems Development Section

The X-band downlink receiver frequency is situated very close to the fourth harmonic of the S-band high-power transmitter. When wideband modulation is applied to the high-power transmitter, the sidebands of the fourth harmonic are of such magnitude to the X-band receiver that they interfere with X-band downlink or will saturate the X-band maser. To alleviate this problem, a fourth harmonic filter was added to the output of the high-power transmitter. No quantitative results of this experiment were obtained. To make an analytic measurement, a fourth harmonic analyzer has been developed to measure the power at the fourth harmonic of the S-band high-power transmitter with and without a fourth harmonic filter.

I. Introduction

With the development of an X-band downlink from spacecraft to be used simultaneously with an S-band uplink, a more sophisticated and sensitive X-band receiving system has been developed and installed at DSS 14. With the use of the X-band downlink receivers a problem was discovered. This problem was that the fourth harmonic of the high-power transmitter (S-band uplink) was of sufficient magnitude that its sidebands were stronger than the X-band downlink signal expected from a spacecraft. To alleviate this problem an X-band filter was added to the feed system of the high-power transmitter. To determine if this was an effective solution to the problem, a source for measuring the fourth harmonic magnitude is required. An analyzer has been developed (Fig. 1) to measure the magnitude of the fourth harmonic in the S-band waveguide (WR-430) in any mode or combination of modes and to develop operational techniques in measuring harmonics.

II. Description

The fourth harmonic analyzer is basically a harmonic filter of a leaky-wall type (Fig. 2), utilizing secondary waveguides which are beyond cutoff of the fundamental, second and third harmonics of the S-band high-power transmitter. The secondary waveguides are mounted on one broad wall and both of the narrow walls of the primary waveguide. There are 60 secondary waveguides mounted on each of the narrow walls and 120 on the broad wall (Fig. 3). The large number of secondary waveguide couplings are necessary because of the many modes that can exist in a fourth harmonic. There can be in excess of 29 different modes at the fourth harmonic. There are slits cut in the wall of the primary waveguide (WR-430) to allow coupling to the secondary waveguides (WR-90). The secondary waveguide has a movable load mounted within the waveguide. As the load is removed, a coupling loop is exposed so that the power within the secondary waveguide can be measured using a power meter. Because

of the spacing of the secondary waveguide on the walls, a special probe was developed to slide into each of the secondary waveguides so that the power meter could be coupled to the secondary waveguide. The removable load has an "O" ring gasket to maintain the pressure integrity of the waveguide system.

III. Performance

The absorption loss of the primary waveguide at the fourth harmonic was supposed to be at least 6 dB. After the unit was made and measurements taken, it was determined that the absorption loss is as low as 4.8 dB. The design goal of 6 dB would cause a maximum measurement uncertainty of 1.25 dB. The actual insertion loss causes a maximum measurement uncertainty of 1.75 dB. The difference between the calculated and the actual insertion measurement results is due to poor mismatch of the secondary waveguides. The VSWR of each of the secondary

waveguides was measured. A correction factor for each secondary waveguide power measurement will correct the reading and improve the accuracy of the fourth harmonic measurement.

Presently the fourth harmonic analyzer is being used in the laboratory to develop more exact measurement techniques. A computer program is being developed to take the raw data and to format them into usable results. It is hoped that the use of the learning method in the laboratory and the computer program will result in a lower measurement error.

IV. Future Plans

In the near future the analyzer will be inserted into the high-power microwave system at DSS 13, and actual high power measurements will be made.

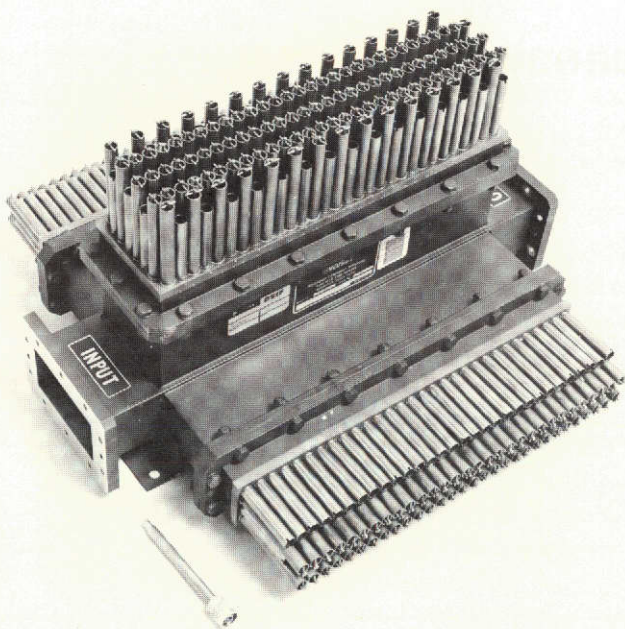


Fig. 1. Fourth harmonic analyzer with RF probe

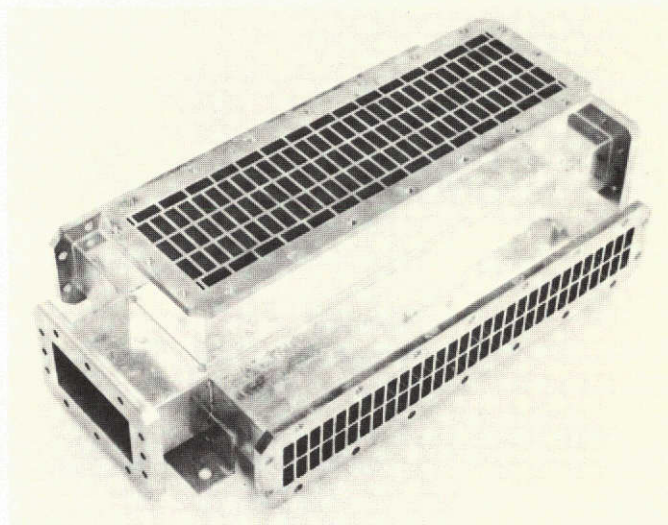


Fig. 2. Main waveguide (WR-430) and fourth harmonic coupled waveguide (WR-90) of the fourth harmonic analyzer

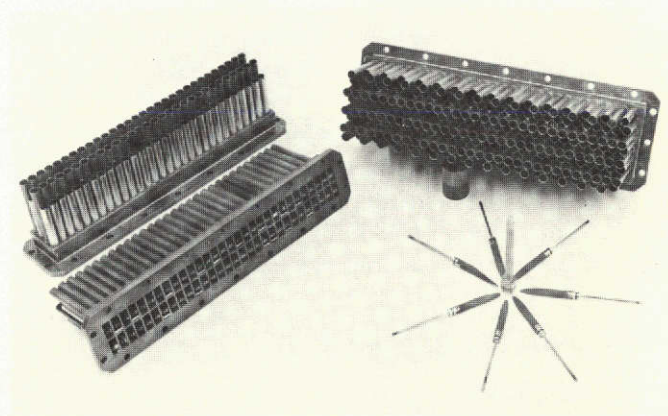


Fig. 3. Broad wall and narrow wall load and sample ports and load and sample of the fourth harmonic analyzer

DSN Research and Technology Support

E. B. Jackson

R.F. Systems Development Section

The activities of the Development Support Group in operating and maintaining the Venus Station (DSS 13) and the Microwave Test Facility (MTF) are discussed and progress noted. Activities noted include planetary radar experiments, station automation demonstration development, weak radio source observations, 26-m antenna pattern sidelobe measurements, and testing of an adhesive planned to be used for construction of an insulated subreflector for the overseas 64-m antennas. Support for the Block IV receiver/exciter at DSS 14 is noted; a capsule progress report on the 400-kW X-band planetary radar is given; and high-power transmitter maintenance at DSS 14 and testing of DSN klystrons are discussed. Differential very long baseline interferometry (VLBI) transmissions and Pioneer 10 science support are also discussed.

During the two-month period ending February 15, 1974, the Development Support Group, in its operation of the Venus Station (DSS 13) and the Microwave Test Facility, made progress on projects as discussed below.

I. In Support of Section 331

A. Planetary Radar

Continuing with mapping of the planet Venus (as part of the support of the Mariner Venus/Mercury 1973 Project), the Venus Station, in cooperation with the Mars Station (DSS 14) and the National Radio Astronomy Observatory (NRAO) (Greenbank, West Virginia), received signals reflected from the planet Venus. The planet was illuminated with the 400-kW Transmitter at DSS 14 using the 64-m antenna, and simultaneous reception was accom-

plished by DSS 13 and DSS 14 or DSS 13 and NRAO. Excellent data were obtained and a total of 253 signal runs was received during the 49 hours devoted to this activity.

B. Station Automation (Pulsars)

As part of the overall DSN Station Automation Project (RTOP 68, "Station Monitor and Control"), a demonstration is planned using the Venus Station to perform a pulsar track under remote control from JPL in Pasadena. A new receiver designed to be interfaced with a computer has been installed at DSS 13 for pulsar reception. The necessary computer programs are undergoing testing, so pulsar reception is being accomplished using the new receiver with manual control while awaiting the installation of the necessary computer and completion of the

appropriate programming. Pulsars as tabulated in Table 1 have been received during the 68 hours of development and observation devoted to this project during this period.

II. In Support of Section 333

A. Weak Source Observation

This project, which gathers data on radio sources that might be useful for calibration sources for 64-m antennas, received 75 hours of tracking during this period. The data are collected using the 26-m antenna with right circular polarization selected and the maser/receiver tuned to 2295 MHz. The receiver feeds a semiautomatic data collection system under the control of a computing counter. The overall receiver gain is stabilized by a noise adding radiometer and the data are recorded by a digital printer and analog chart recorder. The radio sources whose fluxes have been measured during this period are listed in Table 2.

B. Radio Star Calibration

As part of a program to measure the gain of the 26-m antenna at DSS 13, longterm calibration on selected radio sources is performed. During this reporting period a total of 44 hours was devoted to the reception at 2278.5 MHz, right circular polarization of the radio sources 3C123 and Cygnus A.

C. 26-m Antenna Sidelobe Measurements

As part of a project to measure the angular distribution and amplitude of the sidelobes on the DSS 13 26-m antenna pattern, before and after covering the quadripod with sheet metal, a computer program was developed to control the pointing of the antenna using the station SDS-930 computer. This program moves the antenna in circles about the sun and the receiver noise output power is recorded as a function of angular position. By changing the radius of the circles traversed, the sidelobe structure of the antenna pattern can be examined as far out as the strength of the signals from the sun will permit. The project has been completed through the prequadripod covering phase, and a total of 127 hours of tracking and computer program testing was carried out during this reporting period.

D. Adhesive Testing

It is planned to construct, for noise abatement purposes, a subreflector for the overseas 64-m antenna, which would have its reflecting surface insulated from the support/back-up structure. In preparation for this construction, samples of the proposed adhesive were tested

on the 26-m antenna. With the power densities adjusted to be appropriate to a 64-m antenna operating at 400 kW, tests were made with the samples suspended in free space above the main reflector and then fastened to the subreflector itself. Data were collected during a total test time of 20½ hours.

E. Sky Survey

With an automatic data collection system, the 26-m antenna at Venus is used to record data on radio sources that the rotation of Earth carries through the antenna pattern with the antenna fixed in angle pointing. This data collection is done at night, weekends, and during holiday periods when the station is closed. The 26-m antenna is moved to an azimuth of 180 deg and fixed at various elevation angles from 80 to 90 deg for each data run. Data are collected using the noise adding radiometer to stabilize receiver gain at 2295 MHz with the antenna receiving right circular polarization. A total of 632 hours of data were recorded during this period.

III. In Support of Section 335

A. Block IV Receiver/Exciter

While DSS 14 personnel are being trained to operate and maintain the Block IV receiver/exciter installed at DSS 14 for the support of the Mariner 10 and subsequent spacecraft, personnel from DSS 13 provide emergency and routine maintenance of the system. Additionally, we provide operation of the system during testing, particularly testing that took place in preparation for the encounter of Mariner 10 with Venus on February 5, 1974. During the period, a total of 275.5 manhours of support was provided.

B. X-Band Planetary Radar

As part of the development and construction of a 400-kW X-band planetary radar transmitting system, component testing and dual klystron test setup fabrication continued. After achieving stable 200 kW RF power output for a few hours, two (VA-949J, S/Ns 29, 31) of the three klystrons available failed. All three klystrons have been returned to the manufacturer (Varian Associates) for analysis. Narrowband testing of the repaired waveguide directional couplers, as well as the 150-kW waterloads, was accomplished. The dual klystron test setup was approximately 73% completed at the end of the reporting period.

A traveling wave resonator has been assembled at the Microwave Test Facility to be energized by the X-band klystron used for transmission of clock synchronization

signals during the development phase. Initial energization at input power levels up to 10 kW at approximately 8500 MHz will take place during the latter days of February 1974.

C. DSS 43 and DSS 63 100-kW Transmitter Testing

In preparation for commencement of testing of the first transmitter system, the 1-MW dc water-cooled load was cleaned up, the insulating oil purified and the load moved into position north of Building G-53A. A protective enclosure 3.66×4.88 m was procured for enclosing the transformer rectifier, crowbar cabinet, filter choke, and vault junction box while undergoing testing. These items, with the enclosure around them, will be situated on a concrete pad north of G-53A. The transmitter cabinet to be tested has been positioned inside of G-53A, on the western-most cone hoist, and testing is scheduled to commence on February 18, 1974 with the arrival of the control cabinet.

IV. In Support of Section 391

In cooperation with DSS 42, differential VLBI observations were made of radio sources OP-192 and OQ-151 paired with one of the Apollo Lunar Surface Experiments Packages (ALSEPs) left on the Moon by the Apollo project. Good data were received for a total of $5\frac{1}{2}$ hours while switching between sources every two minutes.

V. In Support of Section 422

A. Clock Synchronization Transmissions

Only one transmission, to DSS 51, was made during this period.

B. DSS 14 High-Power Transmitter Maintenance

A problem was encountered with the filament voltage on the 100-kW transmitter at DSS 14. The system was restored to operation by repair of instrumentation printed circuit boards. During this repair ECO 73-056 was also installed to provide correct indications of filament voltage and current applied to the 100-kW klystron.

C. DSN Klystron Testing

DSS 12 experienced difficulty with their 10-kW transmitter and delivered a klystron to the MTF for check-out. This klystron proved to be gassy and other klystrons were delivered for testing to discover one suitable for use as a replacement at DSS 12. A total of four klystrons, 4KM50SI, S/Ns H4-71, J4-45, K4-25, and F7-28 were tested to find a good replacement and one additional spare klystron.

In appreciation of the importance of the 100-kW transmitter at DSS 14, a spare 100-kW klystron, X-3060, S/N K5-24, was fully tested and prepared for use as a spare.

Subsequent to the Mariner 10 encounter with Mercury, the 100-kW transmitter at DSS 14 will be converted back to a 400-kW transmitter. In anticipation of that change-over, a repaired klystron, X-3075, S/N H101-R1, received from Varian Associates, has been installed into the DSS 13 High-Power Maintenance Facility for acceptance testing.

VI. In Support of Section 825

With the encounter with Jupiter now past, support to this project has decreased. The radiation from Jupiter at 2295 MHz, right circular polarization, was monitored for 22 hours, while radio star calibrators, as enumerated in Table 3, were observed for 46 hours.

Table 1. Pulsars selected for test reception at DSS 13

0031 - 07	1604 - 00	1929 + 10
0329 + 54	1642 - 03	1933 + 16
0355 + 54	1706 - 16	2021 + 51
0525 + 21	1749 - 28	2045 - 16
0628 - 28	1818 - 04	2111 + 46
0823 + 26	1911 - 04	2218 + 47

Table 2. Weak radio sources observed at Venus Station

3C48	3C147	3C348	Virgo A
3C123	3C286	NGC 7027	
3C138	3C309.1	PKS 0237-23	

Table 3. Radio star calibrators used for Pioneer 10 science support

3C48	3C353
3C123	NGC 891
3C286	NGC 4736
3C309.1	Virgo A
3C348	

Cost Effective Spares Provisioning for the Deep Space Network

I. Eisenberger and F. Maiocco
Communications Systems Research Section

G. Lorden
California Institute of Technology

This report discusses a cost effective procedure for spares provisioning of the various components of an assembly that is assumed to fail if any one of the components fails. The procedure not only provides a means for obtaining a given operational availability at minimum cost, but it is also applicable when a constraint is placed upon the total cost of the spares for the components making up the assembly.

I. Introduction

An efficient method for spares provisioning of repairable equipment used in the Deep Space Network (DSN) is given in Ref. 1. For simplification we call any such piece of equipment a module. That method can be used to determine the minimum number of spares necessary to obtain a required operational availability which, in general, is defined as the stationary probability that a system is operating or operational at any given time and is sometimes referred to as the uptime ratio (*UTR*). The method was applied to two types of situations. In the first case, the goal was to provide a common pool of spares for n identical, independently operated modules, $n = 1, 2, 3, \dots$ situated within a single complex or DSS, and, in the second, to provide a spares complement for a so-called (m, n) system. The requirement for this system is that at least m out of n identical modules must be in operation at any given time in order for the system to adequately perform its required function. It should be noted that a $(1, n)$ system is equivalent to a simple parallel configuration with n components.

For these cases the problem of meeting a cost constraint is not difficult to solve. If it is determined that N spares are needed to achieve a required *UTR* and enough money is available to buy M spares then the number of spares that should be bought is the minimum of N and M . In practice, however, one often has a system configuration containing several types of modules, with the constraint placed on the *total* cost of spares for the entire system. The problem in this case is to choose the number of spares for each type of module in such a way that the system operational availability is maximized within the cost constraint. An equivalent problem is that of achieving a prescribed system operational availability for minimum cost. The method developed in the present report is easily applied to both problems.

II. Statement of the Problem

Let k be the number of types of modules in the system. For each type of module there is a failure rate λ_i , and a repair rate, μ_i , and it is assumed that repair times and

times between failures are exponentially distributed. (As explained in Ref. 1, constant repair times yield the same results to a reasonable degree of approximation.) For $i = 1, \dots, k$, let n_i denote the number of modules of type i in the system and m_i the number that have to be unfailed in order for the system to perform its intended function satisfactorily. It is assumed that whenever fewer than the required minimum m_i are operable for one or more of the module types, the system is down. A further assumption is that failures and repairs of different modules are stochastically independent. Under these assumptions, the system UTR is the product of the k UTR s for the module types. The latter can be calculated by the algorithm in Ref. 1 that allows for so-called (m, n) systems. Of course, a single module constitutes a $(1, 1)$ system while n identical modules form an (n, n) system if in series and a $(1, n)$ system if in parallel.

We define a spares *package* to be a choice of s_1, \dots, s_k , the number of spares for the respective types of modules. If $U_i(s)$ is the UTR for the type i module when s spares are provided, then we have

$$\text{System } UTR = U = \prod_{i=1}^k U_i(s_i) \quad (1)$$

The value of $U_i(s)$ is computed by the procedure given in Ref. 1. Let c_i denote the cost for each module of type i . Then

$$\text{Cost of Package} = C = \sum_{i=1}^k s_i c_i \quad (2)$$

A spares package with uptime ratio U_1 and Cost C_1 is preferable to one with U_2 and C_2 if $U_1 \geq U_2$, $C_1 \leq C_2$, and at least one of these inequalities is strict. A spares package will be called *efficient* if no other package is preferable to it in the sense just defined. Clearly it is only the *efficient* packages one would want to use, since any other package can be improved upon by reducing cost or improving UTR or both. The method presented in Section III constructs spares packages that are efficient under a mild condition on the $U_i(s)$'s. Note that if U and C are the UTR and cost of an efficient package, then U is the maximum possible UTR subject to the cost constraint C , and C is the minimum possible cost of achieving a $UTR \geq U$.

III. A Method for Constructing Efficient Spares Packages

Define the efficiency of the s^{th} spare for module type i as

$$R_i(s) = \frac{\log(U_i(s)/U_i(s-1))}{c_i}$$

for $i = 1, \dots, k$ and $s = 1, 2, \dots$. Then we can rewrite Eq. (1) in the form

$$\log U = \sum_{i=1}^k \log U_i(0) + \sum_{i=1}^k \sum_{s=1}^{s_i} c_i R_i(s) \quad (3)$$

Note that the first summation is constant, i.e., does not depend on the choice of the spares package s_1, \dots, s_k . The total cost of the spares package can be written as

$$C = \sum_{i=1}^k \sum_{s=1}^{s_i} c_i \quad (4)$$

Then Eq. (3) becomes

$$\frac{1}{C} \cdot \log U = \text{constant} + \sum_{i=1}^k \sum_{s=1}^{s_i} \frac{c_i}{C} R_i(s) \quad (5)$$

Since the sum of all c_i 's is C , the sum of the (c_i/C) 's is 1, so that Eq. (5) expresses $1/C \log U$ as a constant plus a weighted average of the $R_i(s)$'s. Since we want to maximize $\log U$, it is plausible that we should proceed inductively as follows:

- (1) Choose the first spare for the type i such that $R_i(1) > R_j(1)$ for all $j \neq i$.
- (2) Continue by choosing the next spare to be the one yielding the largest efficiency among those spares immediately available. Stop at any time.

To clarify step (2), suppose that r_1, \dots, r_k spares of types 1 through k have already been chosen. Then if we choose type i for the next spare, the efficiency of that choice is $R_i(r_i + 1)$. Step (2) calls for choosing i to get the largest of $R_i(r_i + 1), \dots, R_k(r_k + 1)$. Then r_i is increased by one (since we now have one more spare) and step (2) is repeated.

No matter when this process is stopped, the spares package is efficient, provided the condition in statement (6a) below is satisfied. In other words, the process produces a sequence of efficient spares packages, each adding one more spare to the previous package. Naturally, both cost and system UTR increase as more spares are added.

A sufficient condition to insure that the method just described produces efficient spares packages is the following "monotonicity condition."

$$\text{For each } i = 1, \dots, k, R_i(s) \text{ is decreasing in } s \quad (6a)$$

From the definition of $R_i(s)$ it is clear that statement (6a) reduces to

For each $i = 1, \dots, k$, $U_i(s)/U_i(s-1)$ is decreasing in s (6b)

Using the algorithm developed in Ref. 1, condition (6b) was checked for several thousand cases with λ 's and μ 's varying over a broad range (it is sufficient to vary the ratio λ/μ) and s from 1 up to the value required to make $U_i(s) > 0.9999$. The cases tested included sparing for a single module as well as sparing for various (m, n) systems. Not a single exception to condition (6b) was found. Finding a mathematical proof of the condition seems to be very difficult because of the complexity of the recursive equation defining the $U_i(s)$'s.

A proof that the method produces efficient packages when the monotonicity conditions are met is given in Section IV.

To illustrate the use of this method, consider the following example. We have a system that consists of 24 modules, one module each of 12 types and 3 modules each of four types. For each of the latter four types, the modules are arranged in a (2, 3) configuration. We begin by determining $U_i(0)$ and $U_i(1)$ for each type, that is, we calculate by the method of Ref. 1 the UTR for each type when no spare is provided and when 1 spare is provided. From these calculations we determine $R_i(1)$ for $i = 1, \dots, 16$. Now, if $R_j(1)$ is the greatest of these the first spares package consists of one spare of type j and no spares for each of the remaining types. To determine the next spares package (containing two spares) we need only calculate $U_j(2)$ and from this $R_j(2)$. We now look at the new set of $R_i(s_i)$'s where, in this step, $s_i = 0$ for $i \neq j$ and $s_j = 1$. If $R_k(s_k)$ is the greatest of these, the second spares package consists of one spare for type j , one spare for type k , and no spares for the remaining types. We continue in this fashion until a desired stopping point is reached. Each successive spares package generated in this way will contain one spare more than the previous one and will be efficient in the sense defined above. Since the cost of each spares package and the system UTR achieved are easily computed as the process proceeds, a cost vs UTR tradeoff can be made to determine when to stop, or one can continue until a specified UTR is achieved or a cost constraint would be exceeded by continuing.

The procedure was applied to the above described system for specific sets of λ 's and unit costs. The repair time was assumed to be 336 hours for all of the types of mod-

ules. The upper graph in Fig. 1 labeled $\epsilon = 0$ is a plot from step 13 on of the UTR s achieved by the above procedure as a function of the costs incurred. Table 1 lists some of the numeral results. The entries in column 2 show the successive decisions on which type of spare should be added to the previous spares package in order to get the current one. In other words, if k is the entry in the j^{th} row of column 2, add a spare of type k module to the $(j-1)^{\text{st}}$ spares package to obtain the j^{th} spares package (containing j spares). The row denoted by "Final spares package" shows the contents of the last spares package (in this case the 37th). The k^{th} entry in this row denotes the number of spares for the k^{th} type of module (the total number of spares is 37). The entries in this row and those in column 2 enable one to determine the contents of any of the previous spares packages. For example, to obtain the 34th spares package, subtract from the entries in the final spares package one spare each for the fourth, second, and tenth type of module, obtaining the spares package 1, 1, 2, 1, 2, 2, 2, 2, 2, 2, 3, 3, 3, 3, 3 with a cost of 1046 and a system UTR of 0.9936.

Each entry in column 4 of Table 1 is the inverse of the down time ratio (DTR), ($DTR = 1 - UTR$) at each step. These numbers are given because they have an interesting property. Figure 2 is a plot on log paper of $1/DTR$ versus cost starting with step 11, which shows a cost of 348 and $UTR = 0.8647$. In this range, it can be seen that the function is closely approximated by the straight line drawn on the graph by eye. This means that $\log(1/DTR)/\text{cost}$ is very nearly constant in the range of practical interest to a potential user of the procedure. If we denote this constant by b , we have

$$\log(1/DTR)/C = b$$

resulting in

$$e^{-bc} = DTR = 1 - UTR$$

so that a knowledge of b enables us to predict very closely what the UTR will be for a given cost using this method of sparing. Column 5 in the table gives the values of $\log(1/DTR)/C$ for each step and confirm the results shown in Fig. 2. If we think of $1/DTR$ as the average number of random inspections (spread out over time) required to first find the system down, then we have the rule-of-thumb: this average number of inspections grows exponentially as a function of the cost of spares. The exponential growth rate parameter, b , is characteristic of the system configuration, the failure rates, and the repair rates.

IV. The Value/Cost Lemma

By taking logarithms in Eq. (1) it is easily seen that the problem of selecting spares efficiently fits the following general formulation, which is applicable in many contexts.

Let S be a set (e.g., all possible spares) whose members x each have a value $v(x)$ and a cost $c(x)$. It is desired to select subsets R of S whose total value

$$V(R) = \sum_{x \in R} v(x)$$

and cost

$$C(R) = \sum_{x \in R} c(x)$$

are *efficient* in the sense that neither can be improved without hurting the other. It is easy to see that a sufficient condition for R to be efficient is that there exists a $d > 0$ such that $V(R) - dC(R) \geq V(R') - dC(R')$ for all $R' \subset S$. (If, for example, there were an R' such that $V(R') > V(R)$ while $C(R') \leq C(R)$, then $V(R) - dC(R) < V(R') - dC(R')$, contrary to the condition.)

To find such an R for a given $d > 0$, note that

$$\begin{aligned} V(R) - dC(R) &= \sum_{x \in R} [v(x) - dc(x)] \\ &\leq \sum_{x: v(x) - dc(x) \geq 0} [v(x) - dc(x)] \end{aligned}$$

and observe the upper bound on the right is attained if $R = R_d = \{x | v(x) \geq dc(x)\}$. Thus, for all $d > 0$, R_d satisfies the sufficient condition and we have the *Value/Cost Lemma*: R_d is efficient.

A similar result describing efficient performance of statistical hypothesis tests is called the Neyman-Pearson Lemma. The same mathematics has been used in problems close to the present one (Ref. 2) and is related to the more general theory of nonlinear programming (Ref. 3).

To apply this result to the sparing problem, identify the members of S as x_{ij} 's where

$$x_{ij} = j^{\text{th}} \text{ spare of type } i; \quad i = 1, \dots, k; \quad j = 1, 2, \dots$$

In the notation of the previous section, if $s_i = 3$, say, then we understand that x_{i1} , x_{i2} , and x_{i3} have been selected, but not x_{i4} , x_{i5} , etc. We define

$$\begin{aligned} c(x_{ij}) &= c_i = \text{unit cost for spares of type } i \\ v(i, j) &= \log U_i(j) - \log U_i(j-1) \end{aligned}$$

Thus if s_1, \dots, s_k spares of the various types are selected, the total value is

$$V = \sum_{i=1}^k \sum_{j=1}^{s_i} [\log U_i(j) - \log U_i(j-1)]$$

The sum over j telescopes and we get

$$\begin{aligned} V &= \sum_{i=1}^k [\log U_i(s_i) - \log U_i(0)] \\ &= \log \prod_{i=1}^k U_i(s_i) - \log \prod_{i=1}^k U_i(0) \end{aligned}$$

Thus V is the log of system UTR minus a constant not depending on the s_i 's, so that the comparison between system UTR s for different packages is equivalent to a comparison of their values, $V = \sum v(x_{ij})$. Therefore a spares package that selects those spares x_{ij} in R_d (for a $d > 0$) is efficient in the sense of Section II.

To see that the method of Section III produces R_d 's under the monotonicity condition (6a), note that wherever we stop, the efficiencies $R_i(s)$ of the spares selected are all greater than or equal to the efficiencies of the spares not selected. Hence, there is some $d > 0$ that is a lower bound on the efficiency of selected spares and a strict upper bound on the efficiency of spares not selected. Since

$$R_i(s) = \frac{v(x_{is})}{c_i}$$

$R_i(s)$ is \geq or $< d$ according as $v(x_{is}) - dc_i$ is \geq or < 0 ; hence the members of R_d are precisely the spares selected by the method. Actually, for a spares package of this kind costing C , say, to be efficient, it is sufficient that for every i the monotonicity condition holds for values of $s \leq C/c_i$, since this is as many spares of type i as can be bought for C or less.

V. The Cost of Misestimating Failure Rates

Since the results obtained from our sparing procedure depend upon the estimated failure rates of the various types of modules, a decrease in efficiency will result when the procedure is used with a set of estimated $\bar{\lambda}$'s that differ substantially from the true λ 's.

In order to see the effect of this kind of error, we applied the procedure to the system described in Section III under

the assumption that the true λ 's were as given but that the estimated $\bar{\lambda}_j$'s were given by

$$\lambda_j = \begin{cases} (1 + \epsilon) \lambda_j, & j = 1, 3, 5, \dots, 15 \\ \lambda_j / (1 + \epsilon), & j = 2, 4, 6, \dots, 16 \end{cases}$$

for $\epsilon = 0.5$ and $\epsilon = 1.0$.

Thus the contents of each spares package was determined by using the $\bar{\lambda}_j$'s while the *UTR* was computed using the true λ 's. The graphs in Fig. 1 labeled $\epsilon = 0.5$ and $\epsilon = 1.0$ are plots of *UTR* vs cost for the two examples of misestimated failure rates.

It is readily seen that for a given cost one does not achieve as high a *UTR* when the estimated failure rates used to generate the spares package differ from the true ones.

Looking at it the other way around, the cost of achieving a given *UTR* is increased when the failure rates are in error. In the example depicted in Fig. 1, the percentage increase in the cost for fixed *UTR*'s is about 10% when

$\epsilon = 0.5$ and about 20 to 25% when $\epsilon = 1$. Note that in the latter case *all* the failure rates are in error by a factor of two, half of them too high and half too low. If failure rates are in error by random factors less than or equal to two, the degradation in efficiency will be less.

VI. Applications

The principal applications envisaged for the method developed in this report are to the problem of initial spares provisioning and to improving the operational availability of present subsystems that are relatively unreliable. In the former case, only crude estimates of failure rates are available, but the analysis in Section V indicates that the method still yields useful results.

For improving operational availability of existing systems or subsystems, more accurate judgments are possible by utilizing reliability histories to estimate failure rates. Once these rates are determined, the efficiencies of additional spares of all types can be calculated and any improved level of *UTR* can be reached efficiently by purchasing additional spares with the greatest efficiencies.

References

1. Eisenberger, I., Lorden, G., and Maiocco, F., "A Preliminary Study of Spares Provisioning for the Deep Space Network," in *The Deep Space Network Progress Report*, TR 32-1526, Vol. XVIII, pp. 102-110. Jet Propulsion Laboratory, Pasadena, Calif., Dec. 15, 1973.
2. Proschan, F., "Optimal System Supply," *Naval Reserve Logistics Quarterly*, pp. 609-646. Office of Naval Research, Washington, D.C., 1960.
3. Kuhn, H. W., and Tucker, A. W., "Non-linear Programming," *Proceedings of 2nd Berkeley Symposium*, pp. 481-492. University of California Press, Berkeley, Calif., 1951.

Table 1. Results obtained by efficient sparing

Step	Type of spare	Cost C	1/DTR	log (1/DTR)/C	UTR	Parameters		
						Type	$\lambda/10^{-6}$	Cost/unit
1	14	18	1.64	0.02757	0.3911	1	31.25	32
2	10	40	1.76	0.01406	0.4301	2	62.50	30
3	15	86	1.97	0.00789	0.4925	3	93.75	34
4	16	102	2.07	0.00711	0.5158	4	125.00	28
5	13	146	2.39	0.00596	0.5814	5	156.25	36
6	11	188	2.81	0.00550	0.6447	6	187.50	26
7	6	214	3.17	0.00538	0.6840	7	218.75	38
8	9	254	3.93	0.00539	0.7456	8	250.00	24
9	7	292	4.96	0.00548	0.7984	9	281.25	40
10	12	312	5.64	0.00554	0.8226	10	312.50	22
11	5	348	7.39	0.00575	0.8647	11	343.75	42
12	3	382	9.22	0.00581	0.8915	12	375.00	20
13	2	412	11.11	0.00584	0.9100	13	406.25	44
14	8	436	13.18	0.00591	0.9241	14	437.50	18
15	14	454	14.79	0.00593	0.9324	15	460.75	46
16	16	470	16.53	0.00597	0.9395	16	500.00	16
17	1	502	19.73	0.00594	0.9493	Final spares package: 1, 2, 2, 2, 2, 2, 2, 2, 3, 2, 3, 3, 3, 3		
18	15	548	24.36	0.00583	0.9590			
19	10	570	27.45	0.00581	0.9636			
20	12	590	30.47	0.00579	0.9672			
21	13	634	39.60	0.00580	0.9748			
22	4	662	47.94	0.00585	0.9791			
23	11	704	65.66	0.00594	0.9848			
24	9	744	88.18	0.00602	0.9887			
25	6	770	104.90	0.00604	0.9905			
26	7	808	140.80	0.00612	0.9929			
27	16	824	163.04	0.00618	0.9939			
28	8	848	206.45	0.00629	0.9952			
29	5	884	280.63	0.00638	0.9964			
30	14	902	320.04	0.00640	0.9969			
31	12	922	361.50	0.00639	0.9972			
32	3	956	436.37	0.00636	0.9977			
33	15	1002	568.77	0.00633	0.9982			
34	13	1046	713.52	0.00628	0.9936			
35	10	1068	811.32	0.00627	0.9988			
36	2	1098	981.96	0.00627	0.9990			
37	4	1126	1206.67	0.00630	0.9992			

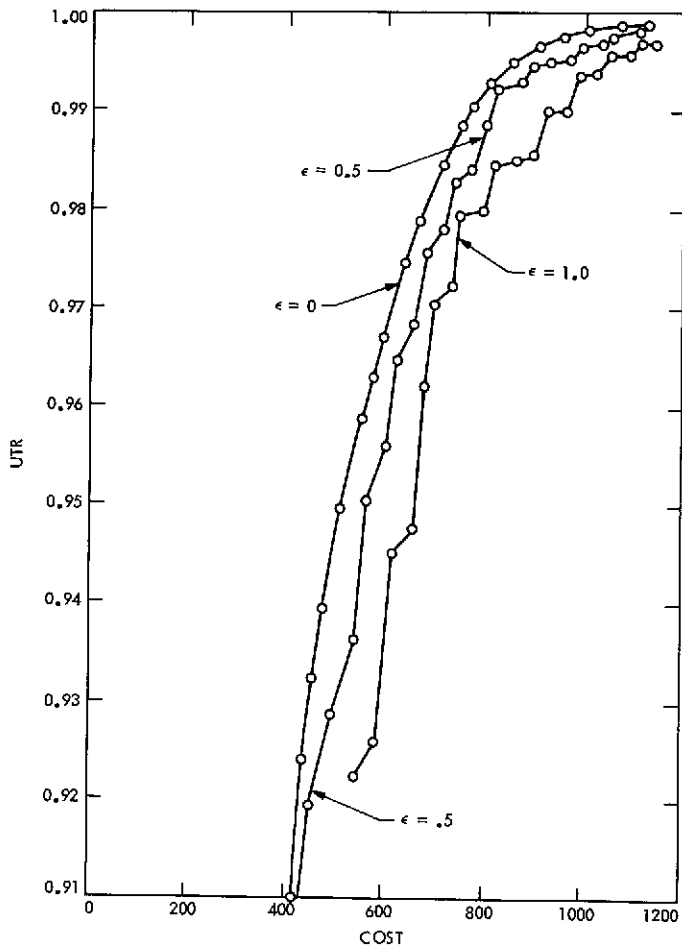


Fig. 1. UTR vs cost for efficient sparing with $\epsilon = 0, 0.5, 1.0$

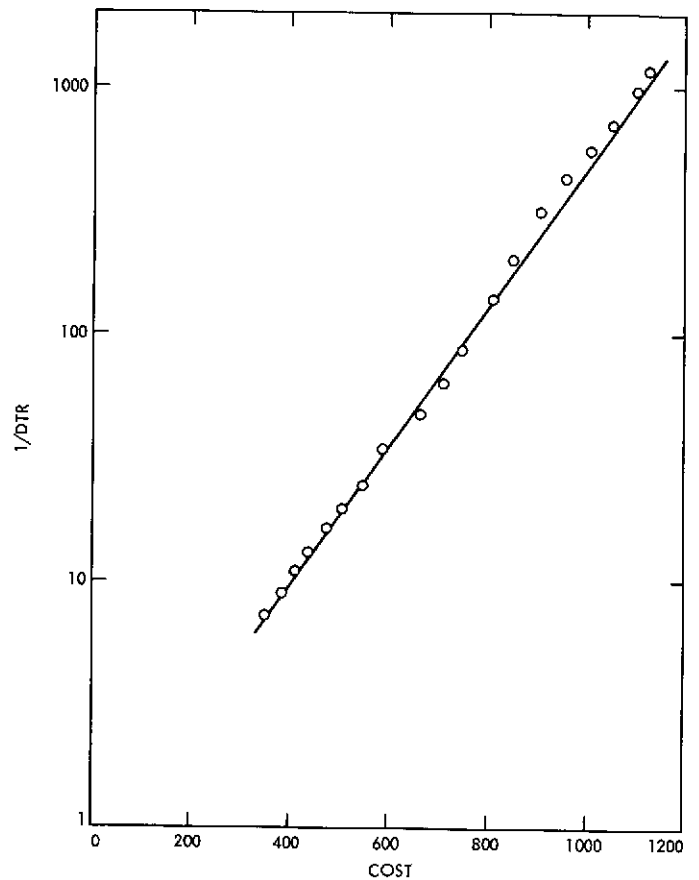


Fig. 2. $1/DTR$ vs cost for efficient sparing

Automated Pulsar Receiver

C. F. Foster

R. F. Systems Development Section

This article describes a self-contained computer-controlled 30-MHz-to-baseband receiver. This receiver has three selectable predetection bandwidths, a diode power detector, an internal level set, and 15 postdetection bandwidths. It is designed to directly interface with an on-site data reduction system. Its primary utilization is the automatic monitoring of pulsar signals.

I. Introduction

A requirement to support the R&D pulsar experiment without placing additional burdens on the DSS 13 operating personnel has resulted in the development of a computer-controlled receiver.

II. Implementation

The pulsar receiver (Figs. 1-3) is a completely self-contained 30-MHz-to-baseband system. The 30-MHz input signal (Fig. 4) is amplified by 20 dB before being applied to a step attenuator; the step attenuator allows the experimenter to maintain a constant (within 0.5 dB) noise power, thus preventing signal distortion due to noise overloading. The 30-MHz signal is then shaped with one of three possible predetection bandpass filters. This shaped 30-MHz signal goes to the final RF amplifier, and the output of this amplifier is converted to baseband frequencies by a wideband diode detector operating in the square law range. The detected signal is then amplified

100 times and shaped by one of a possible 15 postdetection filters. This signal is then transmitted to the DSS 13 data system.

The unique feature of this receiver is that all functions, predetection bandwidth, gain, and postdetection bandwidth, are controlled by the computer, therefore allowing the experimenter to have complete control of his receiver through the software generated for the individual task. Figures 5 and 6 show the results of two final measurements made to determine receiver performance. These curves are typical and the pulsar receiver achieved all engineering design requirements.

III. Conclusion

This pulsar receiver has been interfaced with the planetary radar receiver and the on-site data system at DSS 13. It is presently supporting the pulsar experiment in a manual mode, and after the software program now under development is complete, no further development has been planned.

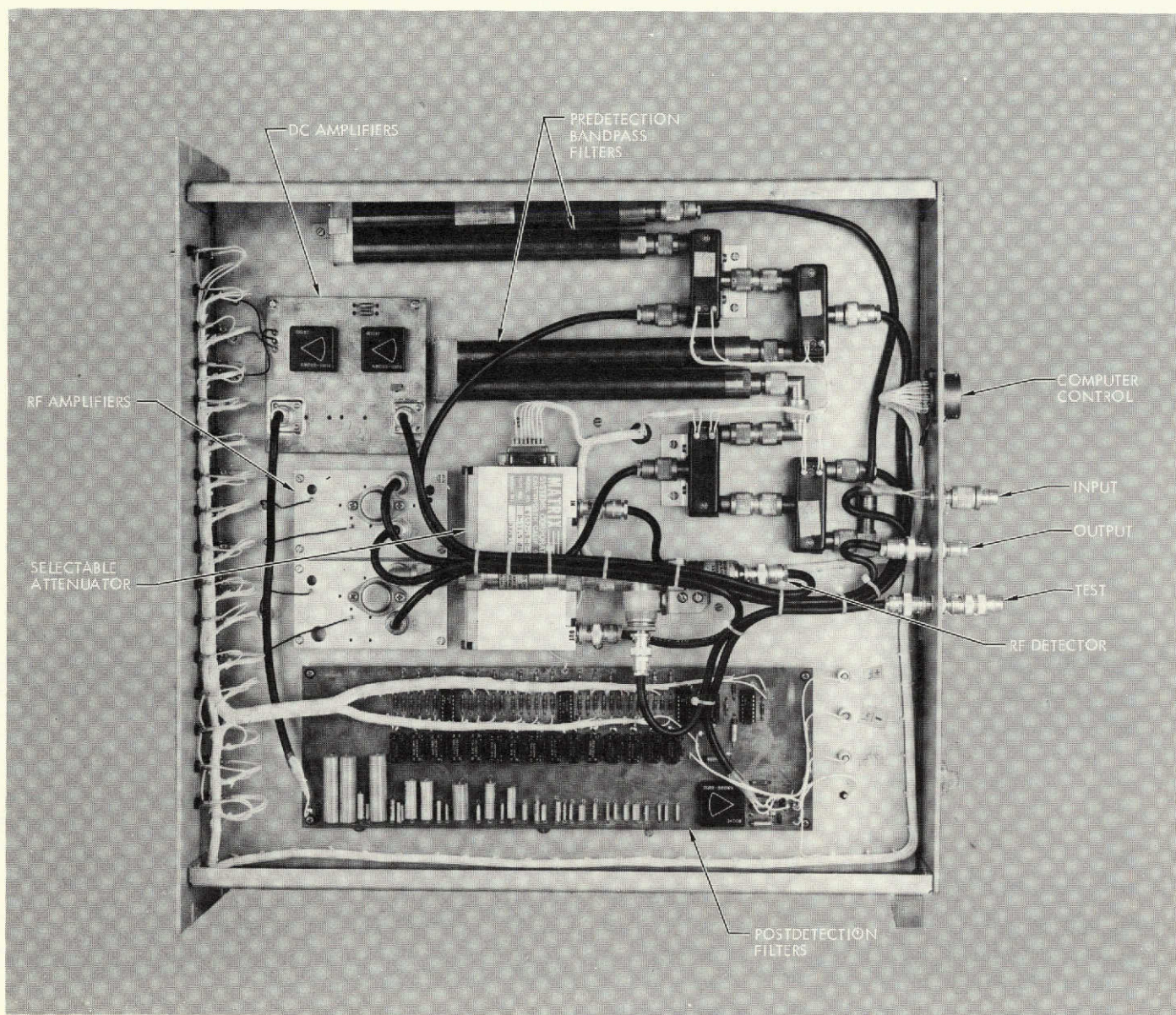


Fig. 1. Pulsar receiver, top view

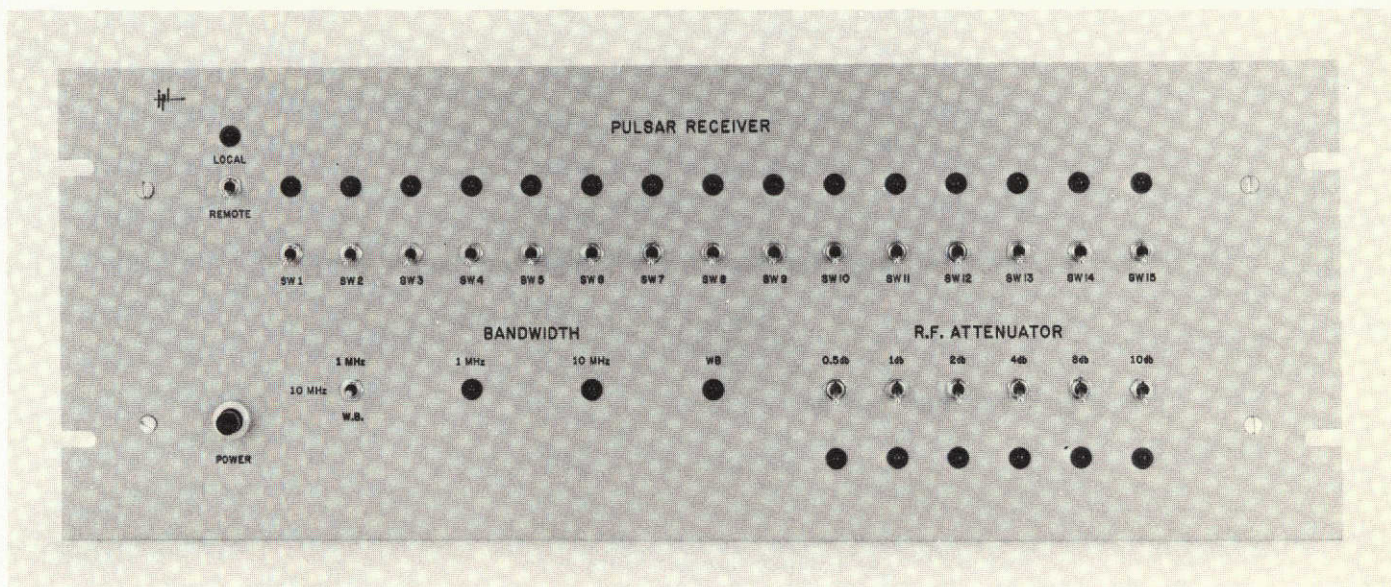


Fig. 2. Pulsar receiver, front view

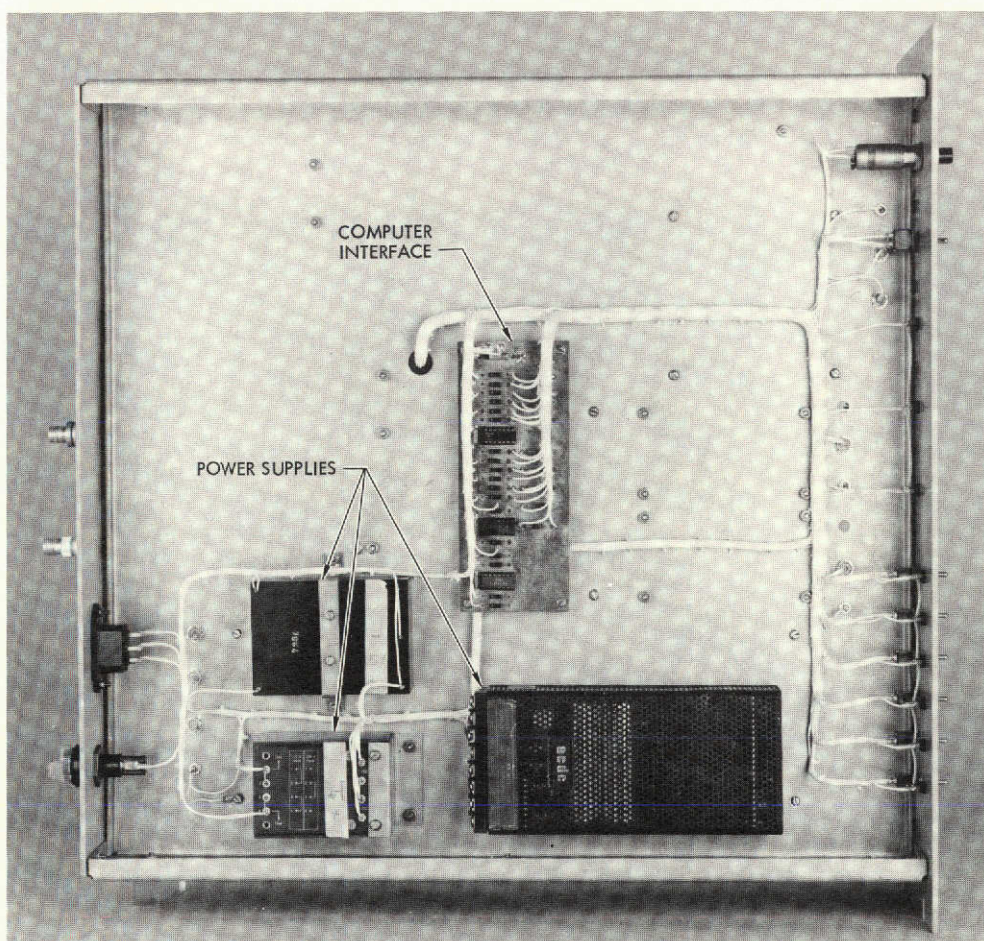


Fig. 3. Pulsar receiver, bottom view

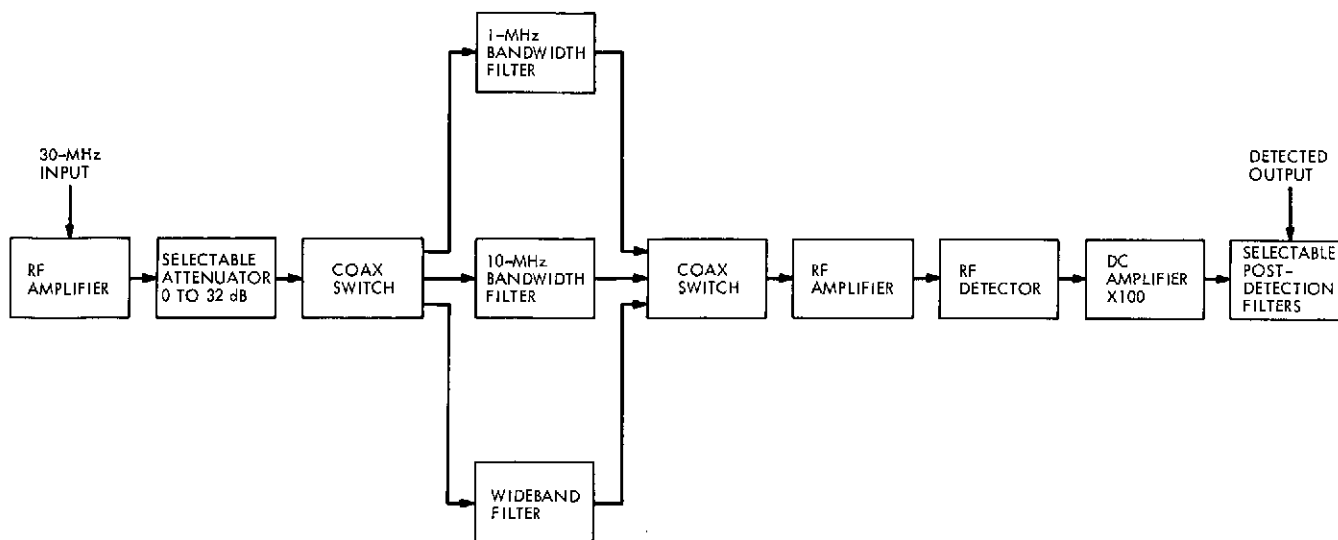


Fig. 4. Pulsar receiver block diagram

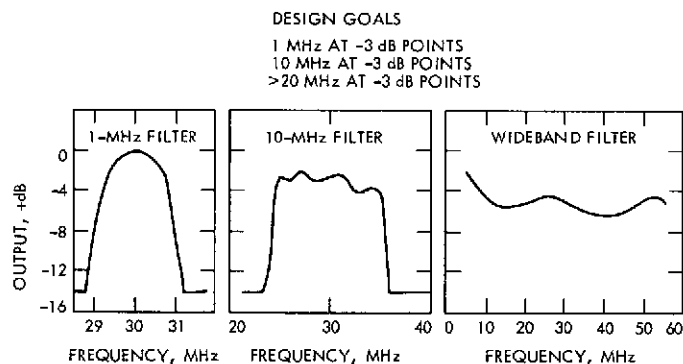


Fig. 5. Predetection bandpass filters

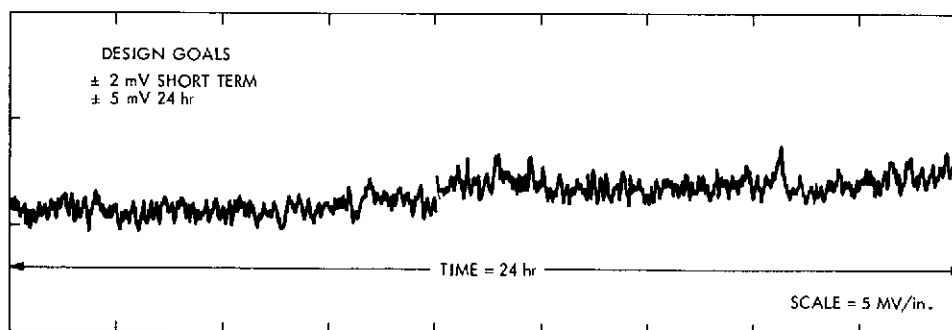


Fig. 6. DC stability pulsar receiver

Open-Loop Receiver/Predetection Recording System for the DSN

S. S. Kent and A. G. Sleky
R. F. Systems Development Section

A configuration for recording the telemetry IF output of an open-loop receiver and reproducing the data at minimal loss, incorporating a digital time-jitter compensator on playback is described. Results of tests performed at CTA 21 in a DSN-compatible environment show a total system degradation of less than 0.5 dB (ST_b/N_o) at bit rates as low as 16 bps and over a range from -2 to 9 dB (ST_b/N_o).

I. Introduction

A practical configuration for an open-loop receiver/predetection recording system for use in the DSN with existing standard hardware is described. The breadboard model was implemented in tests at CTA 21 in a DSN-compatible environment. Results demonstrated the feasibility of recording/reproducing telemetry data from an open-loop receiver with a total system loss of less than 0.5 dB (ST_b/N_o) at bit rates as low as 16 bps and over a range from -2 to 9 dB (ST_b/N_o). Description of the analog hardware required to frequency down-convert and band-limit the telemetry IF output on record and to up-convert on playback is followed by a brief analysis of the time-jitter compensator introduced earlier (Ref. 1). Results of tests using the experimental configuration at CTA 21 are presented.

II. Test Configuration

Figure 1 is a block diagram of the experimental setup. The programmable Simulation Conversion Assembly (SCA) modulates the test transmitter with simulated data and feeds receiver 2 through a low-noise amplifier. The IF output of receiver 2, operating in an open-loop mode, is bandpass-filtered to a total bandwidth of 80 kHz and frequency-translated to a center frequency of 50 kHz. The filtering is necessary for image rejection and to ensure that the recorded signal spectrum remains within the bandwidth capability of the breadboard time-jitter compensator used on playback. This bandpass output is then amplified, linearly added to a synchronizing sinusoid at a frequency of 201 kHz and recorded at 76.2 cm/s (30 ips) on an Ampex FR 1400 tape unit. During recording (switches positioned at "B"), the signal is simultaneously

frequency up-converted to S-band and sent through Receiver 1 and the subcarrier demodulator assembly (SDA), where the data are detected. The detected bit stream is acquired and tracked by a software loop in the Telemetry and Command Processor Assembly (TCP) computer, utilizing a Mariner test program, DOI 5081TP. Estimates of ST_b/N_0 and calculated bit error rates corresponding to the recorded data are generated. These statistics, when compared with the program output generated in the direct mode (switch at "A"), show the degradation introduced in the frequency down-conversion, filtering, and up-conversion phases.

The tape is played back on an Ampex FR 2000 unit, which exhibits about an order-of-magnitude better instantaneous phase stability than the FR 1400 recorder. Present memory size limitations of the breadboard time-jitter compensator prevent its use exclusively with the FR 1400 units (Ref. 1).

The compensated playback signal (with the synchronizing sinusoid removed) is then up-converted to S-band (switch at "C") and sent through Receiver 1 and the data detection hardware, and performance statistics are again generated. Losses introduced in the record/playback system and total system losses are determined.

III. Open-Loop Receiver

Figure 2 is a block diagram of a portion of the Block 3-C receiver used in an open-loop configuration. The standard Block 3-C receiver can be operated as an open-loop receiver (OLR) simply by "shorting" the tracking filter and operating the voltage-controlled oscillator (VCO) manually. Receiver gain control is also accomplished manually. In this configuration (see Fig. 2), the signal is frequency-translated to 10.040 MHz using an offset in the VCO and then filtered by a special 80-kHz bandpass filter which is inserted in the telemetry B channel. The linear output of the telemetry IF amplifier is then translated to 50 kHz for output to the time-jitter compensator (TJC).

The main areas of concern in terms of preventing signal degradation are (1) maintain the gain distribution so as to prevent saturation on noise, (2) provide filtering adequate to pass the data with minimum sideband losses yet sufficient to eliminate image noise, and (3) provide sufficient gain so as to minimize thermal noise contributions from all following stages. Saturation on noise, which results in signal suppression, is prevented by maintaining the rms

noise levels at least 20 dB below the 1-dBm compression limit of all OLR components. This is achieved by first setting the gain equal to that which results from the input signal level in the normal mode of receiving. The variable attenuator in the telemetry B channel is then adjusted so that the rms signal-plus-noise power equals -13 dBm as measured at the linear output of the 10-MHz IF amplifier. The square-wave subcarrier frequency was set at 1.7 kHz for data rates of 16 bps and at 3.197 kHz for 2048 bps, to remain within the filter passband of 70 kHz. With these subcarrier frequencies, either 19 or 11 sidebands were passed. Figure 3 shows the characteristics of the filter.

The OLR output level of -13 dBm insured more than adequate gain to overcome thermal noise contributions introduced in following stages of analog hardware.

Figure 4 shows the block diagram of the breadboard upconverter. It is a dual-conversion unit employing doubly balanced commercial mixers. Dual conversion is employed to space S-band signal harmonics so that they are several channels away from the desired signal. The first local oscillator (LO) of 2.457 MHz mixed with the 50-kHz input signal provides harmonic spacing at S-band of 2.507 MHz, which is more than adequate since receiver channel spacing is 370 kHz. The choice of 2.507 MHz is also convenient in that summing it with the second LO of 2292.49 MHz results in an S-band signal in receiver channel 14, which is already available in both receivers and one of the test transmitters at CTA 21. Not coincidentally, the second LO frequency is in receiver channel 7, which also is currently available in a test transmitter at CTA 21.

To prevent saturation in the upconverter, the rms signal-plus-noise levels into both mixers are set at -16 dBm. The 50-dB output attenuator is necessary to prevent saturating the Block 3-C phase-locked receiver used for data recovery. The bandpass filter in the unit has a 1-dB bandwidth of 100 kHz centered at 2.507 MHz.

IV. Record/Playback System

Figure 5 shows the experimental setup for performing recording of 10-MHz telemetry IF. Additionally, an amplifier and a linear mixer are required to add in a sine-wave sync signal at a frequency at least twice the baseband width. Since the record/playback speed ratio is unity, the tape speed at record is set to the value that provides sufficient bandwidth for accommodating the signal

spectrum. Table 1 lists the available tape speeds and associated bandwidths for the Ampex FR 1400 tape unit. With

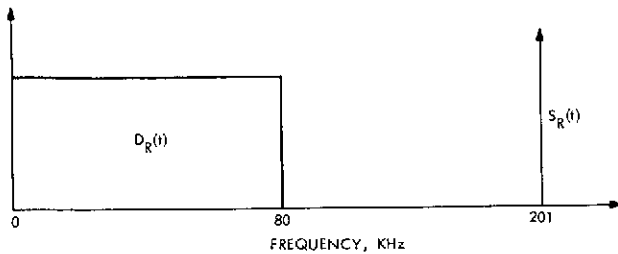
$$D_R(t) = \text{data signal at record}$$

$$S_R(t) = \text{timing signal at record}$$

where

$$S_R(t) = A_R \sin(\omega_0 t + \theta_R), \quad \left(\frac{\omega_0}{2\pi} = 210 \text{ kHz}\right)$$

the input recorded spectrum ideally has the form shown below:



On playback, the output becomes $D_p(t) + S_p(t)$, where now

$$S_p(t) = A_p \sin(\omega_0 t + \theta_p + \int \omega_f(t) dt) + \text{noise}$$

The signal has thus been frequency-modulated by the random flutter frequency $\omega_f(t)$, which may be negative, and experimentally was found to be limited to about a 100-Hz bandwidth.

The instantaneous playback frequency is

$$[\omega_0 + \omega_f(t)]$$

Since both $S_p(t)$ and $D_p(t)$ are recorded/reproduced on the same tape track, they are both equally modulated by $\omega_f(t)$. Therefore, $S_p(t)$ can be used to digitally sample $D_p(t)$ and to clock the samples into a first-in/first-out buffer memory. After the memory is half full, the data are clocked out at a constant rate equal to the frequency of $S_R(t)$ (or ω_0), thereby removing the flutter modulation. This is the function of the TJC.

Figure 6 details the playback arrangement. The sync signal is removed from the output signal track in a phase-locked loop tracking filter with a tracking bandwidth of 100 Hz. The sampled signal is written into the digital buffer at the modulated rate and read out at a constant rate, equal to the frequency of the originally recorded

sinewave sync signal. The output is then passed through a digital-to-analog converter and low-pass filter with a cutoff frequency of half the sync-signal frequency, thus providing a reconstructed and compensated version of the baseband signal. The recorded clock (write clock) directly triggers the analog-to-digital converter (ADC). Therefore, the buffer input rate is

$$\left(\frac{\omega_0 + \omega_f(t)}{2\pi}\right) \left(\frac{\text{samples}}{\text{sec}}\right)$$

The output data rate is

$$\left(\frac{\omega_0}{2\pi}\right) \left(\frac{\text{samples}}{\text{sec}}\right)$$

Figure 7 details the buffer memory organization. A $1K \times 6$ bit array of shift registers is partitioned into 8 independent read/write access lines. Data are shifted through the i th column of registers by either a read or write clock pulse appropriately gated by R1 or W1, each high for 128 read and write clock pulses, respectively. The only forbidden state is when both W1 and R1 are high simultaneously, resulting in an overflow (or underflow) condition. This occurs if the total number of input samples in time T in excess of output samples for the same time T exceeds the buffer capacity. That is, in general, for no overflow, require

$$\frac{1}{2\pi} \int_0^T |\omega_f(t)| dt < \left(\frac{N-1}{N}\right) M$$

for an M sample memory partitioned by N unique read/write lines. Here, $N = 8$, $M = 1K$.

V. Experimental Results

Table 2 summarizes the tests performed and their results. The subcarrier frequency (F_{sc}) was originally set to 8.1 kHz. However, with a total available bandwidth of 80 kHz, centered at 50 kHz, only the first and third harmonics were detected in tests 1 and 2. This sideband suppression introduced about 0.3 dB (ST_b/N_o) data degradation. With the lower subcarrier frequency of 1.7 kHz, sufficient harmonics were passed, thus removing this possible source of error.

Owing to the problem of accurately measuring the signal-to-noise ratio into the receiver, the calculated direct mode bit error rate (BER) was averaged and plotted on

the theoretical BER versus ST_b/N_0 curve to determine the ST_b/N_0 operating value. The playback averaged BER was then plotted on the same curve at the direct ST_b/N_0 value to give an estimate of the data degradation. Figure 8 shows the theoretical BER versus ST_b/N_0 curve with the direct and playback results plotted.

It can be seen that the measured total system loss is within 0.5 dB (ST_b/N_0). Plots of the probability density of occurrence of values of bit error rates are shown in Figs. 9 through 14. Each value of P_D represents the cumulative average number of bit errors that occurred within the range of values represented in a one scale interval of the abscissa. With sufficient statistics it is expected that the curves follow a binomial distribution. The curves of Figs. 9, 11, and 14 best illustrate this, while an insufficient number of BER statistics caused the misleading "bimodal" forms shown in Figs. 10, 12, and 13. The curves point up the fact that the OLR/record/playback system does not introduce any additional data degradation in the form of altering the error distributions, such as causing burst errors, which become more important when coded data are handled.

Overflows in the TJC occurred on an average of twice per one hour playback. This resulted in about a 10% total loss of data typically in an hour's run, due mainly to the time required for the software data loop to reacquire after an overflow. With an automatic reset (not available with the breadboard TJC), the amount of data lost in an overflow, in seconds, is given by

$$\left(\frac{N-1}{N} \right) M \frac{\omega_0}{2\pi}$$

In the tests this quantity equals $(7/8 \times 1024/201 \times 10^3)$, or about 4.5 msec.

VI. Conclusions

A breadboard model of an open-loop receiver/predetection recording system has been effectively demonstrated at CTA 21 in a DSN-compatible environment. Results indicate a total system degradation within 0.5 dB (ST_b/N_0), measured over a range of signal-to-noise and data rate values, including tests performed close to the real-time system data detection threshold.

Reference

1. Sleeks, A. G., "Implementation of a Flutter Compensator for DSN Predetection Recording," in *The Deep Space Network Progress Report*, Technical Report 32-1526, Vol. XVI, pp. 132-139, Jet Propulsion Laboratory, Pasadena, Calif., Aug. 15, 1973.

**Table 1. Tape speed vs bandwidth and recording time
for the Ampex FR1400 tape unit**

Tape speed, cm/s (in./s)	Recording bandwidth, kHz	Recording time, h
304.8 (120)	1500	0.25
152.4 (60)	750	0.5
76.2 (30)	375	1
38.1 (15)	187	2
19.05 (7½)	93	4
9.52 (3¾)	46	8
4.76 (1¾)	23	16

Table 2. Experimental data summary

Test	F_{sc} , kHz	Uncoded rate, bps	Mode	BER	ST_b/N_0 , dB	Loss, dB	BER values	Bits per BER value
T7	3.197	2048	Direct	0.000016	9.40	—	37	100,000
			Playback	0.000020	9.25	0.15	63	100,000
T3	1.70	16	Direct	0.004061	5.50	—	17	1000
			Playback	0.003966	5.50	0	54	1000
2	8.1	16	Direct	0.041107	1.80	—	298	96
			Playback	0.046761	1.50	0.30	115	96
1	8.1	16	Direct	0.049992	1.35	—	249	96
			Playback	0.058408	0.95	0.40	224	96
T6	1.7	16	Direct	0.063121	0.70	—	34	1000
			Playback	0.067182	0.50	0.20	43	1000
T5	1.7	16	Direct	0.113225	-1.35	—	71	1000
			Playback	0.127155	-1.85	0.50	35	1000

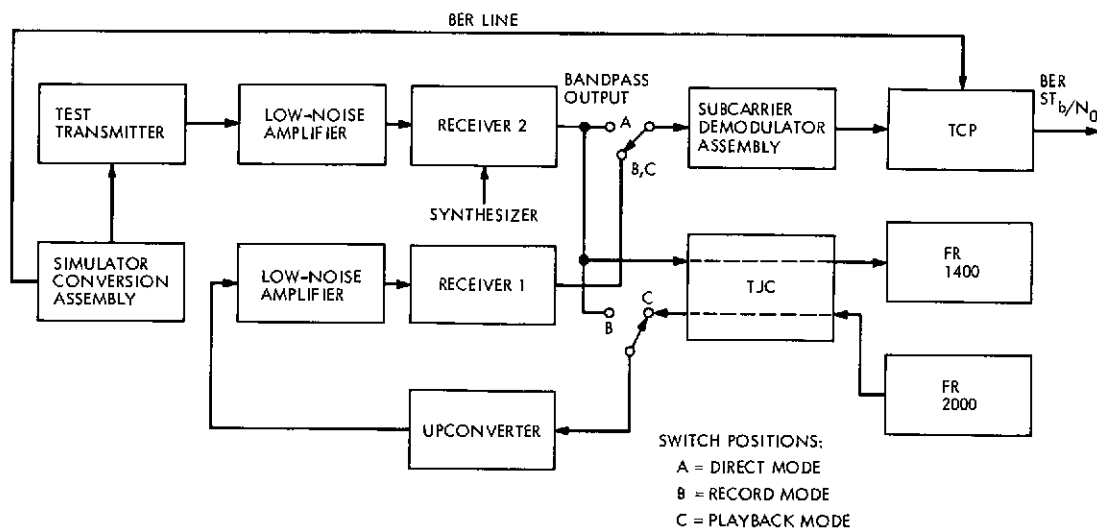


Fig. 1. Block diagram of experimental setup

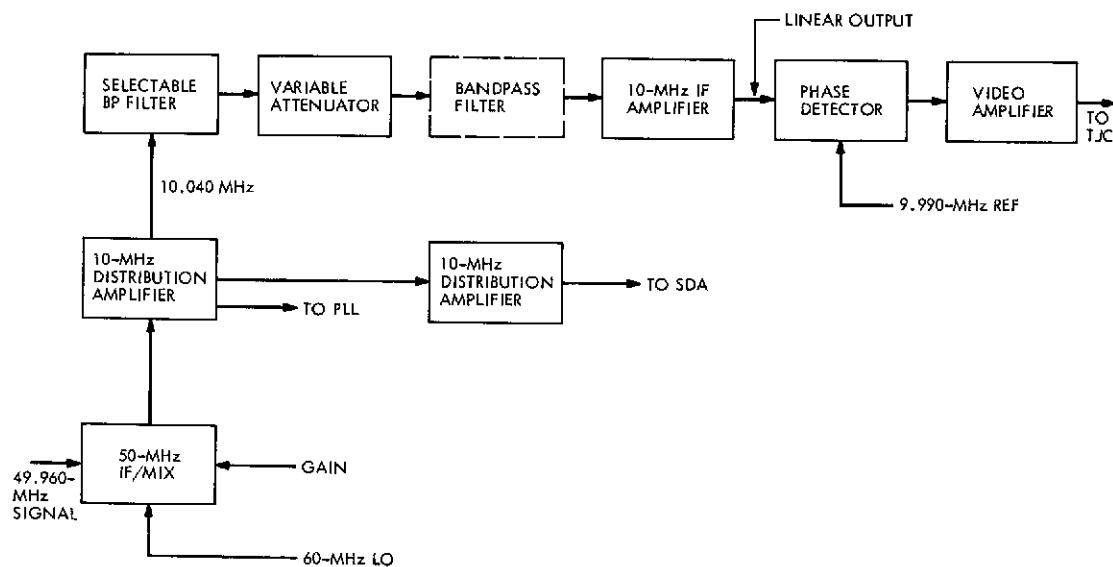


Fig. 2. Partial diagram of the Block 3-C receiver showing open-loop configuration

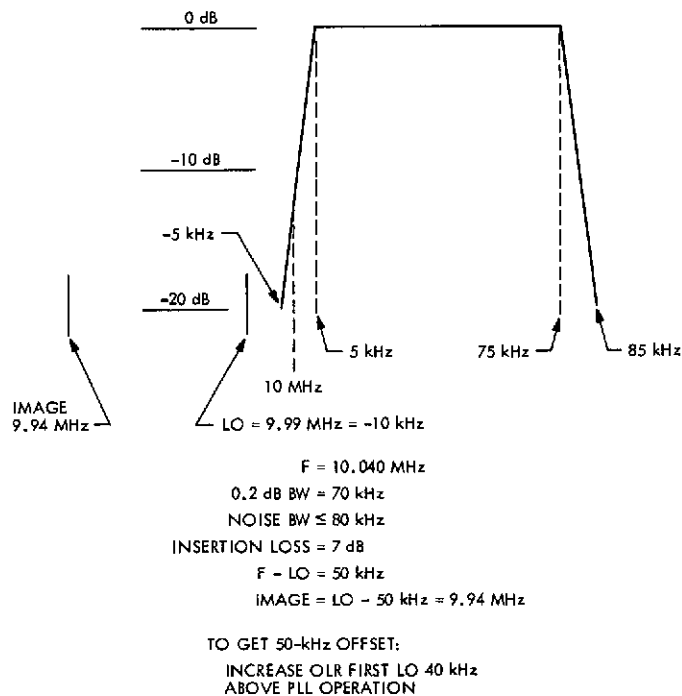


Fig. 3. Open-loop receiver bandpass filter

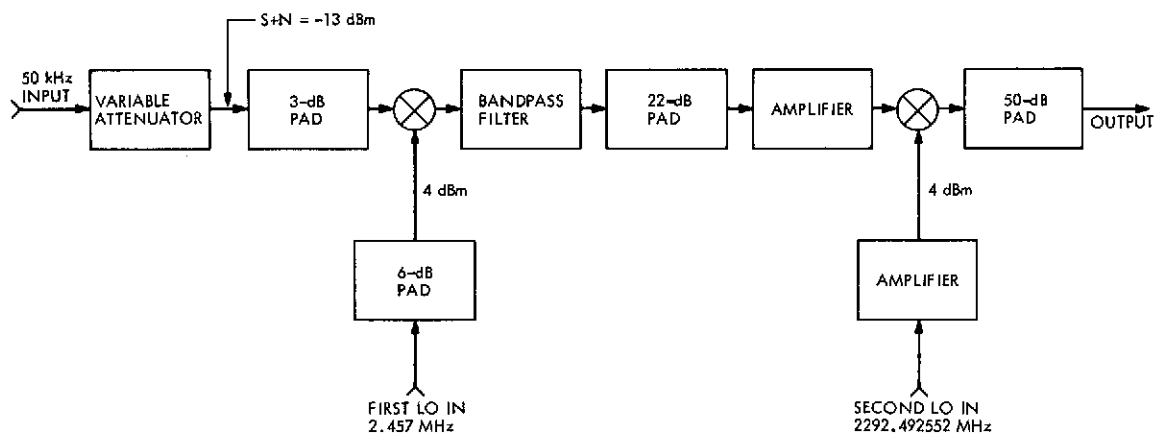


Fig. 4. Upconverter block diagram

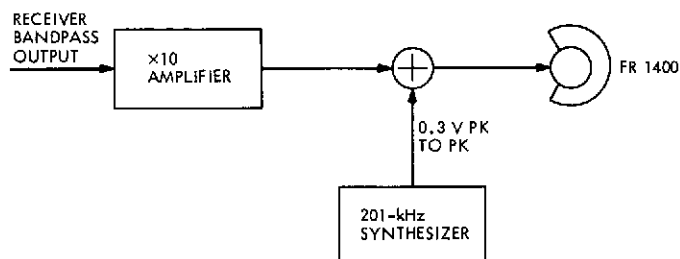


Fig. 5. Recording setup

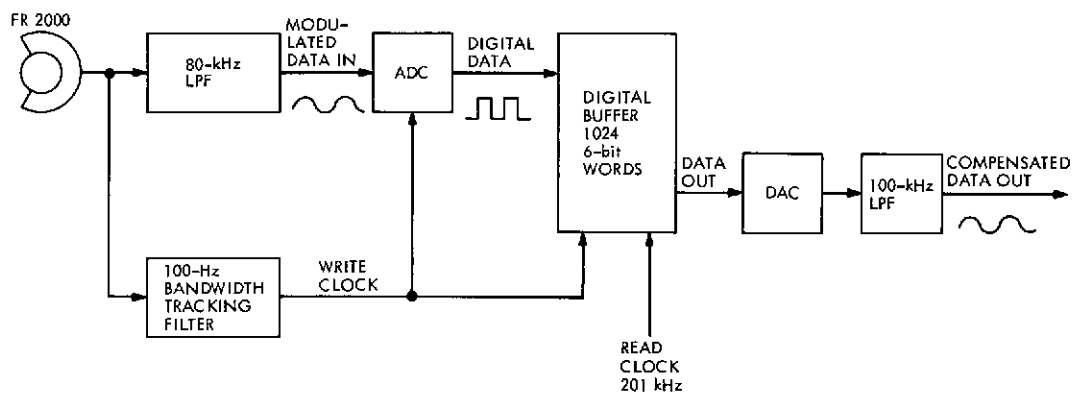


Fig. 6. Playback setup with TJC

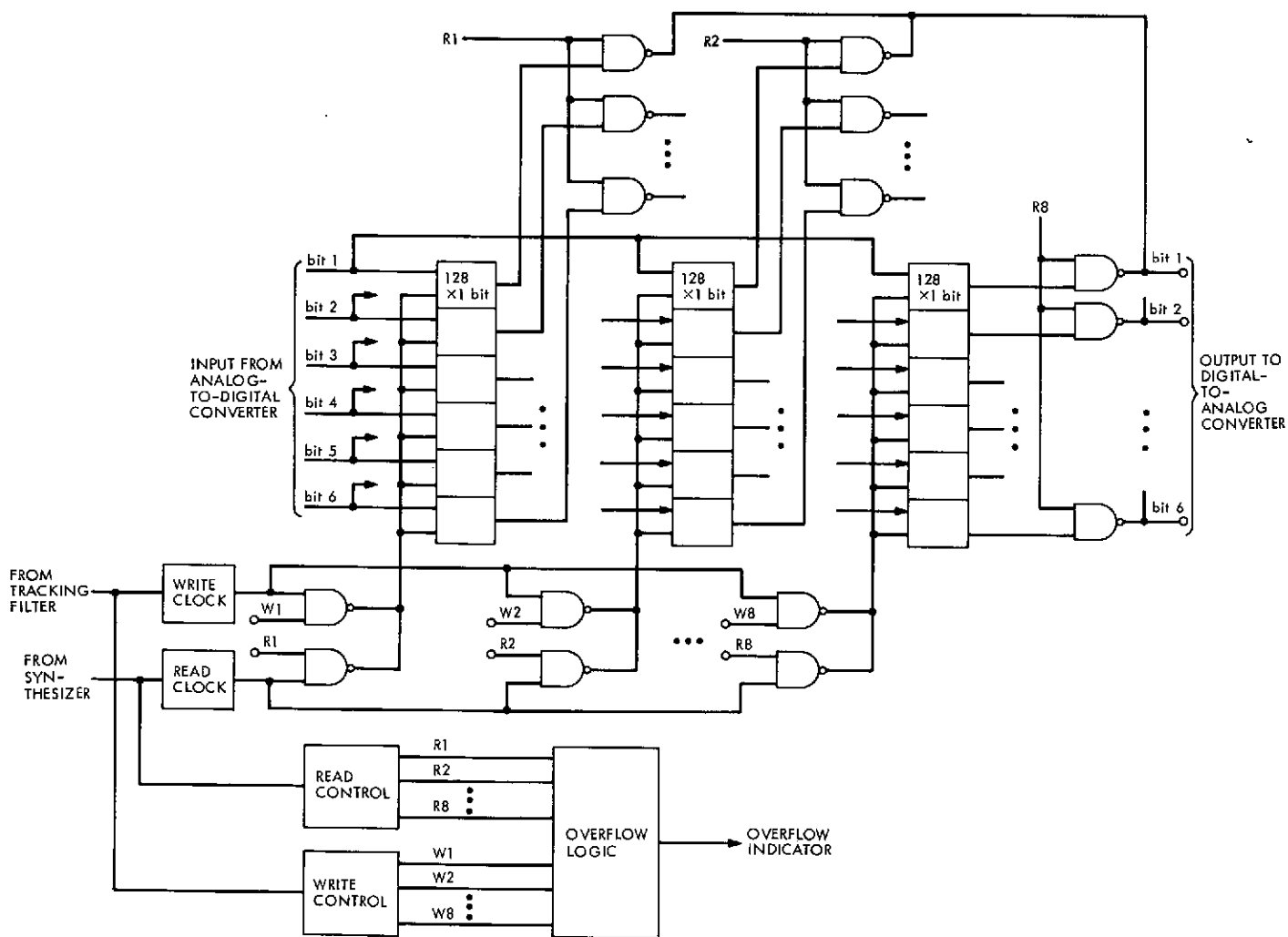


Fig. 7. Memory organization 1K \times 6 bit array

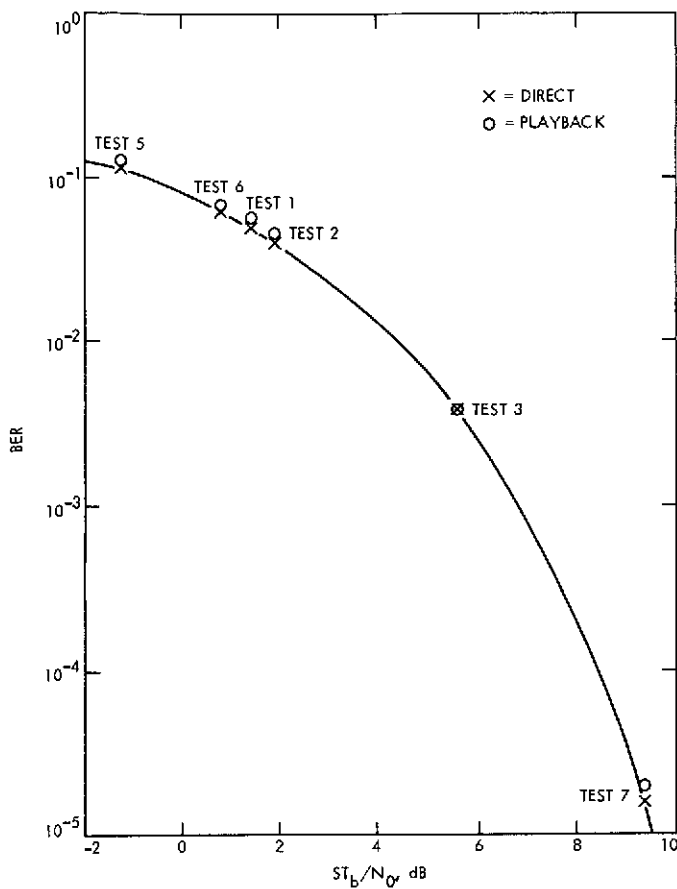


Fig. 8. Experimental results

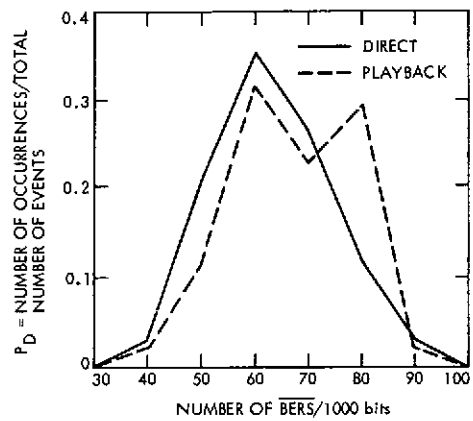


Fig. 10. Test 6 results (0.7 dB)

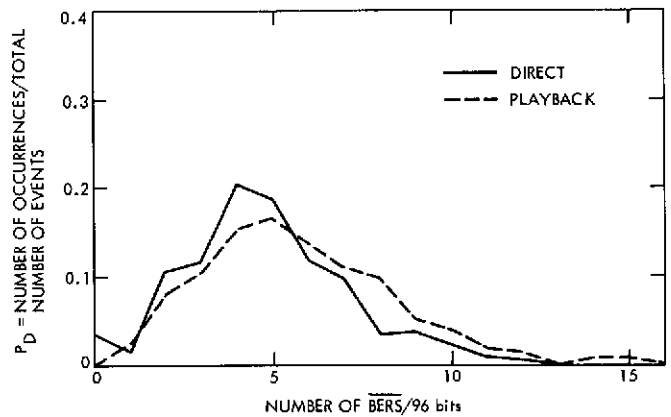


Fig. 11. Test 1 results (1.35 dB)

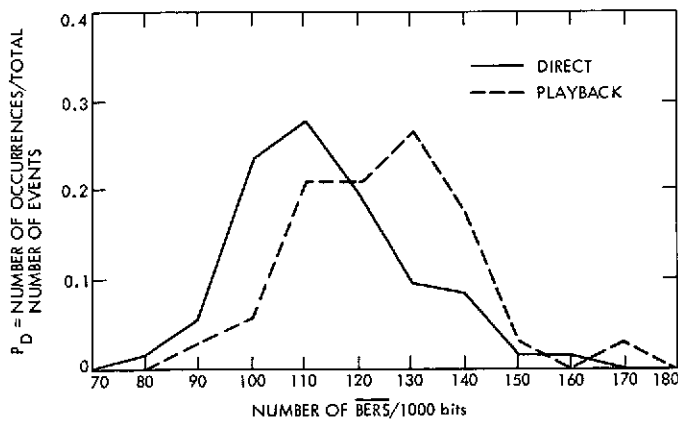


Fig. 9. Test 5 results (-1.35 dB)

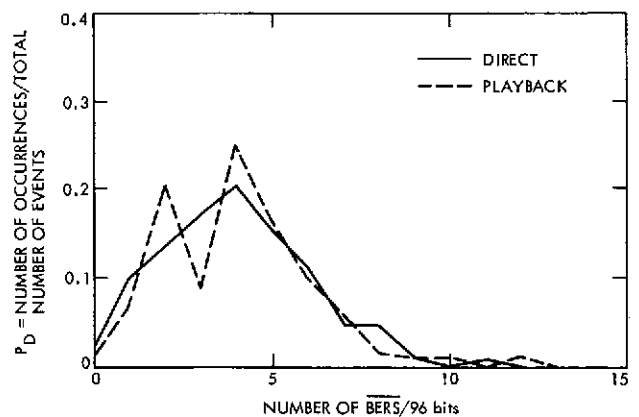


Fig. 12. Test 2 results (1.8 dB)

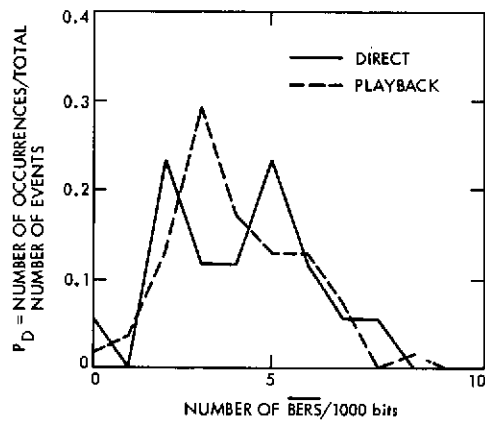


Fig. 13. Test 3 results (5.5 dB)

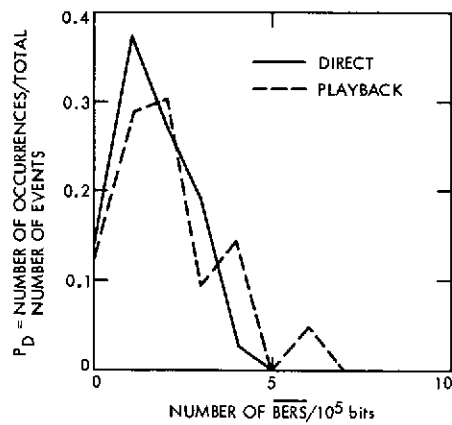


Fig. 14. Test 7 results (9.4 dB)

High-Speed Data Block Bursts

J. P. McClure

DSN Data Systems Development Section

It is well established that ground communications bit errors occur in groups, or bursts. A recent study shows that 1200-bit high-speed data blocks that contain errors also tend to occur in groups. A study of these block bursts indicates that single block errors are most common, but that about 10% of the block bursts are composed of seven or more blocks. A significant number of good blocks are contained within these bursts. The single block errors are apparently the result of random happenings, however the longer bursts represent deteriorating circuit conditions.

I. Introduction

An examination of the data available from the central communications terminal decoders discloses that faulty blocks may be isolated events but that many times they occur in groups. These groups, or block bursts, are evidently the result of poor line conditions extending over many block times. In the limit, the line fails and the resulting long burst becomes indistinguishable from an outage.

(As used herein, a block burst (or just burst) is a string of contiguous blocks starting with a faulty block, ending with a faulty block, and containing no more than nine consecutive good blocks. A burst may be as short as one block in which case it starts and ends with the same faulty block. Faulty blocks are those that contain bit errors, or that are not received at all.)

Raw data for a seven-day period (July 1-7, 1973) were manually analyzed to determine the high-speed data (HSD) burst characteristics. This analysis yields information of value to the user of the Ground Communications (GC) and to data system designers. It will also be used within the GC to aid in the design of error control systems.

II. Burst Length Distribution

Figure 1 depicts the burst length distribution for the DSS-to-JPL circuits. On this plot the abscissa shows the percentage of bursts having a length equal to or less than the ordinate value.

Per Fig. 1, the majority of the bursts, 71%, consist of only a single block in error. This high figure somewhat undermines the concept that faulty blocks run in bursts. These single block bursts reflect random errors, whereas the longer bursts denote deteriorating circuit conditions.

III. Good-Bad Ratio

The longer bursts have many good blocks imbedded in them. Table 1 gives the ratio of faulty blocks to good blocks within a burst for several DSSs and the Ames Research Center, as well as the combined DSSs.

For the complete 7-day sample the combined DSS figure of 6.95 indicates that bursts contain nearly seven times as many faulty blocks as good ones. This figure, while accurate, includes all of the faulty blocks during outages (when only faulty blocks can be received).

Condition B deletes the long outages, and condition C, eliminates all outages longer than those that the proposed HSD error correction system could correct. Finally, condition D removes all one-block outages as well to show an all-DSS ratio of 1.11 – just about as many good blocks as bad ones during this condition.

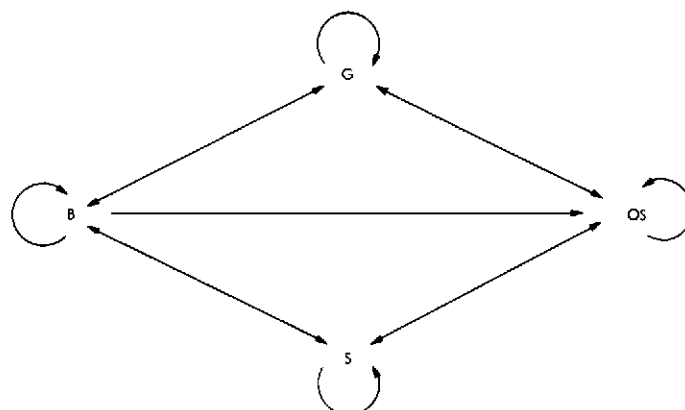
IV. Transitions

During burst periods the blocks may be divided into four different categories:

- (1) G: good blocks, free of errors. These blocks occur only during nonburst periods.
- (2) B: bad blocks, which contain bit errors but are recognizable as blocks.
- (3) OS: out-of-sync blocks that are either not received, or if received cannot be recognized. (Same as being out of lock.)
- (4) S: satisfactory blocks that are error-free, but contained within a burst.

Bursts are composed of B, OS, and S category blocks.

Blocks follow one behind the other down the line, without gaps. Transitions occur at every block boundary. For instance, a good block followed by a bad block is a good-to-bad ($G \rightarrow B$) transition. The permissible transitions between the four categories are as follows:



As shown, it is possible to have transitions from good-to-bad ($G \rightarrow B$), bad-to-good ($B \rightarrow G$), bad-to-bad ($B \rightarrow B$), etc. Due to hardware design it is not possible to have $OS \rightarrow B$ transitions. The definition of a burst prohibits transitions between the G and S states.

The following table shows the transition probabilities between each of the states for the combined DSSs. This matrix is read from the top down. For instance, given a bad block (B), the probability it will be followed by an OS block is 0.087 while the probability of a bad followed by another bad is 0.170.

	G	B	OS	S	
G	0.999536	0.554	0.020	0	
B	0.000450	0.170	0	0.291	
OS	0.000014	0.087	0.972	0.008	DSS total
S	0	0.189	0.008	0.701	Full sample

The next matrix is similar, but in this case all outages of 33 blocks or more have been deleted. This case is representative of the probabilities faced by the proposed HSD error correction system.

	G	B	OS	S	
G	0.999544	0.548	0.317	0	
B	0.000442	0.173	0	0.291	
OS	0.000014	0.088	0.567	0.008	DSS total
S	0	0.191	0.116	0.701	Outages > 32 blocks omitted

V. Burst-Outage Relationship

A previous article (Ref. 1) discussed HSD outages, defining them as events consisting of ten or more consecutive faulty blocks. Outages occur when the transmission

system completely fails. In contrast, bursts normally reflect system degradation. Most bursts are short, with the median burst being only one block long. The typical outage is much longer, 60 blocks or so.

Correlating the outage and burst data produces the burst-to-outage ratio:

Location	Bursts per outage
Canberra	60.5
Madrid	51.2
Goldstone	25.0
Hartebeesthoek	61.4
Ames	80.0
DSS Total	51.6

In comparison to bursts, outages are rather rare events — though not as rare as desired.

VI. Conclusion

Data blocks containing errors tend to occur in groups, though there are a substantial number of single blocks in error.

Most of the bursts are short and quite amenable to error correction without incurring significant data delay. Outages are much less frequent than short bursts.

Reference

1. McClure, J. P., "High-Speed Data Outage Distribution," in *The Deep Space Network Progress Report*, Vol. XIX, Technical Report 32-1526, pp. 161-164. Jet Propulsion Laboratory, Pasadena, Calif., Feb. 15, 1974.

Table 1. Ratio of faulty blocks to good blocks

Condition	Faulty/good ratio within a burst					
	Canberra	Madrid	Goldstone	Hartebeesthoek	Ames	All DSSs
A. Complete 7-day sample	5.4	5.1	34.3	1.5	8.2	6.95
B. 7-day sample, less all outages of 100 blocks or more	2.2	1.5	7.2	1.5	2.4	2.27
C. 7-day sample, less all outages of 33 blocks or more	1.7	1.1	4.7	1.4	2.3	1.72
D. 7-day sample, less all outages of 33 blocks or more, and less all 1-block outages	1.2	0.7	2.8	0.9	1.3	1.11

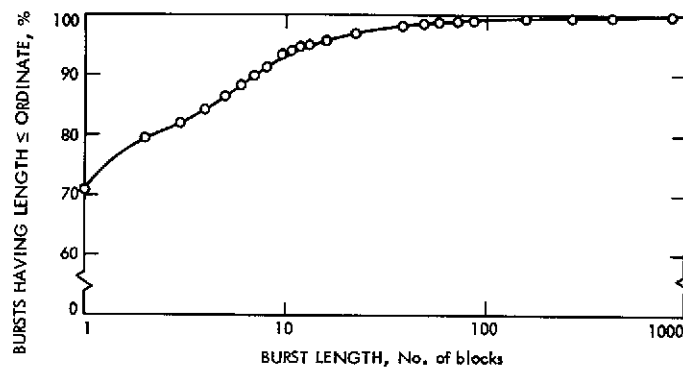


Fig. 1. Burst length distribution—DSS total

Helios Spin Modulation Simulation Tests

N. C. Ham

R.F. Systems Development Section

Additional analysis and study have completed the mathematical model of the Helios spacecraft low-gain antenna and permitted the formulation of experimental tests for simulating the spin modulation effects at a typical Deep Space Station communication system. The details of the test technique, system test configuration, and results of the simulation tests are explained.

I. Introduction

Previous analysis and study of the Helios low-gain antenna (LGA) were covered by Ref. 1, in which a mathematical model of the LGA was developed, with particular emphasis on the region of signal interferometry.

As a result of this modeling effort, a better understanding of the affected telecommunication link elements was achieved thus permitting formulation of realistic experimental tests by simulating these effects at a typical Deep Space Station communication system.

This article is a study extension of the LGA mathematical model, detailing the experimental test technique and results of the simulation testing that was performed at the JPL Compatibility Test Area, (CTA 21).

II. LGA Mathematical Model

The general equation of the mathematical model used in Ref. 1 follows:

$$E_s \gamma = E_D \left[1 + \left(\frac{E_H}{E_D} \right)^2 + 2 \left(\frac{E_H}{E_D} \right) \cos \beta \right]^{1/2} \times \arctan \left(\frac{\frac{E_H}{E_D} \sin \beta}{1 + \frac{E_H}{E_D} \cos \beta} \right) \quad (1)$$

where $E_s \gamma$ is the magnitude and phase of the resultant combined signal of the dipole and horn radiated signals

(E_D and E_H , respectively) of similar polarization, and β is the relative phase angle between the radiated signals.

Figure 1 is a reproduction of the computer plot and measured data comparison (from Ref. 1) of the carrier signal phase variation vs the spacecraft rotational angle for one complete rotation. A study of the figure reveals poor correlation near the region of $\phi = 180$ deg due to the assumed initial lead phase angle relationship between the horn and dipole antenna signals.

Figure 2 illustrates the spacecraft mockup test setup used to measure the resultant LGA radiation patterns. The reference antenna shown is used as the reference signal input to the network analyzer, while the LGA provides the input to the other terminal, which is designated the measured input. The phase relation of the reference antenna signal to the LGA signal, both of which are received from the radiating test antenna, is an initial phase condition that must be accounted for in the mathematical model. This initial condition is different for each value of the aspect angle (the angle formed by the spacecraft Z-axis and the centerline of the test antenna); this angle is set for a pattern test prior to rotating the spacecraft about the Z-axis. Associated with this phase relation between the reference signal and the LGA signal is an internal phase relation, within the spacecraft microwave circuitry, between the horn and dipole antenna.

Figure 3 depicts these initial phase conditions for a specific aspect angle. Figure 3a is the vector diagram, where only the internal phase is considered, and Fig. 3b shows the relation with the phase of the test measurement physical configuration included; β is the horn antenna internal leading phase angle, and Ω is the initial phase existing between the reference and LGA antenna signals. Also shown are the expressions for the resultant phase angle (combined horn and dipole signals) due to these conditions.

The computer plot of the configuration expression of Fig. 3b,

$$\gamma = \Omega + \arctan \left(\frac{1 + \frac{E_H}{E_D} \sin \beta}{\frac{E_H}{E_D} \cos \beta} \right) \quad (2)$$

is shown in Fig. 4, where Ω is set to a value of 90 deg.

Figure 5 is a recomparison of the new computer plot to the measured antenna pattern previously shown, and reveals a better correlation at $\phi = 180$ deg.

Suffice it to say, the mathematical model, to a first approximation, is a valid representation of the Helios LGA. The goal for its development was to assess the nature of the rapid phase deviation of the carrier signal in the interferometry region in terms of its discontinuity (i.e., varying $\pm \infty$ deg) or its deviation in known and predictable magnitudes.

The assumption, derived from the model and measured patterns, is that the periodicity of the amplitude and phase variations is an average 25 Hz per spacecraft revolution (at 1 revolution per second). Similarly, the respective magnitude of these variations can be tabulated from the measured patterns made with various aspect angles and combinations of polarized signals, namely, right circular polarization (RCP), and horizontal or vertical linear polarization.

III. Spin-Modulation Variable Values

A summary of the spin-modulation effects is shown in Fig. 6 for the downlink signal case, where the ground receiving system is polarized for RCP.

The amplitude modulation variation shown, as a function of the aspect angle, is the magnitude of the significant average values that occur per spacecraft revolution at the specific aspect angle. The average is a visual integration of the measured pattern response whereby the deep nulls with narrow width are integrated and normalized; the normalizing value is determined by the pulse duration of the 128 and 256 symbol-per-second pulse-code modulation (PCM) telemetry data and the receiver automatic gain control (AGC) loop bandwidth.

The rationale for determining the average value follows: to simulate the actual varying magnitude response pattern per spacecraft revolution requires a complex function generator or computer program that would be costly. Instead, the use of a constant-magnitude continuous-simulation waveform equal to the average value simplifies the testing and should be a valid representation of the effect.

The magnitude of the phase modulation within the interferometry region is similarly obtained from the measured patterns. The heavy lines indicate the predomi-

nant magnitude per spacecraft rotation over the interferometry span of the aspect angle. In other words, the large phase modulation (PM) variations (>90 deg) occur for only a small percentage of one revolution. For aspect angles greater than 50 deg, the phase variation magnitude is fairly constant per revolution, decreasing in value as the aspect angle increases.

The frequency modulation (FM) effect was not covered by the mathematical model and was only briefly treated in Ref. 2; therefore, it will be further expanded here.

The FM effect is caused by the horn element of the LGA because of the horn's physical offset of approximately 6.5λ (wavelength at the downlink frequency) from the spin axis, and takes the form of an added doppler frequency component, $\Delta F_D = \sin \psi \cdot 6.5\lambda \sin 2\pi f_s t$, varying about the normal Earth radial velocity doppler frequency (Fig. 7). Here f_s is the spacecraft rotational rate and ψ is the aspect angle. For the stabilized condition of 1 revolution per second, the equation becomes $\Delta F_D = \sin \psi \cdot 13\pi \sin 2\pi t$, where $13\pi = 6.5\lambda$ because 2π radians occur for one wavelength. Thus, for the RCP mode, the FM deviation increases as a function of the aspect angle to a maximum value of approximately 28 Hz at an aspect angle of 40 deg, and rapidly decreases at greater angles because the gain of the RCP horn is decreasing and the gain of the dipole antenna is increasing.

Since the FM occurs at a 1-Hz rate, the maximum rate of change of frequency deviation, or doppler rate, occurs at the aspect angle producing the maximum frequency. For example, the 28-Hz magnitude is equivalent to an effective offset displacement of 4.2λ , (i.e., $6.5\lambda \times \sin 40$ deg); by differentiation of the deviation expression,

$$\begin{aligned}\Delta \dot{F}_D &= \frac{d}{dt} (8.4\pi \sin 2\pi t) \\ &= -16.8\pi^2 \cos 2\pi t\end{aligned}\quad (3)$$

or $\Delta \dot{F}_D = -165 \cos 2\pi t$ Hz/s. It is this rate of change of doppler that has a stressing effect on the receiver carrier phase-locked loop.

Figure 8 is the similar characteristic where the ground receiving antenna can be configured to receive either horizontal linear or vertical linear polarization. When the horizontal linear mode (for aspect angles from 0 to 50 deg) that is orthogonal to the vertically polarized spacecraft dipole LGA is used, the interferometry amplitude modulation (AM) effects are less severe than those in the RCP

reception case; however, the FM effect is greater, since the rotating horn antenna now remains dominant over a greater range of aspect angles. The result is that ΔF_D and \dot{F}_D reach maximum values of 31 and 197 Hz/s, respectively, at the aspect angle of 50 deg. Associated with the FM deviation are some low PM deviations of ± 15 deg near this region.

During the vertical linear reception mode, the vertical linear component of the RCP horn element and the normal vertical linear signal from the dipole element combine to create interferometry effects (as in the RCP case) within the range of aspect angles of 40 to 50 deg.

IV. Simulation Test Model

Figure 9 is a functional block diagram depicting the simulation model that is used for obtaining experimental test data resulting from spin modulation effects.

The spin modulation effects FM, PM, and AM are separated to permit stimulating the transmission system, at various magnitudes and rates, either individually or combined, in concert with the values determined and delineated in the preceding section. Similarly, the data signal can be adjusted separately to phase-modulate the system; this is the primary modulation for evaluating spin modulation effects.

The FM signal is $e_{FM}(t) = E_1 \sin 2\pi t$, where the magnitude E_1 sets the peak frequency deviation, $\pm F_D$, and $2\pi t$ is the 1-Hz rotational rate of the spacecraft.

The PM signal

$$\begin{aligned}e_{PM}(t) &= \frac{2}{\pi} E_2 (\sin 2\pi 25t \\ &\quad - \frac{1}{2} \sin 4\pi 25t + \frac{1}{3} \sin 6\pi 25t - \dots)\end{aligned}$$

represents the Fourier series for a sawtooth waveform and is illustrated in Fig. 10 for the fundamental frequency of 25 Hz.

Similarly, the AM signal

$$\begin{aligned}e_{AM}(t) &= \frac{2}{\pi} E_3 (1 + \frac{2}{3} \cos 4\pi 12.5t \\ &\quad - \frac{2}{15} \cos 8\pi 12.5t - \frac{2}{35} \cos 12\pi 12.5t + \dots)\end{aligned}$$

is the Fourier series of a full-wave rectified sine wave, which is used to simulate the interferometry amplitude variation characteristics. Figure 11 illustrates this waveform, where the fundamental sine-wave frequency is set to 12.5 Hz to drive the bridge rectifier, whose output is the desired signal with a periodicity of 25 Hz.

The data signal is comprised of a square-waveform sub-carrier, at a fundamental frequency of approximately 32 kHz, biphas-modulated by the information data symbol expressed as $e_D(t) = E_{sc} \sin(\omega_c t + m_p \cos \omega_{sp} t)$, where $E_{sc} \sin \omega_{sc} t$ is the subcarrier square-waveform, m_p is the biphas-modulation index (± 90 deg), and $\cos \omega_{sp} t$ is the square-waveform pseudo-noise (PN) sequence. The data symbol rate is set to values of 128 symbols per second (SPS) to simulate the uncoded telemetry mode, or to 256 SPS to simulate the convolutionally-coded rate half-mode.

The space attenuation simulation is achieved by the variable attenuator and determines the values of the carrier power, P_c , and sideband power S . The ratio of P_c to S is set by the data signal amplitude E_{sc} — the modulation index. The exact value of the space attenuation is determined by the desired value of the carrier power to noise spectral density ratio P_c/N_0 , or data power per symbol rate to noise spectral ratio ST_s/N_0 .

In the case of obtaining simulation data with no applied data modulation, the characteristics of the carrier phase-locked loop (PLL) are evaluated and the P_c/N_0 ratio is normalized to an independent variable M , which is the margin in decibels above the loop threshold signal level, and carrier cycle slippage to the dependent variable.

When data modulation is applied, ST_s/N_0 is the independent variable, and symbol error rate the dependent variable.

V. System Test Configuration

Figure 12 is the functional block diagram of the system test configuration used at CTA 21.

The method of setting the magnitude of the frequency deviation (or FM) was first to determine the sensitivity value of the exciter voltage-controlled oscillator (VCO) (which was 400 Hz/peak volts) and then to adjust the output level of the 1-Hz sine-wave generator to 10,000 times the desired frequency deviation, followed by inserting a 40-dB attenuator in series with the generator/VCO

interface. For example, the ΔF_D desired was ± 31 Hz at S-band; thus, the peak voltage setting is $E_1 = (31 \text{ Hz} \times 10,000)/(96 \times 400 \text{ Hz/V}) = 0.08 \text{ V peak}$, where 96 is the frequency multiplication factor of the exciter.

An "L" network, consisting of a series element of 100,000 Ω and a 50- Ω shunt element, was used to terminate the 50- Ω , 40-dB attenuator and high input impedance of the VCO input terminal.

The information data simulating the downlink telemetry were obtained from the Simulation Conversion Assembly (SCA), which provided the square-wave sub-carrier biphas-modulated by the square-wave PCM data. The PCM data were also simultaneously sent to the Symbol Synchronizer Assembly (SSA) as reference symbols for comparison against the detected data to compute symbol error rate (SER) statistics.

The carrier modulation index, when modulated by the information data, is established by the carrier suppression method, where the suppression $P_c/P_T = 20 \log \cos$ (phase deviation angle). This suppression was measured by the offset oscillator-mixer and wave-analyzer assemblies.

In like manner, the PM 25-Hz sawtooth waveform was used to phase-modulate the exciter carrier, and the magnitude of the sawtooth peak-to-peak waveform E_2 was set by using the calibration values of the exciter phase modulator obtained from the data/subcarrier signal E_{sc} .

The AM function generator, as shown in Fig. 11, was connected to PIN modulator circuitry to amplitude-modulate the S-band signal by absorption modulation. The degree of AM was set by monitoring the carrier signal, which was translated by the offset-oscillator mixer to 20 kHz, until the desired modulation depth was achieved as observed on the modulation envelope display on an oscilloscope.

The variable attenuator is used to establish the receiver input to the desired level, which is measured by the Y-factor measuring assembly. The values of ST_s/N_0 and P_c/N_0 are the variables changed during the simulation tests.

The carrier loop cycle slip information was recorded by connecting the output of the doppler extractor (0 and 90-deg output ports) to a strip chart recorder. Since the extractor provides the doppler at $1/4$ the S-band value, each cycle slip of the carrier PLL appears as a 90-deg (or

1/4-cycle) change, which is easily discernible as a permanent record on the strip chart recorder. Hence, for a given signal level setting, the strip chart recorder is started and time marks are made on the chart 10 min apart for subsequent data reduction.

VI. Test Sequence and Results

The first experimental test run was conducted by formulating the worst-case conditions when the RCP mode is used for receiving the downlink signal. A review of Fig. 6 reveals that this condition occurs at the aspect angle of 45 deg where the AM is 15 dB peak-to-peak (p-p) and the PM is ± 150 deg p-p. Secondary condition values of 15 dB p-p AM and ± 90 -deg PM (for the aspect angle of approximately 52 deg) and similar values in conjunction with ± 30 -Hz FM (for the aspect angle of 40 deg) were also selected.

The sequence for obtaining test data is as follows: (1) The values for a particular test condition AM, PM, or FM spin modulation were adjusted as previously discussed; (2) the data rate and modulation index (MI) were selected and set; (3) the receiving/telemetry system loop bandwidth values were set; (4) the RF signal level, or ST_s/N_o , was set or measured by the Y-factor technique (performed with data and spin modulation off); (5) the data and appropriate spin modulation were applied; (6) the test was run for an appropriate length of time to gather SER statistics at the Telemetry and Command Processor (TCP) output. The sequence was then repeated at different settings of signal level.

Figure 13 shows the results when the values of AM and PM shown were utilized as the spin modulation parameters. The receiver RF PLL was set to 152 Hz, the AGC loop bandwidth (BW) to wide, the Subcarrier Demodulator Assembly (SDA) and SSA BWs to medium, and the information data at 256 bits/s (uncoded) to produce a carrier modulation index of 42 deg. Also shown are the results when ± 30 -Hz FM together with 15-dB AM, and ± 38 -Hz FM with 15-dB AM were applied in conjunction with the information data. The performance characteristics of the ideal coherent phase-shift-keyed (PSK) curve are also shown as a reference to indicate the degree of degradation resulting from spin-modulation effects.

Figure 14 shows the test results where the spin modulation values were ± 90 -deg PM plus 15-dB AM, with the information data rate at 256 SPS and the receiver PLL bandwidth, as the parameter, set to 48- and 152-Hz values.

A recheck of Fig. 8 for the linear polarized reception mode shows that the AM and PM values are less severe than in the RCP mode. However, the FM deviation increases as the aspect angle increases, particularly for the horizontal linear polarization mode. This is due to the orthogonal rejection of the vertical linear polarized signal from the dipole antenna and permits the horn to remain dominant for greater values of aspect angles. Figure 15 shows the results of the spin modulation effects for this horizontal linear condition where the AM values were 7.5 to 9 dB, PM was constant at ± 15 deg, and the FM deviation frequencies were 31 and 36 Hz. These parameters are shown grouped in the respective combinations, where the additional parameters used were the symbol rates at 256 and 128 SPS and the exciter modulation index was set to 42 and 55 deg.

To gain insight into the individual contribution to the system degradation from the spin modulation effects, Fig. 16 shows the results of the tests when ± 90 -deg PM only, and 15-dB AM spin modulation only, were applied.

Similarly, the RF carrier PLL cycle slippage characteristics show the sensitivity of this loop to the spin modulation effects, and Fig. 17 illustrates the results for the loop bandwidth of 152 Hz. As one would expect, the ± 150 -deg PM requires a greater margin level than the ± 90 -deg PM value for a given number of cycles slipped, and the addition of the AM component has a devastating effect.

Figure 18 illustrates a similar test result and test condition, with the PLL bandwidth set to 48 Hz, and shows that a greater margin level above the spin-modulation reference condition is required for the same cycle slippage rate than in the case of the wider loop bandwidth value. This is as expected, since the wider bandwidth loop, as it becomes wider at larger margin levels, tends to track out more of the PM sawtooth sideband frequency components (see Fig. 19).

References

1. Ham, N. C., "Helios Spacecraft Low-Gain Antenna Model," in *The Deep Space Network Progress Report*, Technical Report 32-1526, Vol. XVIII, pp. 147-162. Jet Propulsion Laboratory, Pasadena, Calif., Dec. 15, 1973.
2. Ham, N. C., "Amplitude and Frequency Modulation Effects to Telemetry Link Reception," in *The Deep Space Network Progress Report*, Technical Report 32-1526, Vol. XIV, pp. 149-160. Jet Propulsion Laboratory, Pasadena, Calif., Apr. 15, 1973.

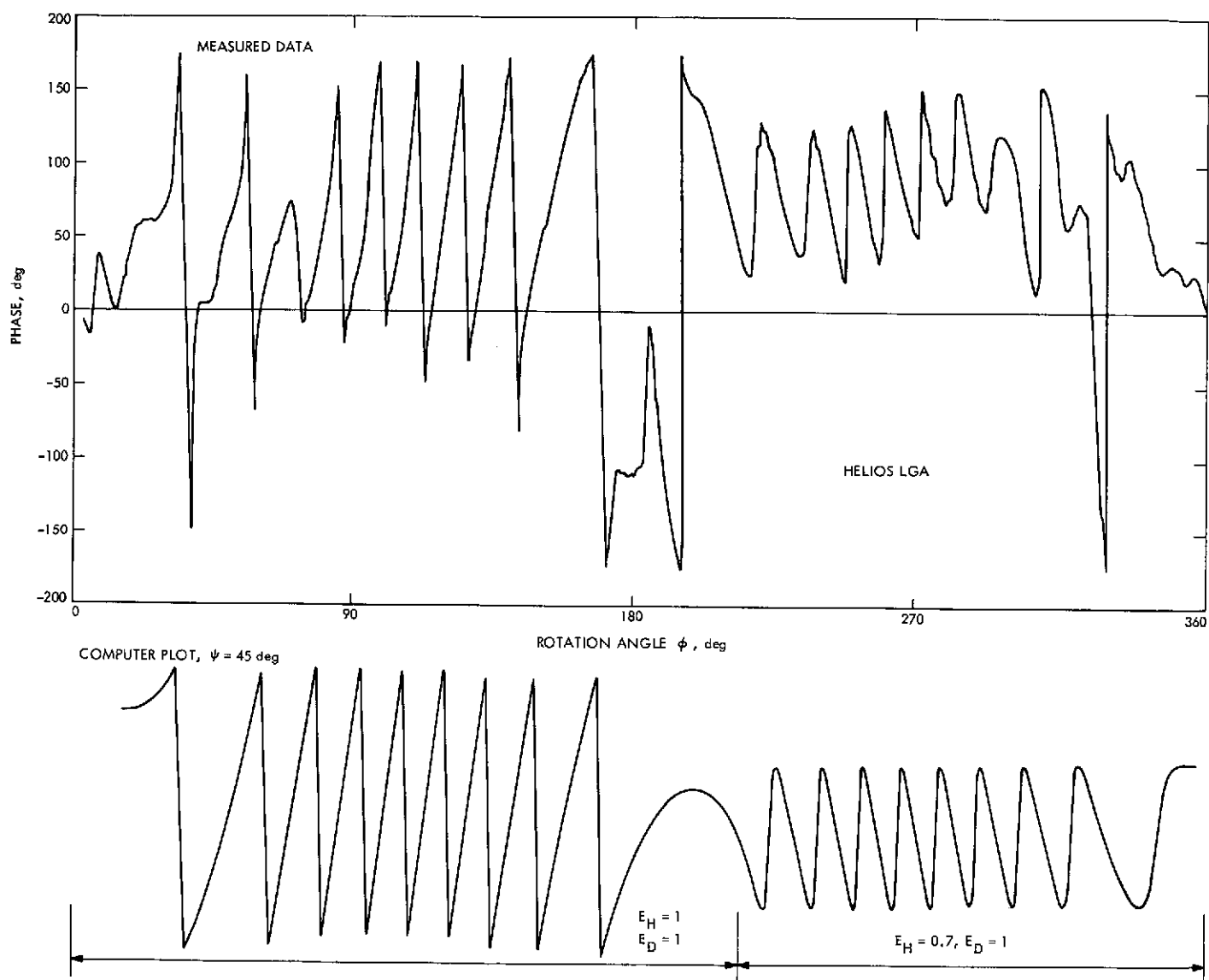


Fig. 1. Computer plot vs measured phase data, $\psi = 46$ deg

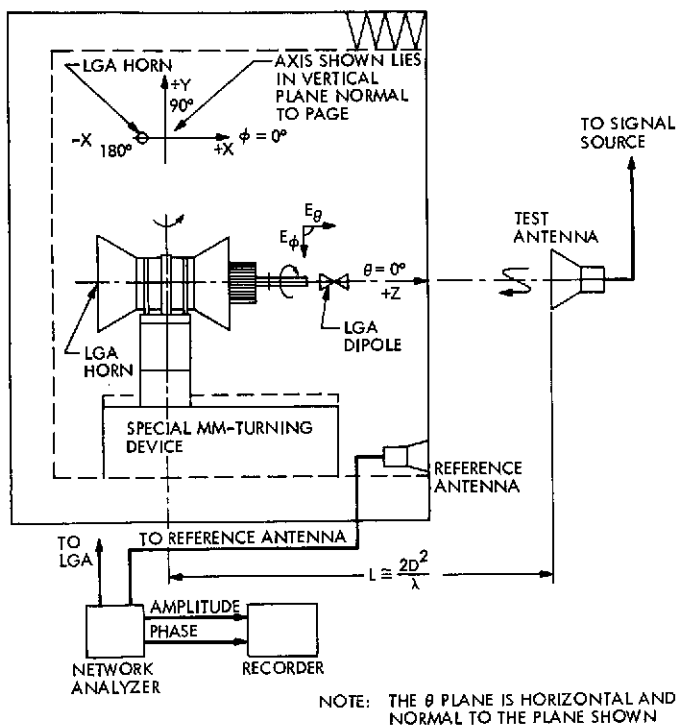


Fig. 2. Radiation pattern test setup

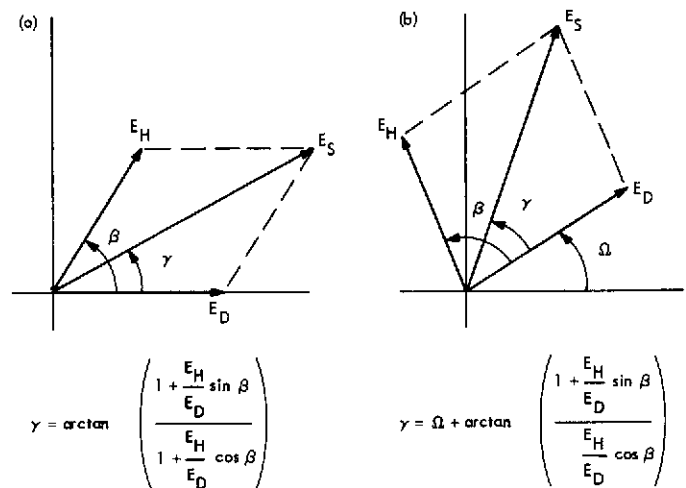


Fig. 3. Initial LGA phase relations: (a) within spacecraft at $\phi = 0$ deg; (b) within spacecraft plus measurement configuration at $\phi = 0$ deg



$$\gamma = 90 \text{ deg} + \arctan \left(\frac{1 + \sin \beta}{\cos \beta} \right); \frac{E_H}{E_D} = 1, \psi = 45 \text{ deg}$$

Fig. 4. Computer plot with initial phase conditions of Fig. 3b

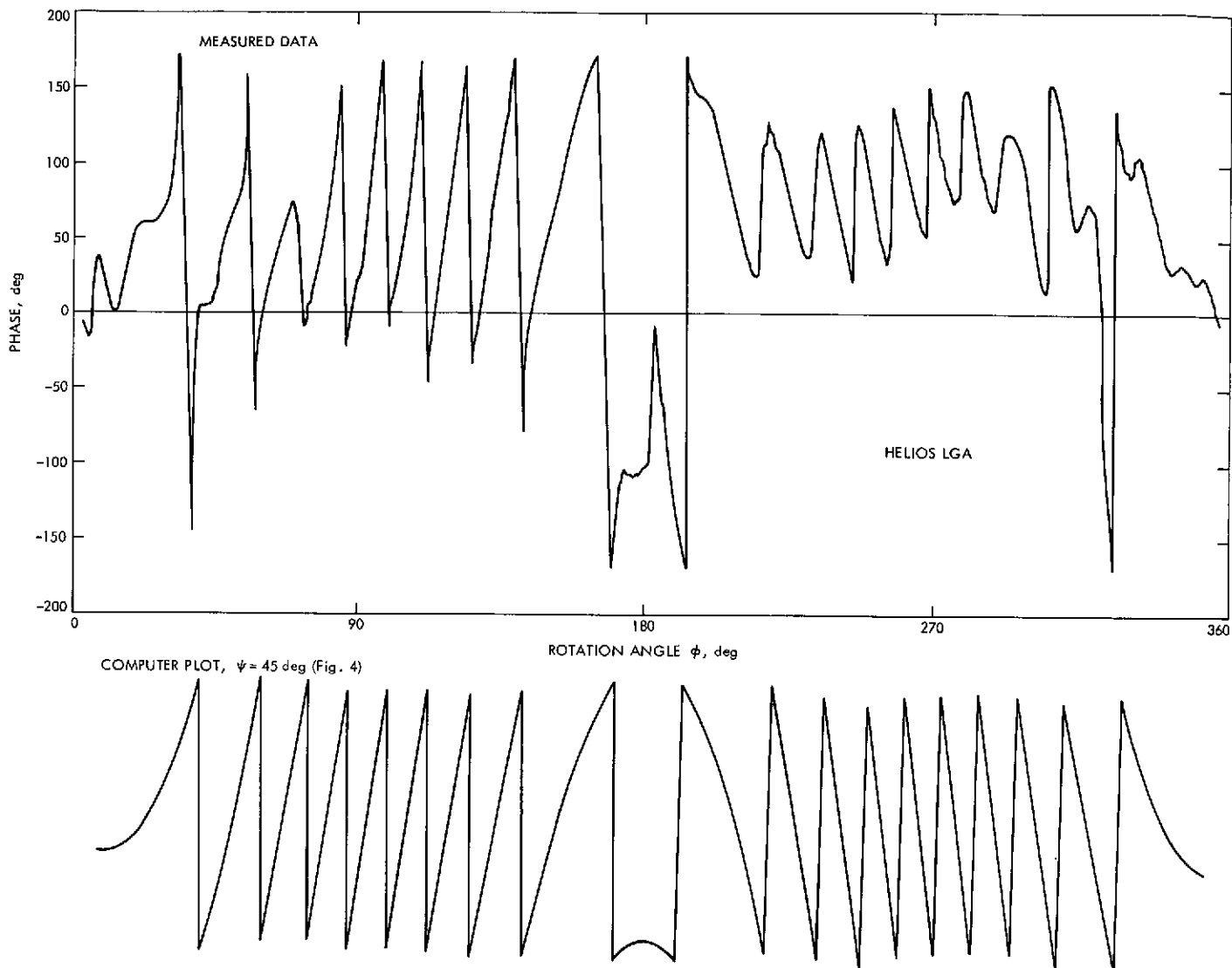


Fig. 5. Comparison with new computer plot

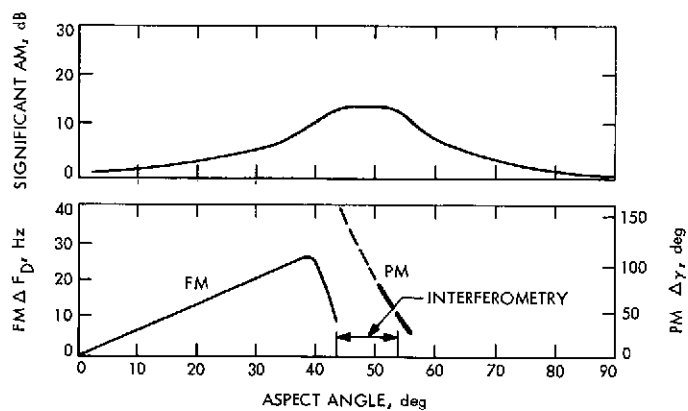
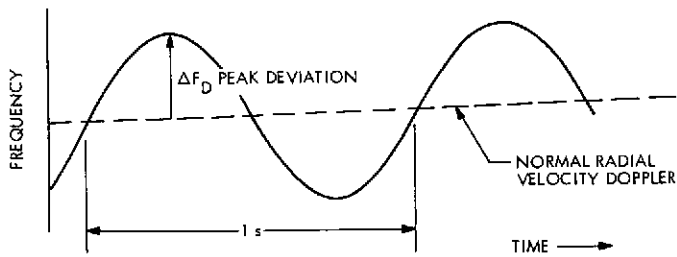


Fig. 6. Summary of spin modulation effects vs aspect angle for RCP



$$\Delta F_D = \sin \psi (6.5 \lambda \cos 2\pi f_s t)$$

WHERE ψ = ASPECT ANGLE, deg

6.5λ = HORN OFFSET, radians AT S-BAND

f_s = SPIN RATE, 1 rev/s

Fig. 7. Instantaneous doppler variation

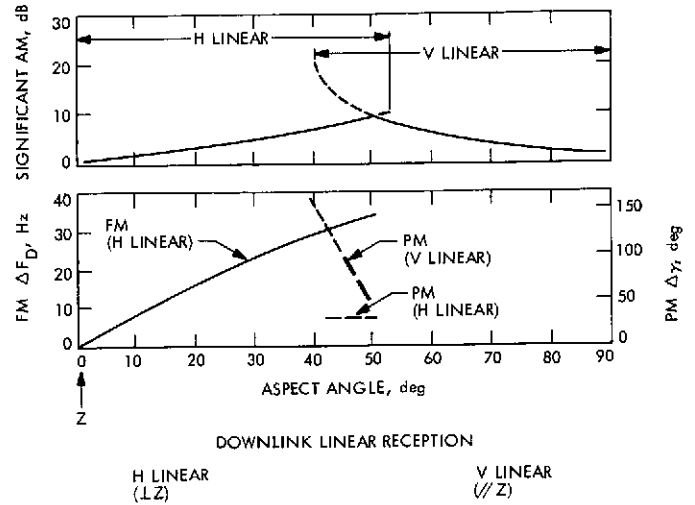


Fig. 8. Summary of spin modulation effects vs aspect angle for linear polarization

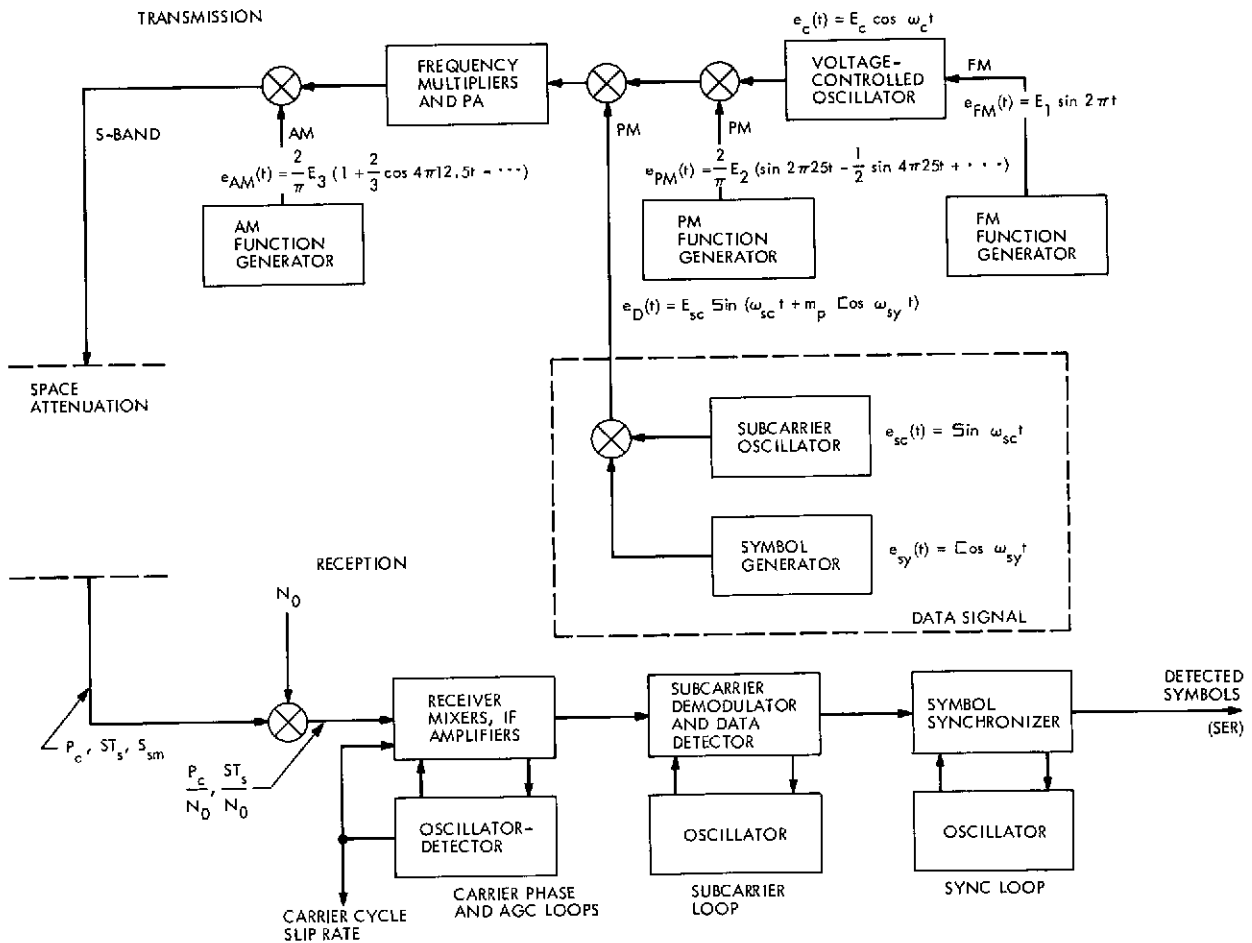


Fig. 9. Spin modulation simulation model

FOURIER SERIES FOR PHASE MODULATION SIGNAL:

$$e_{PM}(t) = \frac{2}{\pi} E_2 \left(\sin 2\pi 25t - \frac{1}{2} \sin 4\pi 25t + \frac{1}{3} \sin 6\pi 25t \dots \right)$$

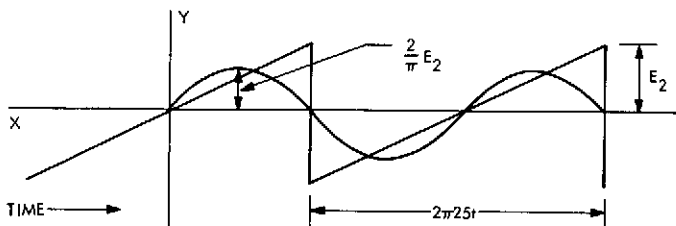


Fig. 10. Phase modulation signal for simulating spin modulation effect

FOURIER SERIES FOR AMPLITUDE MODULATION SIGNAL:

$$e_{AM}(t) = \frac{2}{\pi} E_3 \left(1 + \frac{2}{3} \cos 4\pi 12.5t - \frac{2}{15} \cos 8\pi 12.5t + \dots \right)$$

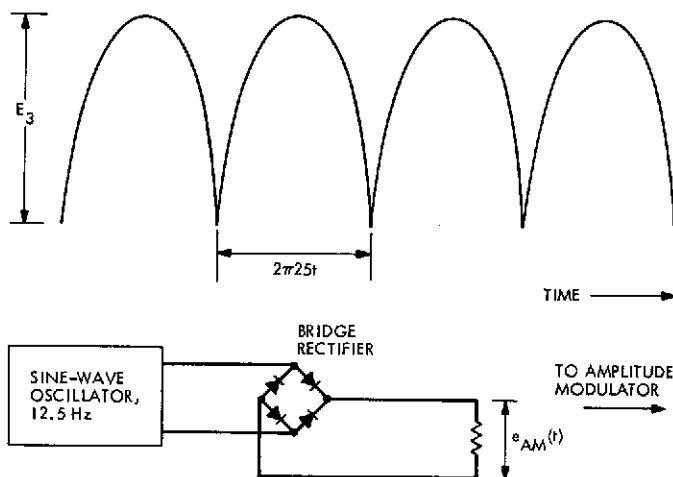


Fig. 11. Amplitude modulation signal for simulating spin modulation effect

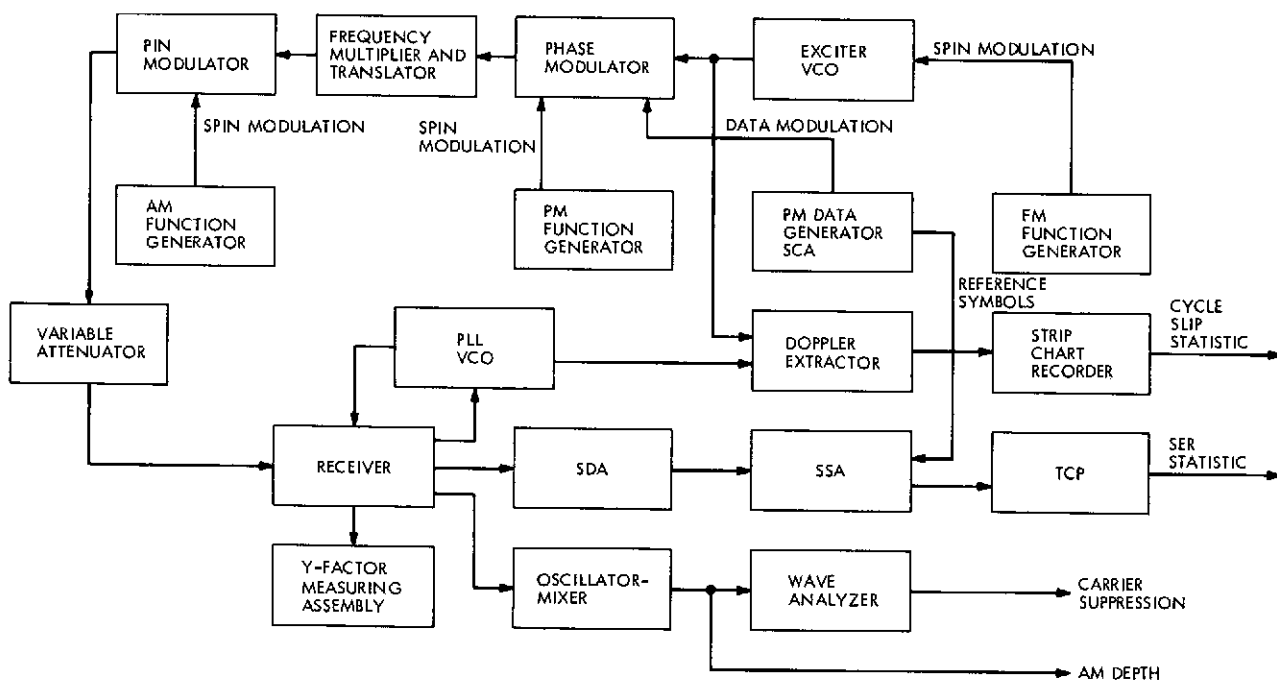


Fig. 12. Block diagram of system test configuration

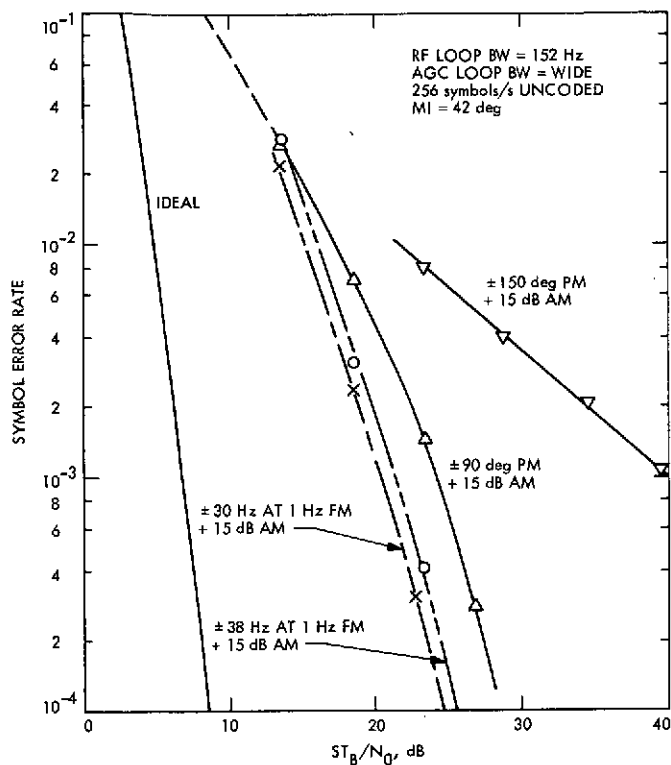


Fig. 13. Spin modulation effects under worst-case conditions

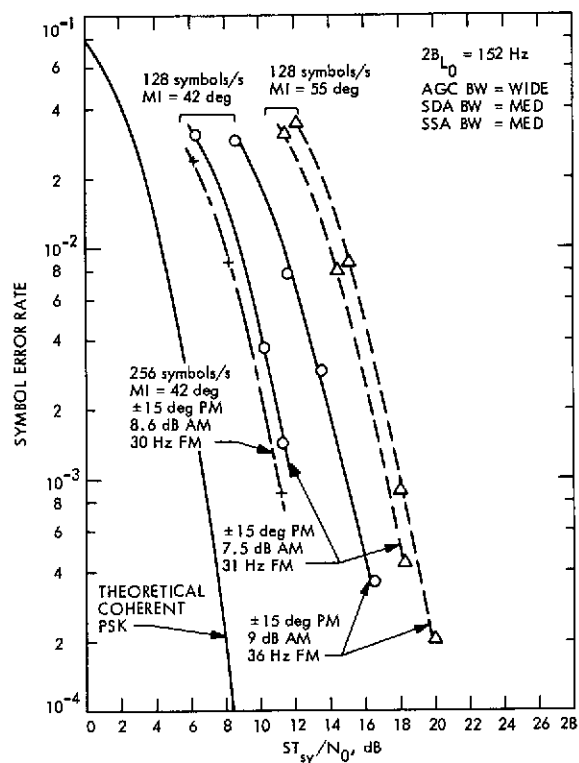


Fig. 15. Spin modulation effects for linear polarization

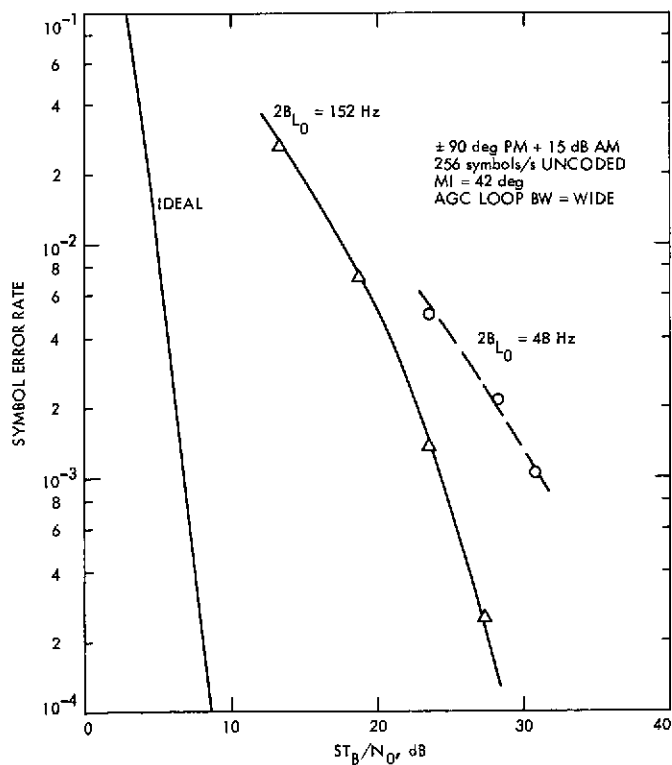


Fig. 14. BER vs SNR with spin modulation for two loop bandwidths

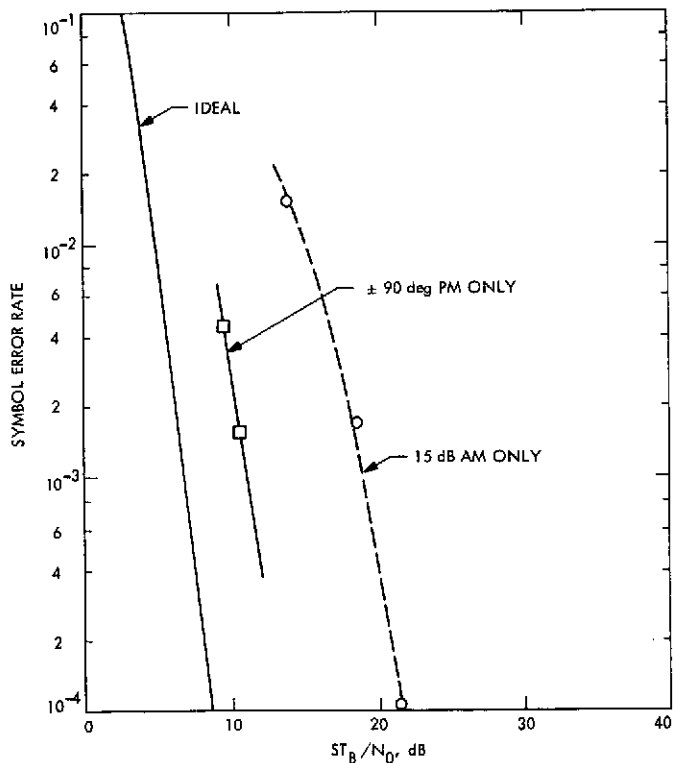


Fig. 16. BER vs ST_B/N_0 with AM and PM spin modulation

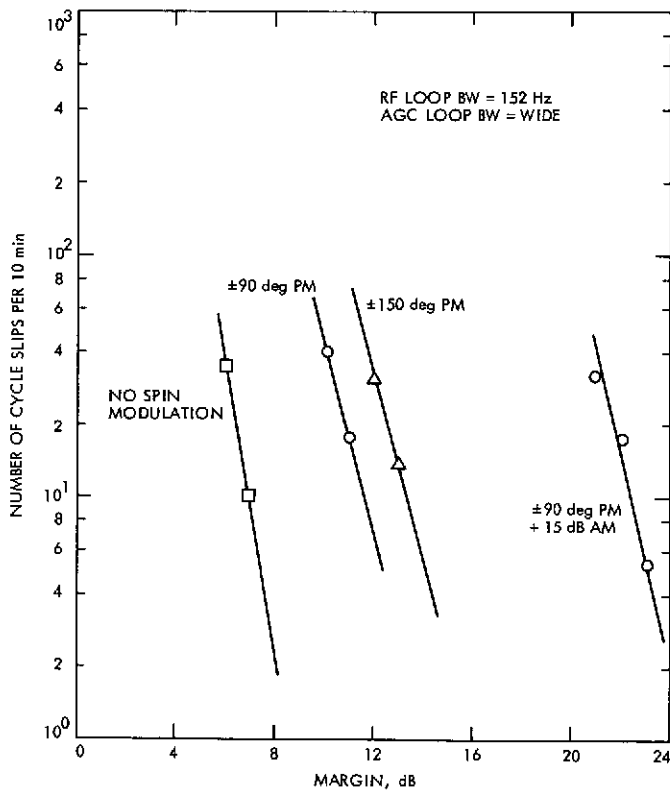


Fig. 17. RF loop cycle slippage vs spin modulation

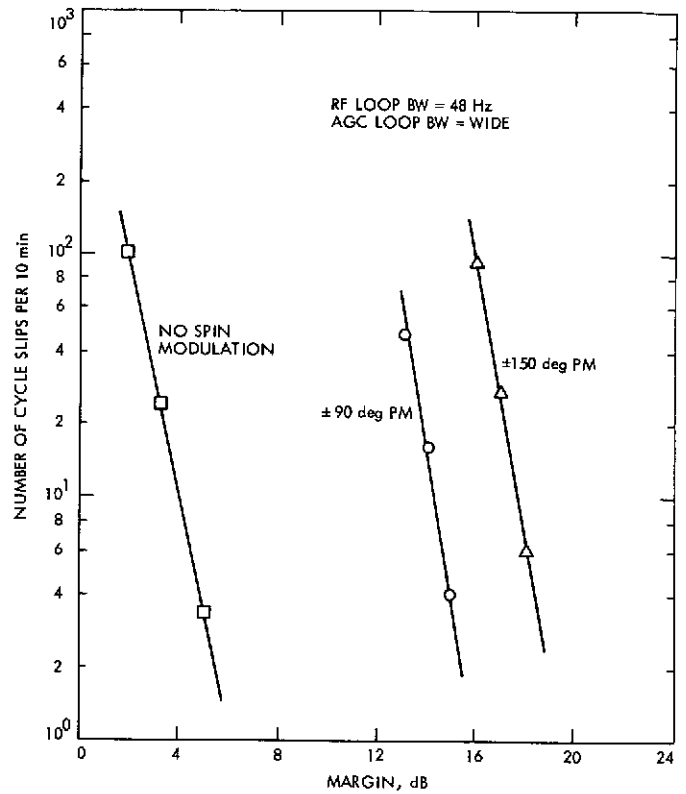
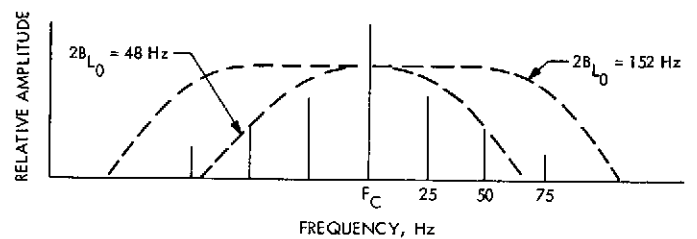


Fig. 18. RF loop cycle slippage vs phase spin modulation



$$\text{MODULATING SIGNAL: } e_{PM}(t) = \frac{2}{\pi} E_2 \left(\sin 2\pi 25t - \frac{1}{2} \sin 4\pi 25t + \frac{1}{3} \sin 6\pi 25t \right)$$

F_C = CARRIER FREQUENCY

Fig. 19. Sawtooth spin modulation spectrum and receiver loop bandwidth response

DSN Programmed Oscillator

M. R. Wick

R. F. Systems Development Section

This article describes the programmed oscillator installed in the DSN Block III receiver/exciter subsystem at DSS 14 and DSS 43 for Pioneer 10 support during the Jupiter flyby. A brief description is given of the Block III receiver/exciter subsystem modifications required to implement the programmed oscillator and design changes to add the capability of providing timed linear frequency sweeps in the manual operating mode.

I. Introduction

Programmed oscillator development for the Block III receiver/exciter has been described in a previous progress report (Ref. 1). Additional capability was incorporated to provide operator-selected timed frequency ramps for high-rate doppler tracking. Programmed oscillators were installed in the Block III receiver/exciter subsystems at DSS 14 and DSS 43 to support Pioneer 10 tracking during the Jupiter flyby.

II. Block III Receiver/Exciter Modification

Modifications to the Block III exciter and receiver to incorporate the programmed oscillator are described in the following.

A. Exciter

The programmed oscillator is inserted into the exciter (Fig. 1) at 66 MHz by mixing the Dana Synthesizer output frequency with the 5-MHz standard frequency multiplied

by 4 in a new RF module exciter-mixer. The exciter-mixer replaces the $\times 3$ frequency multiplier and distribution module providing doppler extractor references, an exciter frequency monitor at 22 MHz, and 22 MHz to the tracking data handling subsystem (TDH). Exciter channel frequencies are selected and exciter tuning is accomplished using the exciter programmed oscillator control panel. The output frequency of the programmed oscillator, f_{SYNTH} , is determined as follows:

$$f_{SYNTH} = \frac{f_{XMT}}{32} - 4f_{REF}$$

f_{XMT} = S-band channel frequency (MHz)

f_{REF} = 5-MHz station standard

The exciter frequency $f_{XMT}/96$ (22 MHz) is monitored on the frequency counter as previously provided. Exciter tuning using the programmed oscillator control panel replaces the previously used exciter loop controls.

B. Receiver

The programmed oscillator is inserted into the receiver loop at 70 MHz (Fig. 2) as previously described in Ref. 2. The VCO is operated at 7 MHz with a gain of 400 Hz/V to retain the existing loop gain. The synthesizer output frequency is summed with a voltage-controlled oscillator (VCO) in a new RF module (RCVR VCO & MIXER). The output frequency (70 MHz) is divided by 3 to retain the receiver frequency monitor at 22 MHz.

Receiver tuning is accomplished with the programmed oscillator control panel replacing the previously used VCO and ACQUISITION controls.

The received frequency (f_{RCV}) is related to the programmed oscillator output frequency (f_{SYNTH}) as follows:

$$f_{RCV} = 32(f_{SYNTH} + f_{VCO}) + 50 \text{ MHz}$$

$$f_{VCO} = 3(7.0000 \text{ MHz}) \pm 3\Delta f$$

Δf is the residual offset of the VCO. Selection of the programmed oscillator output frequency (f_{SYNTH}) for receiver acquisition is as follows:

$$f_{SYNTH} = \frac{f_{RCV} - 50 \text{ MHz}}{32} - f_{VCO}$$

The receiver frequency monitor $f_{RCV VCO}$ is retained for compatibility with existing predict format by providing a divide-by-3 stage at the output of the receiver VCO and mixer; thus

$$f_{RCV VCO} = \frac{f_{RCV} - 50}{96} = \frac{f_{SYNTH} + f_{VCO}}{3}$$

Figure 3 is typical of the RF subassemblies installed to adapt the Block IV programmed oscillators to the Block III receiver and exciter. Figure 4 is a photograph of the cabinet assembly containing the programmed oscillators and the frequency and timing subsystem (FTS) interface used to translate and distribute station binary coded decimal (BCD) time codes to the programmed oscillators.

III. Programmed Oscillator Modifications

Both the control assembly and the synthesizer have been modified to increase capability. The programmed oscillator control described in Ref. 1 was modified to

provide manually programmable timed linear frequency ramps. Front panel controls and storage registers were added to enable the subsystem operator to manually store in advance a timed sequence of four tuning rates without further adjustment during this tracking period. In addition, the four rate values can be refreshed to provide several additional timed frequency ramps during a tracking period. Ramp rates selectable from 10 $\mu\text{Hz/s}$ to 10 kHz/s (see Ref. 1) with start times (h:m:s) in increments of 1 s can be used.

The digiphase synthesizer described in Ref. 1 was modified to improve the phase control resolution and reduce radiated RF leakage. These modifications are described in the following:

A. Control Modifications

The added manual controls and displays provide the capability to visually monitor the programmed oscillator operation, to inspect stored control register contents and to manually operate the programmed oscillator. The added controls provide flexibility in the manual selection of frequency ramp rates and related monitoring. One section of pushbutton controls (see the front panel, Fig. 5), provides addressing and selection of one of the four rate registers that will control the frequency register when a sweep is initiated. The addressing permits storage of BCD selector switch contents and inspection of stored contents. Pushbuttons located at the center of the front panel control the sweep activation and termination. These pushbutton controls are described below.

(1) The SWP pushbutton initiates or terminates the frequency ramp at the current selected rate as indicated by the SWP light ON or OFF. (2) The TRK pushbutton turns the TRK light ON or OFF and if ON arms the control logic to automatically turn the SWP light ON when the stored time of the selected rate equals station time plus 1 s. Thereafter, the TRK light ON enables the succeeding rates to be selected at the next rate start time equals station time plus 1 s. (3) The LIM ENBL pushbutton turns the LIM ENBL light ON or OFF and if ON arms the control logic to terminate the frequency ramp and the TRK mode when the frequency reaches the stored upper or lower limit towards which the frequency is advancing. (4) The ACQ pushbutton arms the control logic when the ACQ light is ON to produce a triangular frequency sweep between the stored upper and lower limits when the SWP light is ON, and terminates the sweep when an external acquisition signal (ATZ) is received from an acquisition detector.

The choice of four rate and time registers was a compromise based on reasonable and adequate manual programming capability, limited panel space for manual controls and the existence of a transistor-transistor logic (TTL) medium scale integrated (MSI) circuit "4 × 4 register file" suited to this application. This integrated circuit (IC) contains 16 bits of read/write storage addressable as 4 words of 4 bits each. This IC features "read while write," and is implemented in the control to permit storage of a new rate and time digital code while simultaneously controlling the frequency at one of the other three previously stored codes. In addition, it permits continuous monitoring of any of the stored codes while concurrently controlling at a selected code. This is accomplished by applying a digital address code that alternately enables the contents of the selected control rate to be transferred to a control latch and the contents of the desired rate for display to be transferred to a display latch. The register addressing code is produced by depressing the corresponding rate pushbutton. Storage of a new rate value into one of the 4 addresses occurs by depressing the appropriate rate pushbutton when the STORE ENBL light is ON. Selection (SEL) of the rate that will control the frequency register when SWP is ON occurs when SEL ENBL is ON or as automatically advanced when the TRK and SWP lights are ON.

Figure 6 is a simplified logic diagram showing a typical stage of the rate register for manually storing four rates, addressing of one of the four rates to control the rate generator, and addressing of one of the four rates for front panel display. The display and control clock signals are derived from the 1-MHz clock that alternately enables selection of the rate number to be displayed or controls the rate generator, depending on the phase of the timing signal. When the timing signal is a logic 1 level, the number addressed with the read select code is transferred to the rate display buffer. The manual switch disables the front panel store, select and sweep control pushbuttons transferring control of the programmed oscillator to the computer as shown. The rate and limit selector pushbuttons permit operator monitoring under computer control.

Figure 7 is a simplified logic diagram of one of the decades of the stored start times. Four time numbers consisting of h:m:s are stored with the four corresponding stored rates. Depending on the sweep control logic status (TRK light ON and/or ACQ light ON), the stored time activates the related rate to produce a timed frequency ramp. A comparator senses equality between station time and the time related to the current selected rate to turn the SWP light ON if OFF. If the TRK light is ON and the

ACQ light is OFF, the control logic selects the next stored time for equality comparison to produce a series of timed frequency ramps.

Station time is normally displayed except when a rate pushbutton is depressed to permit visual inspection of the corresponding stored time.

B. Synthesizer Modifications

The Model 7010-S-179 Dana Digiphase Synthesizer described in Ref. 1 was improved to provide increased phase control resolution and reduce radiated leakage of internally generated RF. The phase control resolution was extended to the 10^{-3} Hz control decade to reduce the incremental phase steps at X-band frequency ($\times 168$ multiplication) from 0.6-deg peak to less than 0.01-deg peak. This modification also improved the delay to output response of a 1-mHz frequency control increment from 10 s to approximately 40 μ s. The packaging was modified to reduce radiated leakage; these modifications included the deletion of the unnecessary front panel controls, and the addition of RF gaskets and vent screens. The modified synthesizer is shown in Fig. 8.

IV. Programmed Oscillator Tracking Characteristics

The synthesizer output frequency tracks a programmed frequency ramp with a known constant delay and phase error. These errors and typical frequency ramp capabilities are described as follows:

A. Frequency Ramp Tracking Errors

The actual frequency ramp output of the digiphase synthesizer is delayed (offset) relative to the programmed ramp (Fig. 9). This offset is due to the inherent hardware computing rates that produce the digital frequency ramp and subsequently the related digital phase reference to the synthesizer phase-locked loop. The total delay in computing and converting the digital frequency ramp to an analog reference to the synthesizer loop is $40 \mu\text{s} \pm 5 \mu\text{s}$.

The synthesizer computes the phase reference from a programmed frequency control input during a period of two 10- μ s sample intervals and then converts the digital result to an analog value in the next sample interval for a total delay of 30 μ s. An additional sample period of 10 μ s occurs in generating the frequency control ramp input to the synthesizer. An uncertainty of $\pm 5 \mu\text{s}$ is due to the random relationship of the station 1-s tick and the synthesizer phase computer sampling rate (100 kHz).

The effect of this delay in computing the digital ramp results in an accumulative phase error (Fig. 9), and results in an offset in doppler residuals. The following expressions represent the actual frequency ramp and phase output of the synthesizer except for small phase variations less than 1×10^{-7} cycle due to quantization effects that are not accumulative.

$$f_T = f_0 + \dot{f}(T - \tau) \quad (\text{Hz})$$

$$\phi_T = \omega_0(T - \tau) + \frac{\dot{\omega}}{2}(T - \tau)^2 \quad (\text{radians})$$

where

$$\tau = 40 \mu\text{s} \quad \pm 5 \mu\text{s}$$

The synthesizer phase-locked loop tracks the digital frequency ramp with a very small tracking error of less than 1.2×10^{-8} cycles/Hz/s.

The loop tracking error with a frequency ramp, A (Hz/s), applied to the loop reference phase input ϕ_R is given as follows:

For a frequency ramp, $\phi_R(t) = At^2$

$$L[\phi_R(t)] = \phi_R(S) = \frac{2A}{S^3}$$

The equation for the loop phase error ϕ_E with the ramp applied is:

$$\phi_E(S) = \frac{1}{1 + G(S)} \phi_R(S)$$

where

$$G(S) = K \left(\frac{S\tau + 1}{S^2} \right) \text{ is the open loop gain.}$$

The loop error time response $\phi_E(t)$ is then:

$$\phi_E(t) = L^{-1}[\phi_E(S)] = \frac{2A}{K} \left[1 - \frac{\epsilon^{-\alpha t}}{\beta} \sin(\beta t + \psi) \right]$$

where

$$K = \alpha^2 + \beta^2 = 1.78 \times 10^8$$

$$\tau = 1.65 \times 10^{-4} \text{ s}$$

$$\alpha = \frac{\tau K}{2}$$

$$\beta = \pm \sqrt{K - \alpha^2}$$

$$\psi = \tan^{-1} \frac{\beta}{\alpha}$$

The steady-state error term in the phase error time response to the frequency ramp ($2A/K$) is of interest:

$$\phi_E(t)_{ss} = \frac{2A}{K} = \frac{2A}{(1.78 \times 10^8)}$$

This tracking error represents an offset of the output ramp relative to the reference ramp input of 1.1236×10^{-8} cycles/Hz/s and is a fixed offset in phase that does not accumulate with time.

B. Frequency Ramp Techniques

A variety of frequency ramping sequences can be derived, some of which are shown in Figs. 10a, 10b, 10c, and 10d.

Figure 10a illustrates a ramp sequence automatically initiated at T_0 and terminated at the stored upper limit (f_{UL}) as enabled with the TRK light ON and LIM ENBL light ON. Note that the sweep terminates at the limit towards which the sweep is advancing with LM ENBL light ON. Figure 10b illustrates a similar sequence with opposite polarities and use of the low limit (f_{LL}).

Figure 10c illustrates a triangular sweep between selected upper and lower frequency limits at a selected rate. This ramp sequence is initiated with the ACQ light ON with SWP start (SWP-ON) occurring at the selected rate time stored. Automatic reversal of the rate polarity occurs when the advancing frequency becomes greater than the limit reached. The figure illustrates a change entered to the upper limit and a resulting sweep termination at that limit when enabled as indicated by the LM ENBL light turned ON.

Figure 10d illustrates a ramp sequence of stored rates with R0, R1, and R2 refreshed with new rates as the sequence progresses. The termination, in this example, is at a selected upper limit (f_{UL}). The sequence is initiated by turning the TRK light ON. When the limit is reached, the sequence is terminated as indicated by the SWP and TRK lights OFF. Such a ramp sequence can be used for aided uplink or downlink doppler tracking.

Other combinations of ramp sequence can be generated to produce any desired frequency profile with ramp intervals as small as 1 s within a 24-h period.

Uplink (exciter) frequency ramping was used at DSS 14 and DSS 43 during the Pioneer 10 Jupiter flyby. Uplink frequency ramping was used to return the spacecraft receiver to best-lock frequency prior to entering Io occul-

tation and subsequently at the Jupiter occultation to facilitate recapture of two-way lock after exit. Additional ramping was used to insure recapture of two-way lock after exit from Io occultation and to provide coherent doppler tracking up to 30 min before periapsis.

A tuned oscillator range analysis (TORA) experiment was performed at DSS 14 using the programmed oscillators as reported in Ref. 3. Frequency ramping of the up-link to Pioneer 10 was completed with received two-way doppler data compared to a locally generated reference.

V. Conclusion

Block III receiver/exciters at DSSs 14 and 43, utilizing the programmed oscillators, were used to track Pioneer 10 Jupiter encounter. The results are described below.

A. Doppler Phase Jitter

Doppler jitter measurements [using (Ref. 4)] taken at DSS 14 by the Network Systems Support Group both before and after the programmed oscillators were installed are tabulated in Table 1. Measurements at DSS 43 were not completed at the time of this article.

B. Doppler Residuals While Ramping

Analysis of ramped radio metric data as processed by the pseudo-residual program indicated that the doppler data noise while ramping was similar to the noise encountered with a constant frequency.

Pioneer 10 commands were sent to the spacecraft during frequency ramps without any associated errors occurring.

References

1. Wick, M. R., "DSN Programmed Oscillator Development," in *The Deep Space Network Progress Report*, Technical Report 32-1526, Vol. VIII, pp. 111-124. Jet Propulsion Laboratory, Pasadena, Calif., Apr. 15, 1972.
2. Donnelly, H., and Wick, M. R., "Programmed Oscillator Development," in *The Deep Space Network Progress Report*, Technical Report 32-1526, Vol. X, pp. 180-185. Jet Propulsion Laboratory, Pasadena, Calif., Aug. 15, 1972.
3. Liu, A., "Range Measurements to Pioneer 10 Using the Digitally Controlled Oscillator," in *The Deep Space Network Progress Report*, Technical Report 32-1526, Vol. X, pp. 180-181. Jet Propulsion Laboratory, Pasadena, Calif., Aug. 15, 1972.
4. *Doppler System Evaluation Test*, DSIF Standard Test Procedure 853-60/2B-11. Jet Propulsion Laboratory, Pasadena, Calif., Sept. 15, 1973. (JPL internal document.)

Table 1. Doppler (degrees rms phase jitter)

Signal source	Before		After	
	Theoretical	Actual	Theoretical	Actual
Test transmitter:				
Signal level:				
120 dBm	7.2	5.9	7.2	5.6
Signal level:				
162 dBm	20.1	22.6 ^a	20.1	23.0 ^a
Test translator:				
Signal level:				
120 dBm	2.8	2.3	2.8	2.5
Signal level:				
160 dBm	20.9	— ^b	20.9	23.0 ^a

^aValues high due to signal level setting using old AGC curves.

^bNot available.

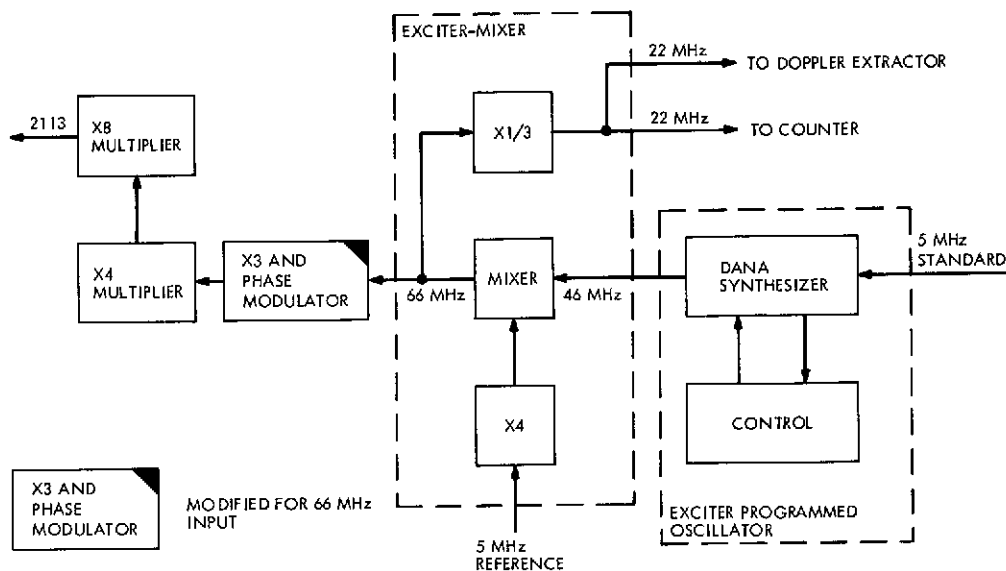


Fig. 1. Exciter modification block diagram

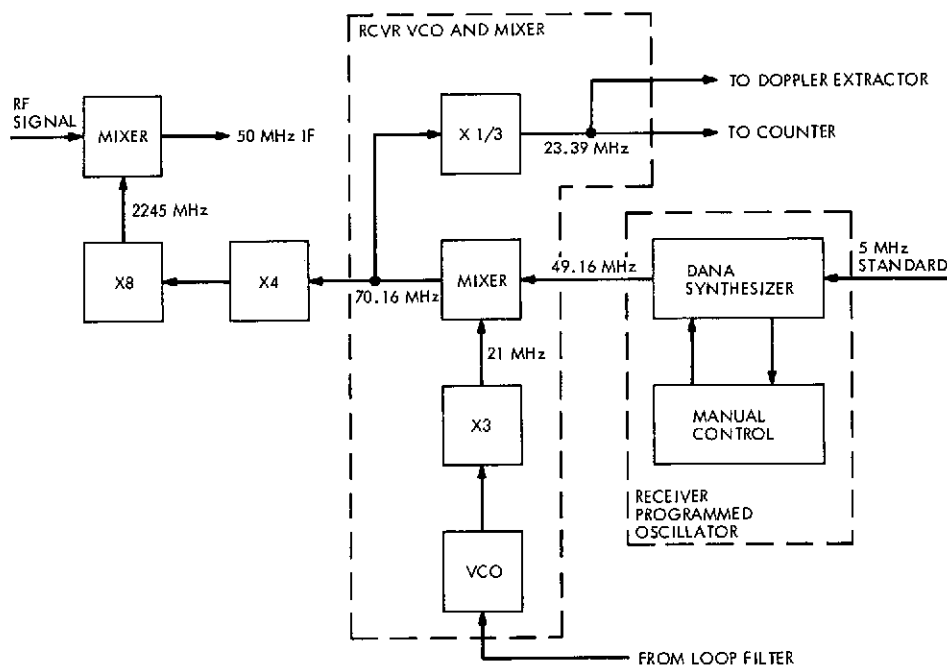


Fig. 2. Receiver modification block diagram

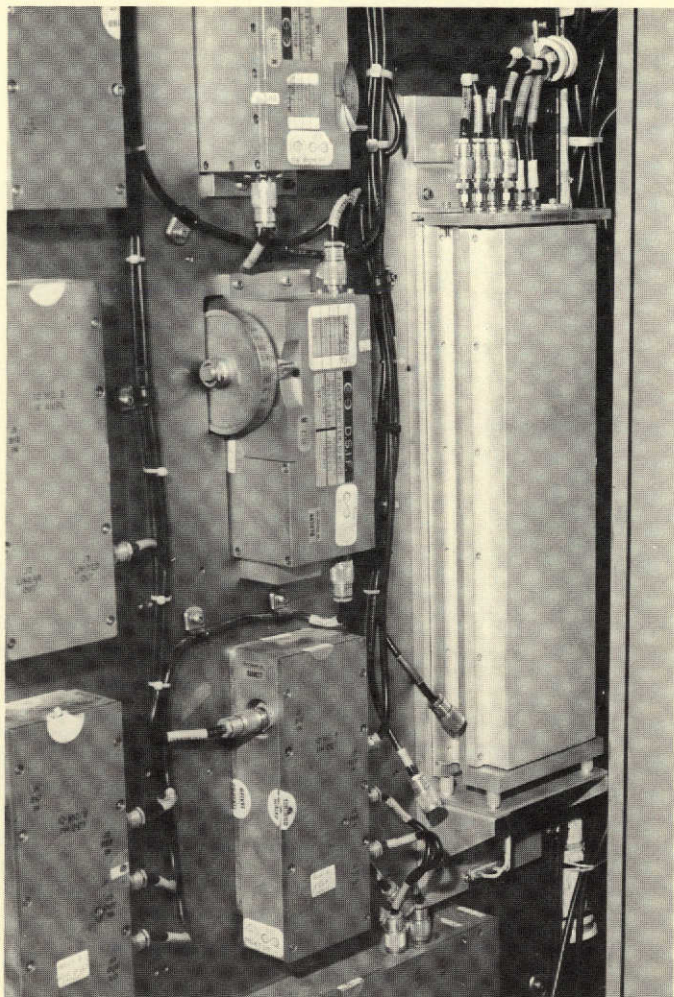


Fig. 3. RF subassembly installation

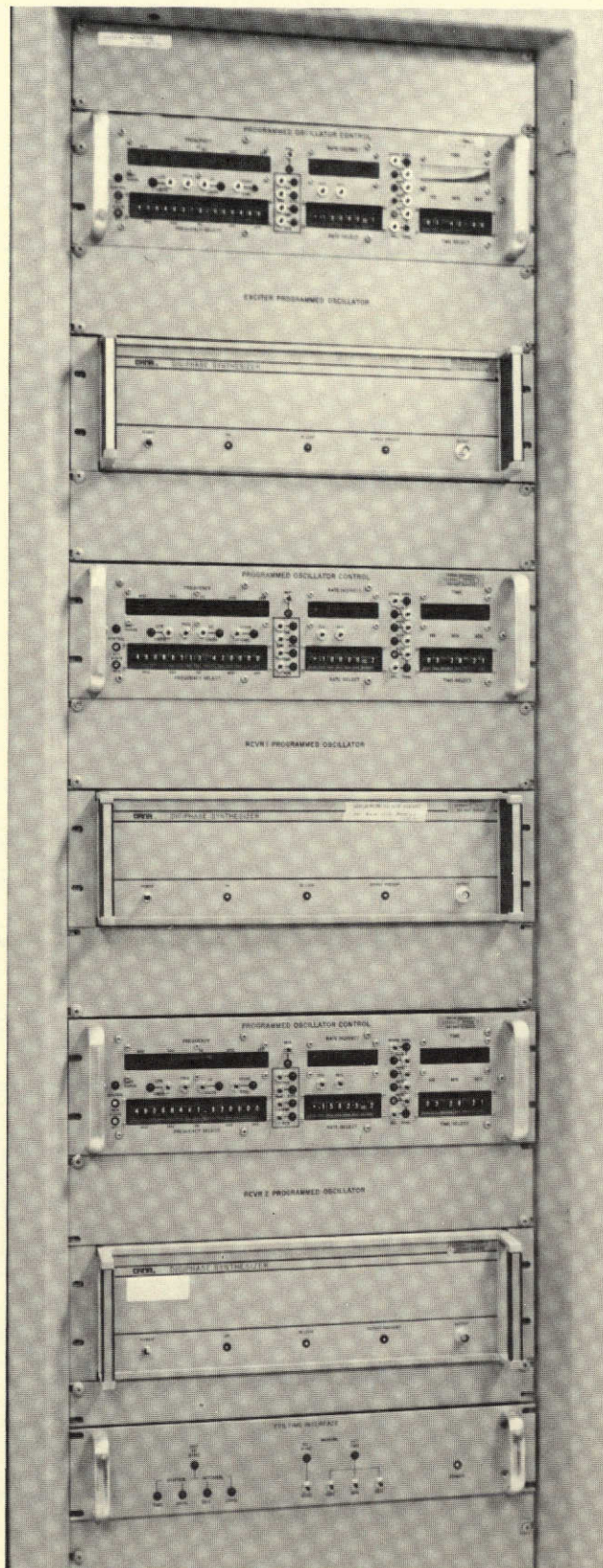


Fig. 4. Programmed oscillator cabinet assembly

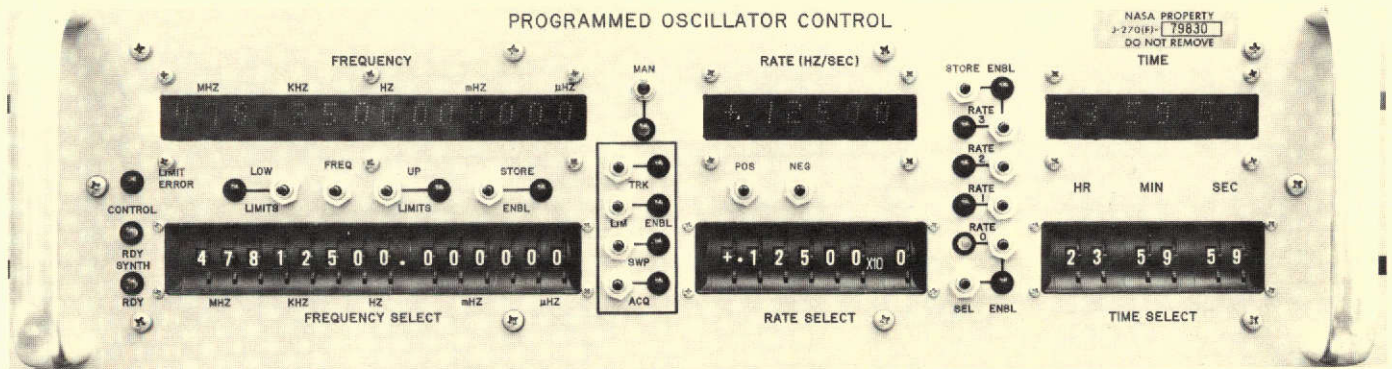


Fig. 5. Front panel control

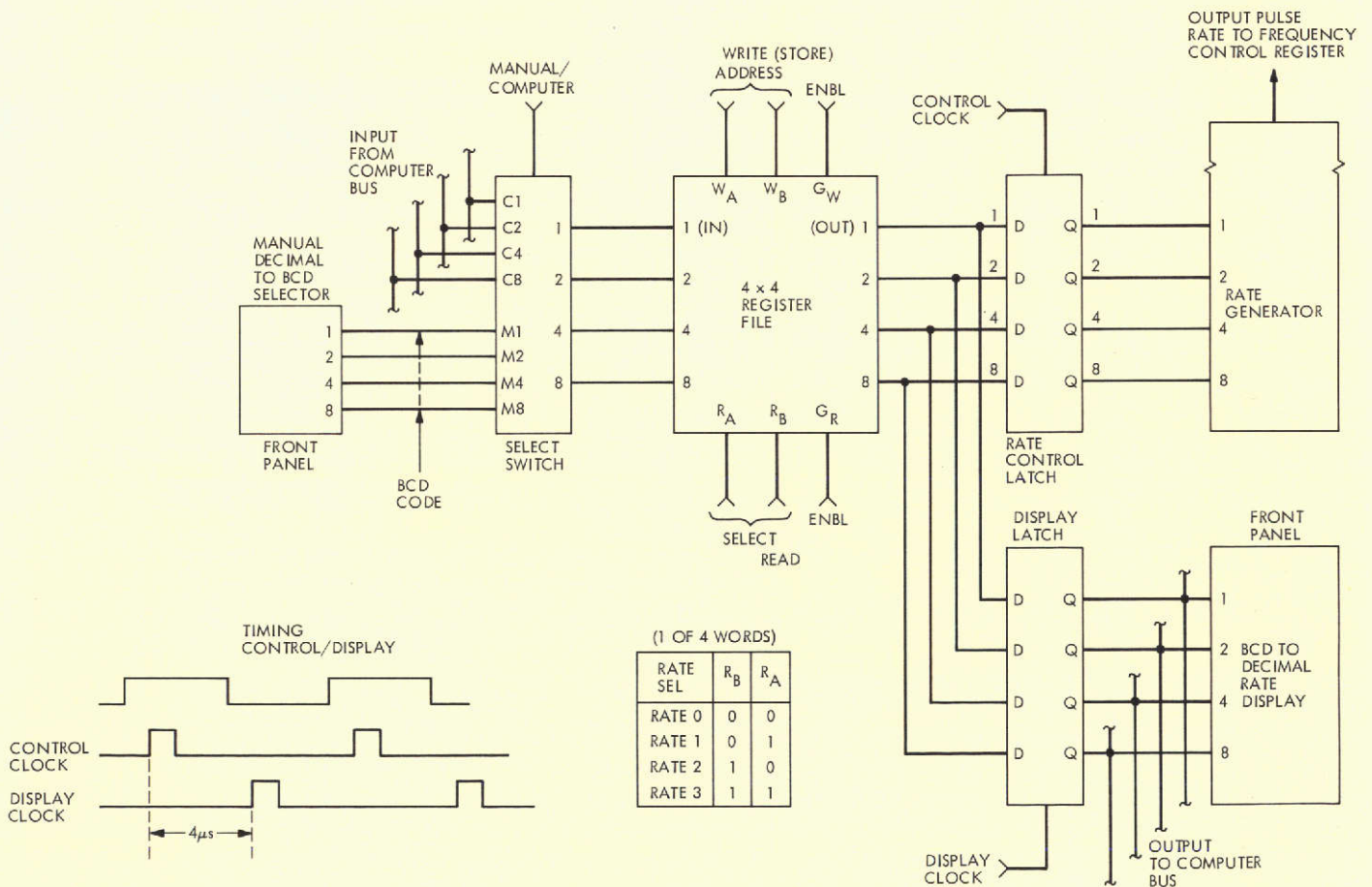


Fig. 6. Rate decade control and display logic

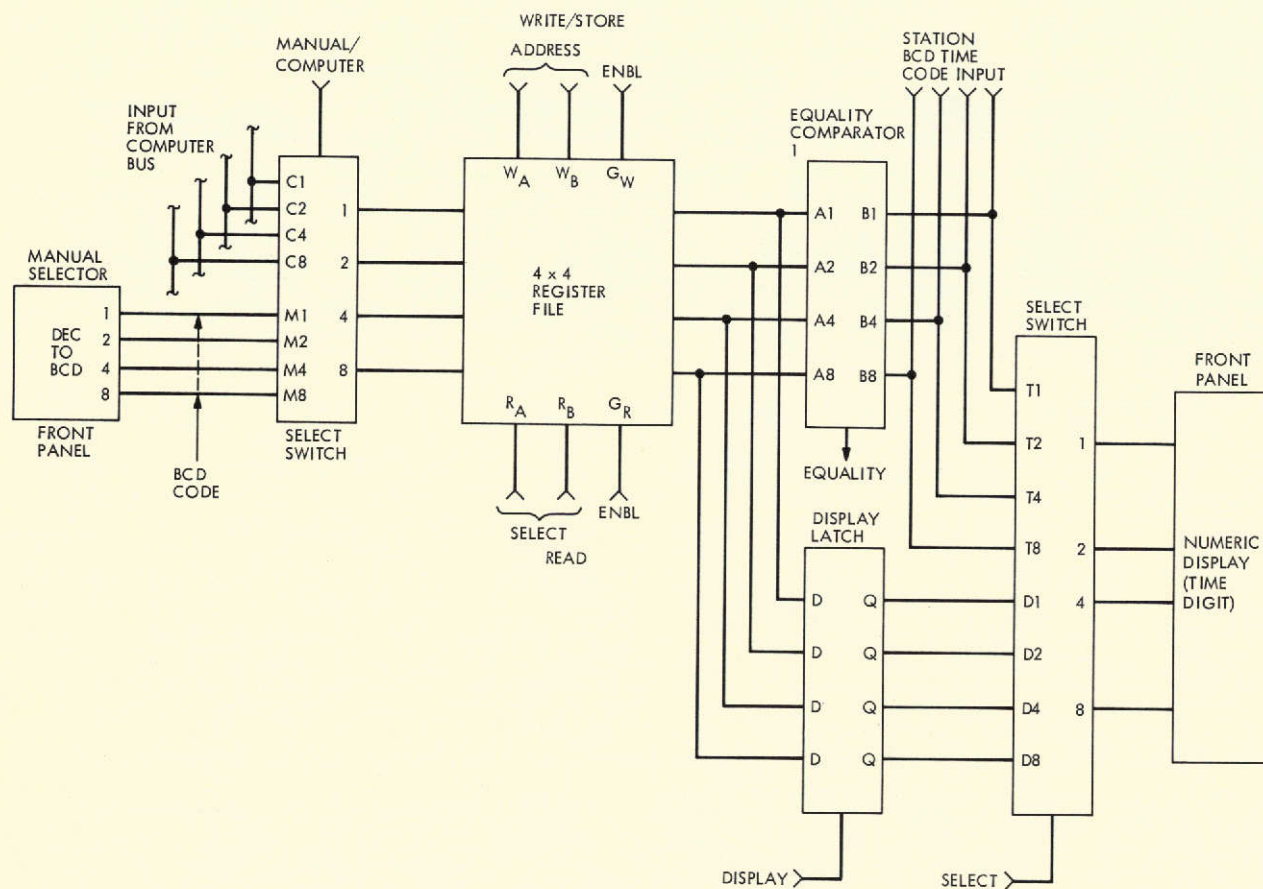


Fig. 7. Time decade control and display logic

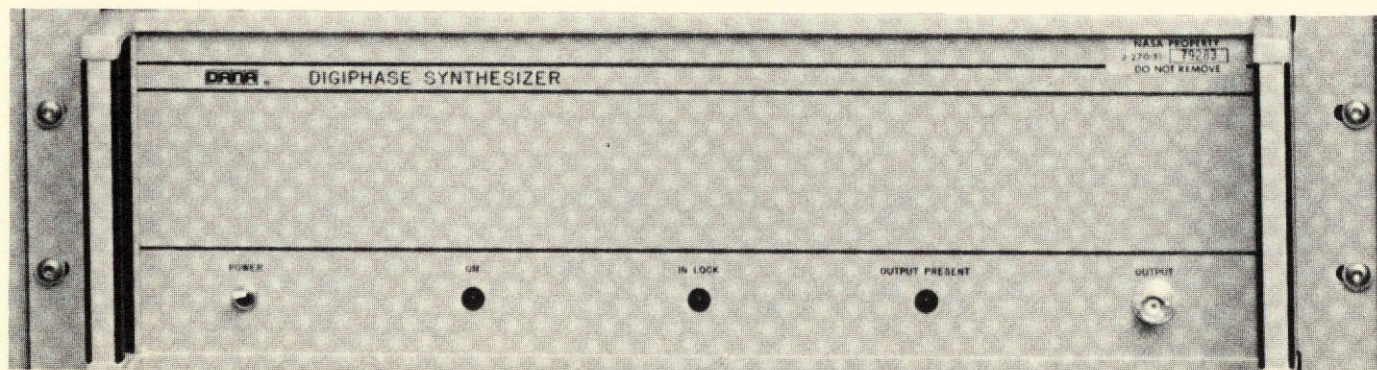


Fig. 8. Synthesizer

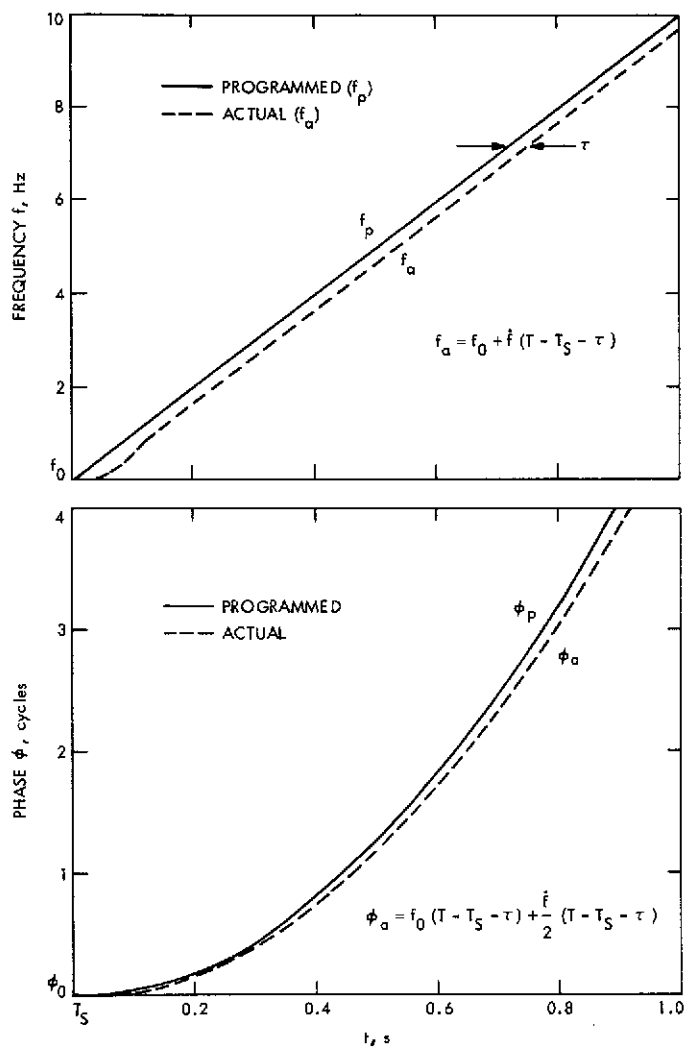


Fig. 9. Ramp errors

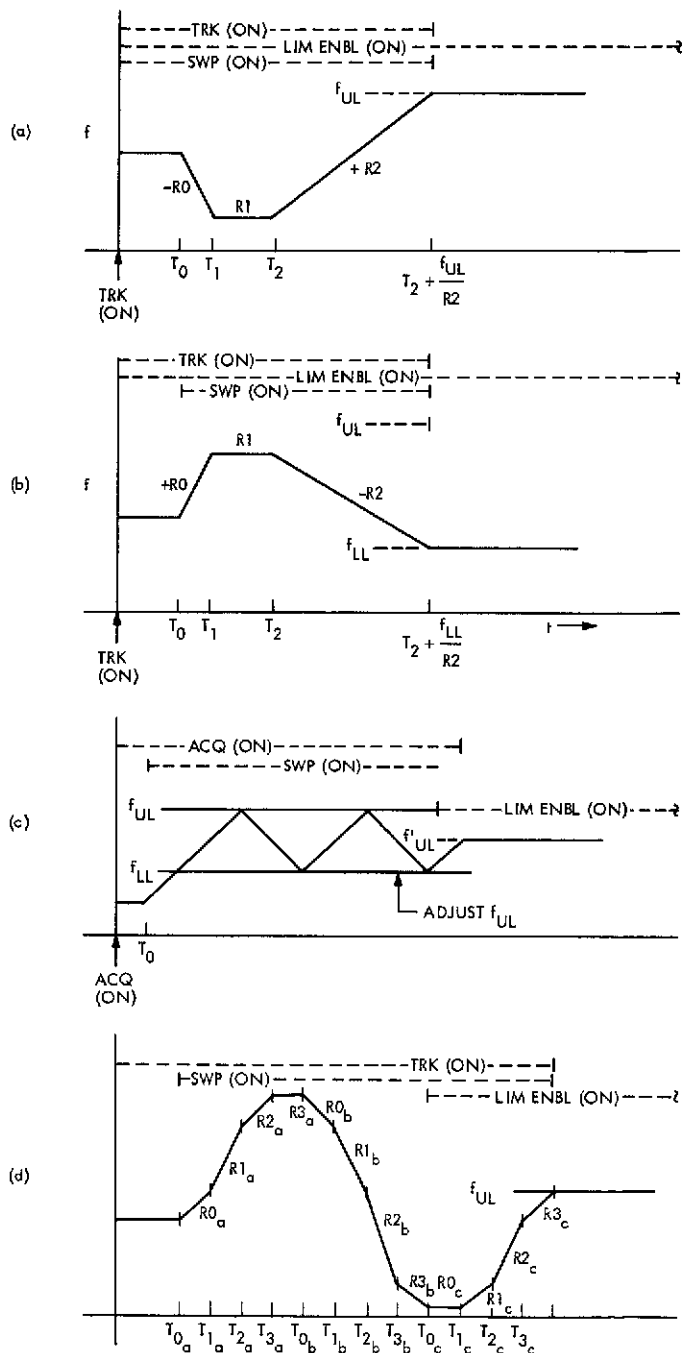


Fig. 10. Programmed ramp sequences; (a) triangular, automatically initiated at T_0 , (b) opposite polarities and the low limit, (c) selected upper and lower frequency limits, (d) typical tracking sequence.

DSN Data Record Generation

E. C. Gatz
DSN Systems Engineering Office

The DSN is implementing a central log (GCF Log) of all data received and/or generated in the Deep Space Network. Selected data from the log are sorted and placed in time order to form an Intermediate Data Record (IDR). This IDR is the principal nonreal-time interface with flight projects.

I. Introduction

The generation and handling of data records for deep space missions has always been included as one of the DSN tasks. Each Flight Project has also provided processing, storage, and distribution of data records as part of its mission. In the past, each project has handled the total data record process in different ways to satisfy the particular needs of the various data users. This article describes a standard data record system being implemented by the DSN, and shows how this system fits into the total data record process.

II. Requirements

The principal requirement for the data record process is to deliver adequate quantities of data in the form of a Master Data Record (MDR) or at least to deliver the data for production of the MDR. There have been numerous attempts to quantify this requirement, but without much

satisfaction. Therefore the requirements evolve to the following:

- (1) Content: all data received or generated above threshold.
- (2) Time: MDR production nearly in real-time (approximately 24 hours).
- (3) Operations: process shall have simple interfaces and simple operation.

III. General Configuration

The data record process configuration is shown in Fig. 1. This diagram indicates the functions performed by the DSN, and also those to be handled by Flight Projects, and by the Mission Control and Computing Center (MCCC). Contents and formats of the various data records are defined in Section V.

A. DSN Functions

The DSN functions indicated in Fig. 1 are as follow:

- (1) Make the Original Data Records (ODRs) at each Deep Space Station (DSS).
- (2) Make a central log (GCF Log) of all data.
- (3) Monitor operation, and effect replays from the ODR.
- (4) Sort and merge the GCF Log to generate the Intermediate Data Records (IDRs).

B. MCCC Functions

The MCCC functions indicated in Fig. 1 include:

- (1) Generate the System Data Records (SDRs) for quick-look and real-time operation.
- (2) Generate the Master Data Records (MDRs) from the IDRs.

C. Project Functions

Finally, project functions include:

- (1) All quick-look processing that is used for mission operations.
- (2) Experiment Data Record (EDR) processing. This is interpreted to include all processing required to select and format mission data for use by the scientific community. Historically, much of the radio metric data processing falls in this category since that processing is done as part of the orbit determination.

IV. DSN Implementation

The significant implementation to be accomplished by the DSN is the central GCF Log and the processing to generate the IDRs. This implementation is included in the Network Control System (NCS), which has been described in Ref. 1. The configuration for these functions is shown in Fig. 2.

The GCF Log is recorded by the communications log processor. Two processors will be implemented, one as a hot standby. All real-time data will be routed to real-time monitors that will generate System Performance Records and data gap summaries. These items are regularly transferred to the Network Support Controller for compilation

into pass summaries. At regular intervals, usually at the end of a pass, the recall lists are generated. These lists are used to recall from the ODR any data missed in real-time.

The playback of ODR recalls is automatically controlled. The processor to accomplish this is the backup NCS display processor. This is also being implemented to perform the off-line conversion of the GCF Logs to IDRs. This conversion consists of the selection of data from the GCF Log, and time ordering of all real-time and recalled data. The selection is on the basis of data type, DSS, spacecraft number, and time interval.

This capability is now planned as part of the Block III NCS (defined in Ref. 1), scheduled to be operational on February 1, 1976. It is planned that the IDR will be generally available within 24 hours after the data have been received at a DSS. The IDRs will cover selected time intervals up to 100% of the data on the ODR, and will be available to projects as requested or negotiated.

V. Data Record Definitions

A. Original Data Record (ODR)

ODRs are those records made by digital recorder at the Deep Space Station at the time of data receipt or generation. The station places time tags on the record that are correlated to the data. ODRs are made for radio metric, telemetry, command, and monitor data. Appended to the data are certain ground system performance measurements, such as receiver automatic gain control (AGC), signal-to-noise ratio, and doppler mode. The records are in high-speed data block format, ordered in Earth-received time (ERT). Multiple recorders at a DSS lead to different tapes, some tapes with multiple data streams mixed together.

B. GCF Log

The GCF Log is that record made at the GCF central communications terminal at JPL of all inbound and outbound GCF blocks in the order of receipt. This record contains data received in real-time, and also data replayed from Deep Space Station records. This record, formatted in GCF data blocks, is on magnetic tape, with data in the order received. Multiple data types are mixed together, and recall data may be at the end of a pass or mixed in with the other data from that pass. A single tape may have data from more than one spacecraft, and more than one pass.

C. System Performance Record (SPR)

SPRs are digital magnetic tape records of a time history of DSN performance as generated by the network control tracking, telemetry, and command subsystems and compiled in the NCS. These records are organized according to DSN System, spacecraft and station. They identify all missing or defective data and system status. The SPR compiled by the network control monitor and control subsystem contains a time history of overall DSN performance and is called the Network Performance Record (NPR).

D. Intermediate Data Record (IDR)

This digital record (made from the GCF Log) contains all the GCF blocks, time ordered by Earth-received time, of a given data type, spacecraft, and Deep Space Station pass. This record contains, as minimum, the same data that is contained on the ODRs. This record is on magnetic tape and is an official interface to the Mission Control and Computing Center and remotely located projects for data records. The tape is in the same format as the digital ODR.

E. System Data Record (SDR)

The SDR is that digital data record generated separately at the MCCC by spacecraft and by system (tracking, telemetry, and command). The data in each record consist of data received in real-time as well as data received from nonreal-time sources. It may contain time gaps, duplicate information and extraneous data. Where

applicable, ground system performance measurements, such as receiver AGC, signal-to-noise ratio (SNR), equipment configuration and lock status, and doppler mode, are included in SDR records. The SDR is ordered by time of receipt of the data at the MCCC.

This record is a standardized format for all flight projects and provides the MCCC interface with each flight project for project processing. The permanent form of this record is magnetic tape.

F. Master Data Record (MDR)

MDRs are digital data records obtained through specialized processing of data on the IDR, or equivalent. These consist of real-time data with data gaps filled in to achieve a required level of completeness. The data are organized in time-ordered sequence with respect to ground received time and usually tagged with spacecraft event time. Duplicate and extraneous data resulting from station overlaps are removed. An MDR may contain data for more than one system. Telemetry data are organized into frames rather than high-speed or wideband data blocks.

G. Experiment Data Record (EDR)

These digital data records are extracted from the MDR to provide the Principal Investigator (PI) with data associated with his experiment. The EDR is in instrument cycles and is ordered by spacecraft event time (the time at which the measurement is taken). The permanent form of the EDR is magnetic tape. This record is made by the flight project.

Reference

1. Edwards, J. N., "Network Control System Development," in *The Deep Space Network Progress Report*, Technical Report 32-1526, Vol. XVII, pp. 113-119. Jet Propulsion Laboratory, Pasadena, Calif., Oct. 15, 1973.

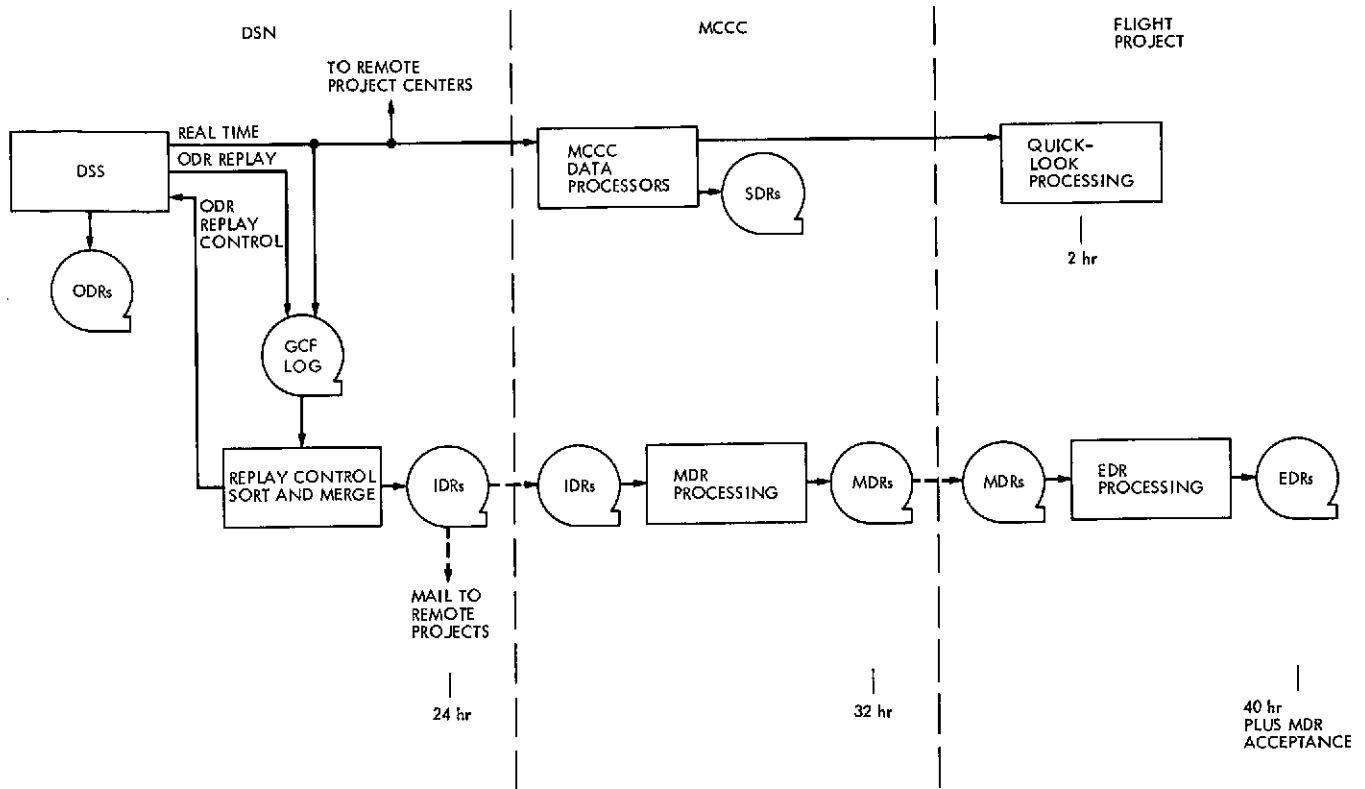


Fig. 1. Data record process — general configuration

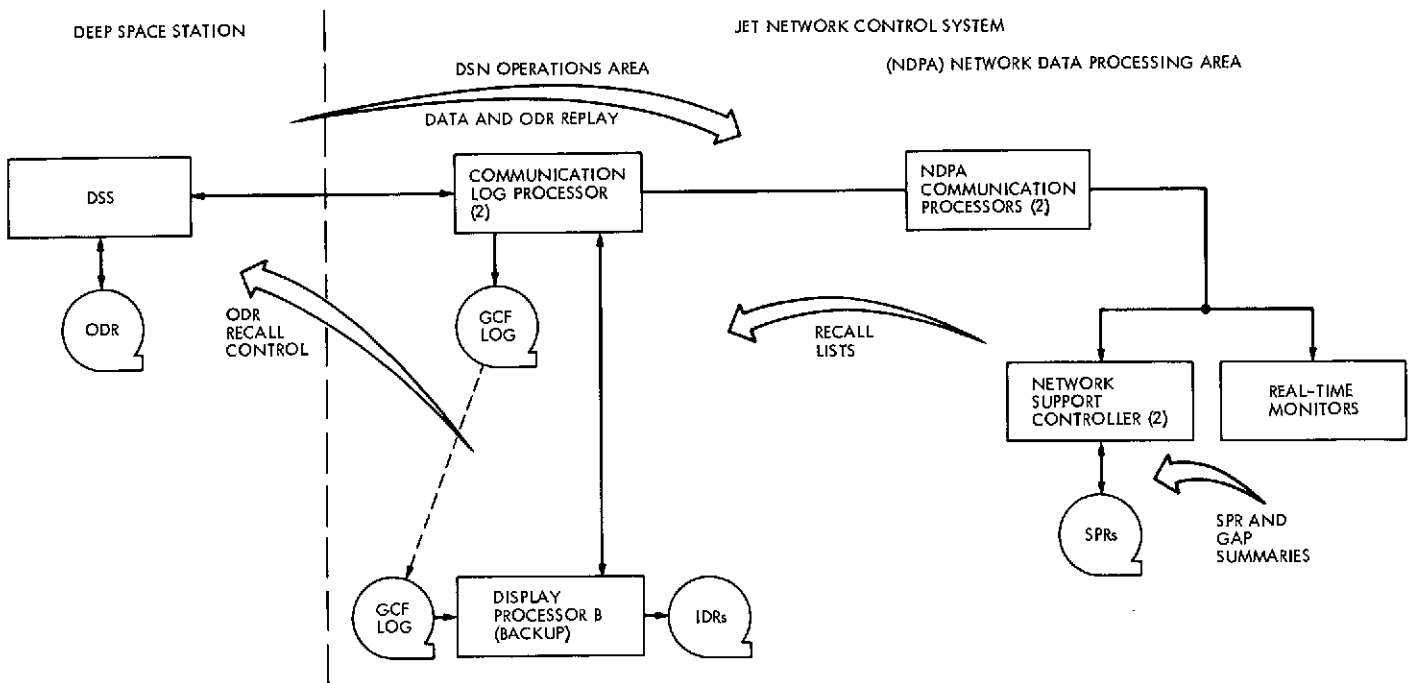


Fig. 2. DSN data record generation

Short-Term Frequency Measurement Capability in DSN Equipment Maintenance Facilities

R. M. Smith, D. Crawford, and C. H. Fournier
DSN Facility Operations Office

A short-term frequency measuring capability has been established at the Goldstone and Madrid DSN Complex Maintenance Facilities to afford rapid, complete service to DSN synthesizers. Future development of the capability may include the testing of station frequency standards.

The DSN Maintenance Center (DMC) recently conducted a training seminar covering the servicing of DSN frequency synthesizers and the performance of precision short-term frequency measurements. Representatives of the Goldstone and Madrid Complex Maintenance Facilities (CMFs) attended.

Early in 1971 it was realized that, with the expected increase in types and quantity of synthesizers, a uniform testing capability was required. Without such a capability the CMFs at Tidbinbilla, Madrid, and Goldstone would be at a serious disadvantage not only in synthesizer test and repair but later in the testing of other precise frequency sources. DMC personnel assembled a small system, using mostly commercially available equipment, that affords a capability for present DSN synthesizer requirements and is expandable to accommodate future

requirements for short-term frequency testing. In the future the test system will be modified as necessary and practicable, to allow testing of station frequency standards and newly added synthesizers.

Concurrent with the planning of the test system, a training seminar was planned and developed to aid in developing expertise at the CMFs. The seminar provided: knowledge of, and exposure to, specific test methods for DSN synthesizers; insight into peculiar problems and specific, positive treatment of those problems. This, plus the equipment given to the attendees, provided the Madrid and Goldstone CMFs with the capability for diagnostic and functional test of DSN synthesizers to the limits of DSN requirements. The advantage of this capability is that synthesizers can be repaired and fully tested in the field and returned to the DSS or to spares with a high degree of confidence established for the synthesizers.

In contrast, at a location not so equipped, synthesizers must be returned to the DMC if complete confidence is desired or, alternatively, repaired and returned to the DSS with no suitable level of confidence, to be "smoke tested" in the system.

Figure 1 is a view of the test system taken during the training seminar at the DMC. Don Irwin of the Goldstone CMF and Domingo Duarte of the Madrid CMF are shown operating the system. Each attendee was required to assemble a test system during the course and to deter-

mine his system's noise figure. Delivery of the systems to each CMF was subject to a representative being present at the seminar.

Figure 2 is a block diagram of the system that includes expanded capabilities planned for fiscal year (FY) 1975 (selectable 1 to 160 MHz reference and a distribution amplifier).

Table 1 lists the system parameters and system accuracies and stability.

Table 1. Synthesizer test set capabilities

Parameters	
$S/N_\phi(f_L, f_H)^a$	for $f_L = 1$ Hz, $f_H = 100$ Hz, 1 kHz, 15 kHz, or 50 kHz
$S/N_{AM}(f_L, f_H)^a$	for $f_L = 1$ Hz, $f_H = 100$ Hz, 1 kHz, 15 kHz, or 50 kHz
$\{f_m\}^a$	for $f_m = 10$ Hz to 50 kHz
$\sigma(2, T, \tau)^a$	for $T \cong \tau = 0.01$ to 100 s
Long term stability at 0.1, 1, or 5 MHz	
Accuracies	
$S/N_\phi(1$ Hz, 15 kHz) measurements to 100 dB; tolerance $\cong \pm 2$ dB	
$S/N_{AM}(1$ Hz, 15 kHz) measurements to 110 dB; tolerance $\cong \pm 2$ dB	
$\{f_m\}$ measurements from -110 dB/Hz to measurement floor of -135 dB/Hz at $f_m = 20$ Hz increasing to an eventual floor of -160 dB/Hz at higher offset frequencies; tolerance $\cong \pm 2$ dB	
$\sigma(2, T, \tau)$ measurements to 2×10^{-12} , expressed in proportional parts, with $T \cong \tau = 1$ s with a system noise $\cong 7 \times 10^{-13}$; tolerance $\cong \pm 2 \times 10^{-13}$	
Long Term Stability measurement limited to aging rate of quartz oscillator, ($< 5 \times 10^{-10}/24$ h)	
^a These parameters can be measured at carrier frequencies from 1 to 160 MHz.	

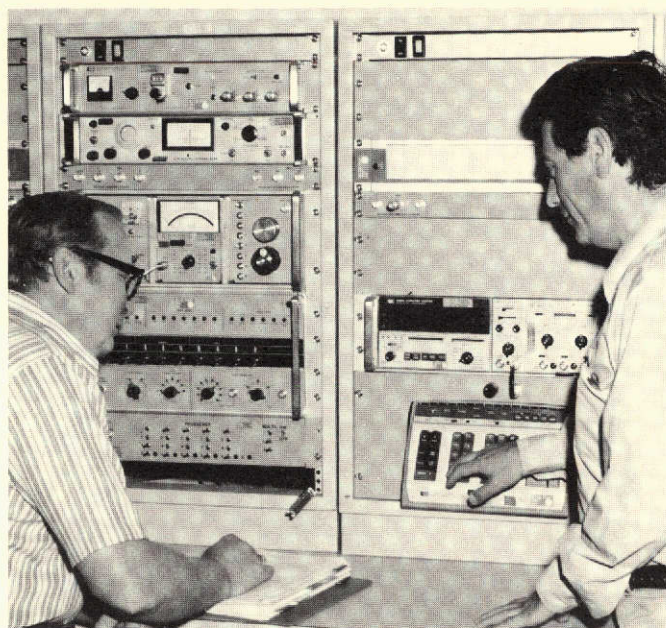


Fig. 1. Front view of synthesizer test set

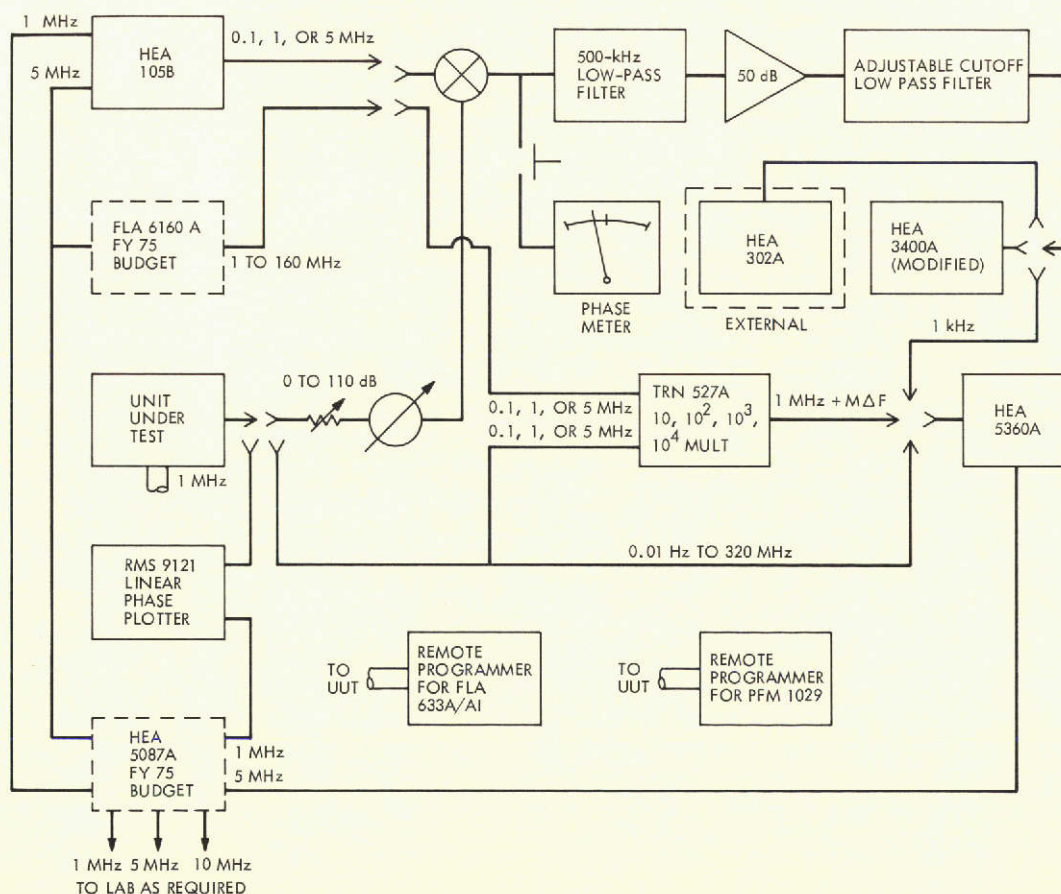


Fig. 2. Block diagram of synthesizer test set

Verification of Commands From the Transmitting Medium

J. R. Lesh
Network Operations Office

A system for bit-by-bit verification of Pioneer command modulation by sampling the S-band transmitted signal directly at the antenna is described. This system was installed at DSS 14 and operated flawlessly during the entire 60-day Pioneer 10 encounter sequence.

I. Introduction

The very long round trip light times and the lack of on board command storage associated with the Pioneer project necessitate an extremely high confidence in the accuracy of commands transmitted to the spacecraft. Ideally, one would like to monitor directly the signal sent to the spacecraft to ensure that no anomalies in command transmission have occurred. In September 1973, the concern for command verification increased in light of the extremely high command activity anticipated for Pioneer 10 encounter (approximately 400 per day). In response to this concern, a system was devised and implemented at DSS 14 that monitored the S-band transmitted energy at the station antenna, detected uplink command modulation, and compared the detected command sequence bit by bit with a replica from the Com-

mand Modulator Assembly (CMA). The only ground rules for the system were that it could not interfere in any way with the operating system and that it must be capable of installation within two months. The scheme was named Command Medium Verification, since it verified commands directly at the transmitting medium.

II. Description of the System

A block diagram of the system is shown in Fig. 1. The S-band transmitted energy is monitored by using the old zero delay antenna. This antenna consists simply of a WR430 waveguide to coaxial adapter mounted in the antenna dish and coupled to the control room through a hardline coaxial cable. Once in the control room, the S-band signal was demodulated by using the Deep Space Instrumentation Facility (DSIF) test transponder.

The DSIF test transponder contains a crystal voltage-controlled oscillator (VCO) and is similar in structure to the Block III C S-band receivers. However, the tracking range of the transponder was significantly less than the doppler profile for the Pioneer spacecraft. To broaden the tracking range, the VCO section was disabled and replaced by a more elaborate VCO consisting of a Fluke 533A synthesizer and a frequency doubler. The Fluke synthesizer was selected since it has a remote search capability that is symmetrical around the selected center frequency. The transmitter section of the transponder was not required and was consequently disabled.

The baseband output of the transponder receiver containing the Pioneer frequency-shift keyed (FSK) command modulation was applied to the Command Medium Verification control unit (shown in Fig. 2) along with the tone output of the appropriate CMA. The purpose of the control unit was to provide bit detection and comparison as well as to provide an interface with an oscillograph recorder. The recorder provided a permanent visual record of the command activity.

The transponder baseband and CMA output were applied to filter amplifiers for amplitude separation of the tones on the recorder. In addition, the signals were applied to phase locked tone decoders that demodulated each tone stream to a command bit sequence. Each bit sequence was then applied to a three-level amplifier for recording on the oscillograph. The three-level amplifier provided one level for a data "1", a second level for a data "0", and a level midway between the others when neither tone frequency was present.

To provide bit error detection, a bit centered clock stream was generated. This was accomplished by utilizing the 100-pulse-per-second (100 pps) signal from the frequency and timing subsystem (FTS) to drive a symmetrical divide by 100 circuit. The divider was inhibited until the time when command modulation was detected. From this point on, the divider would produce a 1-Hz

squarewave with a negative going transition at the center of each command bit. This transition was used to sample each decoded bit stream and, if the samples of the two streams differed, generate an error pulse. The error pulse was recorded on the oscillograph and also was used to turn on an error indicator lamp. To establish the time at which commands and/or errors occurred, a 28-bit digital NASA time code available in the FTS was amplified and recorded on the oscillograph.

The oscillograph recorder used for the system was a Honeywell Model 1508 "Visicorder." This oscillograph uses light reflecting galvanometers to record on photosensitive paper. A sample recording of a 22-bit Pioneer command is shown in Fig. 3.

III. System Performance

The command verification system was installed at DSS 14 in time for the Pioneer 10 encounter sequence. Upon implementation, the system was exercised to determine its operational capabilities. It was found that the modified test transponder could track doppler offset frequencies in excess of 100 kHz (at S-band) on either side of the selected frequency, and that it could follow S-band frequency ramps in excess of 200 Hz/s. Furthermore, the command demodulation and comparison capability was found to be unaffected by these stress conditions until the time at which the transponder receiver broke lock. After initial testing, the system was used without incident by operations personnel during the entire Pioneer encounter period.

IV. Conclusions

The system described in this article represents a satisfactory method for the bit-by-bit verification of the uplink Pioneer command modulation directly at the antenna. Furthermore, the modified receiver scheme presented herein may prove useful in the future for monitoring almost any type of uplink modulation.

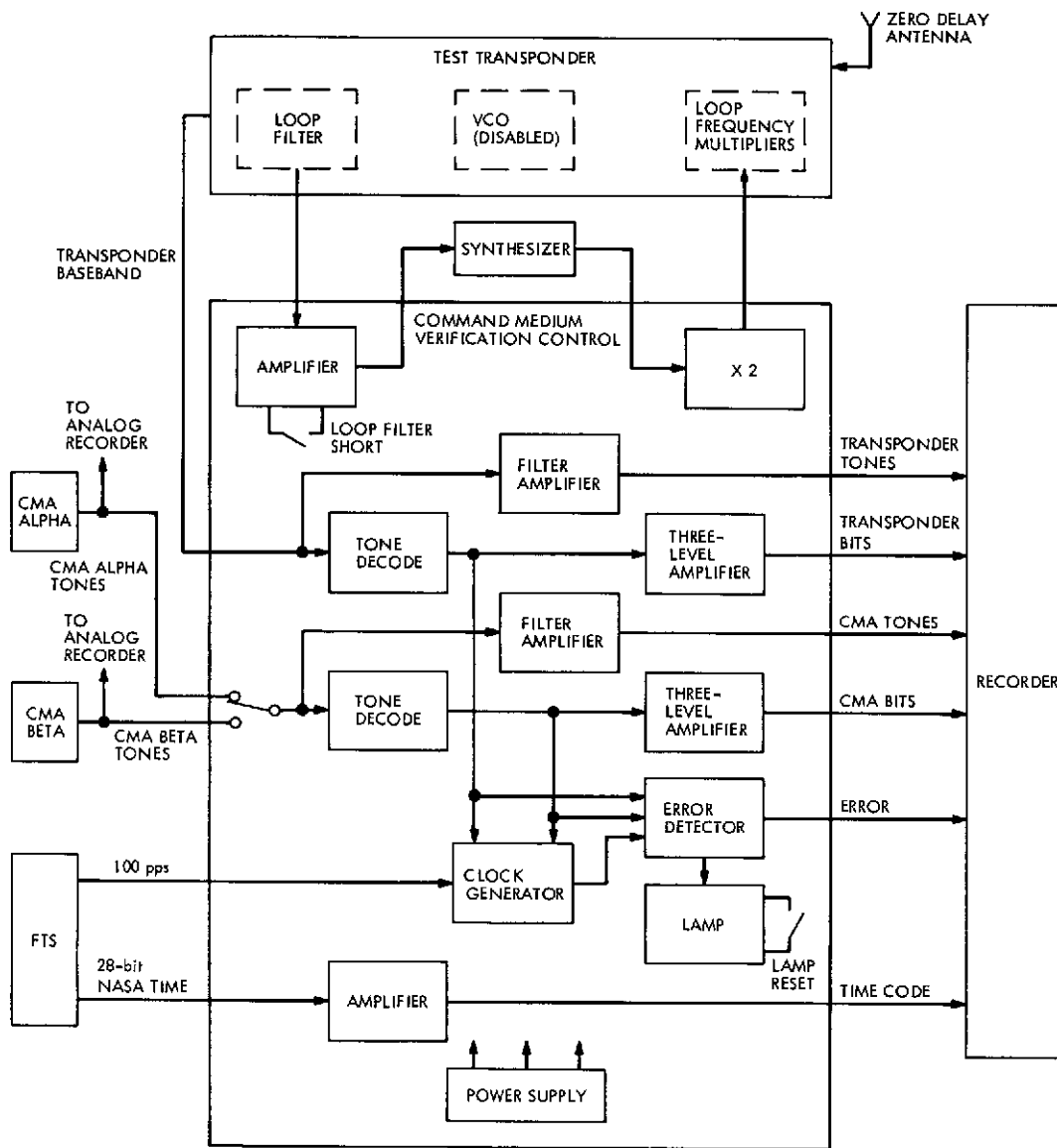


Fig. 1. Function block diagram, Command Medium Verification System

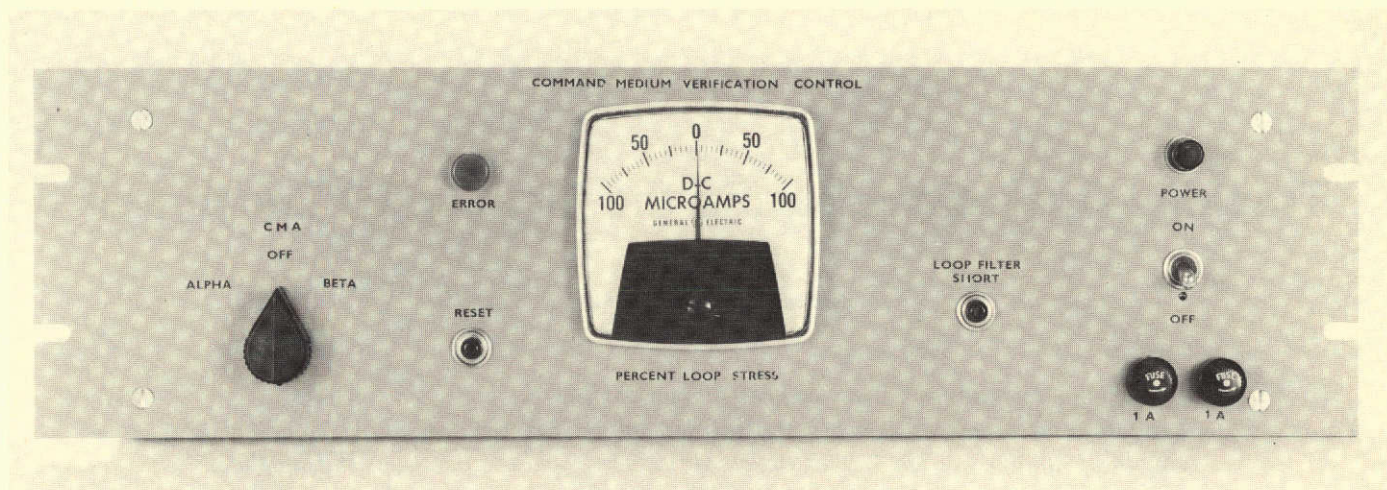


Fig. 2. Front panel, Command Medium Verification control unit

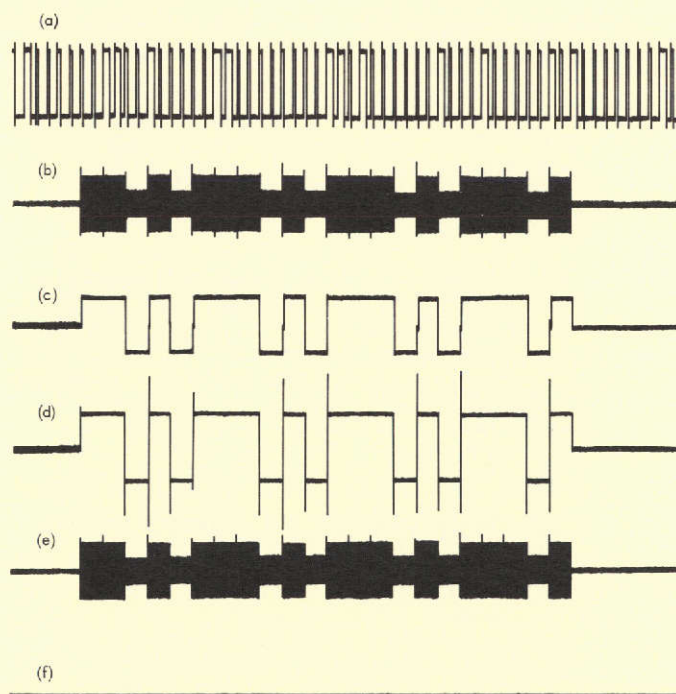


Fig. 3. Typical oscillograph recording of a Pioneer command. Individual traces are: (a) NASA time code; (b) CMA tones; (c) CMA bits; (d) transponder bits; (e) transponder tones; and (f) bit error line (no bit errors present on this recording)

Tracking Operations During the Pioneer 10 Encounter

A. L. Berman
Network Operations Office

Tracking operations during critical mission phases have become increasingly complex due to more sophisticated mission objectives and expanded tracking capability within the DSN. This article describes tracking operations during the Pioneer 10 Jupiter encounter phase with special attention paid to the role of the newly-installed digital controlled oscillator.

I. Introduction

On December 4, 1973, at 02:25:28 GMT (spacecraft time), the Pioneer 10 Spacecraft reached closest approach to the planet Jupiter. During the near encounter period, which bracketed the closest approach time by several hours, the spacecraft was occulted in turn by the Jovian moon Io and by Jupiter itself. Complicating this encounter was a round-trip light time (RTLTL) of approximately 92 min, which was a considerably longer RTLTL than had been experienced during any of the previous planetary encounters conducted by the Jet Propulsion Laboratory. At the same time, the Deep Space Network (DSN) tracking system had entered a period of rapid expansion; for instance, new capabilities recently or shortly to be committed for support are: high speed data (HSD) transmission, Block IV receivers, X-band capability, planetary discrete ranging, 10/s data sample rate and the digitally controlled oscillator (DCO). To varying degrees, implementation of each of the above complicates tracking operations, and, in the case of Pioneer 10 encounter, just the use of the DCO added greatly to the complexity of critical phase tracking operations.

At this point, a brief description of the DCO is in order (greater detail is available in Refs. 1, 2, and 3). Basically, the DCO consists of a Dana Model 7010-S-241 digiphase synthesizer and a control assembly. The control assembly contains manual programming capability to generate frequency sweeps that can be manually programmed in advance to occur at specified station times in hours: minutes:

seconds. A total of four rates can be stored with corresponding start times to generate a sequence of up to four linear ramps without further adjustment during a given period. As each ramp is executed, an additional ramp can be manually programmed to bring the stored total back to four. Two other sweep control features are included to aid acquisition and station handovers. Primarily for use in the receiver is the acquisition (acq) mode, which generates a triangular frequency sweep at a fixed sweep rate between prestored upper and lower limits, and primarily for use in the exciter is the track (trk) mode, which provides the capability to start a frequency sweep at a precise time and at a fixed sweep rate and to sweep to another fixed frequency.

The most obvious advantages of the DCO are apparent in its use in the exciter. Sweeps to acquire the uplink can now be set up well in advance of the actual time, and can be effected with an exact start time, an exact tuning rate, and an exact end time. Furthermore, the precision of the DCO is so great that doppler data during tuning is of the same order of quality as doppler data at a constant track synthesizer frequency (TSF). The more obvious complications posed by the DCO appear in conjunction with its use in the receiver. Previous to the DCO, tuning to acquire the downlink was done manually by an operator who swept the receiver against page print predicts and waited to detect an audio beat—the flexibility of this system residing in the fact that the operator could easily reverse the direction of the sweep if he felt that he was

not sweeping in the right direction or was in the wrong frequency region. The DCO in the receiver, on the other hand, must be exactly preprogrammed as to sweep rates and sweep limits, and if for some reason these do not result in an acquisition, new receiver sweep limits must be calculated by hand or electronic calculator (DCO receiver predicts are not included in regular JPL tracking prediction output), and manually entered into the DCO registers—both functions being time consuming and prone to error.

In the following sections, the frequency management strategy for the Io and Jupiter occultations and the ground receiver reacquisition strategy at Io and Jupiter exit occultations are discussed, with special attention paid to the role of the DCO in both events.

II. Io Occultation

The original intent for the Io occultation was to have DSS 14 enter Io occultation in the two-way mode, with DSS 43 acquiring the uplink shortly after exit Io occultation. After the initial meeting of the Pioneer 10 Occultation Planning Committee, it became evident that something far more desirable might be attainable—exit Io occultation in the two-way mode. This would be of considerable importance to the occultation experimenters and would provide as a bonus additional two-way data for the celestial mechanics experimenters. The fortuitous combination of circumstances that allowed this enhanced goal were:

- (1) The spacecraft best lock corrected for doppler (XA) during the time period surrounding Io occultation was very nearly linear.
- (2) The newly installed DCOs at DSS 14 and DSS 43 could follow the XA curve during the Io occultation period almost exactly with just one linear ramp.

The general plan to attempt an exit Io occultation in the two-way mode follows: DSS 14 would begin ramping with the DCO at exactly the predicted XA and with a rate equal to the XA rate sometime prior to predicted enter Io occultation (this to account for the sizable uncertainties in the enter and exit times), and would continue until some time after the predicted Io exit time. This would cause the spacecraft receiver to be left at exactly the predicted XA and subsequently would hit the spacecraft with the predicted XA at exactly the moment of exit occultation. Although the spacecraft would be left at the predicted XA at enter occultation, it would immediately begin to drift to whatever the actual XA was. However,

the amount of drift would be quite small. Weeks prior to the occultation, the following $3\text{-}\sigma$ uncertainties were assumed:

$$\text{one-way doppler } (3\sigma) = 15 \text{ Hz (at voltage-controlled oscillator (VCO) level)}$$

$$\text{spacecraft best lock } (3\sigma) = 25 \text{ Hz (at VCO level)}$$

These result in a combined XA $3\text{-}\sigma$ uncertainty of approximately 30 Hz. The length of Io occultation was approximately 90 s and the spacecraft receiver relaxation constant was 1320 s, so that one could calculate a total drift away from predicted XA in the $3\text{-}\sigma$ case as:

$$XA_A = \text{actual best lock with doppler}$$

$$XA_P = \text{predicted best lock with doppler}$$

$$XA_S = \text{spacecraft receiver at a given time}$$

so that at enter:

$$XA_A - XA_P \cong 30 \text{ Hz}$$

and at exit:

$$\begin{aligned} \Delta XA &= XA_S - XA_P \\ &= 30 \text{ Hz } (1 - e^{\Delta t/t_0}) \\ &= 30 \text{ Hz } (1 - e^{-90/1320}) \\ &\approx 2 \text{ Hz} \end{aligned}$$

Considering a more reasonable $1\text{-}\sigma$ case, one would have a total drift of only $\frac{2}{3}$ Hz (at VCO level) away from the transmitted signal (XA_P) at exit, so that one would expect to lock up at the spacecraft almost immediately.

After exit, DSS 14 would be presumed to have the uplink, and a transfer to DSS 43 would be effected. Finally, in the event that DSS 14 did not reacquire the uplink, DSS 43 would sweep the uplink with its exciter DCO as a backup to insure acquisition of uplink. Using the following definitions:

let

$$T_1 = \text{time of } 3\text{-}\sigma \text{ earliest enter Io occultation at DSS 14}$$

$$T_2 = \text{time of } 3\text{-}\sigma \text{ latest exit Io occultation at DSS 14}$$

$$T_E = \text{nominal time of enter occultation at DSS 14}$$

$$T_X = \text{nominal time of exit occultation at DSS 14}$$

so that:

$$T_1 = T_E - 3\sigma$$

$$T_2 = T_X + 3\sigma$$

with 3σ defined as 45 s, the finalized strategy was as follows:

- (1) Prior to enter, DSS 14 transmits a constant uplink DCO frequency equal to predicted XA at $T_1 - 30$ s.
- (2) At time = $T_1 - 30$ s, DSS 14 begins tuning at a DCO rate equal to the predicted XA rate and continues until time = $T_2 + 32$ s, at which time the transmitter is turned off.
- (3) At time = $T_2 + 30$ s, DSS 43 turns on its transmitter at a DCO frequency equal to its predicted XA at $T_2 + 30$ s, and begins tuning at a DCO frequency rate equal to its predicted XA rate until time = $T_2 + 60$ s is reached.
- (4) At time = $T_2 + 60$ s, DSS 43 sweeps its DCO frequency up to predicted XA + 40 Hz, down to XA - 20 Hz, and then remains at that DCO frequency until Jupiter occultation.

The above strategy is shown in Fig. 1. This graph was prepared from predictions based on an orbit determination (OD) solution (actually Probe Ephemeris Tape (PET) Number 6526), which was available approximately five days prior to encounter. However, one problem remained—how to recompute and transmit to the stations in a timely fashion all the new frequencies, rates, and times based on each new OD solution as it might become available. This problem turned out to be amenable to a very simple procedure. The key to this procedure was the fact that XA (upon which the ramps were based) was essentially linear during this period, and the degree of linearity was essentially independent of OD solution (whereas event times and doppler were definitely not):

$$\frac{d(XA)}{dt} \approx C_0$$

where C_0 is relatively insensitive to differing OD solutions.

Since the above was true, none of the ramp rates need change, regardless of the OD solution. Choosing the center of Io occultation (time of, XA of) as a reference point, one only need plot this one event point from each new solution to update the strategy—the horizontal displacement between the new solution and reference point gives

the time bias to be applied to all times and the vertical displacement between the reference point and the new solution similarly gives the frequency bias to be added to all frequencies. Center of Io points from solutions (PETs) 6527 through 6530 can be seen plotted on Fig. 1. Solution (PET) 6529 was that actually used during the encounter (it was available approximately 48 h prior to encounter) and biases from the reference OD solution (6526) were:

$$\Delta \text{ frequency} = -4 \text{ Hz}$$

$$\Delta \text{ time} = +80 \text{ s}$$

The results of this effort were not immediately known, as the closed loop ground receivers failed to acquire the downlink immediately following exit Io occultation, however, subsequent investigation of the open loop receiver data taken during exit Io occultation shows that the downlink was indeed two-way at exit.

III. Tuning to Acquire the Uplink After Exit Jupiter Occultation

A simple sweep of predicted XA ± 50 Hz (at VCO level) was planned to acquire the uplink after exit Jupiter occultation (note: this sweep takes place before ground observed *enter* occultation); this sweep can be seen in Fig. 2, based on solution 6526. It was planned to keep both the ramp times and rate fixed and only adjust the start and end frequencies based on each solution; thus, the doppler at 04:12:00 GMT from each new solution was plotted on Fig. 2. A conflict within the sequence of events (SOE) necessitated a last minute change to the times of the sweep also so that the final biases applied to the sweep were:

$$\Delta \text{ frequency} = +33 \text{ Hz}$$

$$\Delta \text{ time} = -4 \text{ min}$$

The frequency bias was composed of the XA change between solutions 6526 and 6529, plus the XA change caused by a time shift of 4 min. This uplink sweep successfully acquired the spacecraft.

IV. Fast Ground Receiver Acquisitions

As was mentioned in Section I, use of the ground receivers in time-critical reacquisitions of the downlink is somewhat complicated by the DCO, as compared to the previous manual timing performed by the receiver operator; the Pioneer 10 encounter marked the first use of the

DCO during a critical phase. The three events when rapid reacquisition of the downlink was of considerable importance, were (in order of importance):

- (1) Jupiter exit occultation.
- (2) Io exit occultation.
- (3) One-way out of lock condition at transmitter off time prior to Jupiter enter occultation.

It was decided that the DCO acq mode would provide the best chance for a fast reacquisition in the above events. In the acq mode, the DCO drives the receiver back and forth over a fixed frequency range with a fixed sweep rate. This has one obvious drawback in that for the most optimum case of a ground receiver search, one wishes to sweep back and forth about a doppler profile that is not a fixed frequency but more usually a strongly varying function of time. The trade-off with the acq mode is that one must increase the sweep range to encompass the amount of doppler change as well as doppler and other uncertainties during the period in which one expects to lock up. As mentioned previously, the most important fast reacquisition was that upon exit Jupiter occultation; Fig. 3 shows the one-way doppler and the one-way doppler with expected atmospheric corrections as of solution 6526 approximately 5 days before encounter. Successive solutions 6527 through 6530 are also plotted as exit occultation points (time of, *DI* of). In this particular case it was felt that a sweep of ± 3000 Hz (S band) about both *DI* and *DI* plus atmospheric corrections would suffice to include both uncertainties due to doppler and the spacecraft auxiliary oscillator; however, since there was also a large uncertainty in time of exit occultation, it was decided to increase the sweep to ± 4500 Hz to account for change of doppler with time. This allowed both the doppler and atmospherically corrected doppler to be swept ± 3000 Hz from a time of nominal exit -135 s to a time of nominal exit $+135$ s. A sweep rate of 300 Hz/s (S band) was selected (based upon pre-encounter test results) which meant that with both station receivers being swept asynchronously, one could expect a lock up of the downlink no later than 60 s after exit. The receivers were started at

exit occultation $-12:00$ min and the center point of the sweep corresponded to the doppler at exactly exit occultation. The time and doppler were chosen from solution 6529; see Fig. 3. Two changes were made to this procedure in near real time: (1) the center doppler value was adjusted for a $+2200$ -Hz frequency change in the auxiliary oscillator, which was noted just prior to enter occultation, and (2) because of slow ground receiver lock up times at Io exit occultation and at the transmitter off time (one-way out of lock), one of the two receivers was swept at 100 Hz/s (S band) instead of 300 Hz/s. As it turned out, the receiver sweeping at 300 Hz/s locked first at approximately 05:30:24 GMT, which was 33 s after the best estimate of exit Jupiter occultation at 5:29:51. This falls within the expectation of ground receiver lock no later than 60 s after exit occultation.

The results of downlink reacquisition at Io exit and especially at the transmitter off time are less satisfactory. In both cases the doppler at exit Io occultation and at the one-way out of lock condition (an RTLTL after transmitter off) were swept ± 4500 Hz at 300 Hz/s. The best estimate of exit Io occultation was 03:29:18 GMT and DSS 43 locked up receiver 1 at 03:29:40 GMT or 22 s later. However, the doppler extractor was connected to receiver 2 and it did not lock up until 03:31:06 GMT or 108 s after Io exit. DSS 14 was not able to reacquire the downlink until 03:35:35 or 6 min 17 s after exit. Finally, reacquisition of the one-way downlink after transmitter off, which should have been the easiest of the three reacquisitions, turned out to be the most difficult. The ground received time of transmitter off was 04:03:56 GMT, and the first station to reacquire lock was DSS 14 at 04:05:33 GMT or 97 s later. DSS 43 was not able to confirm good one-way downlink until 04:10:40 GMT or 6 min 44 s after transmitter off. The unexpectedly long downlink reacquisition time at Io exit and at transmitter off time are under continuing investigation, but to date this analysis has yielded contradictory results (at the same time it should be noted that open loop predicts were provided for both Io and Jupiter occultations, and open loop data were successfully acquired in each case).

References

1. Wick, M. R., *Operational Procedure—Block III High Rate Doppler Receiver/Exciter Subsystem*. Specification OP 509255 A. Jet Propulsion Laboratory, Pasadena, Calif., Aug. 15, 1973 (JPL internal document).
2. Donnelly, H., and Wicks, M. R., "Programmed Oscillator Development," in *The Deep Space Network Progress Report*, Vol. X, pp. 180–185. Technical Report 32-1526. Jet Propulsion Laboratory, Pasadena, Calif., Aug. 15, 1973.
3. Wick, M. R., "DSN Programmed Oscillator Development," in *The Deep Space Network Progress Report*, Vol. VII, pp. 111–124. Technical Report 32-1526. Jet Propulsion Laboratory, Pasadena, Calif., Apr. 15, 1972.

